Modelling the hydrology of the Greenland Ice Sheet

Alison F. Banwell

ST CATHARINE'S COLLEGE

SCOTT POLAR RESEARCH INSTITUTE

UNIVERSITY OF CAMBRIDGE

This dissertation is submitted for the degree of

Doctor of Philosophy

2012

Declaration

This dissertation is the result of my own work and includes nothing which is the outcome of work done in collaboration except where specifically indicated in the text and Acknowledgements. It has not been submitted in whole or in part for a degree at any other university. This thesis is 185 pages long, including text, illustrations, tables and references.

Alison Banwell

September 2012

Acknowledgements

First and foremost, I would like to thank my PhD supervisors, Ian Willis and Neil Arnold. Their continual guidance, encouragement and support throughout my time at the Scott Polar Research Institute (SPRI) has been invaluable and I feel privileged to have had the opportunity to undertake such a fascinating research project.

The research presented in this thesis was undertaken whilst I was the recipient of a Natural Environment Research Council (NERC) studentship (ref. LCAG/133) (CASE studentship with Geological Institute of Denmark and Greenland (GEUS)). I am very grateful to Andreas Ahlstrom at GEUS for his helpful advice, data provision and logistical help with fieldwork equipment. The Royal Geographic Society, St Catharine's College, the Scandinavian Studies Fund, and the B.B. Roberts Fund are all acknowledged for financially supporting part of the fieldwork activities.

I would like to thank Marco Tedesco from City College of New York for inviting me to join his fieldwork team in the Paakitsoq region in summer 2011, and Alun Hubbard for his logistical help in collecting the longwave radiation data on Russell glacier in summer 2009. I am grateful to Doug Benn for his help and support while I was based at UNIS. Thanks also go to Koni Steffen and co-workers for providing the GC-Net weather station data. The proglacial discharge and precipitation data were generously provided by Dorthe Peterson at the ASIAQ Greenland Survey.

Many thanks also go to Philip Stickler from the Cartography Unit in the Department of Geography and to MPhil Student Jerome Mayaud for producing several of the schematic diagrams that are used in the text. I am also very grateful to Mike Bithell, Shane Harvey, Dan Scott and Martin Lucas-Smith in the Department of Geography for all their computer and web support.

Thanks too to all the glaciology post grads, past and present – Adrian, Allen, Cameron, Christine, Craig, Martin, and Narelle – for their company and inspiration during my time at SPRI. Additional thanks go to Nick Barrand at BAS for his help and support during my PhD. Finally, I am very grateful to my family, and in particular, my parents, Sally and Tony, for their support and encouragement over the last four years.

Abstract

There is increasing recognition that the hydrology of the Greenland Ice Sheet plays an important role in the dynamics and therefore mass balance of the ice sheet. Understanding the hydrology of the ice sheet and being able to predict its future behaviour is therefore a key aspect of glaciological research. To date, the ice sheet's hydrology has tended to be inferred from the analysis of surface velocity measurements, or modelled in a theoretical, idealised way. This study focuses on the development of a high spatial (100 m) and temporal (1 hour) resolution, physically based, time-dependent hydrological model which is applied to the ~2,300 km^2 Paakitsoq region, West Greenland, and is driven, calibrated, and evaluated using measured data. The model consists of three components.

First, net runoff is calculated across the ice sheet from a distributed, surface energy-balance melt model coupled to a subsurface model, which calculates changes in temperature, density and water content in the snow, firn and upper-ice layers, and hence refreezing. The model is calibrated by adjusting key parameter values to minimize the error between modelled output and surface height and albedo measurements from the three Greenland Climate Network (GC-Net) stations, JAR 1, JAR 2 and Swiss Camp. Model performance is evaluated in two ways by comparing: i) modelled snow and ice distribution with that derived from Landsat-7 ETM+ satellite imagery using Normalised Difference Snow Index (NDSI) classification and supervised image thresholding; and ii) modelled albedo with that retrieved from the Moderate-resolution Imaging Spectroradiometer (MODIS) sensor MOD10A1 product. Second, a surface routing / lake filling model takes the time-series of calculated net runoff over the ice sheet and calculates flow paths and water velocities over the snow / ice covered surface, routing the water into 'open' moulins or into topographic depressions which can fill to form supraglacial lakes. This model component is calibrated against field measurements of a filling lake in the study area made during June 2011. Supraglacial lakes are able to drain by a simulated hydrofracture mechanism if they reach a critical volume. Once water is at the ice / bed interface, discharge and hydraulic head within

subglacial drainage pathways are modelled using the third model component. This consists of an adaptation of a component (EXTRAN) of the U.S. Environmental Protection Agency Storm Water Management Model (SWMM), modified to allow for enlargement and closure of ice-walled conduits.

The model is used to identify how the subglacial hydrological system evolves in space and time in response to varying surface water inputs due to melt and lake drainage events, driven ultimately by climate data. A key output from the model is the spatially and temporally varying water pressures which are of interest in helping to explain patterns of surface velocity and uplift found by others, and will ultimately be of interest for driving ice dynamics models.

List of Abbreviations

ASTER	Advanced Spaceborne Thermal Emission and Reflection Radiometer
AWS	Automatic weather station
CSA	Cross-sectional area
DEM	Digital elevation model
DMI	Danish Meteorological Institute
EB	Energy balance
EXTRAN	Extended Transport block (of SWMM)
GC-Net	Greenland Climate Network (AWSs)
GDEM	Global digital elevation model
GRACE	Gravity Recovery and Climate Experiment
GrIS	Greenland Ice Sheet
IPCC	Intergovernmental Panel on Climate Change
ETM+	(Landsat) Enhanced Thematic Mapper
MAR	Modèle Atmosphérique Regional
MODIS	Moderate-Resolution Imaging Spectroradiometer
MODFLOW	Modular Finite-Difference Groundwater Flow Model
NAMOC	North Atlantic Meridional Overturning Circulation
NAO	North Atlantic Oscillation
NDSI	Normalised Difference Snow Index
PDD	Positive degree-day
RCM	Regional climate model
RMSE	Root mean square error
SEB	Surface energy balance
SMB	Surface mass balance
SRLF	Surface routing / lake filling (model)
SWIF	Shortwave infrared
SWMM	Storm Water Management Model
UDG	Ultrasonic depth gauge
USGS	United States Geological Survey

Mathematical Notation

σ	Stefan-Boltzmann constant (W m^{-2} K^{-4})
ρ_i	Ice density (kg m^{-3})
ρ_w	Water density (kg m^{-3})
ρ_{top}	Density upper subsurface grid element (kg m^{-3})
θ	Surface slope (°)
ϕ	Hydraulic potential (Pa)
α	Surface albedo
α_{ice}	Ice albedo
α_{snow}	Snow albedo
A_c	Cross-sectional area of conduit (m^2)
A_f	Cross-sectional area of flow (m^2)
B	Degree-day factor (mm w.e. d^{-1} °C^{-1})
$B2$	Landsat Band 2
$B5$	Landsat Band 5
C	Rate of conduit closure (m^2 t^{-1})
C_i	Water velocity across bare ice (m s^{-1}),
C_s	Water velocity under a snowpack (m s^{-1})
e	Vapor pressure (Pa)
E_{cs}	Clear sky emissivity
E_{oc}	Overcast sky emittance
f_r	Friction coefficient
g	Acceleration due to gravity (m s^{-2})
GHF	Ground heat flux
h	Ice surface elevation (m)
H	Hydraulic head (m)
K	Snow porosity
k	flotation fraction (P_w / P_i)
L	Latent heat of fusion of water (J kg^{-1})
LHF	Latent heat flux

$LW\uparrow$	Outgoing longwave radiation
$LW\downarrow$	Incoming longwave radiation
LW_{net}	Net longwave radiation
m	Exponent in Glen's flow law
M	Rate of conduit-wall melting (kg t^{-1})
N	Calculated melt (mm w.e.)
n	Manning roughness coefficient ($m^{-1/3}$ s)
P_w	Water pressure (Pa)
P_i	Ice pressure (Pa)
Q	Discharge (m^3 s^{-1})
Q_M	Energy available for melt
R	Hydraulic radius (m)
RH	Relative humidity
SHF	Sensible heat flux
S_f	Friction slope
$SW\downarrow$	Incoming shortwave radiation
$SW\uparrow$	Outgoing shortwave radiation
SW_{net}	Net shortwave radiation
SWIR	Shortwave infrared
T	Temperature at 2 m above the ice surface (°C)
T_{pdd}	Sum of positive daily mean temperatures (°C)
T_s	Temperature of top grid cell (°C)
t	Time-step (s)
μ	Water viscosity (Pa s)
v	Cloud amount (%)
V	Water velocity (m s^{-1})
x	Snow permeability (m^2)
X	*S*now permeability / effective snow porosity (m^2)
z	Ice bed elevation (m)
Z	Threshold snowpack thickness for Darcian / channelized flow switching (m w.e.)

Contents

List of Figures

List of Tables

1. Introduction

1.1 Rationale

The Greenland Ice Sheet (GrIS) is the largest terrestrial permanent snow and ice covered area in the Northern Hemisphere. It lies between 60 and 83° N, and extends 2,500 km from north to south and up to 1,000 km from east to west. At its thickest point, the ice is 3,300 m thick. With a volume of 2.93 million km^3, the GrIS contains 10% of the Earth's total fresh water [*AMAP,* 2009]. The GrIS has a major climatic influence in the northern hemisphere, affecting atmospheric circulation, North Atlantic ocean currents, and global sea level [*Clark et al.,*1999].

Assessing the impact of climate change on the GrIS is important as the average temperature rise in the Arctic has increased at almost twice the global average rate in the past 100 years [*Meehl et al.,* 2007] and is likely to continue at this rate into the future [*AMAP*, 2009; *Graversen et al.,* 2011]. Previous modelling studies have shown that a 1 °C rise in surface air temperature over Greenland produces 20% – 50% more melt [*Oerlemans* 1991; *Braithwaite and Olesen,* 1993; *Ohmura et al.,* 1996; *Janssens and Huybrechts*, 2000; *Hanna et al.,* 2005], so a predicted rise in air temperature of 2 – 5 °C would approximately double total melt [*Mernild et al.,* 2008]. Although feedbacks associated with increased surface melt are complex and the overall sign of the feedback (positive or negative) is unknown, increased surface melt is likely to result in reduced albedo and increased incident energy absorption leading to further melt [*Tedesco et al.,* 2011].

Currently the GrIS is losing more mass through meltwater runoff and iceberg calving than it is gaining through snowfall, indicating that it has a negative net mass balance [*Fettweis*, 2007; *Rignot et al.,* 2008; *Velicogna,* 2009; *Box et al.,* 2011; *Rignot et al.,* 2011]. Recent estimates from the Gravity Recovery and Climate Experiment (GRACE) indicate that the rate at which the GrIS is losing mass accelerated from 137 Gt a^{-1} measured over 2002 - 2003, to 286 Gt a^{-1} measured over 2007 - 2009, and then to 430

Gt a^{-1} measured over 2010 - 2011 [*Velicogna and Wahr*, 2006; *Velicogna,* 2009; *Box et al.,* 2011]. The mass budget record over the last 18 years (which shows a good agreement with GRACE data over the last 8 years), indicates that the acceleration in mass loss from the GrIS has been 21.9 ± 1 Gt a^{-2} [*Rignot et al.,* 2011]. This rapid increase in mass loss is mainly a result of increased wastage at the margins [*Alley et al.,* 2010; *Chen et al.,* 2011; *Seale et al.,* 2011; *Zwally et al.,* 2011], due partly to increased iceberg calving and associated acceleration and thinning of marine-terminating outlet glaciers [*Rignot and Kanagaratnam*, 2006; *Howat et al.,* 2011], but also to increased surface meltwater runoff affecting both marine- and land-terminating outlet glaciers [*Mote,* 2007; *van den Broeke et al.,* 2009], which may be facilitated, at least in part, by increases in the melt area extent [*Tedesco,* 2007; *Fettweis et al.*, 2010].

A key consequence of future climate change concerns likely future sea level rise, predicted to be between 18 and 59 cm over the 21st Century, with a significant proportion of this likely to come from shrinkage of the GrIS [*Meehl et al.,* 2007]. If it were to melt completely, the GrIS has the potential to contribute 7 m to global sea-level rise [*Alley et al.,* 2005]. Additionally, a sudden flux of cold freshwater from the GrIS into the North Atlantic has the potential to weaken, or turn off, the North Atlantic Meridional Overturning Circulation (NAMOC) by suppressing the formation of dense waters off the coast of Greenland [*Broeker et al*., 1998; *Fichefet et al.,* 2003; *Rahmstorf et al.,* 2005]. Using an Earth system model, which includes coupled atmosphere, ocean, and ice sheet components, *Vizcaino et al.* [2008] show that NAMOC shuts down in the most extreme warming scenarios predicted for the future. However, once the NAMOC shutsdown, the rate of GrIS melt decreases in response to a colder northern hemisphere climate. Historically, this occurred during the demise of the Laurentide ice sheet, and such an influx is the suspected cause of the ~ 1,400 year Younger Dryas cold period [*Anderson,* 1997; *Broeker,* 2006]. A key question is whether the shrinkage of the GrIS melt will be able to cause a similar abrupt climate change in the near future [*Alley,* 2007; *Thornalley et al.,* 2010]. Other ocean modelling studies have been undertaken in an attempt to understand both the short- and long-term influences on ocean circulation and climate of a large freshwater flux entering the North Atlantic [*Hu et al.,* 2004; *Mu et al.,* 2006], but compared to the *Vizcaino et al.* [2008] analysis, these studies lack predictions of future GrIS runoff from high-resolution models.

Although the GrIS has been known to speed up during the summer and slow down

during the winter for over 20 years [*Andreasen,*1985], identifying the links between these dynamic variations and ice sheet hydrology has only been attempted more recently. Several studies have shown that surface meltwater can reach the bed of the ice sheet through moulins and crevasses, often as a result of supraglacial lake drainage events [*Zwally et al.,* 2002; *Alley et al.,* 2005; *Joughin et al.,* 2008]. Rapid lake drainage via hydrofracture is thought to be an important mechanism for generating hydrological linkages between the surface and the bed, since the large volumes of surface water are necessary to propagate crevasses to the base of the ice sheet [*Das et al.,* 2008; *Krawczynski et al.,* 2009]. The ice sheet can respond quickly to these events, and both surface uplift, due to higher transient water storage and pressures at the bed, and increases in surface velocity, due to decreased basal stress, have been observed and modelled [*Das et al.,* 2008; *Pimentel and Flowers,* 2010; *Tedesco et al.,* in review]. Once connections form between the ice surface and bed, subsequent diurnal variations in ice velocity in response to daily ablation cycles suggest that the connections can remain open throughout the melt season [*Shepherd et al.,* 2009; *Bartholomew et al.,* 2010; *Catania and Neumann*, 2010]. Seasonal variations in ice velocity suggest that when integrated over weeks to months, these shorter-term dynamic events associated with lake drainage and diurnal cycles are sufficient to cause faster motion in the summer and slower movement in the winter. It has been suggested recently that it is the *variability in magnitude and timing of meltwater input* to the subglacial drainage system of the GrIS, rather than the *total volume of meltwater input to the system*, that has the greatest influence on subglacial water pressures and therefore ice motion [*Schoof,* 2010; *Bartholomew et al.,* 2011b*; Colgan et al.,* 2011]. Rapid short-term increases in surface water input to a low capacity drainage system early in the summer may cause bigger increases in water pressure and hence uplift and basal motion, than long, sustained higher volumes of surface melt water later in the season. Similar results were found in response to field measurements and numerical modelling conducted on valley glaciers [*Iken et al.,* 1983; *Iken and Bindschadler*, 1986; *Hooke et al.,* 1989; *Mair et al.,* 2003].

There is still much uncertainty, however, about how the surface hydrology of the GrIS interacts with the englacial and subglacial drainage system, and affects basal water pressures, uplift and ice velocity over seasonal timescales. There is even more uncertainty about how changes in melt and surface hydrology in the future will influence the spatial and temporal patterns of ice movement into the 21st century. If

average air temperatures over Greenland continue to increase the intensity of surface melt, recent evidence suggests that lakes will drain earlier in the melt season and that the lake population will extend to higher elevations, likely exposing an increased inland area of the ice sheet to sudden lake drainage events and subsequent hydraulic connections between surface and bed [*Sundal et al.,* 2011; *Liang et al.,* 2012]. Thus, a key question is how the GrIS hydrological system will evolve over decadal and longer timescales to increased surface melt [*Bartholomew et al.,* 2010; *Schoof,* 2010].

As a consequence of the uncertainties outlined above, the effect of surface melt and hydrology on ice sheet flow is not explicitly accounted for in current predictive ice sheet models, leading to possible underestimation in Intergovernmental Panel on Climate Change (IPCC) projections of future sea level change [*Rignot and Kanagaratnam,* 2006; *Meehl et al.,* 2007]. A better understanding of the linkages and feedbacks between climate, surface melt, and the surface, englacial and subglacial drainage systems of the GrIS is needed to determine the sensitivity and response of the ice sheet's dynamics to an increasingly warmer climate.

As the review above demonstrates, there have been a series of field-based geophysical studies recently that have attempted to infer the behaviour of the GrIS's subglacial drainage system from measurements of meteorology and surface velocity and uplift [e.g., *Zwally et al.,* 2002; *Das et al.,* 2008; *Bartholomew et al.,* 2010; 2011; *Tedesco et al.,* in review]. Additionally, there have been a few small-scale, largely hypothetical idealised modelling studies that have attempted to incorporate hydrological theory into a time-dependent modelling framework to investigate specific attributes of ice sheet hydrological behaviour [e.g., *Pimentel and Flowers,* 2010; *Schoof,* 2010]. To date, however, there has been little attempt to develop a physically based, time-dependent, distributed hydrological model and apply it to a real situation on the GrIS, driven, calibrated and evaluated with measured data, This is the key aim of this thesis.

1.2 Research aim and approach

The discussion above creates a key focus for this thesis:

- To develop a high spatial (100 m) and temporal (1 hour) resolution, physically based, time-dependent hydrological model and apply it to the ~2,300 km^2 Paakitsoq region, western Greenland, and drive it, calibrate it, and evaluate it

using real data. The model will be used to identify how the subglacial hydrological system evolves in space and time in response to varying surface water inputs due to melt and lake drainage events, driven ultimately by climate data. A key output from the model will be spatially and temporally varying water pressures which will be of interest in helping to explain patterns of surface velocity and uplift found by others, and will ultimately be of interest for driving ice dynamics models.

The overall aim of this thesis can be divided into three objectives, one for each key component of the complete physically based, distributed, time-dependent ice sheet hydrology model:

- Develop and apply a surface mass balance (SMB) model to the Paakitsoq region. This model will consist of a surface energy balance (SEB) model coupled to a subsurface model which will calculate changes in temperature, density and water content in the snow, firn and upper-ice layers, and hence refreezing and therefore net runoff. The model will be forced using a full range of meteorological variables, predominantly from the JAR 1 Greenland Climate Network (GC-Net) weather station [*Steffen and Box*, 2001]. Coastal precipitation data will be obtained from ASIAQ Greenland Survey. The model will be calibrated by adjusting key parameter values to minimize the error between modelled output and surface height and albedo measurements from the three GC-Net stations, JAR 1, JAR 2 and Swiss Camp. Model performance will be evaluated, first, by comparing modelled snow and ice distribution with that derived from Landsat-7 ETM+ satellite imagery using Normalised Difference Snow Index (NDSI) classification and supervised image thresholding; and second, by comparing modelled albedo with that retrieved from the Moderate-resolution Imaging Spectroradiometer (MODIS) sensor MOD10A1 product. Output from this model will be hourly runoff for each grid cell.

- Develop and apply a surface water routing and lake filling model to a subset of the Paakitsoq region. This model will take the time-series of runoff (melt minus refreezing) calculated by the SMB model over the area and calculate flow paths and water velocities over the snow / ice covered surface, routing the water into topographic depressions which may either contain an existing moulin (at the

deepest part of the depression), or can fill to form lakes. Lakes will be prescribed to drain to the ice sheet bed by hydrofracture once they reach a critical volume, or if this volume is not reached, lakes can overflow into the next downstream catchment. If hydrofracture occurs, a moulin will be assumed to exist at the deepest part of the depression for the remainder of the melt season. The model will be calibrated against field measurements of a filling lake in the study region. The key output will be moulin input hydrographs for different lake filling / drainage scenarios.

- Develop and apply a subglacial routing model to the Paakitsoq region. This model will be driven with moulin input hydrographs calculated by the surface routing and lake filling model for various lake filling / drainage scenarios. The model will be calibrated and evaluated by comparing modelled proglacial discharge with the discharge measured at a proglacial gauging station maintained by ASIAQ Greenland Survey. The key output will be spatially and temporally varying subglacial water pressure.

1.3 Thesis structure

The structure of this thesis closely follows the order in which the work was undertaken in response to the objectives outlined above. It consists of a total of six chapters. The present chapter has briefly introduced the rationale for developing a hydrological model for the GrIS. The overall aim of the thesis has been stated, along with a list of the research objectives to be achieved. Chapter 2 places this thesis more fully into the context of previous scientific research. With a general focus on the GrIS, it briefly reviews: (1) mass balance; (2) glacier hydrology; (3) mass balance and hydrological modelling; and (4) the Paakitsoq region, including key reasons for choosing this region as a study site. The next three chapters each focus on the development, application, calibration and evaluation of the three components of the complete glacier hydrological model; the SMB model (Chapter 3); the surface routing and lake filling model (Chapter 4); and the subglacial routing model (Chapter 5). Finally, the thesis is concluded in Chapter 6, which discusses the main findings of the preceding chapters, and provides a summary of necessary developments that should be considered in future research.

2. Greenland mass balance, hydrology and modelling – A review

This chapter aims to place the thesis objectives (as outlined in Chapter 1) in the context of previous scientific research. The following literature review consists of four key components: i) Mass balance with a focus on the Greenland Ice Sheet (GrIS) (Section 2.1); ii) GrIS hydrology, including the influence of hydrology on ice dynamics (Section 2.2); iii) Glacier and ice sheet hydrological modelling (Section 2.3); and iv) an outline of the study site; the Paakitsoq region, including a review of relevant research in the region (Section 2.4).

2.1 Mass balance

2.1.1 Global climate and ice sheet and glacier mass balance

Earth's mean surface temperature has been increasing since the instrumental record of global surface temperatures began in 1850. However, 11 out of 12 years from 1995 to 2006 were ranked the warmest on record [*IPCC*, 2007]. Natural causes, especially a small increase in solar radiation, contributed to the early part of this 'global warming'. By the end of the 20th century, however, the majority of the cumulative warming (including most of the warming since 1970), has been due to increased absorption of longwave radiation by greenhouse gases (including carbon dioxide, methane, nitrous oxide, tropospheric ozone and various industrial compounds), which have increased due to human activities [*IPCC*, 2007; *Cuffey and Paterson*, 2010]. The 'best estimates' of temperature rise in the 21st century vary between 2 and 4 °C, but the full range of uncertainty is much wider [*IPCC*, 2007]. The cryosphere is changing rapidly in response to a warming climate, as documented by the worldwide loss of ice that has been occurring over the last century, and accelerating in recent decades [*Shepherd and*

Wingham, 2007; *Velicogna*, 2009; *Radic and Hock*, 2011; *Jacob et al.*, 2012].

Ice sheets and glaciers, like most parts of the environment, can be viewed as systems with inputs, throughputs, storage and outputs. It is the balance of the inputs, known as accumulation, and the outputs, known as ablation, which determine the mass balance of a glacier. The term accumulation is taken to include all processes by which mass (snow and ice) is added to a glacier and the term ablation is taken to include all processes by which snow and ice are lost from a glacier [*Meier*, 1962]. An ice sheet can accumulate mass from snowfall, the freezing of rainwater and meltwater, and the transport of snow by wind. Ablation results from a number of processes, including melting, iceberg calving, evaporation, sublimation, and wind erosion [*Cuffey and Paterson,* 2010]. An ice sheet that is gaining overall mass has a positive net mass balance; an ice sheet that is losing overall mass has a negative net mass balance. In both cases, there is still accumulation near the centre, and ablation, through melting or calving of icebergs, near the margin [*Cuffey and Paterson,* 2010]. Therefore, ice has to flow from the centre to the margin under gravity in order for the ice sheet to maintain a steady-state. The ice velocities needed to maintain this steady-state are known as the balance velocities which can be calculated through modelling [*Bamber et al.,* 2000].

The mass balance of an ice sheet or glacier can be subdivided into two categories: static and dynamic [*Cogley et al.,* 2011]. The static mass balance (often referred to as the surface mass balance) is the total change in mass excluding adjustments due to ice flow and processes at the bed. The response is static because it does not involve a change in glacier geometry, only the surface height due to accumulation and ablation. In contrast, the dynamic response is the reaction of the glacier area and volume to the change in surface thickness (i.e. the advance or retreat of the glacier due to ice flow) [*Cogley et al.,* 2011].

Net mass balance measurements can either be made at a specific point [*Ahlmann,* 1948], termed the 'specific net mass balance', or can be made using geodetic techniques. Traditionally, the specific mass balance is measured directly for a number of points along transects across an ice sheet or glacier using stakes, ice cores and snow pits to determine the amount of accumulation and ablation [*Ohmura and Reeh,* 1991; *Bamber and Payne*, 2004]. In order to include the dynamic response of an ice sheet or glacier into net mass balance calculations, time series' of area and velocity change are required to calculate changes in ice flux (often known as the 'mass budget method').

Geodetic techniques involve the use of photogrammetry, airborne / satellite altimetry, or satellite gravimetry to measure the change in mass over time [e.g., *Shepherd and Wingham*, 2007; *Rignot et al., 2*008; Veligcogna, 2009; *Rignot et al.,* 2011]. It is these techniques which have resulted in substantial improvements in ice sheet and glacier mass balance estimates in recent years [*Rignot et al.,* 2011]. One important example of such a technique is the Gravity Recovery and Climate Experiment (GRACE) satellite mission which has provided invaluable monthly global gravity field solutions since 2002 [*Tapley et al.,* 2004; *Wahr et al.,* 2004]. The most recent estimate obtained by GRACE for the mass loss rate from all global glaciers and ice sheets (> 100 km^2) from 2003 to 2010 is 536 ± 93 Gt a^{-1} [*Jacob et al.,* 2012]. Of this, the Greenland and Antarctic ice sheets have a mass loss rate of 384 ± 71 Gt a^{-1}, and all other glaciers and ice sheets in the world have a combined mass loss rate of 148 ± 30 Gt a^{-1} [*Jacob et al.,* 2012].

Rignot et al. [2011] found a good agreement between the mass budget records and GRACE data for global glaciers and ice sheet mass balance over the last 8 years. This supports the last 18 year mass budget record which indicates that the combined acceleration of mass loss from the Greenland and Antarctic Ice Sheets over the last 18 years (36.3 ± 2 Gt a^{-2}) is three times larger than for mountain glaciers and ice caps (12 ± 6 Gt a^{-2}) [*Rignot et al.,* 2011]. Therefore, if this trend continues, ice sheets will be the dominant contributor to sea level rise in the 21st century.

2.1.2 Greenland climatology

The GrIS affects northern hemisphere atmospheric circulation by acting as a large, cold barrier. It influences storm tracks and cyclone evolution, which in turn influence northern hemisphere cloud cover and therefore temperatures [*Abdalati and Steffen*, 1997]. The climate of the GrIS itself exhibits large interannual variability, in terms of both temperature and precipitation [*Hanna et al.,* 2006; 2008]. Much of the variability in temperature is associated with shifts in the relative strength of the Icelandic Low and the Azores High, often known as the North Atlantic Oscillation (NAO) [*Hall et al.,* 2008]. Various studies have established a significant correlation between the NAO index and melt extent on the GrIS [*Mote,* 1998; *Johannessen et al.,* 2005; *Fettweis et al.,* 2011]. A positive NAO index results in colder winters in Greenland, whereas a negative NAO index results in milder winters over the GrIS. Although the relationship between the NAO index and variations in average precipitation over the GrIS is less clear [*Hanna et al.,* 2006], correlations can be found at a regional scale. For example, when

the NAO index is more negative, precipitation in south west GrIS is greater due to strong southerly moisture bearing winds [*Fettweis,* 2007].

The climate of the GrIS has also been affected by large, low-latitude volcanic eruptions. For example, particularly cool years followed eruptions of Mount Pinatubu, Phillipines (1992), El Chichon, Mexico (1982) and Agung, Bali (1963) [*Hanna et al.,* 2005; *Box et al,* 2006].

However, although the climate of the GrIS has displayed significant variability over the past 100 years, the overall trend has been one of temperature increase [*IPCC*, 2007]. For example, from 2005 to 2007, whilst the global annual average temperature anomaly was 0.7 ˚C compared to the reference temperature of 1951 to 1980, the average temperature anomaly for Greenland was more than double the global average at 1.5 ˚C [*AMAP,* 2009]. To date, 2010 was the warmest year on record, with large positive near-surface temperature anomalies occurring along the coast of the GrIS [*Box et al.,* 2010]. For example, at Aasiaat, on Greenland's west coast, 2010 was the warmest year since records began in 1951, with records also set for winter, spring, May and June temperatures [*Box et al.,* 2010; *Cappelen et al.,* 2010; *Tedesco et al.,* 2011a].

2.1.3 Greenland Ice Sheet mass balance

Although the GrIS was thought to have been in near balance with the colder climate of the 1970s and 1980s, the ice sheet has responded particularly rapidly to post-1990 warming [*Hall et al.,* 2008; *Hanna et al.,* 2008; *Rignot et al.,* 2008]. The GrIS is losing more mass through meltwater runoff and iceberg calving than it is gaining through accumulation, thus the result is a net mass loss [*Box et al.,* 2011, *Fettweiss et al.,* 2011].

Over the entire GrIS, recent estimates from GRACE indicate that from the end of April 2010 to the end of April 2011, which roughly corresponds to the period between the beginning of the 2010 and 2011 melt seasons, the ice sheet cumulative loss was 430 Gt, 70% (or 2 standard deviations) larger than the 2003 to 2009 average annual loss rate of 250 Gt a^{-1} [*Velicogna and Wahr*, 2006; *Velicogna,* 2009; *Box et al.,* 2011]. This 2010 to 2011 mass loss is equivalent to a eustatic sea level rise contribution of 1.1 mm, and is the largest annual loss rate for Greenland in the GRACE record (2002 to present), 180 Gt more negative than the 2003 to 2009 average [*Box et al.,* 2011].

Mass balance calculations, validated with satellite gravity observations, have enabled

the quantification of the individual components of recent Greenland mass loss. Current mass loss from the GrIS appears to be relatively evenly split between surface processes (runoff and precipitation) and the effect of ice dynamics [*Shepherd and Wingham,* 2007; *Van den Broeke et al.,* 2009]. These two components of mass loss are discussed in the following two sections.

2.1.3.1 Greenland Ice Sheet surface mass balance

There has been a significant increase in melt season temperature, melt area, and meltwater runoff since the 1990s [*Alley et al.,* 2007]. However, during this time, large interannual variability has been measured. For example, from 2000 to 2008, greater than average melt was measured in 2002, 2005, 2007, and lower than average melt was measured in 2000, 2001 and 2006 [*Hall et al.,* 2008]. In addition to 2010 holding the record of the warmest year to date, analysis of spaceborne microwave brightness temperatures [e.g., *Mote and Anderson*, 2005] indicate that large areas of the ablation zone in south Greenland underwent melting up to 50 days longer in 2010 compared to the 1979 to 2009 average [*Box et al.,* 2010]. Melting in 2010 also started exceptionally early at the end of April and ended quite late in mid September [*Box et al.,* 2010; *Tedesco et al.,* 2011a]. Data based on the seasonal melt departure (SMD) (i.e. the sum of the daily melt extent anomalies over each summer [*Mote,* 2007]), indicate that the melt area for the period June through August 2010 ranked highest since 1979, with 2007 and 2011 in second and third place respectively [*Box et al.,* 2010; 2011]. However, *Tedesco et al.* [2011b] note that although the high melt season of 2010 was largely driven by its long duration, 2011 was characterized by a relatively short but intense melting season due to the relatively early exposure of bare ice and reduced precipitation. This intense melting was thought not to be captured by analysis of spaceborne microwave data because of the technique's limitation in estimating the amount of liquid water within the snowpack [*Tedesco et al.,* 2011b].

In addition to melt, there has been a significant increase in accumulation over Greenland in recent decades [*Hanna et al.,* 2005; *Box et al.,* 2010]. Data from snow pits and from climatic modelling indicate that total accumulation currently averages 299 ± 23 kg m^{-2} a^{-1}, but shows significant interannual variability [*Cogley,* 2004]. For example, a pattern of below average precipitation for the period September 2010 through to August 2011 is evident at the west, southwest and southeast stations of the Danish Meteorological Institute (DMI, 2010, 2011), with the largest negative anomalies (above

one standard deviation) in the south [*Tedesco et al.,* 2011b]. Conversely, in east and northeast Greenland, precipitation was above average [*Box et al.,* 2011].

The result of the overall trends of increased melt (particularly at low elevations) and increased accumulation (particularly at high elevations) has caused the GrIS to thin at low elevations (< 2000 m), and thicken at higher elevations (> 2000 m) [*Krabill et al.,* 2000, 2004; *Zwally et al.,* 2005; *Pritchard et al.,* 2009]. Through positive feedback, thinning at lower elevations can cause a further increase in melt rate if a larger area of the ice sheet is brought down into the ablation zone [*Parizek and Alley,* 2004].

Until the mid-1990s, increased accumulation has largely offset the trend towards increasing ablation when only the surface mass balance (SMB) (i.e. excluding mass loss due to ice dynamics) is considered [*Hanna et al.,* 2005; *Box et al.,* 2006]. However, since the mid-1990s, runoff has increased with only a small increase in accumulation, resulting in a reduction in the SMB of around ~200 Gt since 1996 [*Rignot et al.,* 2008; *AMAP*, 2009; *van den Broeke et al.,* 2011]. This trend in SMB appears to be a response to global climate change and above the level expected due to natural variability [*Hanna et al.,* 2008]. The mean SMB, based on three ~50 year records (Modele Atmospherique Regional (MAR) [*Fettweis,* 2007], Polar Mesoscale Model version 5 [*Box et al.,* 2004], and the model by *Hanna et al.* [2002; 2005]), is 284 Gt a^{-1} with a range between estimates of 62 Gt. This range is 22% of the mean value and provides an indication of the uncertainty in the SMB. *Van den Broeke et al.* [2009] calculate that both mass balance components (SMB and mass lost to ice discharge) contributed equally to the post-1996 cumulative GrIS mass loss.

2.1.3.2 Greenland Ice Sheet ice dynamics

Recent observations suggest that the thinning rates of many outlet glaciers exceed those expected from changes in surface mass balance alone [*Abdalati et al.,* 2001; *Pritchard et al.,* 2008; *Sole et al.,* 2008]. Their rapid thinning is therefore attributed to changes in ice dynamics, a process often referred to as 'dynamic thinning'. In the case of marine-terminating glaciers, this process is thought to be due to a combination of factors including: i) changes in calving rate due to the breakup of the seasonal ice mélange (a mixture of fjord sea ice and recently calved ice) [*Joughin et al.,* 2008b; *Amundson et al.,* 2010]; ii) the un-grounding of ice near the terminus [*Luckman et al.,* 2006; *Howat et al.,* 2007; *Nick et al.,* 2009]; and iii) the submarine melting of calving

faces and ice shelves [*Rignot et al.,* 2010; *Straneo et al.,* 2010]. The recent increase in the rate of both of these processes is likely linked to an increase in average surface and subsurface ocean temperatures [*Holland et al.,* 2008; *Seale et al.,* 2011].

Thinning rates of land-terminating outlet glaciers are found to be much less than they are for marine-terminating glaciers [*Rignot and Kanagaratnam,* 2006; *Howat et al.*, 2008; *Sole et al.,* 2008; *Pritchard et al.,* 2009]. For example, *Sole et al.* [2008] found a four-fold increase in mean marine-terminating outlet glacier thinning rates below 1000 m elevation between the periods 1993 to 1998 and 1998 to 2006, while thinning rates of land-terminating outlet glaciers remained statistically unchanged.

However, in the short-term, there are multiple sources of evidence showing that ice sheet acceleration of land-terminating glaciers does occur [e.g., *Zwally et al.,* 2002; *Box and Ski,* 2007; *Das et al.,* 2008; *Price et al.,* 2008]. This process is primarily thought to be due to the lubricating effect of increased meltwater reaching the bed, often as a result of rapid supraglacial lake drainage event, and may have the potential to cause dynamic thinning over the longer-term (see Section 2.2.3 for further details).

2.1.4 Section summary

Although numerous studies have indicated that the SMB of the GrIS has shown a rapid decrease since the mid-1990s, the ice sheet is thought to respond to climate change more quickly than by surface melting alone. Through increased basal sliding, likely due to the lubricating effect of increased meltwater reaching the bed (often as a result of rapid supraglacial lake drainage events), or in the case of marine-terminating glaciers, due to changes at the calving front, evidence suggests that the GrIS is losing mass dynamically at ever increasing rates.

2.2 Greenland Ice Sheet hydrology

During the melt season, the ablation zone of the GrIS undergoes extensive melting of the upper layers of snow, firn and ice. Most of this melt becomes runoff and flows across the ice surface, developing supraglacial streams which can flow into topographic lows to form supraglacial lakes [e.g. *McMillan et al.,* 2007; *Tedesco and Steiner,* 2011; *Selmes et al.,* 2011], or which can drain directly into crevasses or moulins (nearly vertical conduits in the ice) [*Box and Ski,* 2007; *Catania et al.,* 2008]. Once water has

been routed to the base of the ice sheet, it is routed through a subglacial drainage system to the ice margin. The water pressure in the subglacial drainage system, which is primarily dependent on the water flux and storage capacity of the drainage network, is found to have a profound effect on the ice dynamics [e.g. *Bartholomew et al.,* 2010; *Schoof*, 2010].

With a general focus on the GrIS, this section first provides an overview of supraglacial and subglacial hydrology before focussing on the impacts that hydrology can have on the dynamics of an ice sheet.

2.2.1 Supraglacial hydrology

Supraglacial streams on the GrIS evolve from interconnected runnels in an arborescent network on the ice sheet, incising through thermal erosion at a rate that exceeds the surface ablation rate [*Knighton*, 1981; *Marston,* 1983; *Gulley et al.,* 2009a]. *Jarosch and Gudmundsson* [2012] identified the main factors controlling channel incision and depth rate to be channel slope, meltwater flux, and meltwater temperature loss to ice. Typical supraglacial streams have been measured to incise at rates of up to 0.3 m d^{-1} [*Isenko and Mavlyudov,* 2002]. If these streams are not first intercepted by a supraglacial lake or crevasse, meltwater may be directly routed to a moulin [*Colgan et al.,* 2011b].

Moulins are presumed to form through the process of hydraulically driven fracture propagation (hereafter 'hydrofracture') of water filled crevasses [*Weertman,* 1973; *Boon and Sharp,* 2003; *Alley et al.,* 2005; *Van der Veen et al.,* 2008; *Das et al.,* 2008; *Catania et al.,* 2008] and in some cases have been found to persist for multiple years in locations fixed by bedrock geometry [*Catania and Neumann,* 2010]. Moulins concentrate surface meltwater from relatively large catchment areas and deliver it to a single point in the subglacial hydrological system. In contrast, crevasses collect surface meltwater from comparatively small areas and route this water via a more distributed englacial network [*McGrath et al.,* 2011]. This behaviour occurs because crevasses form when the longitudinal strain rate exceeds the critical fracture toughness of ice, hence they are typically linear in nature, transect slopes, and can therefore intercept runoff and prevent large catchments from developing [*Colgan et al.,* 2011b; *McGrath et al.* 2011; *Phillips et al.,* 2011]. The highest spatial concentration of crevasses in western Greenland (60˚ N to 70˚ N) is observed below ~800 m elevation where slopes are

relatively steep (> 4˚) [*Phillips et al.,* 2011]. Above ~900 m elevation, a low albedo 'dark zone', corresponding to a maximum in surface meltwater accumulation, is observed [*Wientjes and Oerlemans,* 2010; *Phillips et al.,* 2011]. It is here that the majority of the ice sheet's large supraglacial lakes tend to form, as slopes are flatter (< 2˚) and so the ice exhibits less fracturing [*Greuell,* 2000; *Phillips et al.,* 2011].

Supraglacial lakes typically cover < 1% of the ablation zone of the GrIS and are concentrated on the western margin, with the majority south of 70˚ N [*Lüthje et al.,* 2006]. They are found to form predominantly in compressive stress regimes [*Das et al.,* 2008; *Krawczynski et al.,* 2009], and are generally found in the same location from year-to-year [*Thomsen et al.,* 1988; *Echelmeyer et al.,* 1991] in depressions that are controlled by the underlying bedrock topography [*Box and Ski.*, 2007; *Lampkin and Vanderberg,* 2011] and by spatial variations in the degree of basal ice lubrication [*Gudmundsson*, 2003]. During the spring and early summer, lake areas and volumes typically increase. The size of a lake depends on: i) the size of the topographic depression; ii) if and when the lake is able to drain; iii) lateral percolation of meltwater through surrounding saturated snow or in sheet-like form across ice; iv) inflow from supraglacial streams; and v) to some extent, a positive feedback of enhanced melt within the lake itself due to the low albedo, and hence increased absorption of shortwave radiation by the lake water compared to the surrounding ice [*Lüthje et al.,* 2006; *Tedesco et al.,* 2012]. Analysis of satellite imagery (Landsat 7 Enhanced Thematic Mapper (ETM+), Advanced Spaceborne Thermal Emission and Reflection Radiometer (ASTER) and Moderate-resolution Imaging Spectroradiometer (MODIS) indicates that supraglacial lakes typically range in diameter from a few hundred metres to > 2 km with a mean water depth of 2 - 5 m, although some have been measured to be up to 12 m in depth [*Luthje et al.,* 2006; *Box and Ski,* 2007; *McMillan et al.,* 2007; *Sneed and Hamilton,* 2007; *Georgiou et al.,* 2009; *Lampkin,* 2011].

During mid to late summer, many lakes shrink in size or disappear altogether by either a fast or slow drainage mechanism [*Hoffman et al.,* 2011; *Selmes et al.,* 2011; *Tedesco et al.* in review]. Few studies have focussed on establishing the proportion of lakes that drain rapidly compared to those that drain slowly. However, *Selmes et al.* [2011] found that out of the 2600 lakes that they mapped, 13% drained rapidly (i.e. in < 2 days). Additionally, they found that 61% of all fast lake draining events occurred in the south west of Greenland.

Observations suggest that those supraglacial lakes that shrink in size may drain slowly by overtopping the lowest part of the lake rim, followed by incision of the channel draining the lake by ice melt, thereby lowering the lake level [*Tedesco et al.,* in review]. This process has been observed to be slow at first as the spillway begins to cut into the lip of the lake basin. As the volume of outflow discharge increases, the channel incises deeper into the ice through the frictional heat produced from the turbulent water flow. If water flow into the lake ceases and the lake level drops to the level of the spillway, the surface drainage of the lake ceases until the lake level rises and breaches the spillway again [*Raymond and Nolan*, 2000]. This may explain why some supraglacial lakes are observed to have only partially drained from satellite imagery [*McMillan et al.,* 2007].

Supraglacial lakes that disappear completely are thought to drain rapidly through hydrofracture at or near the deepest part of the lake, opening a new route between the surface and bed [*Catania et al.,* 2008; *Das et al.,* 2008; *van de Wal et al.,* 2008]. Theoretical considerations based on linear elastic fracture mechanics indicate that crevasse hydrofracture will occur where the combination of tensile stresses and water pressure is large enough to overcome the fracture toughness of the ice [*Rothlisberger and Lang,* 1987; *Van der Veen*, 1998; 2007; *Alley et al.,* 2005]. Once the crack has been initiated, it is the availability of surface meltwater for filling the expanding fracture and offsetting freezing onto the walls which is thought to be the crucial factor in controlling crevasse propagation [*van der Veen,* 2007; *Krawczynski et al.,* 2009]. V*an der Veen* [2007] showed that even for large variations in tensile stress, the depth of fracture penetration depth can be reasonably approximated simply as a function of discharge and time. Although this model does not include the process of water refreezing onto the crevasse walls, it is argued that the rate of refreezing compared to the rate of fracture penetration (assuming constant inflow), makes the effect negligible. *Krawczynski et al.* [2009] built on *van der Veen's* [2007] model by accounting also for the crevasse dimensions (including depth and width) in order to determine the volume of water necessary to open a crack. Through modelling, *Krawczynski et al.* [2009] illustrated that lakes containing at least 8×10^4 m^3 may be capable of driving hydrofractures through ~1 km of cold ice.

Following *Van der Veen's* [2007] theory, *Clason et al.* [2012] developed a spatially distributed modelling routine for predicting the location and timing of delivery of

surface-derived meltwater to the ice / bed interface through moulins and supraglacial lake drainage and applied it to Devon Ice Cap, Canada. In this model, crevasses form where the tensile stress exceeds a prescribed tensile strength, and the formation of moulins to the bed is predicted when calculated crevasse depths equal the ice thickness. However, in contrast to modelling crevasse depths for lake-free cells, the model allows the drainage of supraglacial lakes regardless of whether the tensile stress exceeds the prescribed ice tensile strength, due to the low tensile or even compressive surface stress regimes in which supraglacial lakes have been found to form [*Catania et al.,* 2008]. When a lake volume reaches a level sufficient to drive a crevasse of prescribed dimensions through the full ice thickness, the lake drains instantaneously to the bed within a model time step.

Currently there is uncertainty regarding how the formation and drainage patterns of supraglacial lakes will respond to a warmer climate. However, through the development of an algorithm which automatically detects and tracks supraglacial lakes using visible satellite imagery, *Liang et al.* [2012] demonstrate that the population of lakes extends to higher elevations during more intense melt seasons, exposing an increased inland area of the ice sheet to sudden lake drainage events. Evidence also suggests that as the climate warms and surface melting becomes more intense on the GrIS, supraglacial lakes will drain more frequently and earlier in the melt season [*Liang et al.,* 2012].

2.2.2 Subglacial hydrology

2.2.2.1 Types of subglacial drainage systems

During the winter and early spring, low volumes of meltwater (mainly produced through geothermal and frictional heat sources) travel through a quiescent subglacial hydraulic network which has largely closed during the winter due to creep closure [*Nye,* 1953]. This type of inefficient network is known as a distributed system. One of the most commonly referred to distributed systems is a system of 'linked-cavities', favoured by rapid sliding and high bed roughness [*Walder,* 1986; *Kamb,* 1987]. Energy dissipated by the water flowing through narrow orificies, which 'link' the individual cavities, acts to preferentially enlarge the orifices because that is where the head loss is steepest [*Walder,* 1986]. Other examples of distributed systems include extensive subglacial films [*Weertman,* 1972; *Walder and Hallet,* 1979], flow through a porous

medium at the base of the glacier [*Fountain,* 1994; *Hubbard et al.,* 1995], or a non-arborescent network of wide, shallow, ice-roofed canals eroded into sediment [*Fowler and Walder,* 1993]. Evidence for the existence of distributed systems include high borehole water pressures lacking significant pressure fluctuations [*Hubbard and Nienow,* 1997], high dispersion of tracer dye with low transport velocity [*Nienow et al.,* 1998] and in the case of linked cavity systems, palaeomorphological evidence in proglacial bedrock [e.g. *Sharp et al.,* 1989]. As distributed systems can only accommodate and transmit a relatively low volume of water, both transient and steady-state subglacial water pressures increase with increasing discharge [*Iken et al.,* 1983*, Kamb,* 1987*; Mair et al.,* 2001, *Willis et al.,* 2003] (Figure 2.1).

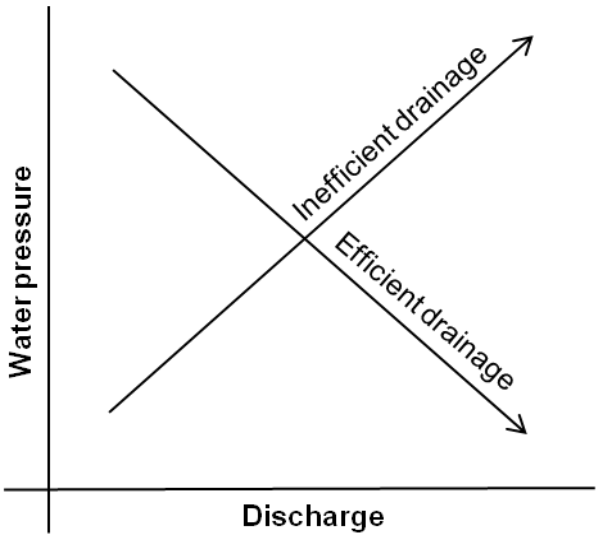

Figure 2.1: Generally speaking, subglacial drainage can be classified as efficient or inefficient. As steady-state discharge increases, steady-state water pressure increases in an inefficient system and falls in an efficient system (after *Kamb*, [1987]).

As the melt season progresses, ice-walled channels, commonly known as conduits, enlarge through melting from the frictional heating of the flowing water, hence the transmission capacity exceeds meltwater input, and the inland development of an efficient channelized subglacial drainage system occurs [*Mair et al.,* 2002; *Colgan et al.,* 2011a]. Typical channel types can include semi-circular conduits formed in basal ice ('Rothlisberger', or 'R' channels) [*Rothlisberger,* 1972], broad flat channels formed in basal ice ('Hooke', or 'H' channels) [*Hooke et al.,* 1990; *Hock and Hooke,* 1993], or conduits incised in subglacial bedrock ('Nye' channels) [*Nye,* 1973]. Evidence for the

existence of this type of drainage includes rapid drops in water levels after borehole drilling, large diurnal borehole water pressure fluctuations with low minimum diurnal values [*Hubbard et al.*, 1995], high system outflow, and rapid tracer dye returns with little dispersion [*Nienow et al.*, 1998].

In contrast to an inefficient distributed system, steady-state subglacial water pressure decreases with increasing discharge in an efficient channelized system (Figure 2.1). In a channelized system, channels maintain an equilibrium state between closing, from creep deformation of the ice, and expanding, due to melting from the frictional heat of water flowing past the ice [*Rothlisberger,* 1972; *Shreve,* 1972]. *Shreve's* [1972] analytical results also indicate that greater viscous heat dissipation in larger conduits causes these conduits to grow at the expense of smaller ones. This results in the formation of an arborescent drainage network, with tributary conduits flowing into successively larger 'trunk' conduits, under steady-state flow conditions. *Röthlisberger* [1972] arrived at a similar conclusion by arguing that higher flow and lower pressure in large conduits causes hydraulically connected smaller conduits to flow into the large conduits. When the water fluxes to the channelized system fall, channels cannot be maintained and they close, eventually resulting in an inefficient subglacial drainage system once again. However, as noted by *Fountain and Walder* [1998], the categorization of drainage systems is more complex than this simplified description, with both types of systems interacting on a variety of spatial and temporal scales.

2.2.2.2 Formation of channelized systems

Based on the theoretical model developed by *Shreve* [1972], the primary driving force for channelized water flow within and under ice sheets and glaciers is the hydraulic potential. This model, which has greatly influenced ideas about the character and evolution of glacial drainage systems [*Hooke,* 1988; *Röthlisberger and Lang,* 1987; *Fountain and Walder,* 1998], is based on three main assumptions: i) the drainage system is in steady-state (i.e. discharge rates and system geometry are constant); ii) water will flow along the steepest hydraulic gradient; and iii) water pressure in conduits is approximately equal to the pressure of the surrounding ice. The assumption that water pressure equals ice overburden pressure stems from the idea that conduits will expand or contract in response to differences between pressure in the conduit and the surrounding ice, and that the conduit will therefore adopt a geometry that equalizes these pressures. Total hydraulic potential (ϕ) (Pa) is the sum of the elevation

and pressure potentials and can be defined as:

$$\phi = k\rho_i g(h - z) + \rho_w gz \tag{2.1}$$

where ρ_i is the density of ice (917 kg m^{-3}), ρ_w is the density of water (1000 kg m^{-3}), g is acceleration due to gravity (9.81 m s^{-2}), h and z are the elevations of the ice surface and subglacial topography (m), respectively, and k is the spatially uniform flotation fraction, defined as the ratio of water pressure to ice overburden pressure, P_w / P_i , with k = 1 representing water at the ice overburden pressure and k = 0 representing atmospheric pressure in conduits (adapted from *Shreve*, [1972] and *Rippin et al.* [2003]). The first term in this equation, the thickness term, represents the tendency of water to flow towards decreasing ice thickness, while the second term, the bed elevation term, represents the tendency of water to flow downhill. *Shreve's* [1972] model predicts that the slope of subglacial equipotential surfaces is ~11 times the ice surface slope, but in the opposite direction. This implies that subglacial water can flow uphill out of over-deepened sections of glacier bed, so long as the magnitude of the water pressure gradient exceeds that of the elevation potential gradient [*Sharp*, 2005]. Although *Shreve's* [1972] formulation requires dramatic simplification of a complex and dynamic system, it is believed to provide insight into stable conduit configurations [*Flowers and Clarke*, 1999; *Hagen et al.,* 2000].

2.2.3 Impacts of hydrology on ice dynamics

Although the delivery of meltwater to glacier beds has long been recognised as an important control on the dynamics of valley glaciers [*Iken and Bindschadler*, 1986; *Hooke et al.,* 1989; *Mair et al.,* 2002], until recently it was believed that this process could not occur where ice is below the pressure melting point (PMP), as 'cold' ice was thought to act as an impenetrable barrier to englacial drainage [*Hodgkins*, 1997]. However, numerous studies now provide abundant evidence for the notion that surface meltwater can reach the bed of the ice sheet through moulins or crevasses. One of the first studies to propose this was that by *Zwally et al.* [2002] who used GPS measurements at Swiss Camp, west Greenland, as evidence for a summer speed-up and winter slowdown. They proposed that the likely reason for this speed-up was increased lubrication at the ice / bed interface due to a local injection of surface meltwater to the bed through moulins in a region where ice is over a kilometre thick

and, near the surface, below the PMP. However, *Price et al.* [2008] questioned this explanation and instead proposed the theory that the ice accelerations at Swiss Camp were caused by longitudinal coupling of downstream melt-acceleration, instead of by local meltwater injection.

There is, however, ample evidence to suggest that the rapid drainage of supraglacial lakes on the GrIS can play a key role in linking the surface melt signal to ice motion by supplying a sufficient volume of water to propagate crevasses through thick, cold ice to the base of the ice sheet by hydrofracture [*Alley et al.,* 2005; *Van der Veen,* 2007; *Catania et al.,* 2008*; Das et al.,* 2008; *Tedesco et al.,* in review]. High volumes of water rapidly transported into the subglacial drainage system by this method are thought to be accommodated through temporary spikes in subglacial water pressure, reducing basal friction and driving transient ice sheet accelerations [*Das et al.,* 2008; *Joughin et al.,* 2008; *Schoof,* 2010]. It has been suggested that this mechanism is responsible for seasonal variations in surface speeds of up to 200% on western margins of the GrIS [*Joughin et al.,* 2008; *Shepherd et al.,* 2009; *Bartholomew et al.,* 2010; *Palmer et al.,* 2011]. For example, *Das et al.* [2008] measured a three-fold increase in the background flow rate of the ice coinciding with the rapid (~2 hour) drainage of a large (~2.7 km diameter) supraglacial lake near Jakobshavn Isbrae in summer 2006. This lake drainage event was characterized by rapid and coincident ice sheet uplift and elevated seismicity providing strong evidence that in this location surface melt water reached the base of the ice sheet by the hydro-fracture process [*Das et al.,* 2008].

It is, however, apparent that the link between hydrology and ice dynamics is more complex than first anticipated [*van de Wal et al.,* 2008; *Bartholomew et al.,* 2010; *Sundal et al.,* 2011]. If surface melting translates directly to an increase in sliding, rising temperatures could generate a positive feedback to mass loss as faster flow causes the ice sheet to lower into warmer elevations [*Zwally et al.,* 2002; *Parizek and Alley,* 2004]. Conversely, if the subglacial hydrologic system of the ice sheet adapts to accommodate higher discharges of water, increased melt could generate a limited, or even decelerating, effect on seasonally averaged sliding. This is because higher water discharges are usually associated with lower water pressure in channelized systems [*Truffer et al.,* 2005; *Joughin et al.,* 2008; *van de Wal et al.,* 2008; *Schoof,* 2010; *Colgan et al.,* 2011a; *Sundal et al.,* 2011].

Recent observations have presented mounting evidence for a seasonal and spatial

evolution of the subglacial hydrologic system beneath marginal areas of the GrIS analogous to that found beneath Alpine glaciers [*Iken and Bindschadler,* 1986; *Mair et al.,* 2002; *Bartholomaus et al.,* 2008; *Bartholomew et al.,* 2010; *Hoffman et al.*, 2011]. Like an Alpine glacier, a distributed system is thought to exist under much of the GrIS through the winter and at the beginning of the melt season. During this time, subglacial water pressures increase with increased discharge, thus basal shear stress decreases; facilitating increased glacier velocities for as long as the meltwater input exceeds transmissivity [*Bartholomew et al.,* 2010; *Colgan et al.,* 2011a; *Hoffman et al.,* 2011]. However, as surface melt rates increase, discharge into the subglacial system increases and channels enlarge due to wall melt, resulting in the inland development of a channelized system [*Bartholomew et al.,* 2010, 2011b]. While a channelized system exists, the ability of a steady-state water supply to cause further ice sheet acceleration is thought to be suppressed as increased discharge results in decreased subglacial water pressures [*Schoof,* 2010; *Pimentel and Flowers,* 2011]. *Bartholomew et al.* [2011a] interpreted proglacial runoff data from the Leverett Glacier, to the south of Jakobshavn Isbrae, west Greenland, in terms of this seasonal transition from an initial widespread distributed network to a more channelized network that expanded upglacier beneath the > 600 km^2 catchment, to distances > 50 km from the ice sheet margin. These observations are supported by observations of ice motion and upglacier evolution in the timing of lake drainage in this section of the ice sheet [*Sundal et al.,* 2009; *Bartholomew et al.,* 2011a]. Similarly, *Colgan et al.* [2012] used GPS observations of ice surface velocity at three stations in the Paakitsoq region to the north of Jakobshavn Isbrae to suggest that the annual ice velocity cycle propagates up to ~70 km inland.

Further, evidence suggests that superimposed on the observed seasonal meltwater cycle are diurnal meltwater input cycles in which inputs exceed the transmission capacity of the drainage system during the day and vice versa at night [*Schoof,* 2010]. Analogous to the behaviour observed on Alpine glaciers, this cycle has been observed to drive localized uplift and enhance basal sliding under the GrIS several hours after peak meltwater production in the afternoon [*Shepherd et al.,* 2009; *Bartholomew et al.,* 2012]. This daily speed-up is followed by a surface lowering and subsequent decrease in ice velocity, as the meltwater input volume falls below the transmission capacity of the drainage system [*Shepherd et al.,* 2009]. For example, *Hoffman et al.* [2011] analyzed GPS data from nine stations to establish that daily pulses in meltwater caused

variations in diurnal sliding rates for a marginal area of central western Greenland, and that these diurnal velocity increases were superimposed on a night time velocity that gradually decreased over the early melt season, presumably as the subglacial hydrological system became more efficient at transmitting water.

2.2.4 Section summary

The configuration of the subglacial hydrological system, and the links between this and the supraglacial hydrological system, can have a profound influence on ice dynamics. Numerous sources of evidence suggest that changes in basal sliding velocity are due to a combination of changes in the rate of glacier water storage (i.e. the total glacier water input minus output, governed by the subglacial drainage system transmissivity [*Fountain and Walder*, 1998]) and changes in subglacial water pressure. This theory, analogous to that for Alpine glaciers, explains why sudden bursts of increased basal motion are associated with meltwater pulses, while sustained water input, which eventually leads to the establishment of efficient subglacial conduits and a lower water pressure, does not lead to enhanced basal sliding. However, although relatively small increases in surface ablation can result in disproportionately large increases in ice velocity in the short-term [*Bartholomew et al.,* 2010; *Schoof,* 2010; *Sundal et al.,* 2011], significant uncertainty exists in determining how the GrIS hydrological system will evolve over decadal and longer timescales to changing volumes of meltwater and thereby influence the dynamics of the ice sheet. There is therefore a need to address the issue of how diurnal and seasonal variations in surface water inputs over a large area of the GrIS are integrated across the bed, and what spatial and temporal patterns in subglacial water pressure would emerge.

2.3 Mass balance and hydrological modelling – a review

This section focuses on providing a short review of modelling approaches for each of the three key components of the complete distributed glacier hydrological model used in this study. These components include: i) a mass balance model to calculated distributed runoff over the ice / snow surface; ii) a surface routing model to route water across ice / snow to either surface lakes or moulins; and iii) a subglacial routing model to water route subglacially to the proglacial outflow point.

2.3.1 Surface mass balance modelling

The ability to accurately model the surface mass balance (SMB) of an ice sheet or glacier is a key component in predicting how the ice mass will respond to projected future climate change. As discussed in this section, SMB models typically consist of three coupled components: i) an ablation routine to model melt; ii) a subsurface model, calculating refreezing and net runoff, and in some cases, changes in temperature, density and water content in the snow, firn and upper ice layers; and iii) an accumulation routine.

2.3.1.1 Ablation

Glacier melt is determined by the energy balance at the glacier-atmosphere interface, controlled by the meteorological conditions above the glacier and the physical properties of the glacier itself [*Hock,* 2005]. However, the interactions between the glacier surface and atmosphere are complex. The atmosphere supplies energy for melt, while atmospheric conditions are modified by the presence of snow and ice due to the specific properties of snow and ice and their high temporal variability. During the last few decades, a large variety of surface ablation models have been developed, ranging from relatively simple 'positive degree-day' (PDD) models (sometimes known as 'temperature-index' models) to more sophisticated 'energy balance' (EB) models [*Hock,* 2005]. Although the primary aim of both types of model is to simulate glacier melt, they differ in terms of their computational method. PDD models assume an empirical relationship between melt and air temperature based on a strong and frequently observed correlation between these quantities. They require only a few data inputs, so are essentially a 'black box' technique which offers no real insight into the physical processes governing ice and snow melt. In contrast, EB models compute melt by assessing the exchange of all the energy fluxes at the surface of a glacier; thus are more physically-based.

Positive degree-day models

The classic PDD method is based on the following equation:

$$N = \beta T_{pdd} \tag{2.2}$$

where N is the calculated melt (mm w.e.), β is the degree-day factor (mm w.e. d^{-1} °C^{-1})

and T_{pdd} is the sum of all positive daily mean temperatures (in °C) over the time period of interest. The degree day factor is a constant that is calculated from the linear fit between observations of *N* and *Tpdd*. Therefore, PDD models are forced entirely using temperature data. Although the concept involves a simplification of complex processes that are more accurately described by the surface EB, these methods are justified because of the high correlation between temperature and various components of the EB equation [*Braithwaite,* 1981; *Ohmura*, 2001; *Hock*, 2005]. Longwave incoming radiation and the turbulent heat fluxes depend strongly on temperature, and temperature in turn is affected by global radiation, although not in a simple way [*Kuhn,* 1993; *Ohmura,* 2001; *Hock,* 2005]. To account for spatial variability in melt rates, while employing spatially constant degree-day factors, melt-runoff models often divide the glacier into elevation bands to account for a decrease in melt with increasing elevation, and may also divide the glacier into aspect classes to account for enhanced melt on south-facing slopes compared to north-facing slopes [*Braun et al.,* 1994; *Hock,* 2005]. This approach has been, and still is, used extensively for modelling the runoff from the GrIS [*Braithwaite,* 1995; *Abdalati et al.,* 2001; *Mote,* 2003; *Hanna et al.*, 2006; *Rignot and Kanagaratnam,* 2006].

Energy balance models

In contrast to PDD models, EB models explicitly quantify the physical processes of the exchange of all the energy fluxes at the surface using the following equation:

$$Q_M = SW_{net} + LW_{net} + SHF + LHF + GHF, \tag{2.3}$$

where Q_M is the energy available for melt, SW_{net} is the net shortwave radiation, LW_{net} is the net longwave radiation, *SHF* is the sensible heat flux, *LHF* is the latent heat flux (*SHF* and *LHF* are referred to as turbulent heat fluxes), and *GHF* is the ground heat flux in the snow or ice (i.e., the change in heat of a vertical column from the surface to the depth at which vertical heat transfer is negligible). All of these components can be calculated from meteorological data, including air temperature, wind speed, relative humidity, and incoming shortwave and longwave radiation. If the energy available for melt, Q_M, is positive then the surplus energy is used to melt snow or ice (if the surface temperature is at 0 °C) or warm the surface and subsurface (if the surface is below 0 °C). If there is a deficit of energy then the glacier surface and subsurface will cool.

EB models include two end member categories: point studies and distributed models

[*Hock,* 2005]. The former assess the energy budget at one location, usually the site of a meteorological station. The latter require a high-resolution digital elevation model (DEM) of the glacier surface in order to spatially distribute meteorological data and compute slope angles and aspects as well as any topographic shading. All types of EB models need to be calibrated against some form of *in situ* or remotely sensed imagery, and preferably then validated against an independent data set.

Instead of driving an EB model with locally-measured meteorological observations which are extrapolated across the model domain, it is sometimes more appropriate to use the down-scaled output from climate reanalyses or a Regional Climate Model (RCM) in mass balance modelling studies [*Fettweis,* 2007; *Ettema et al.,* 2010a; *Fettweis et al.,* 2010; *Rye et al.,* 2010]. The first high-resolution RCM for Greenland was based on a modified version of the fifth generation mesoscale model known as PMM5 [*Box et al.,* 2004]. This model ran at a 24 km resolution, was calibrated using *in situ* data to correct for biases in melt energy and water vapour flux, and was initially driven by ERA-40 reanalysis data [*Box et al.,* 2004; 2006]. More recently, a 25 km resolution RCM, called MAR (Modele Atmospherique Regional), has been developed by *Gallee and Schayes* [1994] and applied to the GrIS by, among others, *Fettweis* [2007; 2008; 2010] and *Tedesco et al.* [2011a]. One of the highest-resolution (11 km) RCMs currently in existence is that used by *Ettema et al.* [2010a; b], originally developed by *Van Meijgaard et al.* [2008] (RACMO2), and adapted specially for the GrIS.

2.3.1.2 Subsurface processes

Although many mass balance models focus on the exchange of energy between the atmosphere and glacier surface, processes occurring within the immediate subsurface of the snow / ice can also be important. In particular, meltwater produced at the surface of a snowpack is likely to percolate downwards where it may refreeze, forming superimposed ice or internal accumulation [*Wadham and Nuttall*, 2002; *Schneider and Jansson*, 2004; *Rye et al.,* 2010]. The amount of refreezing in the subsurface layer depends on the amount of available water, the energy balance of the snowpack and the ability of water to percolate through the snowpack [*Brandt et al.,* 2008]. A widely used technique for quantifying meltwater refreezing is to assume that the maximum amount of annual refreezing can be expressed as a percentage of the total winter snowpack [*Huybrechts et al.,* 1991; *Reeh,* 1991*; Braithwaite et al.,* 1994]. This technique was later developed by *Woodward et al.* [1997] and *Radic and Hock* [2011] by

empirically relating the amount of refreezing to the mean annual air temperature, thus calculating an annually variable amount of water retention. Schematic models like those of *Reeh* [1991] and *Woodward et al.* [1997] are particularly useful where computationally inexpensive approaches are required for large areas of ice sheets [*Janssens and Huybrechts,* 2000] or glacier and ice cap cover *Radic and Hock* [2011]. However, these models are essentially black box methods that offer little insight into the processes occurring or the spatial and temporal variations that have been observed in the field [*Wright*, 2005; *Wright et al.,* 2007; *Rye et al.,* 2010].

A physically realistic treatment of meltwater refreezing requires the use of a detailed thermodynamic model that simulates the vertical evolution of snow properties such as density, temperature and liquid water content [*Greuell and Konzelmann,* 1994; *Bassford,* 2002; *Bougamont et al.,* 2005; *Wright et al.,* 2005; *Rye et al.,* 2010]. These models represent the subsurface of an ice mass as a one-dimensional multi-layer grid, extending from the ice surface to the depth of annual temperature oscillations (typically 10 - 20 m). They are often coupled with surface EB models, which provide the boundary conditions at the top of the grid. Energy and mass transfers between grid cells are then computed and used to model the percolation and refreezing of meltwater within the snowpack.

2.3.1.3 Accumulation

Compared to knowledge about ice and snow ablation, the physical processes governing accumulation are harder to constrain. Knowledge about the local and regional effect of altitude and topography on precipitation is lacking due to a lack of observations [*Humlum,* 2002]. Furthermore, measured data which do exist cannot always be considered to be accurate because precipitation gauges often significantly under-catch the amount of solid precipitation in windy conditions [*Førland et al.,* 1996; *Yang et al.,* 1999]. For most glacier and ice sheet modelling studies, the easiest approach is to extrapolate locally measured precipitation over the surface of a glacier using a linear elevation-dependent precipitation gradient. A temperature threshold is then used to determine whether the precipitation at a given elevation is rain or snow. The elevation-dependent precipitation gradient, rain / snow temperature threshold, and measurement under-catch are often derived from winter mass balance observations [*Hock and Holmgren,* 2005; *Schuler et al.,* 2005*; Wright*, 2005; *Rye et al.,* 2010].

2.3.2 Modelling glacier hydrological systems

As glacial hydrological systems play such an important role in regulating subglacial pressure conditions and proglacial runoff, much effort has been invested in developing predictive numerical models. These modelling efforts have contributed substantially to our understanding of the processes and mechanisms of glacier hydrology.

The majority of early glacier hydrological models were statistical [e.g., *Willis et al.,* 1993] or lumped [e.g., *Baker et al.,* 1982] and were mainly used for predicting output hydrographs for forecasting glacier runoff [*Fountain and Tangborn,* 1985]. However, some conceptual models are still widely used due to their moderate data requirements [*Hock and Jansson,* 2005]. These models generally consist of a series of numerical steps representing the known physical processes in a simplified manner [*Kachroo,* 1992]. For example, some spatial variability of input data is ignored by replacing spatially variable functions by their areal means (lumping). The most widely adopted concept to route water across, through, and under glaciers is the concept of 'linear reservoirs' which accommodates the storage effect and resulting delay of water through the various components of the glacier hydrological system [*Chow et al.,* 1988; *Hock and Jansson,* 2005].

Although conceptual models can provide useful predictions of proglacial stream discharges in the catchments for which they were developed, they are not easily transferable to other catchments, and cannot be reliably used for explanatory purposes. The majority of current modelling attempts aim to build physically-based models which account for all the main processes in a glacier hydrological system [*Hock and Jansson,* 2005]. It is these models which the rest of this review section focuses on.

2.3.2.1 Supraglacial routing models

Physically-based supraglacial routing models are in their infancy and consist of two coupled components. One component calculates a flow accumulation matrix in order to analyse a surface DEM to identify the topographic hollows which can contain lakes, the catchment areas which feed each lake, and the topological routing of water between catchments if the water level in any given lake reaches the overflow. The second component of the model calculates the time delay between the point of melt production, and the final destination cell (which may either be a moulin or supraglacial lake).

Flow accumulation matrix algorithms

The calculation of flow accumulation matrices (also known as upslope area matrices), and hence the identification of surface watersheds (and hence catchment areas) from DEMs has been commonly used in glaciology to: i) calculate the balance flux of ice sheets, defined as the depth-integrated ice flux needed to balance the ice input upstream of the point [*Budd and Warner*, 1996; *Bamber et al.,* 2000; *Le Brocq et al.,* 2006]; ii) to infer the potential locations of subglacial conduits [*Arnold et al.,* 1998; *Sharp et al.,* 1993]; and iii), in conjunction with inferred water flow rates, such algorithms have been used to generate moulin input hydrographs from patterns of surface melt over glaciers [*Arnold et al.,* 1998].

However, to avoid the problem of water getting 'stuck' in surface depressions within the DEM, most algorithms rely on the artificial filling of these surface depressions (see *Arnold* [2010] for a review). Although depression removal has been widely questioned (e.g., *Lindsay and Creed* [2006] and references therein), this procedure can be justified on the basis that, in simple terms, depressions would simply fill with water and then overflow or that water would find some subsurface route out of the depression. Thus, at a catchment scale, preserving the continuity of flow can be considered to be more important than accurately dealing with the processes within a depression [*Arnold,* 2010]. In contrast, the algorithm developed by *Arnold* [2010] for calculating lake and catchment extent does not require the artificial filling of surface sinks, and therefore has the potential to be of great use for studies which are specifically focussing on modelling the filling of these depressions with water to form lakes. This algorithm also determines a flow direction matrix for a given DEM surface so that the water flow path from any given DEM cell to the sink cell (or lake) can be calculated [*Arnold,* 2010] (see Chapter 4, Section 4.2.2.1 for further details).

Flow delay algorithms

In order to calculate the delay of water flow across an ice or snow surface, as well as its path, a flow delay algorithm is required. One such algorithm is that initially developed by *Arnold et al.* [1998]. This algorithm uses the flow direction matrix, and the surface slope matrix, together with assumptions about the physical processes controlling water flow, to calculate a flow delay time between each DEM cell and its sink cell. For every DEM cell, a 'travel time' for water to cross the cell is calculated; this time depends on

the slope of the cell, whether the cell is ice or snow (which governs the physical processes assumed to control the flow), and the parameter values which govern the water flow. However, whilst there is a large amount of research concerning vertical unsaturated flow through snow packs [*Bassford,* 2002; *Wright et al.,* 2005*; Rye et al.,* 2010], there has been less work concerning lateral saturated flow at the base of a snowpack. One of the few studies in this category is that by *Colbeck* [1974] who described the application of Darcian flow equations to snow lying on a slope above an impermeable boundary with a small slope angle:

$$C_s = (\rho_w g/\mu) x\, \theta / K \tag{2.4}$$

where C_s is water velocity under a snowpack (m s^{-1}), ρ_w is the density of water (kg m^{-3}), μ is the viscosity of the water (Pa s), θ is surface slope, x is snow permeability (m^2) & K is snow porosity. *Campbell et al.* [2006] also used dye-tracing to measure rates of lateral saturated flow at the base of the snowpack at Haut Glacier d'Arolla, Switzerland.

Similarly, there has been little detailed work concerning the processes of lateral flow across bare ice surfaces. For this reason, the simple Manning's equation is often used:

$$C_i = R^{2/3}\, \theta^{1/2} / n \tag{2.5}$$

where C_i is the water flow velocity across bare ice (m s^{-1}), R is hydraulic radius (m) and n is the Manning roughness coefficient ($m^{-1/3}$ s).

Lakes effectively fill with water from the original sink cell 'upwards' by successive flooding of the next lowest DEM cell(s). The total accumulated volume of water within each lake at a given can then be calculated, and from this (and the calculated lake hypsometry), the time step at which the lake overflows its rim can be calculated.

Although the approach used by *Arnold et al.* [1998] for modelling lateral flow at the base of a seasonal snowpack gave an estimate of the delay introduced by saturated flow, it did not allow for longer-term storage of meltwater in deeper saturated layers, which anecdotal evidence suggested was potentially significant at Haut Glacier d'Arolla [*Fox,* 2004]. To resolve this issue, *Fox* [2004] applied the Modular Finite-Difference Groundwater Flow Model (MODFLOW) developed by the United States Geological Survey (USGS) [*Harbaugh et al.,* 2000] to model saturated flow through

snowpacks. This model treats the snowpack as an unconfined aquifer, with permeability and storage parameters based upon values estimated for saturated snow, underlain by the impermeable boundary of the ice surface.

2.3.2.2 Englacial and subglacial routing models

Modelling the physics of glacier hydrology is complex as it involves the liquid phase, namely water, moving through the solid phase, namely ice, at the melting temperature. Furthermore, ice is deformable under relatively low stresses, which allows channels and conduits in glaciers to change size and shape much more rapidly than channels eroded in rock or sediment. The glacier system is thus transient on all timescales and over all spatial scales [*Nienow et al.,* 1998; *Hock and Jansson,* 2005].

The first physically-based glacier hydrology models were developed to reproduce simple observable phenomena. For example, *Rothlisberger* [1972] and *Shreve* [1972] presented simple numerical models for water flow in glaciers. Shreve's assumptions were that water pressure is in balance with ice pressure, and that preferential englacial drainage pathways should follow the steepest gradient of the hydraulic potential [*Shreve,* 1972] (See Section 2.2.2.2). In order to predict the subglacial drainage pathways, this formulation was simplified by the assumption of *Bjornsson* [1982] that all meltwater reached the bedrock through moulins and crevasses and drained along the base of the ice sheet, which was assumed to be impermeable. This formulation has been used by multiple previous studies to infer subglacial drainage system structure for different assumptions of steady-state water pressure [*Holmlund,* 1988; *Sharp et al.,* 1993; *Flowers and Clarke,* 1999; *Hagen et al.,* 2000; *Rippin et al.,* 2003; *Fischer et al.,* 2005; Le *Brocq et al.,* 2009; *Fricker et al.,* 2010; *Willis et al.,* 2012].

Rothlisberger's [1972] theory that channels maintain an equilibrium state is based on the assumption that the rate of conduit enlargement through melt is balanced by creep closure. However, although *Rothlisberger* [1972] assumed flow through channels with semicircular cross-sections, discrepancies between measurements and model calculations led *Hooke et al.* [1990] to propose low broad channels (i.e. 'Hooke' channels) in order to be able to apply Glen's flow law deformation with reasonable viscosity parameter values.

Subsequent to *Shreve* [1972] and *Rothlisberger* [1972], *Nye* [1976] and *Spring and Hutter* [1981] (see Chapter 5, Section 5.1.3.1 for further details) presented a physically-

based theory of unsteady flow through englacial channels. *Hooke* [1984] also investigated the effects of unsteady conditions, in particular, open channel flow, on the *Rothlisberger* [1972] system.

Whilst *Shreve's* [1972] model predicts where subglacial pathways are likely to form, it does not deal with the nature of the flow itself. Additionally, the construction of a full hydrologic model not only requires knowledge of the current state of the hydrological system, but also an appreciation of the ways in which it evolves over space and time. As discussed in section 2.2.2.1, subglacial drainage systems are separated into two profoundly differing forms: *channelized* or *fast* systems, and *distributed* or *slow* systems [*Raymond et al.,* 1995; *Fountain and Walder*, 1998]. The latter, in response to increasing water fluxes, will tend to evolve over time toward the former [e.g., *Hubbard et al.,* 1995; *Bartholomew et al.,* 2010; *Sole et al.,* 2011]. It is therefore desirable that subglacial hydrological models are able to replicate this dynamic switch between a slow and fast subglacial drainage system. *Shreve's* [1972] model is not a suitable basis for this adaption as it considers steady-state conditions: isotropic ice and unvaried water flow. Such conditions do not reflect either glacier ice or the diurnal variations in melt rates driving water flow, and numerical models have cast doubt on the stability of a 'Shrevian' drainage system [e.g., *Szilder and Lozowski,* 1997; *Cutler,* 1998].

Arnold et al. [1998] were the first to develop a physically-based time-dependent hydrological model and apply it to an entire glacier. This model was developed for Haut Glacier d'Arolla and was calibrated against extensive discharge and pressure data for the glacier [*Richards et al.,* 1996]. Surface runoff, calculated using an EB model, was routed across the ice or snow surface to known moulin positions, where it was routed directly to the bed. Subglacial drainage pathways were predicted from the hydraulic potential, following *Shreve* [1972], and conduit diameters were able to evolve through time due to melt enlargement and creep closure [*Spring and Hutter,* 1981], thus allowing the capacity of the system to respond to changing inputs from the surface. The configuration of the system was also able to switch between a distributed system and a channelized system represented by different predefined number and geometries of conduits. 'Distributed' links were changed to channelized flow paths as the modelled snowline passed each moulin. From this perspective, the subglacial model is therefore rigid since switching between both systems does not permit smooth transitions with the bed being partially drained by each system. However, the model captured the

essential features of observed proglacial hydrographs, including diurnal and seasonal fluctuations and subglacial water pressure records. The best matches were for the middle of the melt season, when the conduit network was well established, but the model performed less well for the beginning and end of summer when the drainage system would have been in a transition phase between distributed and channelized type systems.

A different approach to physically-based time-dependent hydrological modelling was taken by *Flowers and Clarke* [2002a] who built upon the lumped element model developed by *Clarke* [1996]. Rather than specifying a drainage network, they parameterised basal drainage as two-layer distributed system, analogous to a porous subglacial sheet perched above a sub-till aquifer. The subglacial sheet was allowed to expand vertically to accommodate flow, and its hydraulic conductivity increased with ice thickness. The subglacial sheet and the underlying aquifer were coupled to supraglacial and englacial drainage systems, so that water could flow through or be stored within the system, depending on recharge rates and antecedent conditions. The model was applied to Trapridge Glacier, Yukon [*Flowers and Clarke*, 2002b] and, with some modifications, to Vatnajökull in Iceland [*Flowers et al.,* 2003]. The essential difference between the two versions of the model is that the former assumes that hydraulic potential depends on the balance between recharge rates and the ability of the basal drainage system to evacuate stored water, whereas in the latter it is a simple function of bed elevation and ice overburden pressure. Despite their simplifications, the *Flowers and Clarke*, [2002b] and *Flowers et al.* [2003] models are thought to yield a more realistic picture of ice sheet hydrology in some situations than the *Arnold et al.* [1998] model as they allow for the coexistence of, and a more realistic switch between, distributed and channelized drainage systems [*Benn and Evans,* 2010].

2.3.2.3 Modelling hydrology and basal motion

Feedbacks between basal sliding and subglacial water pressures are a key aspect of the behaviour of the subglacial hydrological system, yet prior to the model developed by *Kessler and Anderson* [2004], no simulation had reproduced the wide range of hydrological behaviours attributed to these feedbacks. *Kessler and Anderson* [2004] linked three hydrological subsystems: i) an englacial water storage reservoir; ii) a centre-line conduit; and iii) a linked-cavity network. In doing so, they were able to simulate the spring speed-up characteristics of a temperate glacier. They concluded

that key glacial hydrological events result not from the forcing or the detailed geometry of the bed and ice pressure, as is inferred by *Shreve's* [1972] theory, but from important interactions between englacial and subglacial storage and subglacial network structure.

In recent years several other authors have also stressed the importance of including interactions between subglacial hydrology and ice dynamics in prognostic models [*Bartholomaus et al., 2008*; *Bell,* 2008; *Stearns et al.,* 2008]. Currently, some of the most advanced models which couple hydrology and ice dynamics currently are those by *Piment3l et al.* [2010] and *Pimentel and Flowers* [2010]. *Pimentel et al.* [2010] used a hydrologically coupled flowband model of higher-order ice dynamics to explore perturbations in response to supraglacial water drainage and subglacial flooding. This model was designed to simulate realistic basal boundary conditions capable of hydrologically-driven acceleration. *Pimentel and Flowers* [2010] further developed *Pimentel et al.'s* [2010] numerical formulation and used hypothetical drainage scenarios inspired by observations. Although the model had some large limitations, it captured the spring transition on the GrIS, and simulations of summer drainage at a Greenland-type outlet glacier produced flow speeds that compare well with *Shepherd et al.'s* [2009] measured seasonal speed-up. *Pimentel and Flowers'* [2010] results support the suggestion that a channelized drainage system can form beneath the margins of the GrIS [*Joughin et al.,* 2008], and may contribute to reducing the dynamic impact of floods derived from supraglacial lakes [*Das et al.,* 2008].

More recently, *Schoof* [2010] constructed what is probably the most sophisticated model to date that captures the 'dynamic switching' [*Kamb et al.,* 1985] between distributed and channelized subglacial drainage systems and its effects on spatial patterns of water pressure beneath an ice mass. Numerical solutions indicate that channelization, water pressure reduction and glacier deceleration, rather than acceleration, should occur above a critical rate of water flow, meaning that higher rates of steady water supply can suppress rather than enhance dynamic thinning [*Schoof*, 2010]. This suggests that the direct positive feedback between surface melt and ice acceleration inferred by various studies [*Zwally et al.* 2002; *Box and Ski.,* 2007; *Das et al.,* 2008] may be a local or short-term phenomenon and may not be universally applicable, especially in the long-term. Nevertheless, short-term increases in water input are accommodated by the drainage system through temporary spikes in water

pressure, and these spikes do lead to temporary ice acceleration. *Schoof's* [2010] model therefore confirms the suggestion of other studies [*Bartholomaus et al.,* 2008; *Hoffman et al.,* 2011; *Sole et al.,* 2011] that ice acceleration is driven by an increase in meltwater variability due to, for example, supraglacial lake drainage events, rather than an increase in mean surface melt supply.

2.3.3 Section summary

Although physically-based time dependent models are becoming increasingly sophisticated with various processes interacting and varying over space and through time, they are still hampered by the largely unknown behavioural characteristics of real drainage systems, their complexity and their variability. Major simplifying assumptions still need to be made in order to represent important physical processes. In particular, determining where surface water should reach the bed in a spatially distributed model, and finding realistic ways of evolving the configuration of the subglacial drainage system through time present major challenges. There is therefore a need to develop a physically-based time-dependent glacier hydrological model for an area of the GrIS which is driven, parameterised and evaluated with real data.

2.4 Study Site: Paakitsoq, West Greenland

This section first gives a brief overview of the Paakitsoq region and outlines the key reasons for choosing it as a study site. Second, previous scientific research in the region, relevant to the present study, is briefly reviewed.

2.4.1 The Paakitsoq region

The study focuses on the Paakitsup Akuliarusersua basin on the western margin of the GrIS. This basin, often referred to as the Paakitsoq region after the nearby bay [*Ahlstrøm et al.,* 2007; 2008], is defined as the ~2,300 km^2 area north east of Jakobshavn Isbrae (Figure 2.2).

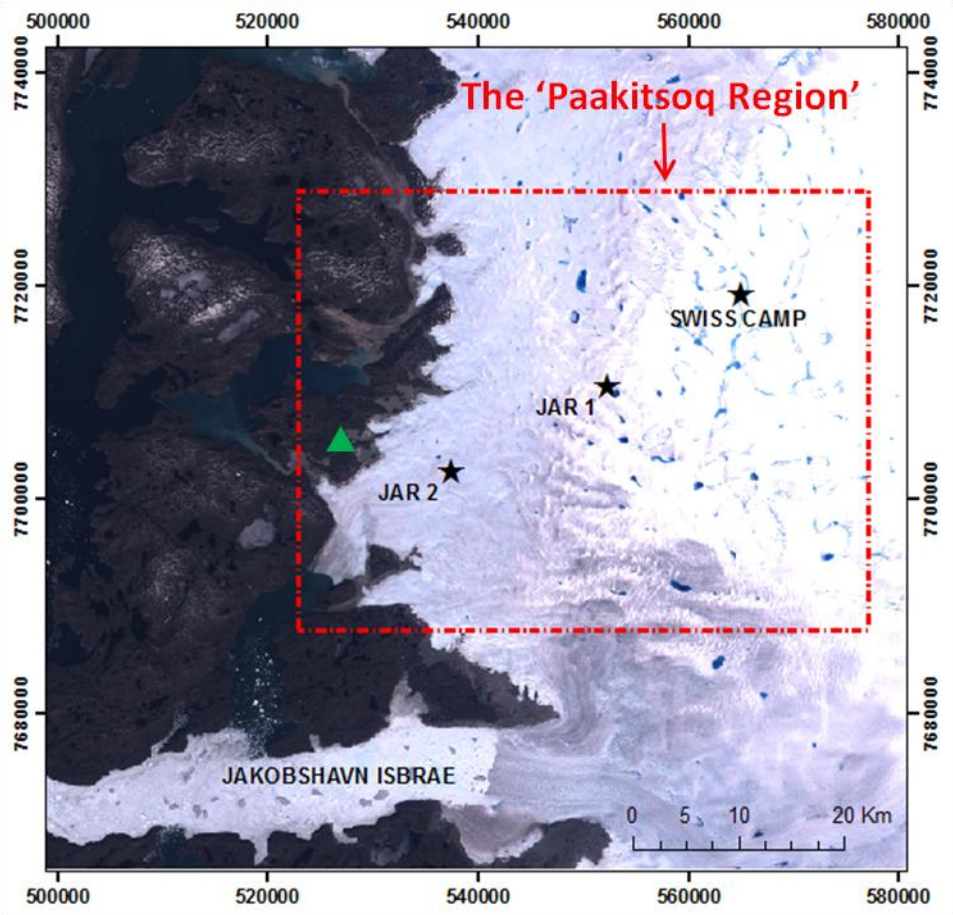

Figure 2.2 Map of the Paakitsoq region. The red box shows the model domain. The green triangle marks the ASIAQ Greenland Survey gauging station where precipitation data are measured.

The Paakitsoq region is chosen as a study site primarily due to the high availability of various data necessary to drive, calibrate and evaluate different components of the complete hydrological model. These include: i) meteorological data from the three GC-Net stations, JAR 1, JAR 2 and Swiss Camp [*Steffen and Box,* 2001] and coastal precipitation data from ASIAQ Greenland Survey Station 437 (190 m a.s.l. ~4 km west of the ice margin) for the surface mass balance modelling component of the study (Figure 2.2); ii) a relatively high-resolution bed DEM necessary for the subglacial modelling component (obtained from Joel Plummer (University of Kansas), see Chapter 5, Section 5.2.1.1); and iii) proglacial stream discharge data measured at the ASIAQ Survey Station 437 for evaluation of the full model.

The Paakitsoq region has been the focus of much scientific work, partly due to hydropower feasibility investigations and the development of hydropower plants

beginning in the 1980s [*Ahlstrøm et al.,* 2007; 2008], but particularly since the establishment of the Swiss Camp research station (~70 °N, ~49 °W; Figure 2.2). To the south of Paakitsoq is Greenland's largest outlet glacier; Jakobshavn Isbrae, which drains 6% of the ice sheet and has experienced a dramatic phase of retreat and thinning since 1998 [*Joughin et al.,* 2008b].

2.4.2 Mass balance at Paakitsoq

The Paakitsoq region includes predominantly land-terminating ice, with a relatively small tidewater glacier, Sermeq Avannarleq ("Dead Glacier"), which calves into a side arm of the Jakobshavn Fjord. Ice elevation in the region varies from near sea level at the western margin to ~1200 m above sea level (a.s.l.) at the easterly edge of the area. Ice flow in the region is predominantly towards the west, although in the south of the area it is influenced by Jakobshavn Isbrae and flows in a more south westerly direction [*Mottram et al.,* 2009; *Joughin et al.,* 2010].

Sermeq Avannarleq has experienced a negative mass balance beginning in 1985 and field observations suggest that since 2000, the tidewater tongue, currently ~2 km in length, has retreated ~2 km [*Colgan et al.,* 2011a]. Additionally, satellite imagery indicates that the ice sheet margin between Sermeq Avannarleq (to the north, south west of JAR 2) and Jakobshavn Isbrae (to the south) has retreated by up to ~1.2 km between 1962 and 1992, despite a decline in average summer temperatures during the time period [*Sohn et al.,* 1998]. The recent retreat of Jakobshavn Isbrae may also be influencing some of the recently observed thinning across the area [*Joughin et al.,* 2004; *Krabill et al.,* 2004].

Thermistor measurements of englacial ice temperature taken by *Thomsen and Olesen* [1990] at one location 9.5 km upstream from the ice margin reveal slightly negative temperatures (-0.3 to -0.1 °C) from the base of the ice sheet to ~ 50 m from the surface, above which temperature drops and reaches a minimum of -2.1 °C. Additional measurements through ice 202 m thick, 4.4 km upstream from the ice margin and 300 m thick, 3.2 km upstream from the ice margin reveal a basal temperature of -0.9 °C and englacial temperatures ranging between -2.1 °C and -0.6 °C [*Thomsen*, 1988]. Farther inland, the anisotropic-ice flowline model of Wang *et al.* [2002] suggests that englacial ice temperatures reach lower values but that temperature at the base is at the PMP of -1.0 °C. The model of Wang *et al.* [2002] was also applied to a flowline

through Swiss Camp to estimate the dates of internal layers detected using radio-echo-sounding measurements. By using present-day data of accumulation rate, surface temperature, surface elevation, and ice thickness along the flowline as model inputs, a close agreement was found between the isochrones generated from the model and the observed internal layers with confirmed dates, indicating that this part of the Greenland ice sheet was primarily in steady-state in 2002 [*Wang et al.,* 2002].

2.4.3 Supraglacial hydrology at Paakitsoq

Water at Paakitsoq drains from the ice sheet supraglacially or subglacially through numerous proglacial lakes (Figure 2.3). The three largest are proglacial lakes 326 and 233 which are connected to the central lake 187 where the ASIAQ 437 gauging station is located [*Thomsen et al,* 1988]. Thus, these proglacial lakes are thought to influence the discharge at the gauging station by introducing a lag. On the ice surface, numerous supraglacial lakes are observed [*Box and Ski*, 2007; *McMillan et al.,* 2007; *Lampkin,* 2011]. These lakes are occasionally observed to drain rapidly by hydrofacture or relatively slowly by overflow [*Das et al.,* 2008; *Tedesco et al.,* in review] (see Section 2.2.1). Numerous studies have focussed on the spatial patterns, evolution, and drainage of supraglacial lakes in the Paakitsoq region. For example, *Lampkin* [2011] used multitemporal Landsat panchromatic imagery for a large area of west Greenland (including the Paakitsoq region) during the 2007 melt season to provide evidence for a high spatial clustering of relatively small lakes (< 0.5 km^2) at lower elevations (~100 – 700 m), and a lower spatial clustering of large lakes (0.5 - 1.5 km^2) at higher elevations (700 – 1200 m). *McMillan et al.* [2007] investigated surface lake development and drainage over a large part of the Paakitsoq region using a combination of Landsat 7 ETM+ and ASTER images from 2001, whereas *Box and Ski* [2007] focussed more specifically on calculating temporal changes in areas, depths and volumes of a few lakes in the area through the use of a supraglacial lake-depth retrieval function, based on the correspondence between MODIS reflectance and water depth measured during raft surveys.

The Danish Meteorological Office (DMO) produced a topographic map, based on 1985 aerial photography, for a 40 x 20 km portion of the Paakitsoq region [*Thomsen et al.,* 1988]. Typical moulin diameters for the region were 1 – 2 m [*Thomsen et al., 1988*] and, as calculated by *Colgan and Steffen* [2009], the observed moulin density increases towards the ice margin with values of 0 - 0.89 km^{-2}. This is slightly lower than the

moulin density of ~0.2 km^{-2} calculated by *Zwally et al.* [2002] for the same region. These 1985 aerial photographs were recently digitized and aggregated into an orthomosaic with the intent of studying changes in the ice geometry of nearby Jakobshavn Isbrae [*Motyka et al.,* 2010]. *Colgan et al.* [2011b] have since compared this historical orthomosaic with the commercially acquired panchromatic 15th July 2009 Worldview-1 image of the same area to establish that the total area occupied by crevasses > 2 m wide, within the overlapping 608 km^2 area, increased by 13 ± 4% from 1985 to 2009. As crevasses and prominent supraglacial features such as large lakes and river systems are typically found to be mutually exclusive [*Thomsen et al.,* 1988], this result implies an increase in the number of smaller catchments [*Colgan et al.,* 2011b].

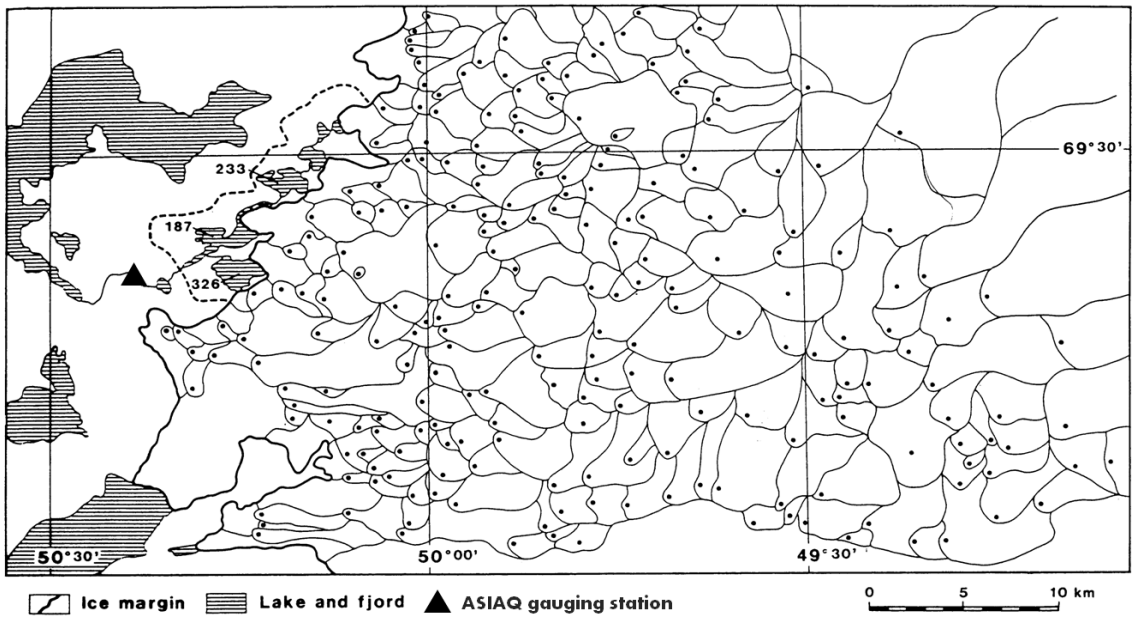

Figure 2.3 Map of the Paakitsoq region. The black lines on the ice define surface sub-catchments feeding moulins (black dots). The black dashed areas depict proglacial lakes through which meltwater flows to reach the ASIAQ gauging station (black triangle) (adapted from Figure 2 in *Thomsen et al.* [1989]).

Various studies with a focus on the Paakitsoq region have linked accelerations in ice velocity with increases in surface meltwater inputs to the subglacial system, often as a result of supraglacial lake drainage, suggesting that local hydraulically induced basal sliding can explain short-term and seasonal variability in ice velocities [e.g., *Zwally et al.,* 2002; *Das et al.,* 2008; *Joughin et al.,* 2008; *Hoffman et al.,* 2011; *Colgan et al.,* 2012] (see Section 2.2.3 for further details).

2.4.4 Subglacial hydrology at Paakitsoq

Although the natural setting of the Paakitsoq region makes dye-tracer experiments difficult [*Thomsen et al.,* 1989], various sources of evidence indicate the existence of an active subglacial system. For example, fluctuating subglacial water pressures measured in several boreholes by *Thomsen and Olesen* [1990] provide evidence for a dynamic subglacial drainage system which changes spatially and temporally through the melt season. A well-developed subglacial system is also indicted by high levels of turbidity in marginal lakes 187, 233 and 326 [*Thomsen et al.,* 1989] (Figure 2.3). While diurnal oscillations in subglacial water pressure during the melt season were positively correlated with surface air temperatures, subglacial pressure peaks were delayed by 2 - 5 hours relative to temperature maxima [*Thomsen et al.,* 1991]. This suggests that supraglacial meltwater flows relatively rapidly through moulins to reach the subglacial system.

Borehole measurements by *Thomsen and Olesen* [1991] and *Thomsen et al.* [1991] indicated that subglacial water pressures are 79% - 105% and 85% - 94% (respectively) of ice overburden pressures for the area within 10 km of the ice margin where ice thicknesses reach 400 m. If these measurements represent long-term average steady-state water pressures, it suggests that the subglacial drainage network could be approximated using *Shreve's* [1972] theory with k values of 0.79 – 1.05 (see Section 2.2.2.2, Equation 2.1). These proposed k values are consistent with *Colgan et al.'s* [2011a] model of the Sermeq Avannarleq flowline which suggests that the hydraulic head (or englacial water table) elevation annually oscillates relatively close to, or at, flotation (i.e. subglacial water pressures are close to, or equal, ice overburden pressures).

2.5 Chapter summary

- The surface mass balance of the GrIS is thought to be close to zero. However, net ice sheet mass balance is negative due to increased ice flux resulting from increased basal sliding. This occurs in two ways: 1) increased basal lubrication of both land- and marine- terminating outlet glaciers due to meltwater reaching the bed; and 2) increased ice velocity and calving flux of marine-terminating glaciers due to thinning and retreat at the calving front.

- Evidence suggests that it is the variability in magnitude and timing of meltwater input to the subglacial drainage system of the GrIS, rather than the total volume of meltwater input to the system, that has the greatest influence on subglacial water pressures and therefore ice motion. However, although large increases in ice velocity have been observed in the short-term, significant uncertainty exists in determining how the GrIS hydrological system will evolve over decadal and longer timescales to changing volumes of meltwater and thereby influence the dynamics of the ice sheet.

- Although physically-based time dependent models are becoming increasingly sophisticated with various processes interacting and varying over space and through time, they are still hampered by the largely unknown behavioural characteristics of real drainage systems, their complexity and their variability. There is therefore a need to develop a physically-based time-dependent glacier hydrological model for an area of the GrIS which is driven, parameterised and evaluated with real data.

- The Paakitsoq region on the western margin of the GrIS is an area of predominantly land-terminating ice to the north east of Greenland's largest outlet glacier; Jakobshavn Isbrae. The region is chosen as a study site primarily due to the high availability of various data necessary to drive, calibrate and evaluate different components of the complete hydrological model. Of key importance are the proglacial stream discharge data measured at the ASIAQ Survey Station for evaluation of the full hydrological model.

3. Surface melt / runoff model

This chapter focuses on the development, calibration and evaluation of a high resolution, surface mass balance (SMB) model for the Paakitsoq region and forms the basis of a recently published paper [*Banwell et al.,* 2012a]. The model consists of surface energy balance (SEB) model coupled to a subsurface model of the upper snow / firn / ice layers and will be used to calculate high temporal (hourly) and spatial (100 m) resolution runoff for the region. This model will provide input for a surface routing and lake filling model (Chapter 4).

3.1 Data and approach

This chapter focuses on a ~7.5 km wide strip which extends diagonally from south west to north east across the Paakitsoq region and includes the Greenland Climate Network (GC-Net) and ASIAQ Greenland Survey stations (190 m a.s.l., ~4 km west of the ice margin) (Figure 3.1). The total area of this strip is 450 km^2.

The SEB model is forced using a full range of meteorological variables, predominantly from the JAR GC-Net automatic weather station (AWS) where data are available [*Steffen and Box,* 2001]. These include hourly measurements of incoming global shortwave radiation, air temperature, relative humidity and wind speed at a height of 2 m above the ice surface. Due to instrument failure, shortwave radiation data are missing from 1st January to 23rd May 2001 so data from Swiss Camp were used for this period instead. Daily precipitation totals in mm w.e., collected at the ASIAQ station, were divided by 24 to produce hourly totals for model input on days with recorded precipitation. As incoming longwave radiation data were not available for the Paakitsoq region, incoming longwave radiation data were calculated using parameterizations based on the work of *Konzelmann et al.* [1994]. Coastal precipitation data were obtained from ASIAQ.

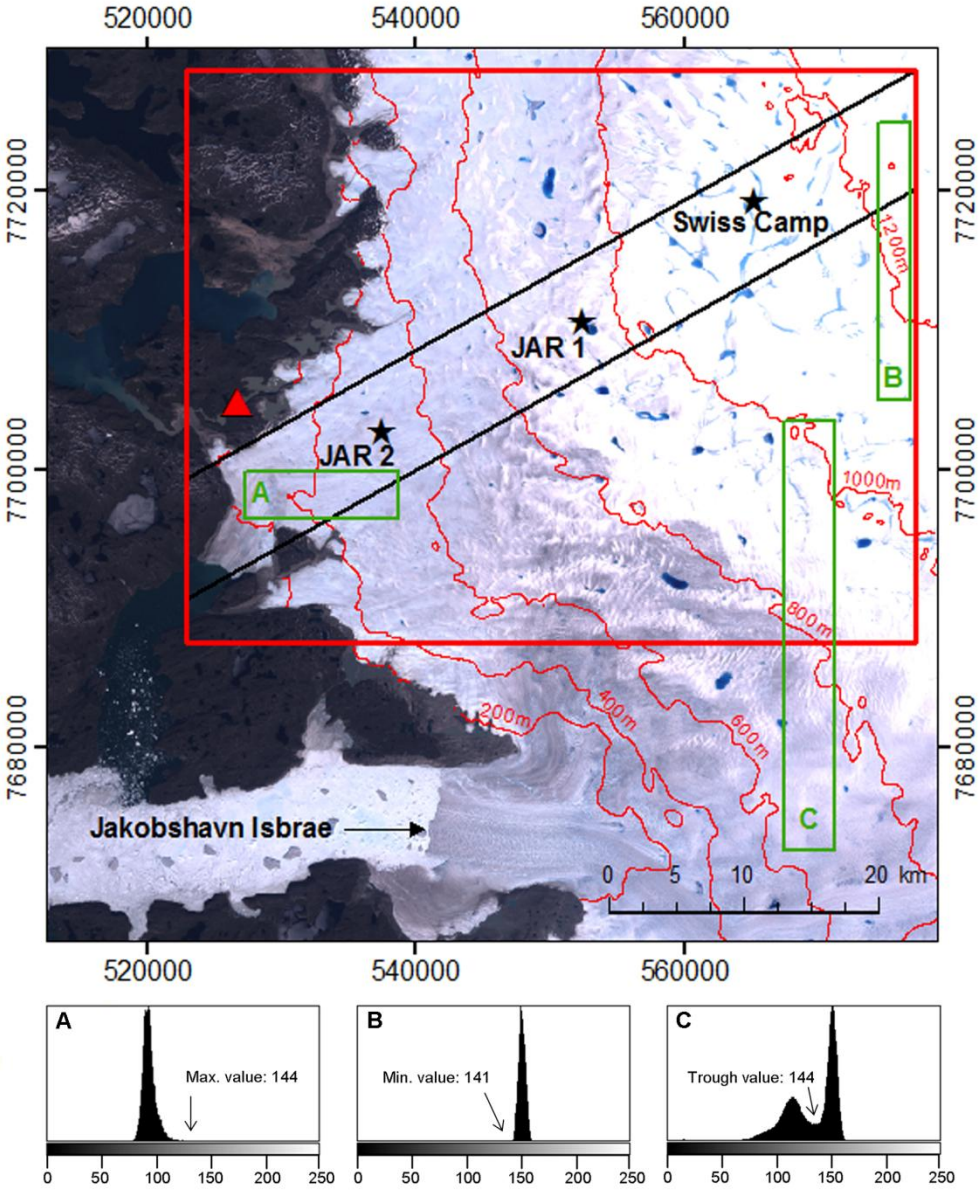

Figure 3.1: Map of the study site. The Paakitsoq region is delineated by the red box. The Landsat-7 ETM+ image behind is dated 07/07/2001. The strip on which this study is focused is outlined in black. The red triangle marks the ASIAQ 437 precipitation and gauging station. Green boxes are example areas of: A) just ice; B) just snow; and C) snow and ice chosen during the thresholding procedure in Section 3.3.2. These 3 boxes correspond to the 3 example histograms of reflectance values shown below the map, where the y axes are normalised to the maximum number of cells of a given brightness within each sample area, and the x axes show brightness numbers.

A DEM of the ice sheet surface is required to spatially distribute meteorological data and compute slope angles and aspects as well as any topographic shading. For this study, the ASTER global digital elevation model (GDEM), which has a nominal grid size of 30 m, is used (http://asterweb.jpl.nasa.gov/gdem.asp). The original GDEM was

checked for obvious artefacts in the area and none were found. The GDEM quality files for the Paakitsoq region show ASTER stacking numbers here lie between 8 and 12, yielding an accuracy of ± 18.2 m (std. dev.) < 500 m elevation, and ± 13.8 m (std. dev.) > 500 m [*MacFerrin,* 2011]. The original data were smoothed with a 6x6 cell median filter to remove small-scale noise then re-sampled to a 100 m resolution using bilinear interpolation.

Although energy balance (EB) modelling is generally used for glaciers with relatively complex terrain, rather than for ice sheets, previous studies have demonstrated that the EB approach is successful at reproducing melt patterns on the GrIS [e.g. *Ambach,* 1977; *Greuell and Konzelmann*, 1994; *Oerlemans and Vugts*, 1993; *van den Broeke et al.,* 2011]. As the aim of this chapter is to model runoff at a high spatial and temporal resolution, it is important to capture as much of the spatial and temporal patterns of albedo, as well as other important parameters and processes. Therefore, an EB model is chosen over a degree-day model.

The EB model is driven by extrapolating the locally-measured data across the model surface domain rather than down-scaling the output from climate reanalyses or a Regional Climate Model (RCM) for a variety of reasons. First, as the study's model domain is relatively small (450 km^2), point station data only needs to be interpolated over a small area. Second, as the model domain is narrow (7.5 km) in width, horizontal gradients will be minimal and this width is less than the horizontal grid sizes of commonly used RCMs [e.g. *Ettema et al.,* 2010*; Fettweis et al.,* 2011]. Third, the chosen approach is computationally less expensive than climate reanalysis or an RCM. Therefore, the use of a high-resolution EB model driven by point station data is a sufficient approach to minimize the uncertainty of the model output for this study [cf. *Machguth and Ahlstrom*, 2010].

The SMB model is calibrated by comparing modelled and measured point data of surface height change and albedo changes at the GC-Net stations: JAR 1, JAR 2 and Swiss Camp [*Steffen and Box,* 2001]. Subsequently, model performance is evaluated in two ways. First, the modelled snowline positions at various stages of the summer are compared to the snowline positions delineated from Landsat-7 ETM+ satellite imagery. Second, the modelled daily albedo over the model domain is compared with the daily surface albedo retrievals from the NASA Terra platform Moderate-resolution Imaging Spectroradiometer (MODIS) sensor MOD10A1 product.

The study focuses on the mass balance years 2000/01 and 2004/05, as during these years there are: i) nearly continuous meteorological data meaning that only limited temporal interpolation is necessary; ii) relatively good albedo and surface melt data for model calibration, and iii) a good availability of cloud-free Landsat and MODIS imagery during the summer months for model evaluation.

3.2 Surface mass balance model

The SEB model is based on that developed by *Rye et al.* [2010] and consists of three coupled components: i) an EB model that calculates the energy exchange between the glacier surface and the atmosphere; ii) a subsurface model, simulating changes in temperature, density and water content in the snow, firn and upper ice layers, and hence refreezing and net runoff; and iii) an accumulation model.

Further details of the SEB subsurface models, and the surface accumulation routine are described in Sections 3.2.1, 3.2.2 and 3.2.3 respectively.

3.2.1 Surface energy balance model

The SEB model is based on that originally developed by *Arnold et al.* [1996] and subsequently updated by *Brock et al.* [2000], *Arnold* [2005], *Arnold et al.* [2006], and *Rye et al.* [2010]. This section primarily focuses on describing adaptations that have been made to the *Rye et al.* [2010] model for application to the Paakitsoq region.

The model determines the total SEB from five main components:

$$Q_M = (SW\downarrow - SW\uparrow) + (LW\downarrow - LW\uparrow) + SHF + LHF + GHF, \quad (3.1)$$

where Q_M is the energy available for melt (if surface temperature is at melting point), $SW\downarrow$ is incoming shortwave radiation, $SW\uparrow$ is outgoing shortwave radiation (i.e. (1 - surface albedo) * $SW\downarrow$), $LW\downarrow$ is incoming longwave radiation, $LW\uparrow$ is outgoing longwave radiation, SHF is the sensible heat flux, *LHF* is the latent heat flux, and *GHF* is the ground heat flux in the snow or ice [*Cuffey and Paterson,* 2010].

3.2.1.1 Shortwave radiation and albedo

Due to lack of detailed cloud-cover records, this study follows *Oerlemans* [1993], and subsequently *Arnold et al.* [1996], in assuming that diffuse radiation from the sky is

one-fifth of the measured global shortwave radiation in all cases. Following the method of *Arnold et al.* [1996], these hourly fluxes of direct and diffuse radiation are then modified at each model grid cell for the local terrain conditions in the case of direct radiation (namely slope angle, aspect, and shading due to surrounding grid cells - although the latter effect is very small over the model domain and is found to negligibly affect the results), and for the sky-view factor in the case of diffuse radiation.

Following *Greuell and Konzelmann* [1994], the surface albedo (α) is calculated as a linear function of the density of the uppermost subsurface grid element (ρ_{top}):

$$\alpha = \alpha_{ice} + (\alpha_{snow} - \alpha_{ice}) ((\rho_{top} - \rho_{ice}) / (\rho_{snow} - \rho_{ice})), \quad (3.2)$$

where α_{snow}, ρ_{snow}, α_{ice} and ρ_{ice} denote fresh snow albedo, fresh snow density, ice albedo and ice density respectively. However, whereas *Rye et al.* [2010] and *Bassford* [2002] denote the top 10 cm of snow and / or ice as the uppermost subsurface grid element, this study follows *Ettema et al.* [2010] and bases the calculations on the top 5 cm of the subsurface grid so that small snowfall events have a more significant short-term influence on the calculations of surface albedo. In the parameterization, changes in surface density represent changes in grain size that affect the surface albedo [*Greuell and Konzelmann,* 1994]. The value for fresh snow albedo is set as 0.82 which is the average snow albedo value calculated from the GC-Net data at JAR 1, JAR 2 and Swiss Camp from 2000 – 2009, and is also consistent with the snow albedo value used by *Ettema et al.* [2010]. If no snow cover exists, then the albedo is set equal to the ice albedo value. The ice albedo, which is assumed constant in time and space, is set at 0.48 which is the average albedo measured at the three GC-Net stations from 2000 to 2009 during periods which are assumed to be snow-free. This value is slightly higher than the value (0.45) used by the MAR model in *Fettweis et al.* [2011], but is lower than the value (0.50) used by *Ettema et al.* [2010]. The value for fresh snow density is set during model calibration (Section 3.3.1). Snow cells within the model are converted to ice once the density exceeds that of superimposed ice (800 kg m^{-3} [*Wright,* 2005]). A value of 910 kg m^{-3} is assumed for ice density [*Cuffey and Paterson,* 2010].

3.2.1.2 Longwave radiation

The net longwave radiation is the calculated sum of incoming flux from the sky ($LW\downarrow$) and the outgoing radiation emitted by the glacier surface ($LW\uparrow$). Since $LW\downarrow$ is strongly dependent on cloud cover, but because there are no cloud cover data available for the

Paakitsoq region, it was first necessary to calculate hourly values of cloud amount. An empirical equation was generated to calculate hourly mean cloud amounts for the Paakitsoq region through the combined use of: i) an existing parameterization for calculating $LW\downarrow$ based on cloud cover [*Konzelmann et al.,* 1994]; and ii) meteorological data (including measured $LW\downarrow$) collected in 2009 from a temporary station on the Russell Glacier near Kangerlussuaq, ~300 km south of the Paakitsoq region (67° 7.240' N, 49° 2.040' W).

For skies that are completely overcast due to low clouds, $LW\downarrow$ is primarily determined by the temperature of the cloud base [*Oke,* 1987]. For completely overcast skies, therefore, the parameterization of $LW\downarrow$ should not contain clear-sky emittance. *Konzelmann et al.* [1994] satisfy this condition by describing emittance as the weighted mean of clear-sky and completely overcast emittances:

$$LW\downarrow = (E_{cs}(1-\nu^{p}) + E_{oc}\nu^{p})\,(\sigma)T^{4}, \tag{3.3}$$

where ν is cloud amount (ν = 1 for a completely cloud covered sky, ν = 0 for clear sky conditions), E_{cs} is the clear sky emissivity, E_{oc} is the emittance of a completely overcast sky, σ is the Stefan-Boltzmann constant (5.67 x 10^{-8} W m^{-2} K^{-4}), T is temperature (K) at 2 m above the ice surface and p is a constant.

Konzelmann et al. [1994] relate clear sky emissivity to measured vapour pressure (e) and T at Swiss Camp, through a modified version of *Brutsaert's* [1975] equation to their data, yielding:

$$E_{cs} = 0.23 + 0.484(e/T)^{1/8}. \tag{3.4}$$

Konzelmann et al. [1994] obtained empirically the emissivity of a completely overcast sky, E_{oc} = 0.952, and the coefficient, p = 4, from hourly means of $LW\downarrow$, T, e and instantaneous observations of ν at Swiss Camp. Thus, the equation for incoming longwave radiation reads:

$$LW\downarrow = ((0.23+0.484(e/T)^{1/8})\,(1-\nu^{4}) + 0.952\,\nu^{4})\,\sigma T^{4}. \tag{3.5}$$

Although the high power (p = 4) resulted from site-specific cloud climatology, where low cloud amounts were caused by high clouds in the sky, and high cloud amounts by low clouds in the sky, this expression has been used successfully at other sites in Greenland [e.g. *Greuell and Konzelmann*, 1994; *Zuo and Oerlemans*, 1996].

Using hourly means of $LW\downarrow$, T and e measured at the Russell Glacier meteorological station from 26th June 2009 to 31st August 2009, hourly mean values for v over the glacier were calculated using Equation 3.5. Since there are no measurements of v for the Paakitsoq region available for use in this study, but a good relationship might be expected between v and relative humidity (RH), for which there are measurements, the first half of the available data (i.e. 26th June – 29th July 2009) from the Russell Glacier dataset is used to investigate the relationship between v and RH for those data. The following equation is obtained:

$$v = (1.848 * RH) - 0.803, \tag{3.6}$$

which has an R^2 value of 0.46 (Figure 3.2).

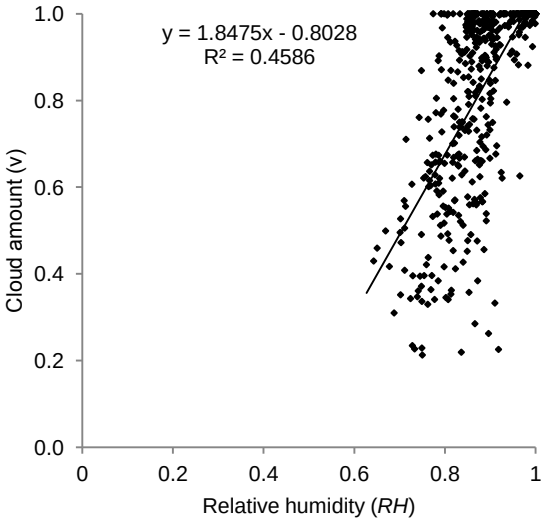

Figure 3.2: Plot of measurements of RH against hourly mean values for v (calculated using Equation 3.5) for Russell Glacier.

As an independent test of this relationship, mean hourly values of v over Russell Glacier for the second half of the available data (i.e. 30th July 2009 - 31st August 2009) were calculated using Equation 3.6, which were then used in Equation 3.5 to calculate the mean hourly $LW\downarrow$ fluxes. The root mean square error (RMSE) between the calculated and measured average daily $LW\downarrow$ fluxes is 19.8 W m^2. In comparison, if a constant value of v = 0.6 [c.f. *Konzelmann et al.,* 1994] is used, the RMSE between the calculated and measured average daily $LW\downarrow$ fluxes is then 51.2 W m^{-2}. Although the data sets used for both parameterizing and testing the relationship between v and RH

are relatively short, the analysis does suggest that in the absence of an alternative approach, *RH* provides a useful proxy for cloud amount on the GrIS and that the *Konzelmann et al.* [1994] parameterization is a robust one. This approach is therefore used in this study to determine hourly $LW\downarrow$ at Paakitsoq.

The outgoing longwave radiation emitted from the glacier surface is computed as a function of surface temperature (T_s) (i.e. the temperature of the top grid cell) and the Stefan-Boltzmann constant (σ):

$$LW\uparrow = \sigma T_s^4. \tag{3.7}$$

3.2.1.3 Turbulent heat fluxes

The sensible and latent turbulent heat fluxes are calculated using the bulk aerodynamic method [*Munro,* 1990], which requires inputs of *T, RH*, air pressure, and wind speed [*Rye et al.,* 2010]. Stability is corrected for following *Dyer* [1974]. *T* at each model grid cell is calculated using the atmospheric lapse rate of 6 °C km^{-1} in summer (1st May to 30th September) and 8 °C km^{-1} in winter (1st October to 30th April). These values are seasonal averages of *Steffen and Box's* [2001] calculations of mean monthly temperature lapse rates between JAR 1 and Summit GC-Net stations. These lapse rates were verified by calculating the average lapse rates for both summer and winter between JAR 2 and Swiss Camp for 2005, which, to one decimal place, were found to be the same as those calculated by *Steffen and Box* [2001]. Air pressure was assumed to decline at a rate of 10 kPa km^{-1}. *RH* and wind speed are assumed to be constant across the ice surface. The surface roughness lengths for snow (0.00022 m) and ice (0.00066 m) for the Paakitsoq region are taken as the mean values from *Arnold and Rees* [2003]. The model is found to be relatively insensitive to surface roughness values. Furthermore, through the calibration process, small errors introduced by prescribing fixed values for some parameters are compensated for by small adjustments to other parameter values during their optimization [cf. *Rye et al.,* 2010]. For each grid cell, the SEB model produces melt in mm w.e. on an hourly time step, provided that $T_s = 0$ °C and $Q_M > 0$. This meltwater is then used as input to the subsurface model (Section 3.2.2).

3.2.2 Subsurface model

This study uses the subsurface model developed by *Rye et al.* [2010], which built on

previous work from *Wright* [2005], *Bassford* [2002], and *Greuell and Konzelmann* [1994]. The model is run using a time step of 15 minutes in order to maintain numerical stability [*Rye et al.,* 2010].

For each model grid cell, the subsurface model calculates temperature, density, and water content on a one-dimensional grid extending at least 25 m vertically from the surface into the ice sheet. Only the upper 25 m of snow / firn / ice is considered as this is the depth at which annual temperature oscillations can no longer be detected [*Greuell and Konzelmann,* 1994]. The vertical grid cells range in size from 5 cm near the surface (where temperature gradients are largest) to 200 cm at the grid base [*Bassford,* 2002]. Meltwater generated by the SEB model is able to percolate downward through the grid. Energy (and therefore meltwater) is also added to the subsurface grid through the penetration of $SW\downarrow$, which is attenuated according to Beer's law [*Greuell and Konzelmann*, 1994; *Bassford*, 2002; *Bougamont et al.,* 2005; *Wright,* 2005; *Rye et al*., 2010]. Refreezing occurs in cells where the temperature is below 0 °C and the density is less than the density of ice. The cell below receives any residual meltwater if either of these conditions is not met, or if there is excess meltwater after refreezing. Meltwater percolates until it reaches the impermeable snow / ice interface. At this layer, superimposed ice may be formed and is calculated using the approach of *Wakahama et al*. [1976]. However, if the rate at which meltwater reaches the snow / ice interface exceeds the rate of superimposed ice formation, then excess water will form runoff from the glacier [*Rye et al.,* 2010]. The hourly runoff for each model grid cell is stored as output and will be used as input for a surface meltwater routing model in forthcoming work.

Following *Rye et al.* [2010], densification of snow and firn in the model is driven entirely by surface melting and refreezing. This is a reasonable assumption as the study area is in the wet zone of the GrIS where these two mechanisms dominate the densification process, unlike at higher elevations in the dry zone where settling and packing dominate [*Cuffey and Paterson*, 2010].

3.2.3 Surface accumulation model

Hourly precipitation is distributed over the ice sheet surface using an elevation-dependent precipitation gradient [*Rye et al.,* 2010]. Estimates of the elevation-dependent precipitation gradient for the western area of the GrIS from sea level to

2000 m vary widely between 5% and 20% per 100 m [*Ohmura and Reeh,* 2001; *Bales et al.*, 2009; *Burgess et al.,* 2010]. This suggests that the precipitation gradient also exhibits substantial year-to-year change and / or varies with distance inland from the coast [*Bales et al.,* 2009]. Owing to this uncertainly, the elevation-dependent precipitation gradient is treated as a tunable model parameter (Section 3.3.1). However, once set, it is constant in space and time throughout the model run. The fractions of precipitation falling as rain and snow in each grid cell are calculated as a function of air temperature using a threshold temperature [e.g., *Oerlemans,* 1993; *Bougamont et al.,* 2005; *Rye et al.,* 2010]. The value for the threshold temperature for solid / liquid precipitation is also treated as a tunable model parameter (Section 3.3.1).

3.2.4 Initial conditions

The separate model simulations for each of the mass balance years, 2000/01 and 2004/05, run from 1st October to 30th September. Following *Rye et al.* [2010], each grid cell is initialized as bare ice and all subsurface cells are set to the mean annual air temperature. Before commencing the main model run for each year, the model is spun-up for five years using that year's climate data. While early sensitivity tests in this study indicated that five years of spin-up were necessary in order for the mass balance and the subsurface temperature profiles to attain a steady-state, *Rye et al.* [2010] found 20 years of spin-up were necessary when modeling mass balance for glaciers in Svalbard, and *Bougamont et al.* [2005] found that only 6 months of spin-up was sufficient for a similar model applied to the whole of the GrIS. This difference in required spin-up times between the three studies may be due to the varying initial conditions, which will not influence the steady-state, only the time taken for the iterative process to reach a stable solution [*Rye et al.,* 2010].

3.3 Model calibration and evaluation

Calibration involves optimizing model parameters so that modeled results are consistent with the available measurements, in this case, continuous recordings of snow depth and albedo made at the GC-Net weather stations JAR 1, JAR 2 and Swiss Camp [*Steffen and Box*, 2001] for both 2000/01 and 2004/05. The model is evaluated in two ways. First the calibrated model output of snowline position is tested against snowline positions derived from satellite imagery. Second, the modelled albedo is

compared with satellite-derived albedo over the model domain. Both of these steps are carried out for various stages of the summer for both 2000/01 and 2004/05. In order to model the temporally and spatially varying magnitude of meltwater runoff as accurately as possible, each of the two mass balance years is parameterized separately.

As suitable observations to constrain values for three key parameters are not available, results from multiple model runs are compared with measurements in order to identify suitable values. The parameters are: i) fresh snow density; ii) elevation-dependent precipitation gradient; and iii) the threshold temperature for solid / liquid precipitation. Combinations of parameter values for model runs were chosen systematically from within defined ranges at specific intervals suggested in the literature [*Oerlemans,* 1993; *Bougamont et al.,* 2005; *Bales et al*., 2009; *Burgess et al*., 2010; *Cuffey and Paterson*, 2010; *Rye et al.,* 2010] (Table 3.1).

	Range tested	Increment	Optimal values for 2000/01 & 2004/05
Fresh snow density (kg m^{-3})	100 – 450	25	400
Threshold temperature for solid / liquid precipitation (°C)	0.0 – 2.0	0.5	2.0
Precipitation gradient (% increase / 100m elevation)	2 – 20	2	14

Table 3.1: Optimal parameter values and the ranges from which they were chosen.

For fresh snow density, the range 100 – 450 kg m^{-3} is parameterized for. As snow densification due to settling, compression and the action of the wind is not accounted for by the model, but is instead driven by melting and refreezing alone, a value towards the upper end of this range might be expected during model calibration [*Bassford,* 2002; *Wright*, 2005; *Rye et al*., 2010]. The value will represent average snowpack density before the onset of melting rather than the density of fresh new snow [*Wright*, 2005]. Not all combinations of parameter values within these three ranges are tested. Instead, runs with combinations of high, medium and low values of the 3 model parameters were performed to identify a first tier of model sensitivity – a total of 3^3 = 27 runs. By analysis of the RMSE between sets of measured and modelled data, regions of parameter space showing the greatest sensitivity were then identified and parameters were tuned further at finer increments as specified in Table 3.1 (Section 3.3.1).

3.3.1 Model calibration using snow depth and albedo measurements

For each of the mass balance years, 2000/01 and 2004/05, the SMB model was run multiple times with different combinations of parameter values for the ~7.5 km wide strip of the Paakitsoq region (Figure 3.1) (Table 3.1). For each year, daily variations in modelled surface height and surface albedo for the cells representing the GC-Net stations JAR 1, JAR 2 and Swiss Camp were compared, where data were available, with surface height measured at these stations by ultrasonic depth gauges (UDGs) and with albedo measured by up and down facing-pyranometers. Modelled surface height at a point was calculated by multiplying the modelled melt in mm w.e. for a surface cell, by the ratio of water density to modelled density for that surface cell.

Surface height data are available at JAR 1 and JAR 2 for 2000/01 and 2004/05 but unfortunately are unavailable at Swiss Camp for either year. Albedo measurements are available at JAR 1, JAR 2 and Swiss Camp for 2000/01, and JAR 1 and JAR 2 for 2004/05.

The aim during model calibration was to identify the combination of parameter values that minimized the RMSE difference between the measured and modelled data. For each possible parameter set for each year, two RMSEs are calculated, one based on all of the available measured surface height data, and one based on all of the available albedo data, from the various GC-Net stations, for that year.

3.3.2 Model evaluation through comparison of modelled and measured snowline position

3.3.2.1 Snowline delineation from satellite data

Landsat-7 ETM+ imagery is used to delineate the 'snowline' position using a combination of the Normalised Difference Snow Index (NDSI) and image thresholding [c.f. *Gupta et al.,* 2005]. Although the word 'snowline' is used, it is realised that in reality this is not a clear-cut boundary, but rather a transitional zone involving patches of snow, ice, and slush.

The NDSI technique has been used previously to distinguish between highly reflective

snow / ice and cloud [e.g., *Hall et al.,* 1995; *König et al.,* 2001]. The method exploits the different spectral signatures of surfaces at different wavelengths. However, it is much harder to distinguish between snow and ice, and therefore the snowline position, using this method alone. Thus, once cloud was detected using NDSI, thresholding of the imagery was used to delineate the snowline (see below). Combined, these methods provide an effective and quick way to delineate cloud from snow / ice, and snow from ice. It should be noted that all kinds of snow including slush, firn and fresh snow are included within the 'snow' category. This is consistent with the definition of the 'snowline' as being the boundary between the wet-snow and superimposed-ice zones, or the boundary between firn and glacier ice at the end of the melt season [*Greuell and Knap*, 2000; *Cuffey and Paterson*, 2010; *Cogley et al.,* 2011].

Landsat-7 ETM+ data were acquired for days of our chosen mass balance years with minimal cloud cover from USGS (http://glovis.usgs.gov). Before the NDSI calculation was made, data were pre-processed. First, an atmospheric correction was applied to raw, 8-bit, level 1b data using the dark pixel subtraction method [*Lathrop et al.,* 1991]. Second, each band was converted from digital numbers (DNs) to radiance and then from radiance to reflectance using the equations of *Chander et al.* [2009].

Bands 2 (*B2*; corresponding to green - 0.519-0.601 μm) and 5 (*B5*; corresponding to the mid-infrared - 1.547-1.748 μm) were then used to calculate the NDSI:

$$\mathrm{NDSI} = \frac{B2-B5}{B2+B5}, \tag{3.8}$$

The NDSI was then used to distinguish between areas of snow / ice and cloud in the images. The technique works best for 'optically thick' clouds such as cumulus clouds. The method exploits the high spectral reflectivity of clouds in the visible and shortwave infrared (SWIR) region compared to the relatively low reflectivity of ice and snow at SWIR wavelengths [*Greuell and Knap*, 2000; *Griffin et al.*, 2005]. In the image produced through NDSI, the thickest cloud is the darkest in colour, and the thinner the cloud, the lighter the grey colour is. Snow is near-white in colour. If cloud is detected, caution was then exercised in these areas when delineating the snowline using the subsequent thresholding technique (see below). However, it is not useful to immediately mask off all areas of the Landsat image overlain by cloud as some cloudy areas are optically thin and give some information on the surface conditions below.

Landsat band 4 (corresponding to the near-infrared band - 1.772-1.898 μm), was

selected to generate thresholded snowline images because it is less susceptible to saturation, thus making snow / ice distinction clearer. The brightness threshold is based on the analysis of Landsat band 4 histograms for each individual satellite image. For each image, the following were identified: a) five areas thought to contain only snow; b) five areas thought to contain only ice; and c) five areas containing an obvious zone between ice and snow. Only cloud-free areas (identified using the NDSI technique) were selected. The size of these areas ranged from ~50 km^2 to ~100 km^2. For illustrative purposes, the Landsat image in Figure 3.1 is overlain by three boxes containing (a) an area of snow only, (b) an area of ice only, and (c) an area containing both ice and snow.

Individual histograms for each of the 15 areas of each image were produced. Again, for illustrative purposes, three histograms are shown in Figure 3.1, corresponding to the three boxed areas: a), b), and c). For each image, the maximum brightness values in each of the five areas of ice were averaged. Similarly, the minimum brightness values in each of the five areas of snow were averaged. For the five areas containing a snow / ice boundary, the brightness values of the troughs in the bimodal histograms were averaged. The average upper limit for ice and the lower limit for snow were used to help better constrain the bimodal trough value. For example, the maximum brightness value for ice in Figure 3.1a is 147, and the minimum brightness value for snow in Figure 3.1b is 140. Therefore the value of the ice / snow threshold value is expected to lie somewhere between 140 and 147. This is confirmed by the minimum brightness value in the trough between the ice and snow peaks in Figure 3.1c, determined to be 144. 144 would therefore be taken as the threshold value for the ice / snow transition, and applied it to the Landsat band 4 brightness values for snowline delineation. Although the threshold value is clear in this example, for histograms with low, broad troughs, or for histograms of Landsat areas containing lakes or large areas of surface water, it is useful to have both the average maximum brightness value for ice and the average minimum brightness value for snow in order to help constrain the limits for the ice / snow threshold value.

3.3.2.2 Snowline delineation from model output

A key output from the calibrated model runs for each year was gridded cell albedo values for each hour. Cells with an albedo greater than that of ice (set at 0.48), were classified as 'snow'. 'Snow' therefore includes a wide range of albedo values

representing snow at different stages of metamorphism and melt, including fresh snow, firn and slush. This is consistent with how snow is categorized in the satellite imagery using the thresholding technique (above).

3.3.2.3 Comparison of measured and modelled snowline position

For each year (2000/01 and 2004/05) and for each day of the summer for which there is a thresholded satellite image available, both the image and the model output consist of a grid containing cells classified as either ice or snow. The cloud cover produced from the NDSI indicated that there was no cloud within the strip on any day for which we were comparing modelled and measured snowline position. To evaluate model performance with respect to the snowline position, the percentage of mismatched cells is calculated (i.e. where modelled snow / ice cover does not match observed). For each year, the calibrated SMB model is run using the optimal set of parameter values selected in Section 3.3.1 and the average value of mismatched cells across the 2 or 3 available satellite images is calculated.

3.3.3 Model evaluation through comparison of modelled and satellite-derived albedo data

The modelled daily albedo are compared to the daily surface albedo retrievals from the NASA Terra platform MODIS sensor MOD10A1 product (version 005), available from the National Snow and Ice Data Center [*Hall et al.,* 2006]. Surface albedo at 500 m resolution is calculated using the first seven visible and near-infrared MODIS bands [*Klein and Stroeve*, 2002*; Klein and Barnett,* 2003]. Original MODIS data downloaded from NSIDC consisted of one tile (1200 km by 1200 km) gridded in a sinusoidal map projection and containing the entire area under study. Albedo values in the product are reported as percent (0 – 100) together with other flag values such as cloud obscuration and self-shadowing. The MODIS re-projection tool (MRT, https://lpdaac.usgs.gov/tools/modis_reprojection_tool) was used to re-project the data in UTM coordinates and extract daily MODIS albedo data from late spring to late summer for the Paakitsoq region for both 2000/01 and 2004/05. Data tiles with > 5% missing data (due to cloud coverage) are discarded. From the remaining data, five relatively evenly spaced dates are selected, from early in the melt season to late in the melt season, in each year. In order for the MODIS-derived albedo data (500 m) to be directly compared to the modelled albedo data (100 m), the model output is re-sampled

to 500 m using bilinear interpolation. As ice albedo is set at the constant value in the model (0.48), all grid cells which have a modelled albedo equal to this are ignored. Thus, snow-covered cells are primarily focused upon. Subsequently, for each date, the MODIS-derived albedo value for each grid cell is plotted against the modelled albedo value for each corresponding grid cell, and R^2 values and RMSEs for the relationships are calculated.

3.4 Results and discussion

3.4.1 Model calibration

The lowest RMSEs between the modelled and measured surface height data for 2000/01, 2004/05 were calculated to be 0.227 m and 0.208 m respectively (Figure 3.3). The lowest RMSEs between the modelled and measured albedo data for 2000/01, 2004/05 were calculated to be 0.084 and 0.118 respectively (Figure 3.4). Optimal values for the key parameters of fresh snow density, elevation-dependent precipitation gradient, and the threshold temperature for solid / liquid precipitation that minimized the RMSEs were the same for both years and were 400 kg m^{-3}, a 14% increase per 100 m, and 2 °C respectively (Table 3.1).

Figure 3.5 shows the relationships between the modelled and measured (a) surface height and (b) albedo data, for all available measurements across both years. The R^2 values for the relationships are 0.99 and 0.70 respectively. Thus, although the match between modelled and measured surface data is very good, the match between modelled and measured albedo data is not as good. Reasons for this are discussed below.

A fresh snow density of 400 kg m^{-3} is in agreement with the value used by *Wright* [2005] and *Rye et al.* [2010]. A linear elevation-dependent precipitation gradient of a 14% increase per 100 m is well within the range of possible values suggested by *Bales et al.* [2009] and *Burgess et al.* [2010]. A value of 2 °C for the threshold temperature for solid / liquid precipitation is consistent with that used by *Bougamont et al.* [2005] and has been widely used in other studies [e.g. *Oerlemans and Hoogendoorn,* 1989; *Arnold et al.* 1996].

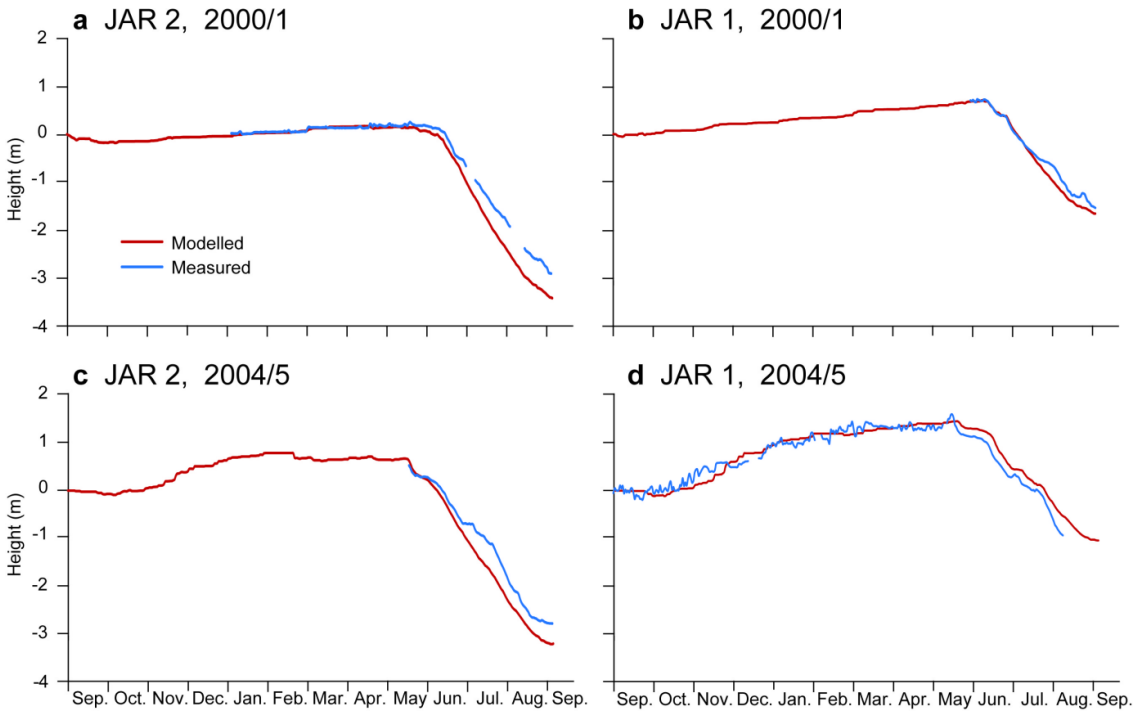

Figure 3.3: Modelled and measured surface height data at the GC-Net stations, JAR 2 and JAR 1 for 2000/01 and 2004/05.

The main discrepancies between the modelled and measured surface height data appear to be due to small snowfall events which are measured by the UDG but not captured by the model, as seen during the accumulation period (September to May) in Figure 3.3d, for example. Furthermore, the model slightly overestimates ablation during the summer, again likely due to the model not capturing small snowfall events during the ablation period. Similarly, the measured albedo values are generally more variable than the modelled values. This is particularly obvious, for example, in March / April 2005 when the effects of snowfall events appear in the measured albedo data at both JAR 2 and JAR 1 but not in the modelled albedo data (Figures 3.4d and e). Additionally, the drop from a high snow albedo to a lower ice albedo in late June 2001 at JAR 1 may be less rapid in the measured data than in the modelled data due to small snowfall events temporally increasing the surface albedo and delaying the snowpack removal and subsequent exposure of underlying ice.

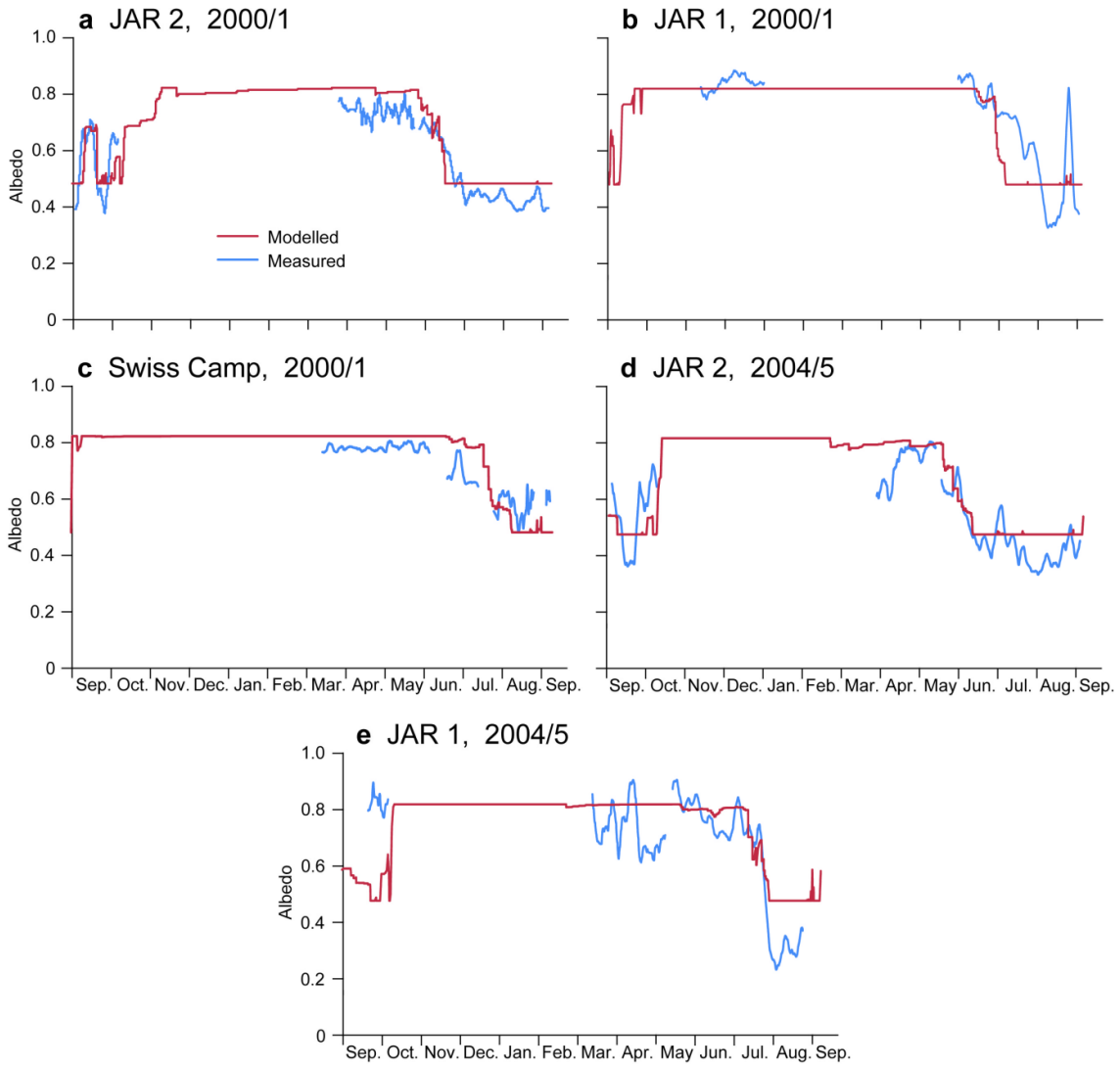

Figure 3.4: Modelled and measured albedo at the GC-Net stations, JAR 1, JAR 2 and Swiss Camp for 2000/01, and JAR 1 and JAR 2 for 2004/05.

These differences between modelled and measured surface height and albedo may be mainly due to: i) real differences in precipitation between the coastal station and the GC-NET sites due to local weather patterns; ii) a fairly high value for fresh snow density (400 kg m^{-3}) meaning a relatively small increase in surface height is modelled compared to that measured by the UDG; iii) the effect of the model's relatively simple empirical albedo parameterization (compared to the more sophisticated, physically based model of *Gardner and Sharp* [2010], for example) which averages the density of the top 5 cm of snow / ice masking the potential increase in albedo from a new snowfall; iv) a single value for the threshold temperature for solid / liquid precipitation not being applicable for all precipitation events; v) the effect of windblown snow not being accounted for by the model; and vi) errors associated with the AWS measurements

used to force the SEB model [e.g. *van den Broeke et al.,* 2004].

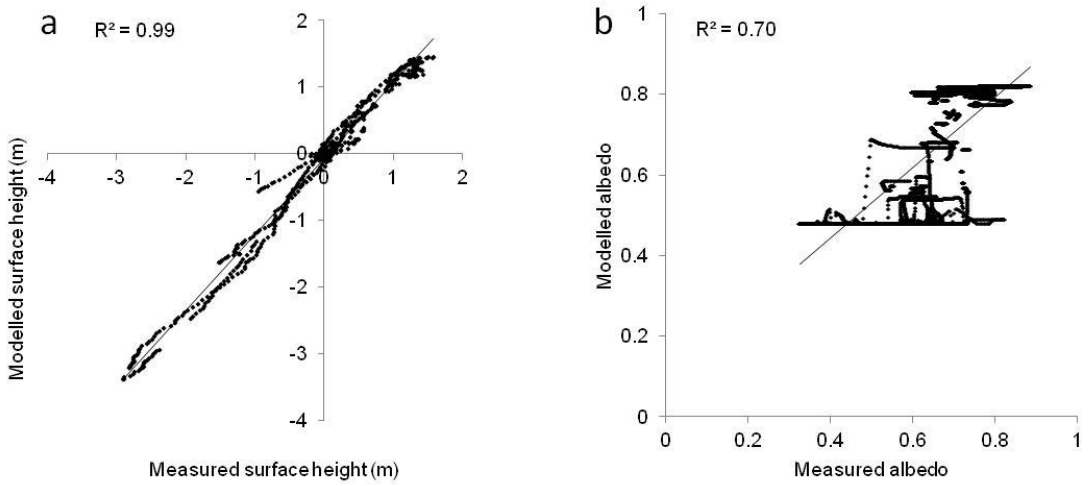

Figure 3.5: Scatter plots of measured and modelled a) surface height data, and b) albedo data. Also shown are the best fit regression lines through each data set.

3.4.2 Model evaluation through comparison of modelled and measured snowline position

Following model calibration, evaluation was first undertaken by comparing the modelled snow distribution with that delineated from Landsat-7 ETM+ satellite imagery using the techniques of NDSI classification and supervised image thresholding, as outlined in Section 3.3.2. When the model was run with the optimal parameter set discussed in Section 3.4.1, on average, the model successfully calculated the distribution of snow and ice for 90.4% and 87.9% of the cells in the years 2000/01 and 2004/05 respectively (Table 3.2). As an example, modelled and measured ice / snow distribution for (a) 7th July 2001 and (b) 8th August 2001 are displayed in Figure 3.6. As shown in Table 3.2, the majority of the total percentage of mismatched cells (96%) is due to the modelled presence of snow where the Landsat image indicates ice, i.e. the overestimation of snow cover.

There are two possible explanations for the small discrepancies between the modelled snowline position and the snow / ice pattern observed in the Landsat imagery. First, the error may lie primarily with the model, rather than with the thresholded imagery. As the model has been calibrated against data at three specific points (JAR 1, JAR 2,

and Swiss Camp), it is not surprising that the overall patterns of snow / ice distribution for the entire 450 km^2 region at different times in the summer are not reproduced exactly. The snow identified through image thresholding is fairly patchy and dispersed, indicating that real snow accumulation patterns are more heterogeneous than modelled patterns, likely due to subtle complexities of the ice sheet surface topography (i.e. patterns of curvature) which affect patterns of snowfall and redistribution by wind. These patterns are not picked up by the model which distributes snow according to elevation only, and cannot account for redistribution by wind. For example, examining the locations of the measured snow patches below the modelled snowline on both 7th July and 8th August 2001 (i.e. the yellow patches on Figure 3.6) with reference to the DEM topography shows that the majority are located on the lee side of ridges in the DEM, (given that the prevailing wind carrying snow is from the west / south west [*Fettweis et al.,* 2007]). Conversely, some of the areas of mismatch above the modelled snowline, where modelled snow is present but not measured (i.e. the light blue areas in Figure 3.6), are on the windward side of ridges in the DEM.

	7 Jul '01	8 Aug '01	31 May '05	15 Jun '05	4 Sep '05
snow + snow (%)	50.7	8.1	17.5	31.8	13.9
ice + ice (%)	40.9	81.1	68.1	57.1	75.3
snow (model) + ice (Landsat) (%)	4.4	7.4	14.3	10.8	10.8
snow (Landsat) + ice (model) (%)	3.9	3.5	0.1	0.3	0.0
Total mismatched cells (%)	8.3	10.7	14.4	11.1	10.8

Table 3.2: Percentages of grid cells in each of the four categories, and the total percentages of mismatched cells, for two dates in 2001 and three dates in 2005, following comparison of modelled snow and ice distributed with that delineated from Landsat imagery.

The second explanation for the small discrepancies between the modelled snowline position and the snow / ice pattern observed in the Landsat imagery is that the error lies primarily with the thresholded imagery, rather than with the model. For example, it is observed that many of the areas of mismatch above the modelled snowline (i.e. the light blue areas in Figure 3.6) are very linear in appearance and are aligned with many of the blue, wet looking areas of snow visible in the Landsat imagery. This is particularly obvious when Figure 3.6a is compared to the Landsat image in Figure 3.1,

which are both dated 7th July 2001. Thus, it is likely that our image thresholding technique has incorrectly classified these wet, dark areas as ice rather than slushy snow. This problem likely arises because the wavelengths of Landsat Band 4 are influenced by changes in grain size and water, meaning that it can be difficult to distinguish between wet snow and ice [*Gardner and Sharp,* 2010].

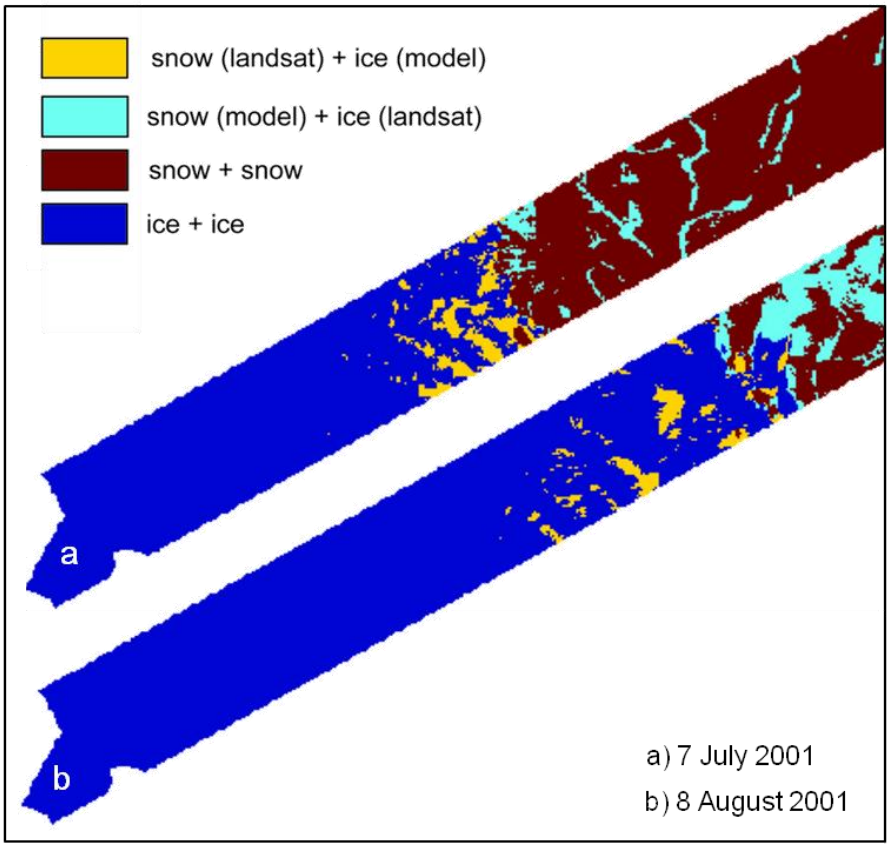

Figure 3.6: Correspondence between modelled and measured snow and ice distribution for a) 7 July 2001; and b) 8 August 2001, produced using the procedure described in Section 3.3.2.

3.4.3 Model evaluation through comparison of modelled and satellite-derived albedo data

The second stage of model evaluation involved the comparison of gridded modelled albedo with the MODIS MOD10A1 albedo product, as outlined in Section 3.3.3. Ignoring all cells with a modelled albedo of 0.48 (i.e. ice) (an average RMSE of 0.081 was calculated between all cells with a modelled albedo of 0.48 and their corresponding MODIS-derived albedo value), the calculated R^2 values and RMSEs for the modelled

vs. MODIS-derived snow albedo data on five dates during both 2001 and 2005 are shown in Table 3.3. As an example, Figure 3.7 shows the relationships between modelled and MODIS-derived snow albedo for three dates in 2001 representing early, mid and late summer, (a) 5th June, (b) 5th July, and (c) 11th August. Figure 3.8 shows the spatially varying difference between modelled and MODIS-derived snow albedo values over the model domain for the same three dates.

	2000/01					2004/05				
Date	5 Jun	13 Jun	5 Jul	25 Jul	11 Aug	5 Jun	17 Jun	10 Jul	21 Jul	8 Aug
R^2	0.812	0.727	0.248	0.243	0.093	0.645	0.55	0.543	0.55	0.351
RMSE	0.084	0.084	0.100	0.099	0.111	0.095	0.138	0.110	0.188	0.192

Table 3.3 Calculated R^2 values and RMSEs of the relationships between the modelled and MODIS-derived snow albedo data for five days in both 200/01 and 2004/05.

In early summer, the modelled albedo spans the complete range of albedo values from new snow (0.82) to old snow or ice with a thin covering of snow (~0.50) and this is generally mirrored in the MODIS data (Figure 3.7a). By mid-summer, the modelled and measured albedo values span approximately the same range but the MODIS albedo values display an increased heterogeneity for a given modelled albedo (Figure 3.7b). By late summer, the majority of the snow has melted, leaving only modelled and MODIS albedo values at the lower end of the range (Figure 3.7c).

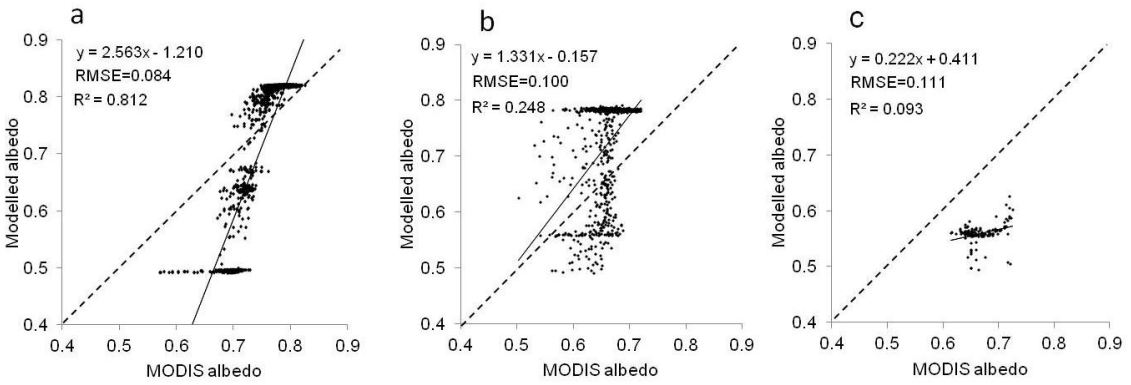

Figure 3.7: Scatter plots of modelled and MODIS-derived albedo data for a) 5 June 2001; b) 5 July 2001; and c) 11 August 2001. All grid cells with a modelled ice albedo of 0.48 have been removed. The 1:1 lines and the best fit regression lines are also plotted for each data set.

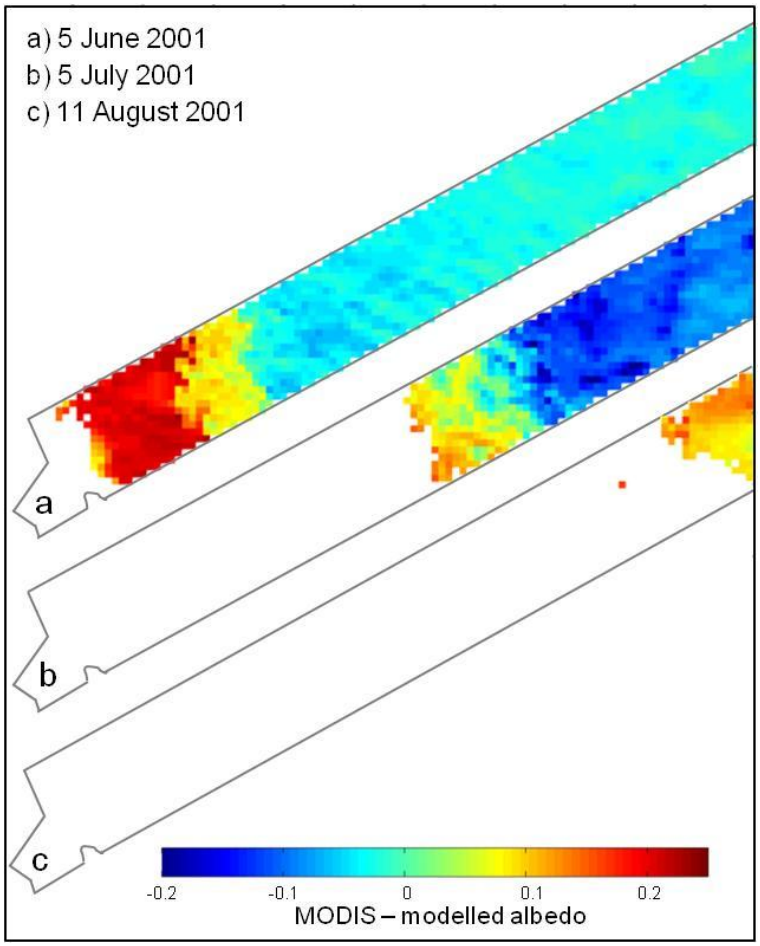

Figure 3.8: Spatially varying differences between MODIS-derived and modelled snow albedo values on a) 5 June 2001; b) 5 July 2001; and c) 11 August 2001. All grid cells with a modelled ice albedo of 0.48 have been removed. Positive (negative) values correspond to a higher (lower) MODIS-derived albedo than modelled albedo.

In general, the model overestimates albedo values at the higher end of the range compared to MODIS values, and underestimates albedo values at the lower end of the spectrum compared to MODIS values (Figure 3.7). The cells corresponding to these albedo values occur in the upper (negative values) and lower (positive values) part of the model domain respectively (Figure 3.8). However, the overestimation of modelled albedo values compared to MODIS values at the higher end of the range is less in early summer (Figures 3.7a and 3.8a) than it is in mid-summer (Figures 3.7b and 3.8b), and the underestimation of modelled albedo values compared to MODIS values at the lower end of the range is greater in early summer (Figures 3.7a and 3.8a) than it is in mid-summer (Figures 3.7b and 3.8b).

There are two possible reasons for this observation. First, it may be due to the model's

albedo parameterization scheme which calculates surface albedo as a linear function of the density of the top 5 cm of the subsurface grid. Thus, during early summer when melt rates are too limited to melt snow layers away and the subsurface snowpack is below freezing point, continuous rounds of melt (during the day) and refreezing (at night) will drive the density up and the albedo down. For higher melt rates and warmer subsurface snowpack temperatures in mid-summer, refreezing rates are lower, thus densities are not increased as much, and albedos are not lowered as much as they are in early summer. Second, this observation may be due to the MODIS product identifying a range of levels of snow water saturation, resulting in an overall decrease in MODIS albedo values compared to values in the model, which does not account for the effect of surface water ponding. This second point is also the likely cause of the increased heterogeneity of MODIS albedos for a given modelled albedo as the summer progresses.

The discrepancies between modelled and MODIS albedo may also be due to unsubstantiated errors associated with the MODIS product [*Stroeve et al.,* 2006] and / or errors associated with the AWS measurements used to force the SEB model [e.g. *van den Broeke et al.,* 2004].

3.4.4 Mass and energy budget

Figure 3.9 shows the calculated average seasonal cycle of the SEB components at the three GC-NET station sites, averaged over the two mass balance years, 2000/01 and 2004/05. As would be expected, the energy involved in melting (Q_M), i.e. the sum of all the incoming and outgoing fluxes, decreases with altitude from JAR 2 to Swiss Camp. The net shortwave flux (SW_{net}), modulated at the surface primarily by albedo, is the dominant factor governing surface melt variability in the ablation area [*van den Broeke et al.,* 2008], and, on average, decreases towards higher elevations. The shape of the seasonal SW_{net} cycle at all three sites is not symmetrical. This is due to a gradual decrease in albedo associated with melt at the beginning of the melt season compared to a more rapid increase in albedo at the end of the melt season due to new snowfall. This effect is more noticeable higher up on the ice sheet at Swiss Camp (Figure 3.9c) than lower down at JAR 2 (Figure 3.9a). The net longwave flux (LW_{net}) is the main energy loss and is strongly dependent on the temperature deficit at the surface, which increases with altitude. The *SHF* contributes significantly to the energy budget, whereas the *LHF* is small. Due to refreezing (which here includes both internal

accumulation and superimposed ice formation), the *GHF* is positive.

As one of the key aims of this chapter was to model melt and runoff at a high spatial resolution, the spatial variability in net mass balance, runoff, accumulation, and refreezing across the model domain was evaluated. As an example, Figure 3.10 presents contour plots of these model outputs for the 2000/01 mass balance year. Spatial variations in the net mass balance are explained by a combination of altitudinal differences in air temperature and precipitation, spatial gradients in the surface albedo, and local variations in the amount of refreezing. Refreezing of subsurface water (which here includes both internal accumulation and superimposed ice formation) is most significant at higher elevations where low snow temperatures at the start of the melt season increase the potential for refreezing. Despite high melt rates in the ablation zone, refreezing is limited by the disappearance of snow during the melt season. Averaged over the entire model domain, refreezing is calculated to contribute 0.13 m w.e. to the mass budget and net runoff averages -2.22 m w.e. Hence, on average, 6% of all meltwater and rainwater at the surface refroze in the snowpack and did not become runoff. Averaged over the model domain in this study, accumulation was 0.42 m w.e. Refreezing therefore accounted for 31% of the average net accumulation per year. In comparison, over the entire ice sheet, *Box et al.* [2006] and *van den Broeke et al.* [2009] calculated that ~34% and ~30% of the melt refreezes within the snowpack. This value is expected to be higher than the value calculated in this study as higher on the ice sheet, the snowpack will be colder and will exist for a longer period of time during the melt season.

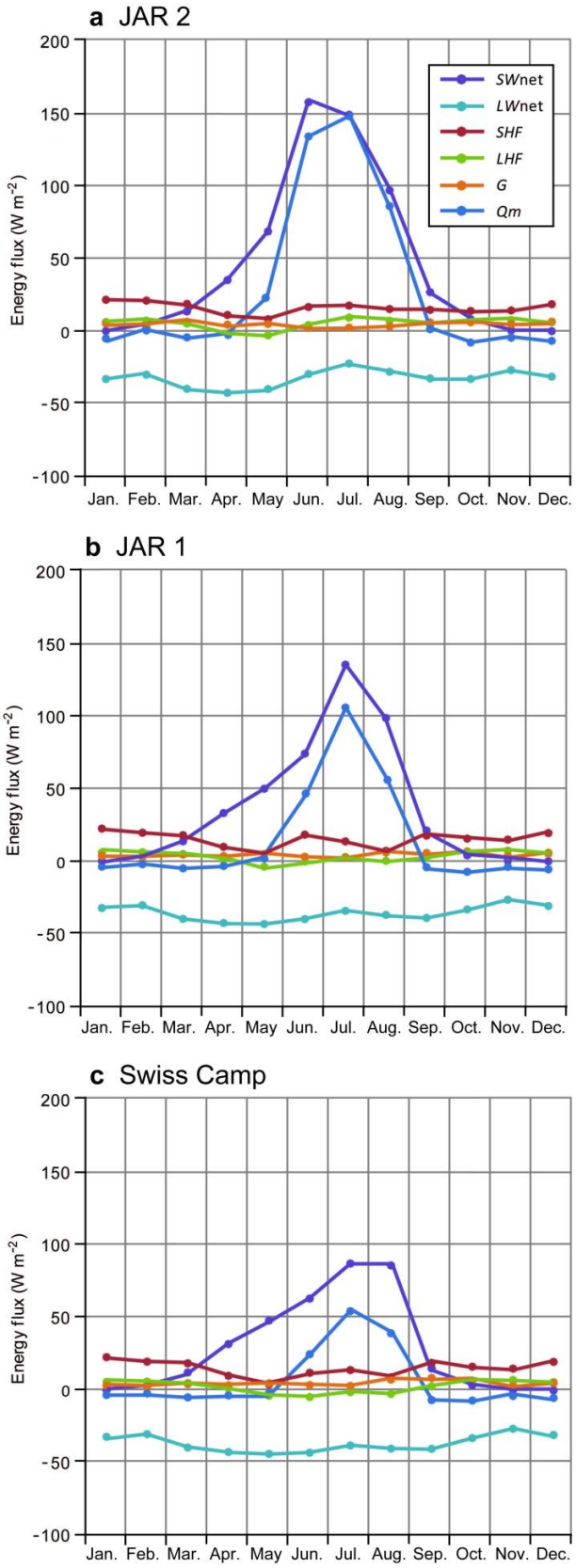

Figure 3.9: Average seasonal cycle of the surface energy balance components at: a) JAR 2; b) JAR 1; and c) Swiss Camp, averaged over the two mass balance years, 2000/01 and 2004/05. By definition, Q_M is negative (energy sink) but is shown as a positive flux here for illustrative purposes.

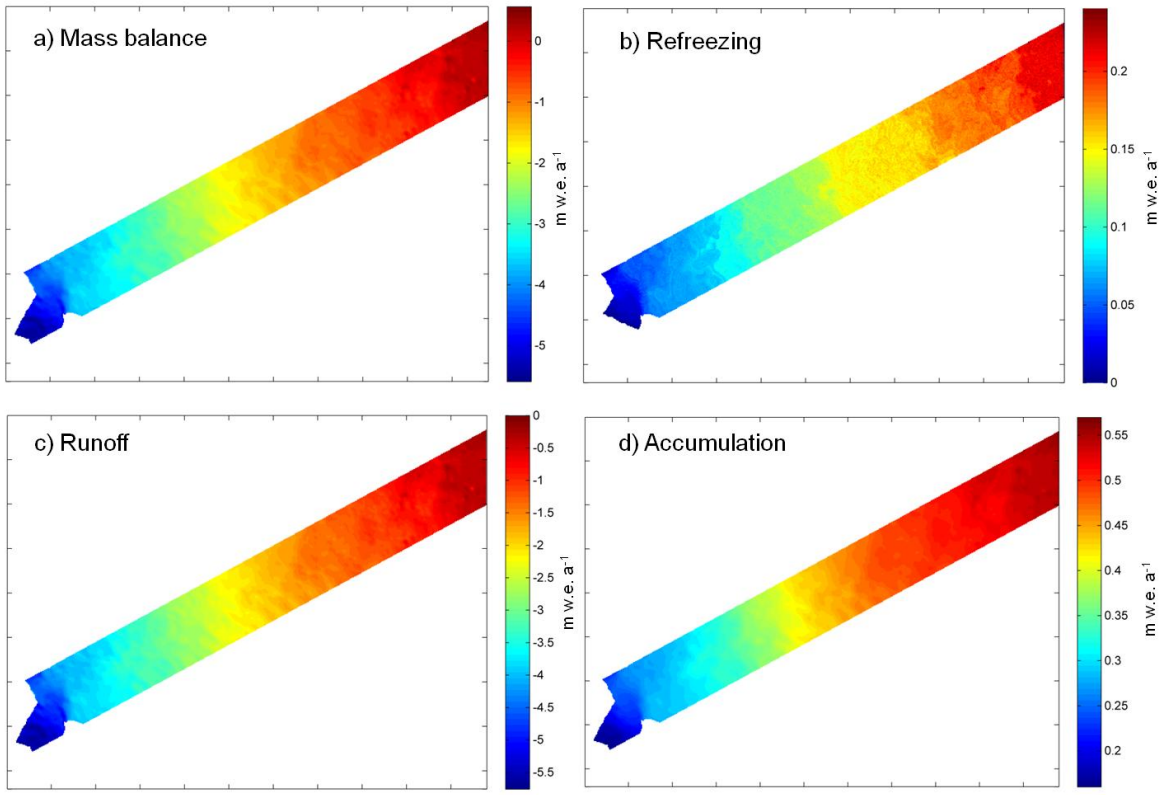

Figure 3.10: Contour plots of modelled: a) mass balance; b) refreezing; c) runoff; d) accumulation for the 2000/01 mass balance year.

3.5 Summary and conclusions

This chapter has focused on the application of a physically based SMB model to the Paakitsoq region. The melt / runoff component was driven with a full range of meteorological variables collected on the ice sheet, predominantly from the GC-Net JAR 1 station. The accumulation component used precipitation data collected off the ice sheet near the coast from the ASIAQ station. The mass balance model was calibrated by selecting sets of parameter values which minimised the RMSEs between modelled and measured surface height and albedo data from JAR 1, JAR 2, and Swiss Camp. Model performance was first evaluated by comparing the modelled snow distribution with that delineated from Landsat-7 ETM+ satellite imagery using the techniques of NDSI classification and supervised image thresholding for various dates during the summers of 2001 and 2005. Second, the model was evaluated through comparison of modelled daily albedo over the model domain with the daily surface albedo retrievals from the NASA Terra platform MODIS sensor MOD10A1 product. The main findings were as follows:

- Model calibration showed that the same set of optimal key parameters (fresh snow density (400 kg m^{-3}); elevation-dependent precipitation gradient (14% increase per 100 m); and threshold temperature for solid / liquid precipitation (2 °C)) were appropriate for both 2000/01 and 2004/05. This gave confidence in the physical basis of the model, suggesting it is transferrable between years. Calculated RMSEs between the modelled and measured surface height data for 2000/01 and 2004/05 were low at 0.227 m and 0.208 m respectively. The RMSEs between the modelled and measured albedo data for 2000/01 and 2004/05 were just 0.084 and 0.118 respectively. The calculated R^2 values between all of the available measured and modelled surface height data, and all of the measured and modelled albedo data, were 0.99 and 0.70 respectively.

- Model evaluation by comparison of modelled snowline position with that delineated from Landsat imagery showed that the average percentage of mismatched grid cells for 2000/01 and 2004/05 is relatively low at 9.6% and 12.1% respectively, with the majority of this mismatch (96%) due to the overestimation of snow cover. The satellite-derived snow accumulation patterns were also found to be more heterogeneous than modelled patterns, likely due to subtle differences in real snow accumulation patterns due to small irregularities in the ice sheet surface topography and the effect of snow re-distribution by the wind. Some areas of error also existed in the thresholding scheme where areas of snow were wrongly classified as ice rather than wet snow.

- Although there was generally a good correspondence between gridded modelled albedo and MODIS-derived snow albedo, the model tended to overestimate albedo values at the higher end of the range compared to MODIS values, and underestimate albedo values at the lower end of the spectrum compared to MODIS values. This may have been due to various reasons including: i) the model's albedo parameterization scheme which calculates surface albedo as a linear function of the density; ii) the MODIS product identifying a range of levels of snow water saturation, not accounted for by the model; iii) unsubstantiated errors associated with the MODIS product; and iv) errors associated with the AWS measurements used to force the SEB model.

- The average seasonal cycles of the SEB components were calculated and the net

shortwave flux, modulated at the surface primarily by albedo, was found to be the dominant factor governing surface melt variability in the ablation area. The net longwave flux was the main energy loss. The spatial variability in annual net mass balance, runoff, accumulation, and refreezing across the model domain was evaluated, and from this, it was calculated that 6% of all meltwater and rainwater at the surface refroze in the snow pack and did not become runoff; refreezing accounted for 31% of the average net accumulation.

4. Surface routing / lake filling model

This chapter focuses on the development and calibration of a surface routing / lake filling (SRLF) model to calculate the surface routing of water across ice / snow and the filling rates of lakes over a 100 km^2 area of the Paakitsoq region of the Greenland Ice Sheet (GrIS). It also forms the basis of a paper currently in press [*Banwell et al.,* 2012b]. The model uses the hourly runoff per 100 m grid cell calculated by the distributed, high spatial resolution surface mass balance (SMB) model (Chapter 3) and is calibrated against field measurements of a filling lake in the study region. Ultimately, this model will provide input to a subglacial routing model (Chapter 5).

4.1 Data and approach

The study site of this chapter, the 'Ponting' area, is a 10 km x 10 km area located within the ~2,300 km^2 Paakitsoq region (Figure 4.1). This area was chosen as a field site because satellite imagery showed the consistent filling and drainage of lakes in this region on an annual timescale at the time of the planned field season. The Ponting area is ~15 km inland from the ice sheet margin with ice elevations between ~750 m and ~980 m above sea level (m.a.s.l). This study primarily focuses on 'Lake Ponting' which is located centrally within the model domain (69.589 N, -49.783 E, 962 m.a.s.l.) (Figure 4.2), ~10 km north of the JAR 1 Greenland Climate Network (GC-Net) automatic weather station [*Steffen and Box*, 2001] (Figure 4.1). The time period 9th to 30th June 2011 is focussed upon as it is during this period that field measurements of snow depth and lake level were collected and will be used for model calibration.

As described in Chapter 3 (Section 3.1), the SMB model used to calculate melt / runoff is driven with a full range of meteorological variables from the JAR 1 GC-Net station [*Steffen and Box,* 2001]. However, although the SMB model was calibrated for the mass balance years of 2000/01 and 2004/05 (Chapter 3, Section 3.3), it is re-calibrated for the melt season of 2011 using average daily snow surface height measurements against four poles drilled into the ice (located at 'Camp', Figure 4.2) from 9th to 29th June 2011, during which time no precipitation fell (Section 4.2.1.1).

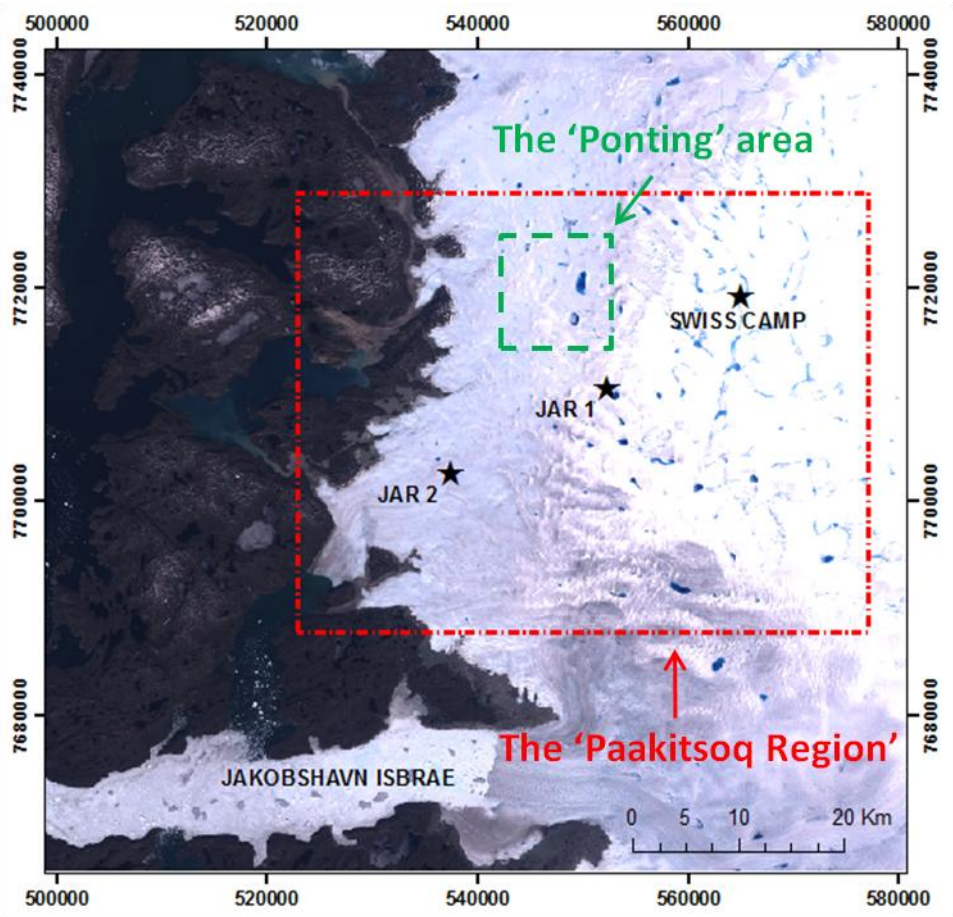

Figure 4.1: Map of the study site. The Ponting area is delineated by the green box, located within the larger Paakitsoq region (red box). The Landsat 7 ETM+ image behind is dated 07/07/2001.

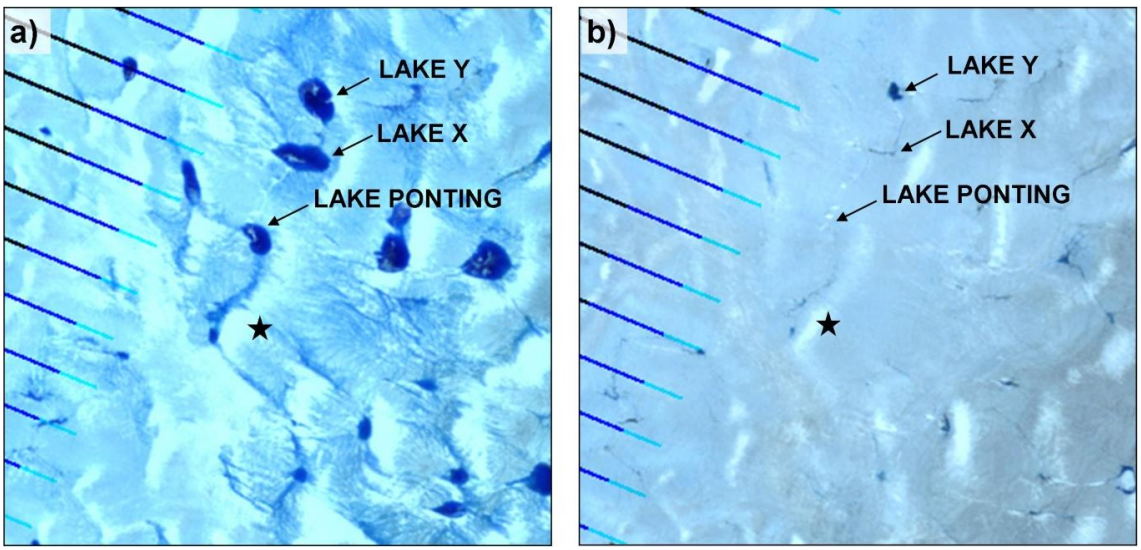

Figure 4.2: Landsat 7 ETM+ images of the Ponting area (green box in Figure 4.1) from a) 17 June 2011; and b) 3 July 2011. The field camp is marked by a star.

The SRLF model is calibrated against measured lake level data (Section 4.2.2.3). Two HOBO pressure sensors were installed in Lake Ponting's lake basin on 13th June 2011. The lake drained via hydrofracture on 19th June 2011, giving six days of lake filling data. One sensor was firmly secured to an aluminium pole drilled into the ice at a height of ~0.5 m above the ice surface. The second sensor was loosely attached to the pole so that it rested on the ice but could slide down the pole as the bottom of the lake melted, while remaining close to the pole. This set-up allowed for the ablation rate at the bottom of the lake to be calculated from the difference between the time series of lake depth recorded by the two sensors [*Tedesco et al.,* 2012]. Both sensors recorded pressure every five minutes on an internal data logger and were recovered following lake drainage. The sensors have a water level accuracy of 0.5 cm and a resolution of 0.21 cm. Pressure data were corrected for altitude and for barometric pressure changes using data from a third sensor located < 1 km from the lake. Measured lake depth data were converted to volume using a depth-volume relationship derived from a digital elevation model (DEM) of the area. For this we used the ASTER Global Digital Elevation Model (GDEM) (as described in Chapter 3, Section 3.1) A hand-held GPS was used to measure the horizontal position of the sensors to an accuracy of ± 5 m. Comparing this position with the 100 m resolution DEM suggested that the sensors were installed in a DEM cell that was 0.7 m higher than the lowest elevation DEM cell of the lake basin; 0.7 m was therefore added to all the pressure sensor data so they are relative to the deepest part of the lake, and the depth-volume relationship for this lowest DEM cell was defined.

The DEM is subsequently used by the SRLF model to route the modelled meltwater across the snow / ice surface to topographic lows to form lakes (Section 4.2.2).

4.2 Methods

4.2.1 Surface mass balance model

Hourly melt and runoff is modelled using the high-resolution SMB model described in Chapter 3. Here, the SMB model is described only briefly, concentrating on the adaptations that have been made to the model which was run for the mass balance years of 2000/01 and 2004/05 (Chapter 3).

Consistent with Chapter 3, the mass balance year runs from 1st October to 30th

September. The period of model output which is of most interest is time period for which there are field measurements of snow surface height and lake filling rates in June 2011. The model also requires a year of meteorological data used repetitively for five years for spin-up purposes (see below). Due to instrument failure at JAR 1 from 1st January 2011 to 17th May 2011, and the commencement of this modelling work in late July 2011, meteorological data for 2011 is only available from 18th May to 25th July 2011. A complete mass balance year is therefore synthesized from the following JAR 1 measurements: 1st Oct to 31st Dec 2010; 1st Jan to 17th May 2010; 18th May to 25th Jul 2011; 26th Jul to 30th Sep 2010. The model is run for five years for spin-up purposes, then during the 6th year, output is generated for the three week period commencing on 9th June 2011 for input to the SRLF model. Values for fresh snow albedo (0.80) and ice albedo (0.45) are set based on average measured albedo values at JAR 1 for the year of climate data (2010/11) used by the SMB model. These values are very similar to those set for fresh snow albedo (0.82) and ice albedo (0.48) in Chapter 3 (Section 3.4.1) which calibrated the same SEB model for a larger 450 km^2 subsection of the Paakitsoq region for two mass balance years (2000/01 and 2004/05).

In addition to the model requiring a five year spin-up period in order for the surface mass balance and the subsurface temperature and density profiles to attain equilibrium (see Chapter 3, Section 3.2.4), a spin-up period is also required in order to produce a snowpack thickness on 9th June 2011 (of the main (6th year) model run) equal to that measured at 'Camp' (Figure 4.2) on the same date. In order to achieve this, the model is prescribed with precipitation at a constant rate per hour, in m w.e., on one random day per week from 1st October to April 30th inclusive (called 'winter precipitation' hereafter). Winter precipitation is prescribed in this way, rather than, for example, having it fall at lower rates continuously throughout the 7 months since it is more realistic and will allow more realistic subsurface temperature and density profiles to evolve over the winter. During model calibration (Section 4.2.1.1, below), the total amount of winter precipitation that is required for the modelled snowpack thickness to match the measured snow thickness on 9th June 2011 is established. Consistent with Chapter 3 (Section 3.4.1), the threshold temperature for precipitation falling as either snow or rain is set at 2 °C. The hourly runoff in mm w.e. calculated by the SMB for each model grid cell is used as input to the SRLF model (Section 4.2.2).

4.2.1.1 SMB model calibration method

The SMB model is calibrated using measured daily snow surface height data measured at 'Camp' (Figure 4.2). The SMB model is calibrated based on: i) measured snowpack thickness on 9th June; ii) day on which superimposed ice becomes exposed; iii) total surface height decrease from 9th June until superimposed ice is exposed; and iv) average rate of snow surface height decrease over this time period. To best match these four criteria, the most suitable values are chosen for two model parameters for which there are not suitable values to constrain them: i) total winter precipitation; and ii) initial snow density (i.e. the density of snow which has just fallen onto the ice sheet surface). For total winter precipitation, a range of values from 0.36 m to 0.44 m are parameterized for, and for initial snow density, a range of values from 300 kg m^{-3} to 400 kg m^{-3} are parameterized for (Table 4.1). Initial sensitivity tests involving a much wider range of values indicated that these ranges gave the best match between measured and modelled snow depth on 9th June and are also consistent with suggested ranges of values in the literature [*Bassford,* 2002; *Bales et al.,* 2009; *Burgess et al.,* 2010; *Cuffey and Paterson*, 2010; *Rye et al.,* 2010]. Although it is appreciated that the range of values for initial snow density appears to be high, as snow densification due to packing and settling is not accounted for by the model, a slightly higher than realistic value for initial snow density is expected to be established during model calibration [*Bassford*, 2002; *Wright*, 2005; *Rye et al.,* 2010] (also see Chapter 3, Section 3.3). For example, the best value for initial snow density for both 2000/01 and 2004/05 was established to be 400 kg m^{-3} in Chapter 3 (Section 3.4.1). All combinations of parameter values at the given intervals in Table 4.1 are used for individual model runs. Subsequently, the measured and modeled ablation curves are plotted and compared qualitatively. The modeled curves that clearly showed a bad match with measured data were immediately discarded. To determine the highest quantitative match, root mean square errors (RMSEs) between the measured and the modeled curves showing good visual matches with measurements are calculated.

	Range tested	Increment
Initial snow density (kg m^{-3})	300 – 400	50
Total winter precipitation (m)	0.36 – 0.44	0.02

Table 4.1: Ranges from which parameter values were chosen for SMB model calibration

4.2.2 Surface routing and lake filling (SRLF) model

Lakes form in topographic hollows on the ice sheet surface. The rate at which they fill (and hence the water volume within any given lake at any given time) is controlled by the size of the supraglacial catchment which supplies the lake, the rate of water production within the catchment, and the rate of water flow within the catchment. The rate of water production is calculated using the SMB model (Section 4.2.1), but the location and size of lakes, their catchment areas, and water routing within and between the catchments are controlled by the surface topography. The SRLF model, initially developed by Neil Arnold, consists of two main components. The first component takes a DEM of the surface and analyses the DEM to identify the topographic hollows which can contain lakes, the catchment areas which feed each lake, and the topological routing of water between catchments if the water level in any given lake reaches the overflow (see Section 4.2.2.1, below) [*Arnold,* 2010]. The second component of the model calculates the time delay between melt production and that of water entering the lake by calculating the route taken by water, and the water flow velocity, within each catchment in order to calculate input hydrographs for each lake (see Section 4.2.2.2, below) [*Arnold et al.,* 1998].

4.2.2.1 Lake and catchment identification algorithm (LCIA)

The identification of watersheds (and hence catchment areas), flow accumulation (upstream areas) and flow directions over a DEM are common operations within the hydrological sciences. However, most algorithms in common use rely on the artificial filling of surface depressions within the DEM [*Arnold,* 2010]. As this study is specifically concerned with calculating the time-dependent filling of these depressions with water to form lakes, another approach is required. Thus, the algorithm developed by *Arnold* [2010] for calculating lake and catchment extent is used as this does not require the artificial filling of surface sinks. The algorithm begins by calculating the surface slope, and from this the direction of steepest descent, for each cell within the DEM [*Arnold,* 2010]. Any cell with no lower neighbour is defined as a sink, and becomes a potential nucleus for a lake. The algorithm then searches the flow direction matrix to find the set of DEM cells which ultimately flow into each sink cell. This identifies a series of separate catchment areas feeding each sink cell. The algorithm then searches each catchment boundary for the lowest possible DEM cell over which

water would pour as the sink (and any surrounding cells lower than their neighbours) flood with water. The maximum areal extent of any lake within each catchment can be calculated, as cells within the catchment lower than the level of the outflow would flood with water as the lake fills. The DEM also allows the lake hypsometry (depth / volume / area) to be calculated. This process also allows the connectivity between catchments to be identified, as the location of the outlet cell, and the DEM cell into which water would pour, are known. Figure 4.3 shows the calculated catchments for each lake basin in the Paakitsoq region, the overflow point for each catchment, the maximum area that each of the lakes can reach before overflow, and the topological links between each catchment if overflow occurs. Figure 4.4 is the same as Figure 4.3, but focussed on the Ponting area (Figure 4.1, green box).

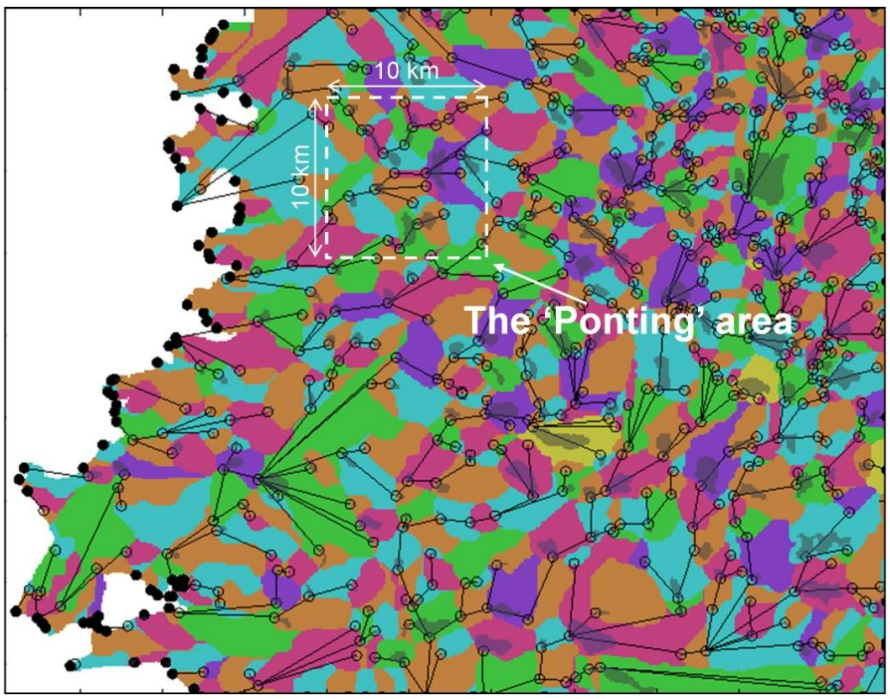

Figure 4.3: Modelled supraglacial catchments (coloured regions) for the Paakitsoq region (red box in Figure 4.1), maximum possible lake extents (grey), catchment overflow points (empty circles), and topological links between catchments (black lines).

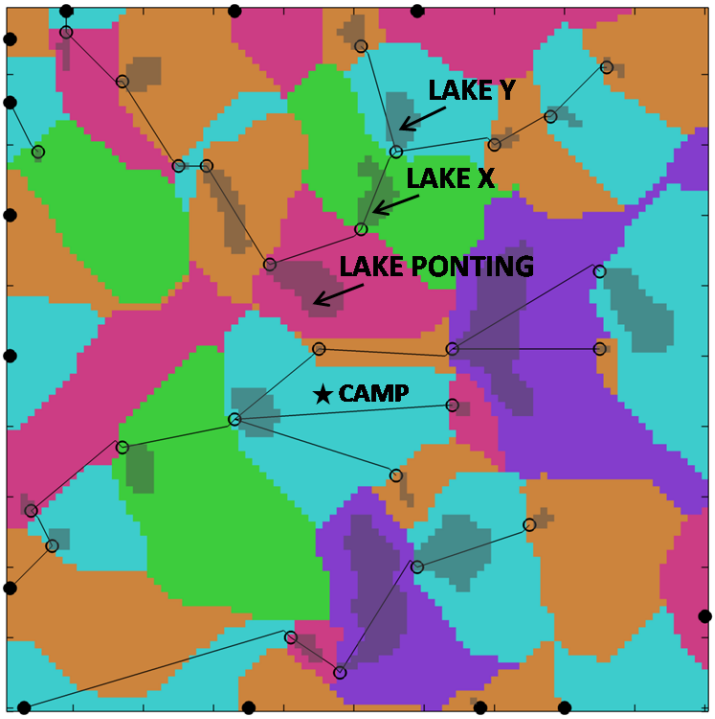

Figure 4.4: Modelled supraglacial catchments (coloured regions) for the Ponting area (green box in Figure 4.1), maximum possible lake extents (grey), catchment overflow points (empty circles), and topological links between catchments (black lines).

4.2.2.2 Flow delay algorithm (FDA)

The flow direction matrix calculated by the LCIA allows the water flow path from any given DEM cell to the sink cell (or lake) to be calculated. However, this information by itself does not allow any flow delay to be calculated. Thus, the LCIA is linked with the flow delay algorithm (FDA) initially developed by *Arnold et al.* [1998]. The FDA uses the flow direction matrix, and the surface slope matrix, together with assumptions about the physical processes controlling water flow, to calculate a flow delay time between each DEM cell and its sink cell. Over a glacier surface, water is assumed to move across snow-covered cells by Darcian flow in a saturated layer at the base of a seasonal snowpack [*Colbeck*, 1978] (Chapter 2, Equation 2.4), or flow across 'bare' ice cells in a supraglacial stream, governed by the Manning's equation (Chapter 2, Equation 2.5) [*Arnold et al.,* 1998]. Thus, for every DEM cell, a 'travel time' for water to cross the cell can be calculated. This time depends on the slope of the cell, whether the cell is ice or snow (which governs the physical processes assumed to control the flow), and the parameter values which govern the water flow. For snow-covered cells, the parameters are the snow porosity and permeability; for ice cells the parameters are the

assumed channel geometry and roughness. By integrating the travel times down-slope along the calculated flow path, a total delay time from any given cell to its sink can be calculated. This travel time will vary as the snow cover across a catchment is lost over the melt season, and as any lake within the catchment expands, as this effectively shortens the path the water follows.

Using the calculated delay times for each time step, each hourly melt increment from the SMB is added to the appropriate sink (or lake) cell(s) at the appropriate time step. As the model run progresses, distinct input hydrographs for each sink are produced. The total accumulated volume of water within each lake at a given time can then be calculated, and from this (and the calculated lake hypsometry), the time step at which the lake overflows its rim can be calculated; lakes effectively fill with water from the original sink cell 'upwards' by successive flooding of the next lowest DEM cell(s) within the catchment until the water depth reaches the level of the calculated outflow cell. Once a lake is full, any further water inputs are passed into the downstream catchment, as calculated by the LCIA. In this way, water can flow in a series of 'cascades' from its initial source cell, through a series of full lakes, until it either reaches a lake which is yet to overflow, or until it reaches the edge of the DEM domain.

Preliminary model runs showed that water tended to be delayed in the catchment for too long and did not fill the instrumented lake fast enough when compared with measurements. Field observations suggested that once the snowpack had thinned to a threshold thickness, water starts to flow quickly in the form of slush flows or in channels incised into the saturated snowpack. Consequently, the algorithm was modified by introducing a parameter of threshold snowpack thickness at which flow switches from Darcian to channelized, rather than assuming that flow switching occurs once all the snow in a DEM cell has melted. This is a simple representation of the physical processes occurring on the surface of the GrIS that is closer to observations made during the summer 2011 field season, and allows more water to reach the lake basin more quickly. This threshold snow thickness parameter is tuned during model calibration (Section 4.2.2.3, below).

4.2.2.3 SRLF model calibration method

The hourly runoff per model grid cell from the calibrated SMB model is used to drive the SRLF model. This model is calibrated through comparison of the modelled and

measured lake filling data (i.e. the cumulative volume over time) for Lake Ponting. Through tuning model parameters, the aim is to best match: i) the onset of meltwater arrival in the lake; ii) the initial lake filling rate before any overflow occurs; iii) the timing of the diurnal cycles in the initial filling rate; and iv) the lake filling rate once potential inflow from overflowing upstream lake(s) has occurred.

As there are not suitable observations available to constrain values for the three parameters which control supraglacial water flow velocity in the snowpack, multiple model runs are performed and the results of these are compared with measurements in order to identify suitable values. The three parameters are: i) snow permeability; ii) effective snow porosity; and iii) the threshold snowpack thickness (which we call Z) for the Darcian to channelized flow switching. However, as snow permeability and effective snow porosity appear as a simple numerator and denominator respectively in *Colbeck's* [1978] equation (Chapter 2, Equation 2.4) , they are combined into one parameter, X, given by X (m^2) = snow permeability (m^2) / effective snow porosity. Suitable ranges of values for snow permeability and effective snow porosity are given in Table 4.2. These ranges fall within those used by *Marsh* [1990], *Arnold et al.* [1998], and *Willis et al.* [2002], and give a range of X values from 1.6×10^{-8} m^2 to 4.8×10^{-8} m^2. For X, initial sensitivity tests encompassing a range of values from 0.00 – 0.40 m w.e. indicated the most appropriate range of values to be between 0.20 – 0.30 m w.e. (Table 4.2). Initial sensitivity tests indicated that the model was quite insensitive to Manning's roughness (n) and hydraulic radius (R). Constant values of R = 0.035 m and n = 0.05 $m^{-1/3}$ s are therefore used [e.g. *Arnold et al.,* 1998; *Willis et al.,* 2002].

	Range tested	Increment
Snow permeability (m^2)	6×10^{-9} - 24×10^{-9}	n/a
Effective snow porosity	0.50 – 0.75	n/a
X (snow permeability / effective snow porosity) (m^2)	1.6×10^{-8} – 4.8×10^{-8}	0.8×10^{-8}
Z (threshold snowpack thickness for Darcian to channelized flow switching) (m w.e.)	0.20 – 0.30	0.01

Table 4.2: Ranges from which parameter values were chosen for calibration of the SRLF model

When the measured lake filling data for Lake Ponting are analyzed (Figure 4.6), we hypothesize that the dramatic increase in lake filling rate at ~12:30 on 18th June is due to the overflowing of one or both of the upstream lakes, Lakes X and Y (Figures 4.2 and

4.4). However, although this was the time at which the magnitude of meltwater discharge into Lake Ponting increased significantly, it is also possible that water started to overflow into Lake Ponting at a lower rate from the upstream lake(s) a few days earlier before a large, high capacity channel was able to form. We calibrate the SRLF model by performing model runs in order to quantitatively establish which combination of parameter values produces the best match between the early period of measured and modelled data. During these runs we focus on the 3.7 km^2 catchment area of Lake Ponting, without allowing for any inflow from the upstream Lakes X and Y. This enables us to best match the onset of meltwater arrival in the lake basin and the initial filling rate of Lake Ponting before the catchment area supplying Lake Ponting increases due to meltwater inflow from overflowing upstream lakes. Once the combination of parameter values for *X* and *Z* which give the lowest RMSE between the early modelled and measured data has been determined, these values are used in subsequent model runs allowing for overflow from the upstream catchment(s), enabling us to observe the effect that inflow from the overflow of Lakes X and Y has on the filling rate of Lake Ponting.

4.3 Model calibration

4.3.1 SMB model calibration

Measured snow depth was 0.99 m on 9th June. A total snow height decrease of 0.64 m was measured between 9th and 25th June when superimposed ice was exposed, suggesting that 0.35 m of superimposed ice formed at this site. 15 SMB runs covering the full range of parameter values in Table 4.1 were undertaken. A selection of graphs of modelled ablation using different parameter value combinations are plotted alongside the measured snow ablation graph in Figure 4.5. Note that the 'snow surface height' on the y-axis has had the total amount of superimposed ice formation (= 0.35 m) removed from the total snow depth on 9th June. The model captures the magnitude of the total snow height decrease and the average ablation rate between 9th June and 25th June. However, the model does not capture the minor variations in measured ablation rate during this time period, likely due to local snow conditions at the measuring stakes. The model run which produces the best match with the measured data has the parameter values of initial snow density = 350 kg m^{-3} and winter precipitation = 0.42 m.w.e. (Figure 4). The calculated RMSE is 0.022 m. This is low in comparison to the

RMSE of 0.049 m calculated when the parameter values of initial snow density = 400 kg m^{-3}, and winter precipitation = 0.44 m are used instead. Importantly, the slightly lower density value of 350 kg m^{-3} (compared to 400 kg m^{-3}) more accurately captures the slight increase in ablation rate on 13th June. These values are therefore set as parameter values in subsequent SMB model runs.

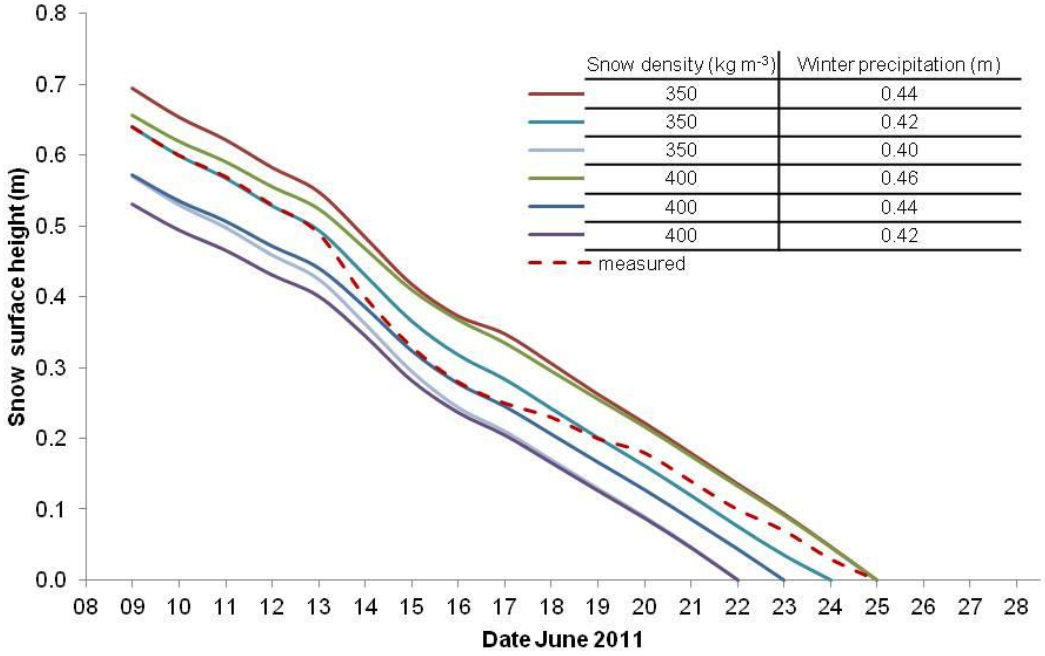

Figure 4.5 Measured and modelled cumulative snow surface height for different combinations of SMB model parameter values for total winter precipitation and initial snow density.

4.3.2 SRLF model calibration

Using hourly melt input per DEM cell from the calibrated SMB model, the SRLF Model is run 25 times in order to explore the full range of parameter values for Z and X (Table 4.2). Graphs comparing the measured lake filling curve to various modelled lake filling curves were produced. By visually inspecting the graphs, it appears that the best fit between the modelled and measured data was produced when parameter values of Z = 0.275 m w.e. and $X = 4.0 \times 10^{-8}$ are used. As examples, Figure 4.6a shows the measured lake filling curve alongside modelled lake filling curves for various X values given a Z value of 0.275 m w.e., and Figure 4.6b shows modelled lake filling curves for various Z values given a X value of 4.0×10^{-8}. However this match is only good up until 16:00 on 16th June. Up until this point (marked by a vertical dashed line in Figures 4.6a and b), the model run using these parameter values produces an RMSE between the measured

and modelled data of 1.7 x 10^4 m^3 (i.e. 4% of the cumulative lake volume at 16:00 on 16th June). Beyond this point, the gradient of the measured lake filling data starts to show a slight increase and deviates from the almost linear gradient of the modelled lake filling graph. These two parameter values are therefore used in subsequent model runs.

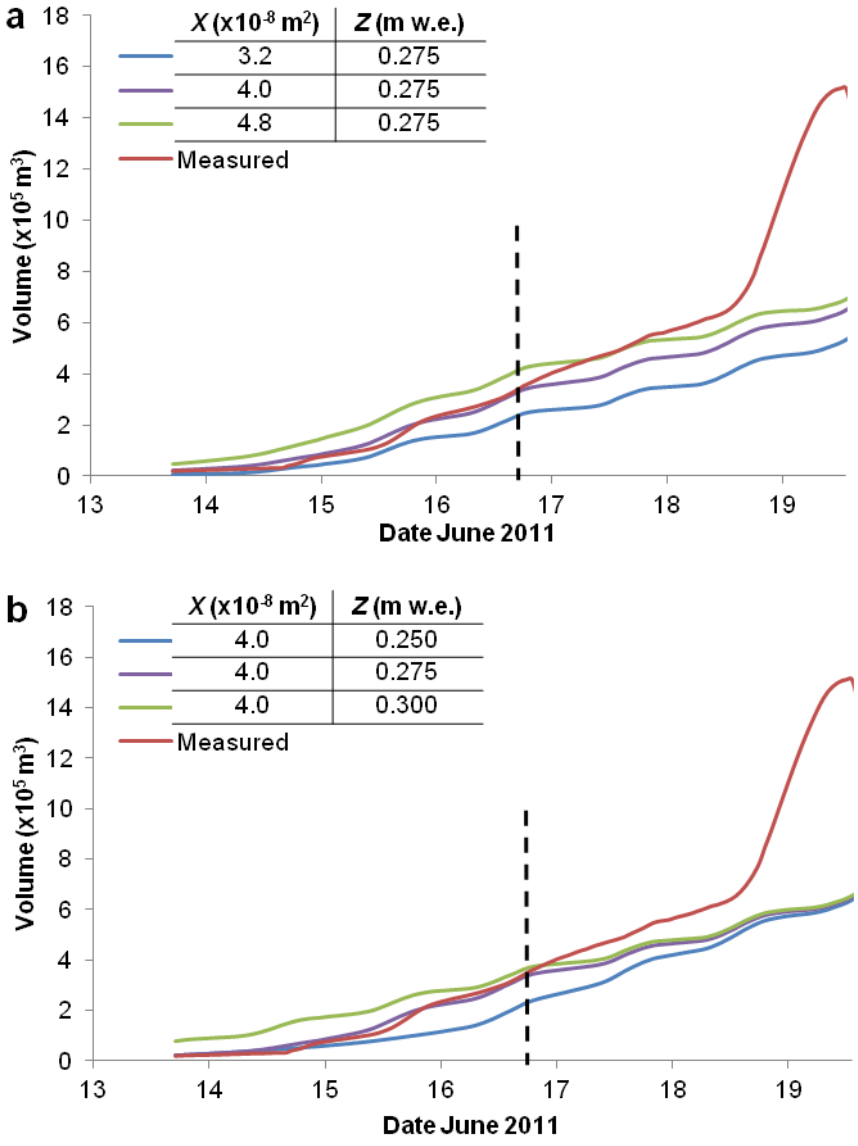

Figure 4.6: Measured Lake Ponting volume over time (red line) together with modelled volume for the Lake Ponting catchment for a) various values of X when Z = 0.275 m w.e.; and b) various values of Z when X = 4.0 x 10^{-8}. The vertical black dotted line marks the time that regression analysis is carried out until.

4.4 Results and Discussion

As previously mentioned in Section 4.2.2.3, the measured volume data for Lake Ponting indicates a sudden rise in filling rate at 12:30 on 18th June (Figure 4.6). Furthermore, field observations on 19th June (a few hours after Lake Ponting had drained by hydrofracture), showed a large incised channel Figure 4.7, containing a river routing water into the Lake Ponting basin coming from the direction of Lakes X and Y (Figures 4.2 and 4.4). This channel had not been visible during the first visit to the basin on 13th June. It is therefore hypothesised that the sudden increase in lake filling rate at 12:30 on 18th June was due to the initiation of, or sudden rise in, meltwater inflow from one or more upstream lakes. However, from the field measurements and observations, is it not possible to determine whether the river was routing water just from Lake X, or whether Lake Y was also overflowing in to Lake X so that Lake Ponting was receiving water from both upstream catchments as well as its own after 18th June 2011.

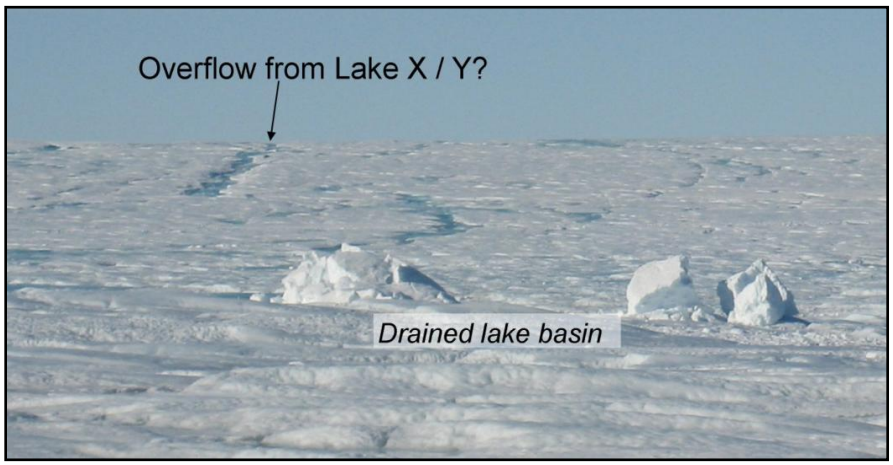

Figure 4.7: Looking North from Ponting's drained lake basin on 19 June 2011.

Having calibrated the SRLF model for the Lake Ponting basin only, without allowing for potential inflow from overflowing upstream lakes, the model is then re-run the model using the optimal parameter set for the whole 10 km x 10 km Lake Ponting area, allowing for lake overflow from basin to basin. The output from this model run is shown together with that from the original run without overflow and the measured lake volume data in Figure 4.8. This figure indicates that the model has successfully simulated: i) the onset of meltwater arrival in the lake; ii) the initial lake filling rate

before any overflow occurs; and iii) to an extent, the lake filling rate once overflow from upstream Lakes X and Y has occurred. The main discrepancies between the modelled and measured lake volume data are related to the timings in the overflow of the two upstream lakes; X and Y.

The graph of modelled Lake Ponting volume allowing for Lake X and Y overflow starts to deviate from the graph of modelled lake volume without upstream lake overflow at 16:00 on 16th June (Figure 4.6). This is when the modelled Lake X volume reached a maximum depth of ~1.5 m and started to overflow into Lake Ponting. As the graph of measured lake volume also deviates from the graph of modelled lake volume without overflow at this time, it is likely that, in reality, Lake X also started to overflow. The modelled Lake Y volume reached a maximum depth of 3.8 m and started to overflow into Lake X (and on to Lake Ponting) at 16:00 on 17th June. This is just over 24 hours before the time (12:30 on 18th June) when we infer Lake Y to have overflowed into Lake X (and on to Lake Ponting) from the measured data. After this time, the modelled rate of filling of Lake Ponting is slightly less than the measured rate. This supports the hypothesis that water from both Lakes X and Y was necessary in order to produce the measured increase in the filling rate of Lake Ponting after 12:30 on 18th June. However, the measured rate may be slightly higher than the modelled filling rate due to channel incision into ice / snow, thereby allowing a higher discharge of water to flow from Lake Y, into Lake X, and on into Lake Ponting. This process is not accounted for by the model.

Thus, it is likely that Lake X overflowed into Lake Ponting at 14:00 on 16th June (creating a slight rise in Lake Ponting's filling rate), before Lake Y then overflowed into Lake X, and on into Lake Ponting, at 12:30 on 18th June (creating a much more significant rise in Lake Ponting's filling rate). In the model, Lake X first overflows into Lake Ponting in agreement with the measured data, but then Lake Y overflows into Lake X on 17th June. Thus, although there are discrepancies between the modelled and measured data, they are not related to the rate of Lake Ponting volume increase after the overflowing of Lake X and Y, but in the timings of the overflow of Lake Y.

In order to provide additional evidence to help constrain the timings of lake overflows, the first available Landsat image after the 18th June 2011, dated 3rd July 2011, is consulted (Figure 4.2b). When this image is compared to the 17th June Landsat image (Figure 4.2a), Lake X appears to have completely drained by 3rd July, whereas Lake Y

is now significantly smaller (estimated to be 0.08 km^2 on 3rd July compared to ~0.39 km^2 by 17th June). It can therefore be inferred that in reality, it was likely that Lake Y did not drain via hydrofracture, but instead probably overflowed into Lake X until the lake level reached the height of the catchment overflow point. Consistent with both measured and modelled lake filling data, it is therefore thought that the rapid increase in Lake Ponting's filling rate on 18th June was due to both the overflow of Lake X and Lake Y (with the overflow of Lake Y likely occurring after the overflow of Lake X). Other sources of time-coincident satellite imagery at appropriate spatial resolutions needed to examine these lake drainage dynamics were not available.

There are two possible explanations for the source of the errors between the timings of the measured and modelled lake overflows. First, as already mentioned, these errors may be due to the model's inability to simulate the process of opening and growth of overflow channels from lakes. Second, the discrepancies between the timings of the measured and modelled lake overflows may be due to inaccuracies in the ASTER GDEM. As a test of this latter hypothesis, additional model runs with altered DEM topography were carried out. It was found that if the average depth of Lake Y was just 0.87 m deeper (giving Lake Y an extra 270,000 m^3 of volume in addition to its current maximum volume of 820,000 m^3), Lake Y would overflow at 12:30 on 18th June, in agreement with the measured data. This modelled curve is plotted in Figure 4.8 (purple line).

It is thought that the sudden increase in Lake Ponting's volume after 12:30 on 18th June resulted in the rapid drainage of Lake Ponting, by hydrofracture, at 14.35 on 19th June, to occur earlier than it would have done had the extra water volume from Lakes X and Y not have been available. Lake Ponting drained completely from its maximum depth of 5.2 m and volume of ~1.5×10^6 m^3 in two hours and ten minutes, with an average discharge of up to 200 $m^3\ s^{-1}$ and a peak discharge of 600 $m^3\ s^{-1}$. The ice dynamic response of this drainage event is discussed in *Tedesco et al.* [in review].

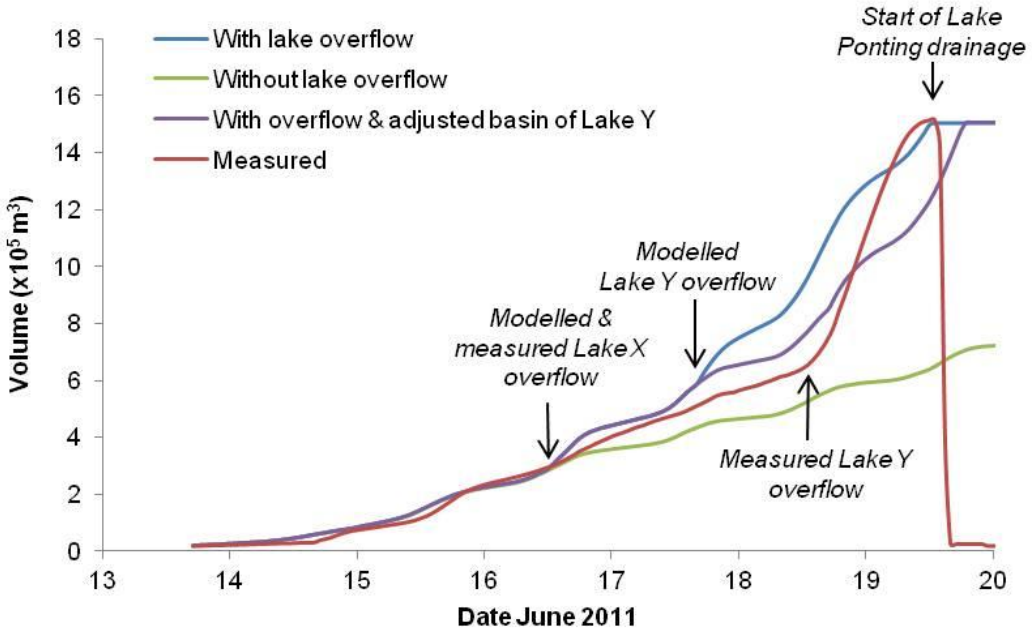

Figure 4.8: Measured volume over time for Lake Ponting (red) alongside graphs of modelled volume over time for runs with (blue), and without (green), lake overflow. The purple line represents the modelled volume over time for Lake Ponting for the case when the basin of Lake Y is adjusted as described in the text.

4.5 Summary and Conclusions

- Using measured snow surface height data, a distributed, high-resolution SMB model has been successfully calibrated for a small (100 km^2) subset of the larger (2,300 km^2) Paakitsoq region of west central Greenland for June 2011. Key SMB model parameter values were found to be: i) total winter precipitation; and ii) initial snow density. Suitable values for these parameters for 2011 were found to be within the ranges found when the model was calibrated against longer time series of measured surface height and albedo over the mass balance years 2000/01 and 2004/05 (Chapter 3, Section 3.4.1).

- This chapter has modelled the routing of this runoff across snow / ice covered cells to topographic depressions which can fill to form supraglacial lakes, and then overflow into their downstream catchment(s) once full. This SRLF model was calibrated using measured volume data from supraglacial Lake Ponting. The key SRLF model parameters were: i) snow permeability; ii) effective snow porosity; and iii) threshold snowpack thickness (Z) for the Darcian / channelized

flow switching.

- The model successfully captured: i) the onset of meltwater arrival lake Ponting; ii) the initial lake filling rate before any overflow occurs; and iii) to an extent, the lake filling rate once overflow from upstream Lakes X and Y has occurred. The modelled data also confirmed that the rapid rise in the measured filling rate of Lake Ponting was due to the overflow of upstream Lake Y, which flowed into Lake X (which had already overflowed), then on into Lake Ponting, so that Lake Ponting suddenly received water from both upstream catchments once Lake Y overflowed its basin. There were discrepancies of around a day or so between the timings of the modelled and measured lake overflows. These discrepancies could be explained by the model's inability to simulate the process of opening and growth of overflow channels and consequent changes in water velocity, and / or inaccuracies in the DEM which could alter calculated lake volumes and hence the timing of overflow events.

- The study is this chapter has shown that through linking a surface hydrology model with runoff input from a calibrated mass balance model, the filling rate of a supraglacial lake in a subset of the Paakitsoq region can be modelled with high accuracy. This study has also demonstrated that water inflow from overflowing lakes in surrounding catchments can play a key role in increasing the filling rate of a lake, and timings of these overflow events have been modelled with relatively high accuracy given the quality of the available surface topographic datasets. Although the dynamics of the ice sheet as a whole are likely to be most influenced by the cumulative effect of multiple lake drainage events across much greater spatial and temporal ranges than explored in this study, this work is an important intermediate step that is necessary before more simplified models of the same process can be developed over larger spatial scales and longer temporal scales.

5. Subglacial Routing Model

Having calculated the distributed net runoff across the ice sheet surface with the surface mass balance (SMB) model (Chapter 3), and routed this across the surface to lakes / moulins using the surface routing and lake filling (SRLF) model (Chapter 4), the water must be routed beneath the ice sheet at Paakitsoq via the subglacial hydrological model. It is this subglacial hydrological model which is the focus of this chapter. Building on the subglacial drainage component of the model discussed by *Arnold et al.* [1998], the model is used not only to calculate outflow hydrographs from the ice sheet, but, more importantly, also to examine spatially and temporally varying subglacial water pressures in response to fluctuating meltwater inputs over the course of a melt season.

5.1 Model description

5.1.1 Model introduction

The subglacial routing model is derived from the Extended Transport (EXTRAN) block of the United States Environmental Protection Agency's (EPA) Storm Water Management Model (SWMM) [*Roesner et al.,* 1988] and is written in the FORTRAN 77 programming language. EXTRAN is a dynamic flow routing model which was originally designed to simulate sewage pipe systems using a network of vertical 'junctions', some of which are 'drains' where water can enter (or leave) the system, connected by sub-horizontal circular 'pipes', which can have individually specified shapes, sizes, lengths and roughness values [*Roesner et al.,* 1988]. Thus, for a glacier hydrological system, the drains are used to represent moulins where surface water can enter (or overflow from) the system, and the pipes are used to represent subglacial conduits whose properties can be specified [*Arnold et al.*, 1998] (Figure 5.1).

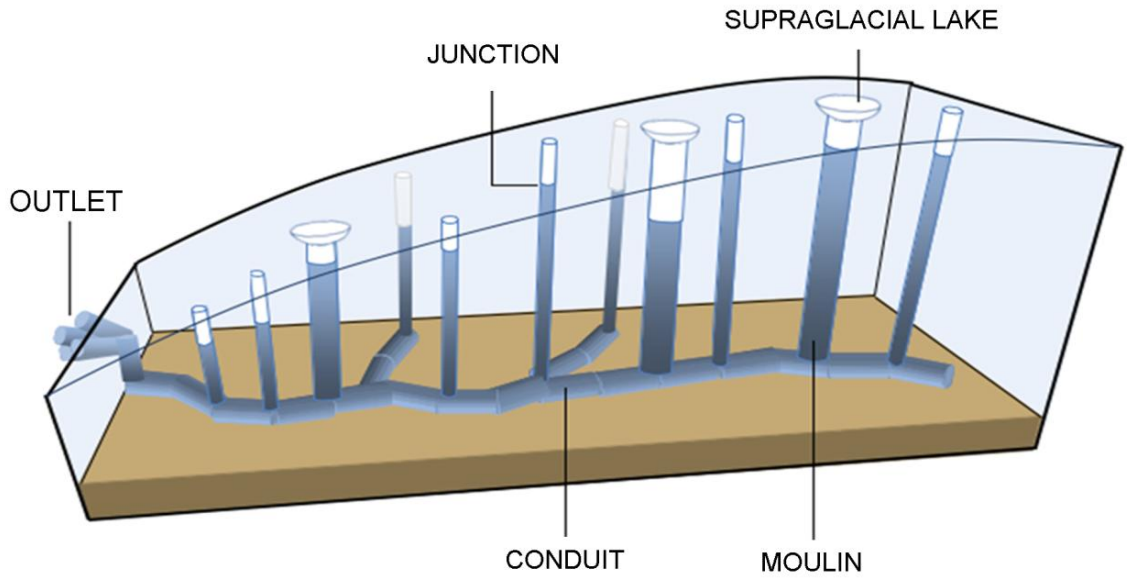

Figure 5.1: The configuration of the EXTRAN component of SWMM.

5.1.2 EXTRAN formulation and solution methods

EXTRAN is a pseudo two-dimensional model because conduits can branch and converge at junctions, but the model solution only requires the conduits' slope and length to be specified as spatial parameters, as well as their location in series relative to other conduits. The length, initial diameter, and Manning roughness are the only independent variables that must be explicitly specified. For each junction that connects to these conduits, the junction 'invert' (ice sheet bed) and 'ground' (ice sheet surface) elevation must be specified, as well as the junction cross-sectional area (CSA). The model calculates the conduit slope automatically based on the invert elevation of each connecting node.

For each conduit and junction in the system, the primary dependent variables are discharge and hydraulic head, respectively [*Roesner et al.,* 1988]. Water input is specified as flow into specific junctions (i.e. those designated as moulins) and the model calculates numerical solutions for discharge in conduits and water pressure in all junctions. *Roesner et al.* [1988] give the differential equations and solution methods employed in EXTRAN, and their explanation is summarised below.

For each link in the system, EXTRAN solves an equation that is a combination of the St. Venant momentum and continuity equations (i.e. the shallow water equations):

$$\frac{\partial Q}{\partial t} + gA_f S_f - 2V\frac{\partial A_f}{\partial t} - V^2\frac{\partial A_f}{\partial x} + gA_f\frac{\partial H}{\partial x} = 0 \quad (5.1)$$

where Q is discharge through the conduit ($m^3\ s^{-1}$), V is water velocity in the conduit ($m\ s^{-1}$), A_f is the CSA of flow (m^2) , H is the hydraulic head (m, here invert elevation plus water depth), S_f is the friction slope and g is acceleration due to gravity ($m\ s^{-2}$). Manning's equation gives the friction slope:

$$S_f = \frac{n^2}{AR^{4/3}}Q|V| \quad (5.2)$$

where n is Manning's roughness coefficient and R is the hydraulic radius of flow in the conduit. Equation 5.1 is converted into finite difference form for the numerical solution [*Roesner et al.,* 1988]. This numerical solution employs the modified Euler (i.e. improved polygon) method to calculate discharge in each conduit and head in each junction for each time-step (t). The values of dependent variables Q and H after each time step (Δt) are calculated by projecting the values from the previous time step across a half time step and then a full time-step according to the slope of the finite-difference form of Equation 5.1. Water is numerically transported through the system following this process, and discharge through the final downstream junction produces the modelled outflow from the system.

EXTRAN allows pressurised flow and allows reversals in the hydraulic gradient. However, as soon as the water level rises above the ice sheet surface elevation, the model treats this as flood water that is lost from the system. The pressure values attainable in the model are therefore limited to $P_w = 1.11P_i$, which represents junction water depth equal to the ice sheet thickness.

5.1.3 Previous adaptations to EXTRAN

Conduit melt and closure

Arnold et al. [1998] adapted EXTRAN to model subglacial drainage through ice-walled conduits by modifying the code to include conduit enlargement due to the release of frictional heat in the water flowing in the conduits, and conduit closure in response to ice deformation [*Rothlisberger,* 1972]. Following *Spring and Hutter* [1981], the rate of conduit-wall melting (M), expressed as the mass melted per unit length of conduit per

unit time, is:

$$M = \left[(\pi A_c)^{1/2} \rho_w (f_r V^3 / 4) \right] / L \tag{5.3}$$

where A_c is the conduit CSA (m^2), ρ_w is the density of water (kg m^{-3}) f_r is a friction coefficient, V is the velocity of water in the conduit (m s^{-1}), and L is the latent heat of fusion of water (J kg^{-1}).

Following *Spring and Hutter* [1981], the rate of conduit closure through ice deformation (C), expressed as the change in CSA per unit time, is

$$C = -(P_i - P_w) \left| P_i - P_w \right|^{m-1} 2(1/mB)^m A_c \tag{5.4}$$

where P_i is ice overburden pressure (Pa), P_w is conduit water pressure (Pa), m is the exponent in Glen's flow law, and B is the Arrhenius parameter in Glen's flow law (N m^{-2} $s^{1/m}$). The friction coefficient and flow law exponent are given values of f_r = 0.25 and m = 3 [*Arnold et al.,* 1998]. A suitable value for the Arrhenius parameter, which is dependent on ice temperature, will be selected in the sensitivity tests in Section 5.3.

Although the *Spring and Hutter* [1981] formulations assume that material derivatives of temperature are negligible compared with other energy terms, which is an oversimplification [e.g. *Clarke,* 2003], they serve as a first-order approximation of conduit melt dynamics. It should also be noted that both water temperature (assumed to equal the ice temperature) and the effect of mechanical abrasion on conduit wall enlargement are also unaccounted for by the *Spring and Hutter* [1981] formulations.

5.1.4 Adaptations to EXTRAN in this study

In addition to the adaptations made to the code as outlined in the section above, a few adaptations have been made to EXTRAN during this study.

5.1.4.1 Spin-up period

Initial sensitivity tests indicated that conduits experienced high creep closure rates at the beginning of model runs due to their initial empty state and the large ice thicknesses typical of the interior of ice sheets. Therefore, a spin-up period of 24 hours was implemented at the start of the model run in which no melt or creep closure

occurred. However, the sudden introduction of the *Spring and Hutter* [1981] equations allowing for conduit melt and closure after 24 hours then caused model instability. Therefore, at the end of the 24 hour spin-up period, a second 24 hour spin-up period was implemented during which these formulations gradually became effective in a linear way with time. So, for example, at 36 hours, conduit closure and melt rates are 50% of their full magnitude. After 48 hours of model run time the *Spring and Hutter* [1981] formulations are fully effective.

5.1.4.2 Model time-step

Although a model time-step of 10 seconds had been implemented by *Arnold et al.* [1998], initial sensitivity tests indicated that reducing this time step to one second increased model stability and did not dramatically increase model run time.

5.1.4.3 Minimum conduit diameter

In order to prevent the impossible model condition of complete conduit closure, it is necessary to set a minimum conduit diameter. However, early sensitivity tests indicated that if this minimum diameter was set too low, the restricted subglacial system during periods of low meltwater inflow prevented enough water flowing through the system when meltwater inflow discharge subsequently increased, which resulted in an exceptionally high rate of water loss onto the ice surface. Although *Arnold et al.* [1998] found that a minimum diameter of 0.1 m was sufficient to stop conduits from closing completely under the relatively thin ice of Haut Glacier d'Arolla, Switzerland, while still allowing enough water to pass through them, initial sensitivity tests in this study showed that a minimum conduit diameter of 0.5 m was necessary for these conditions to be met beneath the thicker ice of the Paakitsoq region.

5.1.4.4 Distributed to channelized transition

As discussed in more detail in Chapter 2, both field evidence [*Bartholomew et al.,* 2010; *Palmer et al.,* 2011] and theoretical considerations [*Pimentel and Flowers,* 2010; *Schoof,* 2010] suggest that the character of the subglacial drainage system under the GrIS changes over the course of a melt season in response to changing water inputs. Early in the melt season, low volumes of meltwater are delivered to an inefficient distributed system, but as the melt season progresses and meltwater volumes increase, elements within this system enlarge through wall melting to become conduits at the

expense of other elements which shrink through creep closure, resulting in the inland development of an efficient channelized subglacial drainage system [*Bartholomew et al.,* 2011a; *Colgan et al.,* 2011] similar to the situation on many valley glaciers [*Fountain and Walder,* 1998; *Nienow et al.,* 1998; *Bartholomaus et al.,* 2008].

Although conduits in the model can enlarge and close due to melt and creep respectively, a limitation of the existing model is that new conduits cannot form, and existing conduits cannot completely close down. Therefore, the actual configuration of the system cannot adjust unless the user manually stops and starts the model run in order to adjust the system's configuration. *Arnold et al.* [1998] attempted to artificially represent the transition from a distributed to channelized system by systematically stopping the model run and then switching bunches of small parallel conduits (representing a distributed system) to single wider conduits (representing a channelized system) as the snowline passed particular junctions on the glacier. However, this model set-up was found to be slow and tedious to run and is therefore not suitable for this study which involves longer model runs and a reduced time-step of 1 second. Thus, in this study, the same subglacial drainage system configuration is set constant for the entire model run.

Although the model's configuration is therefore inherently channelized, and thus the storage / release of water in a distributed system is not adequately accounted for, in order to represent a distributed drainage system beneath Paakitsoq in this study, bundles of four conduits in parallel are used in place of single conduits for all 'first-order conduits' (i.e. conduits fed by no more than one upstream conduit (or series of conduits)). This configuration allows for a higher area of conduit wall for a given water discharge than would be possible with a single conduit, making the system more representative of a distributed system for places in the network where water discharges remain relatively low. The model does not, however, allow for water to be driven out of the channels and into a surrounding distributed system (i.e. linked-cavities or a water film) at times when water pressure is high in the conduits [e.g., *Hubbard et al.,* 1995; *Bartholomaus et al.,* 2008]. Likewise, the model cannot simulate the 'jacking-up' of ice from the bed due to increased water pressures in a surrounding distributed system [e.g. *Iken et al.,* 1983; *Mair et al.,* 2002; *Das et al.,* 2008].

In addition to the model being inherently channelized, another limitation of the model is that although some water will flow into the drainage system during the spin-up

period, it is not likely to be of a large enough volume to pressurize the system as would be expected for a distributed system at the beginning of a melt season. However, although absolute pressures, particularly at the beginning of the melt season, may not be entirely realistic, the overall spatial patterns and general trends in subglacial water pressures through time, especially after the first week or so of the melt season and when the system is full of water, should be instructive. The model will still be useful in identifying those places beneath the ice sheet and the times of the year when average water pressures over several days are likely to be highest and lowest. Similarly, the model will be useful in pointing out those places and times when short-term (hours to days) water pressure fluctuations are likely to be greatest and smallest.

5.2 Data and approach

This section focuses on applying the subglacial routing model to the catchment feeding the ASIAQ 437 gauging station (Chapter 2, Figure 2.2). This catchment is chosen because the proglacial discharge (Q) data measured here will enable the calibration and evaluation of the complete hydrological model through comparison of modelled and measured proglacial Q. Additionally, the supraglacial catchment feeding this outflow point falls primarily within the area of the strip which the SMB model was calibrated for and evaluated against in Chapter 3.

Full system model runs are from 12th May 2005 to 31st August 2005. This time period is chosen as 2005 is one of the mass balance years that the SMB model was calibrated for in Chapter 3, and in this year, ASIAQ proglacial Q measurements commence on 12th May, and by 31st August, measured proglacial Q is negligible.

5.2.1 Subglacial drainage system analysis

5.2.1.1 Subglacial drainage network delineation

In order to predict the configuration of the subglacial drainage network, and therefore the most likely positions of subglacial drainage channels under the Paakitsoq region, *Shreve's* [1972] formulation of subglacial water routing, as described in Chapter 2 (Equation 2.1), is used, together with the simplifying assumption of *Bjornsson* [1982] that all surface water directly reaches the bed and drains along the base of the ice mass which is assumed to be impermeable.

First, *Shreve's* [1972] formulation is used to calculate the hydraulic potential surfaces for a range of k values (i.e. subglacial water pressure as a fraction of ice overburden pressure) from 0.5 to 1.0 (note that throughout the rest of this chapter, the term 'k value' refers to the k in *Shreve's* [1972] equation). k values below 0.5 are thought to be unrealistic below the relatively thick ice in the Paakitsoq region [*Thomsen and Olesen,* 1991; *Thomsen et al.,* 1991]. Although in reality the k value will be spatially and temporally variable, it is necessary to define a fixed k value at this stage in the study. The process through which a suitable k value is selected is described in Section 5.2.1.4 (below).

High-resolution surface and bed DEMs are required for the calculation of hydraulic potential surfaces. The ASTER GDEM (first described in Chapter 3, Section 3.1) provides the surface elevation data. The bed elevation data (initially at a resolution of 750 m) were obtained from J. Plummer (University of Kansas), and were re-sampled using bilinear interpolation to a 100 m resolution.

Second, in order to calculate the flow accumulation (i.e. the upstream area) for each k value, the lake and catchment identification algorithm (LCIA) (explained as part of the SRLF model in Chapter 4, Section 4.2.1.1) is run using the hydraulic potential surface (in place of the surface DEM as was used in Chapter 4) for each k value. Figure 5.2 shows examples of subglacial accumulation networks for a range of k values from 0.5 to 1.0 in the Paakitsoq region. It is observed that the higher the k value, the lower the number, and the smaller the size of concentrated areas of high accumulation. This is because at higher k values, subglacial water pressure is higher (as a fraction of ice overburden pressure), which means that water has a greater ability to flow up reverse bed slopes, following the gradient of the hydraulic potential, rather than having a tendency to pool in subglacial topographic depressions [*Shreve,* 1972].

5.2.1.2 Subglacial catchment delineation

The size and shape of the subglacial catchment feeding the ASIAQ gauging station is also dependent on the k value. Using the LCIA (see Chapter 4), the size and shape of these subglacial catchments are calculated for a range of k values, along with the pit locations, lake-overflow points, and topological linkages between lake-overflow points. Examples of subglacial catchments for k values from 0.5 to 1.0 feeding the ASIAQ gauging station are shown in Figure 5.3.

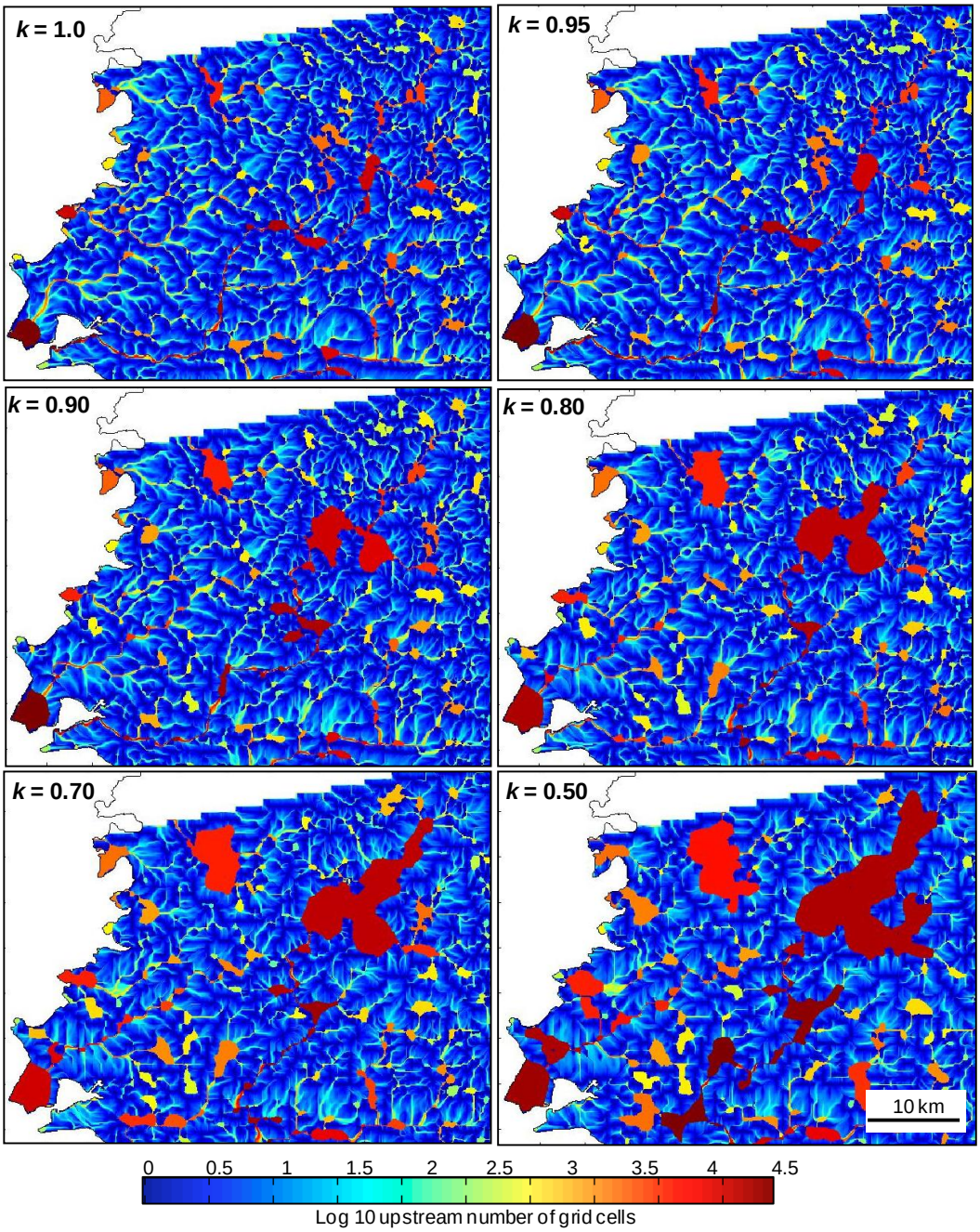

Figure 5.2: Subglacial flow accumulation maps for the Paakisoq region (area delineated by red box, Chapter 2, Figure 2.2) for a range of k values from 0.5 to 1.0. White (on ice) areas represent no data. The dark red areas indicate areas of high accumulation (i.e. those areas of the bed which would be flooded).

It is observed that the higher the k value, the larger the subglacial catchment feeding the gauging station. The reason for this is thought to be analogous to the reason for why higher k values produce fewer and smaller concentrated areas of flow accumulation (Section 5.2.1.1), i.e., that higher k values are likely to result in larger

subglacial catchments as subglacial water at higher pressures is more easily able to flow uphill and so does not pond in subglacial topographic depressions as easily [*Shreve,* 1972]. A sudden decrease in catchment size from k = 0.925 to k = 0.90 is also apparent (Figure 5.3).

5.2.1.3 Supraglacial catchment delineation

In order to calculate locations of surface meltwater inputs to the subglacial routing model, it is first assumed that all depressions in the surface DEM have an existing moulin in their lowest cell [e.g. *Catania and Neumann,* 2010]. It is, however, appreciated that this situation may not be entirely realistic as in reality, it is highly likely that additional moulins, not associated with supraglacial lakes, are present on the ice sheet surface [*Catania et al.,* 2008]. However, it is thought that moulins not associated with supraglacial lakes will not have the ability to rapidly route large volumes of water to the ice sheet bed compared to moulins associated with depressions, thus reducing their potential effect on subglacial water pressures [*Catania and Neumann,* 2010; *Hoffman et al.,* 2011]. Additionally, the areal density of moulins in this study assuming that a moulin is present in the lowest cell of every depression (~0.25 km^{-2}) is not dissimilar to the densities of moulins mapped by *Colgan and Steffen* [2009] (0 - 0.89 km^{-2}) and *Zwally et al.* [2002] (~0.2 km^{-2}) for the Paakitsoq region. Thus, the initial assumption that every surface depression contains a moulin likely represents the maximum possible number of moulins available to route relatively large volumes of meltwater to the bed of the ice sheet.

However, it is also appreciated that not all supraglacial lakes will drain by hydrofracture (and therefore a moulin in the bottom of the lake will not form), but instead may either completely or partially drain by overflowing into downstream catchments, or may not drain at all [e.g., *Das et al.,* 2008; *Catania and Neumann,* 2010; *Tedesco et al.,* in review]. Thus, an alternative approach is subsequently used to calculate locations of surface meltwater inputs to the subglacial routing model. This approach involves the assumption that depressions in the surface DEM will only have a moulin in their lowest cell once a supraglacial lake in the surface depression has drained through by a simulated hydrofracture mechanism (see Section 5.2.2 for further details).

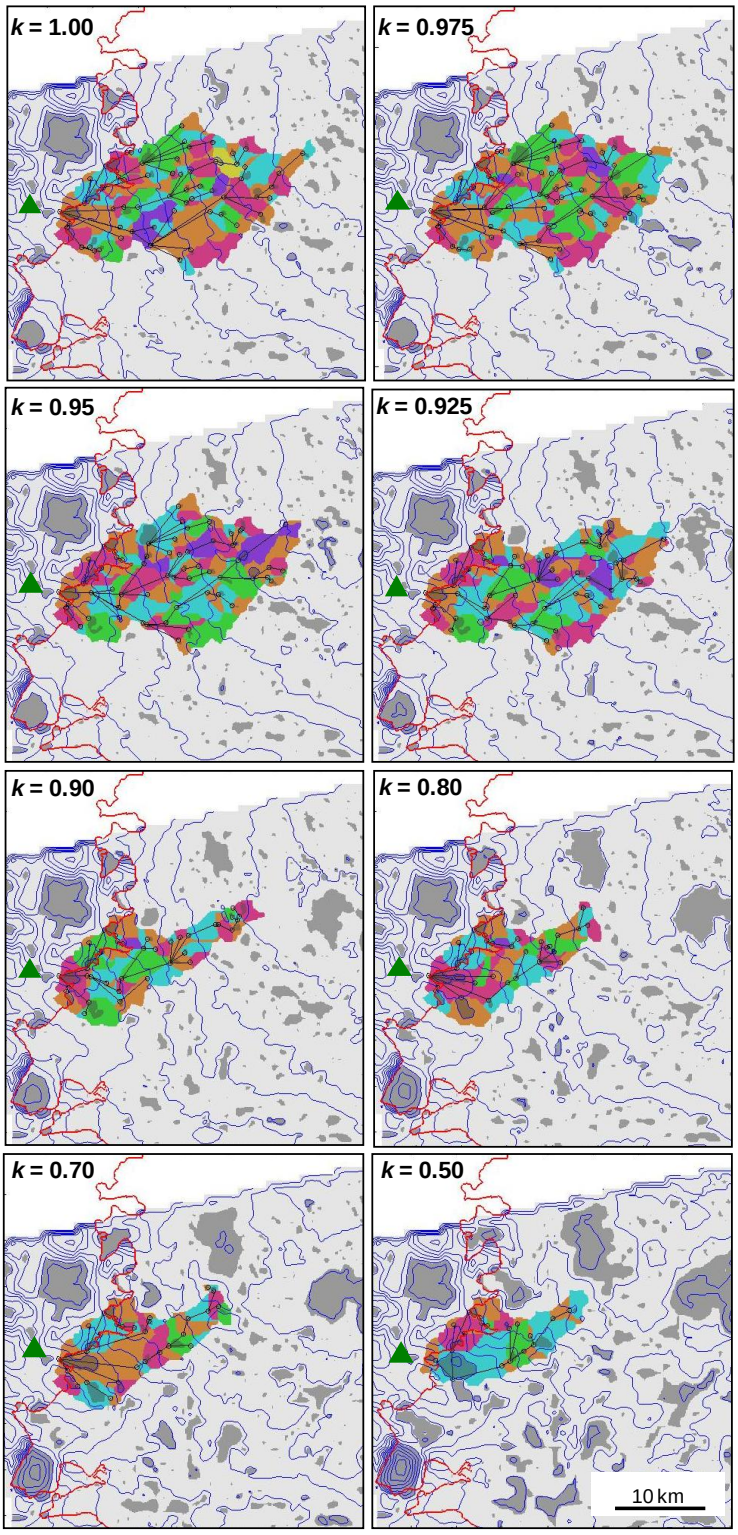

Figure 5.3: Subglacial drainage catchments (including parts of the proglacial area) which feed the ASIAQ gauging station (green triangle) for a range of k values from 0.5 to 1.0. Coloured areas represent sub-catchments for each 'pit' cell. Grey areas represent maximum possible extents of lakes. Hollow circles represent overflow points of the sub-catchments, and black lines represent topological links between each of the sub-catchments. The blue lines represent contour lines of subglacial hydraulic potential (100 m interval). The red line delineates the ice margin. White (on ice) areas indicate no data.

If it is also assumed that moulins are vertical shafts routing water directly from the ice surface to the bed [*Catania et al.,* 2008], with each moulin having its own supraglacial catchment supplying it with runoff, the size and shape of the total supraglacial catchment feeding the ASIAQ gauging station is therefore highly dependent on the size and shape of the subglacial catchment feeding the ASIAQ gauging station. Thus, the LCIA is also run for the surface DEM in order to establish which pit locations (assumed to be potential moulins) fall within the subglacial catchment for each specified k value.

Figure 5.4 shows examples of supraglacial catchment outlines (red lines), overlaid onto corresponding subglacial catchments feeding the ASIAQ gauging station for k values ranging from 0.875 to 0.95. Also shown are moulin locations marked by black dots. Figure 5.5 shows the corresponding supraglacial catchments (including the sub-catchments (coloured areas)) for the subglacial catchments in Figure 5.4. Figure 5.6 shows a bar chart indicating the supraglacial catchment areas for k values ranging from 0.5 to 1.0. Figures 5.4, 5.5 and 5.6 all indicate a sudden decrease in supraglacial catchment area from k = 0.925 to k = 0.90, as was also observed during subglacial catchment area delineation (Section 5.2.1.2).

5.2.1.4 *k* value selection

As the size and shape of the supraglacial catchment is highly correlated with the size and shape of the subglacial catchment feeding the ASIAQ gauging station, this also means that the size of the subglacial catchment is highly correlated with the total surface runoff potentially available to feed a specific outlet point at the ice sheet margin. By inference, this also means that the total surface runoff available to feed a given proglacial outlet point is a function of the k value.

Thus, in order to select a suitable k value to represent subglacial drainage at Paakitsoq, the total volume of measured proglacial Q at the ASIAQ gauging station (Figure 5.7) is compared to the total volume of modelled net runoff (calculated by the SMB model, Chapter 3), over supraglacial catchments for k values ranging from 0.85 to 1.0 (at 0.025 increments), for the time period 12th May 2005 to 31st August 2005 (Figure 5.8).

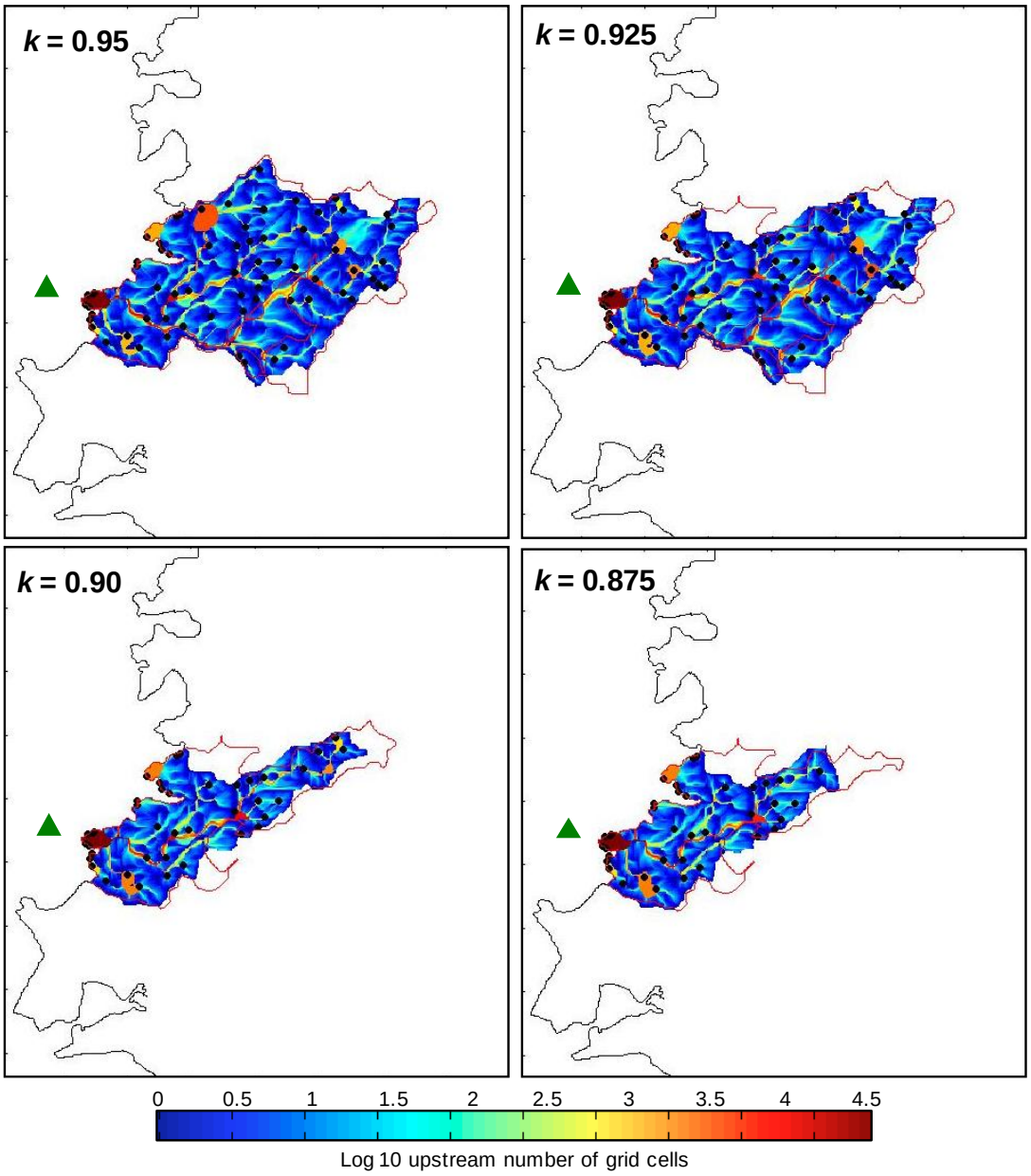

Figure 5.4: Supraglacial catchments (red outline) superimposed onto their corresponding subglacial catchment maps of flow accumulation feeding the ASIAQ gauging station for different k values. Pit locations in the surface DEM (assumed to represent possible moulin locations) are indicated by black dots.

The total volume of measured proglacial Q falls between the total modelled volumes of net runoff for k = 0.90 and k = 0.925 (Figure 5.8). As a proportion of the modelled net runoff will be: i) stored in supraglacial lakes; ii) stored in the subglacial system itself; and / or iii) may not physically manage to enter moulins and so will be 'lost' from the model, the total volume of modelled net runoff will likely be higher than the total measured Q. Thus, as the total modelled net runoff for k = 0.925 is slightly higher than the total measured Q, this k value is focussed on for further analysis. As there is little

difference between the total modelled volumes of net runoff for k values of 0.925 and above, the model is also likely to be relatively insensitive to k values of 0.925 and above. k = 0.925 is thus used to: i) determine the size and shape of the subglacial catchment feeding the ASIAQ gauging station; and ii) to predict paths of subglacial conduits by upstream area analysis using *Shreve's* [1972] formulation combined with the LCIA; and iii) specify the number and locations of moulins, and therefore the size and shape of the supraglacial catchment.

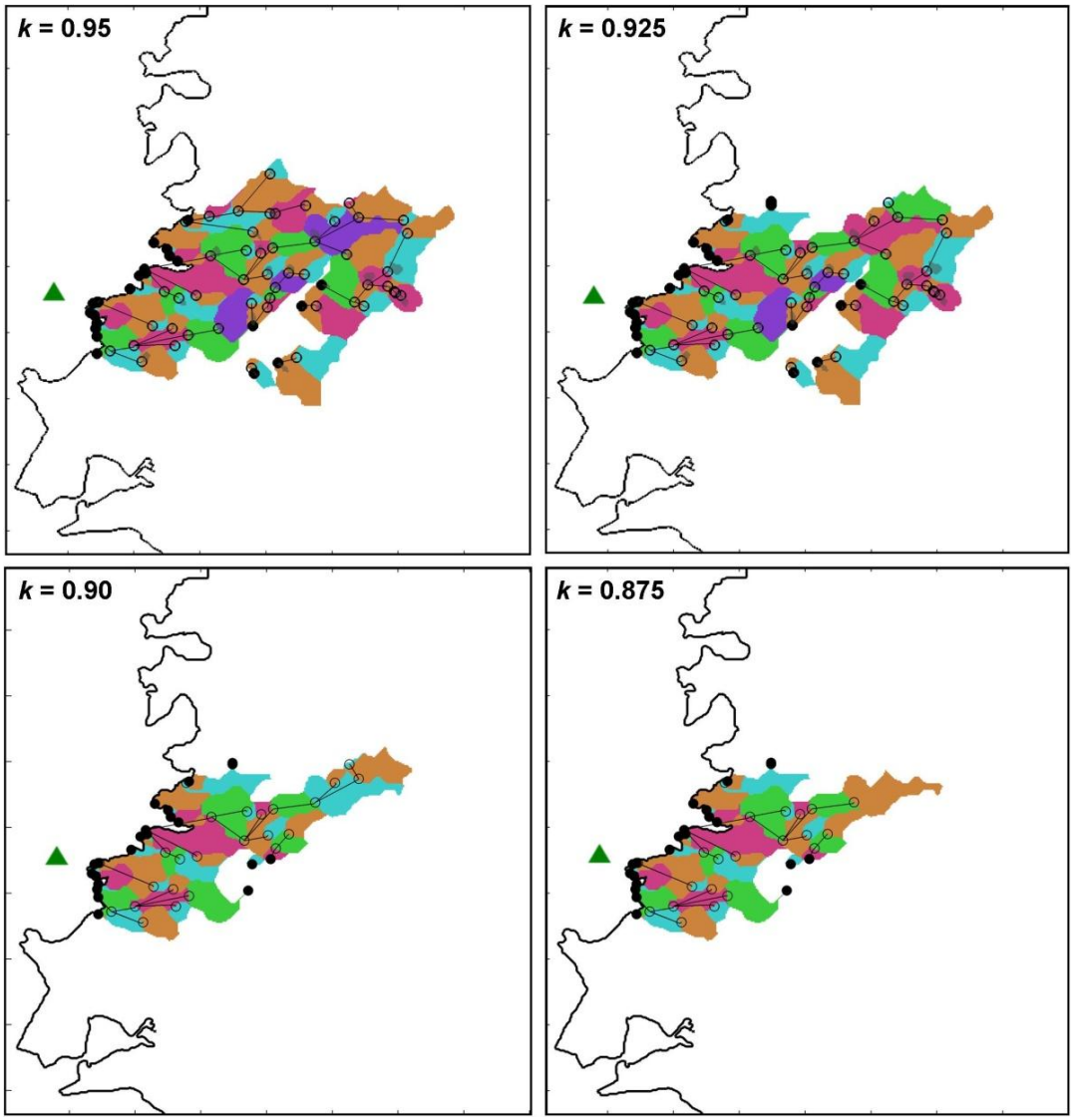

Figure 5.5: Supraglacial catchments for each of the corresponding subglacial catchments for different k values in Figure 5.4. Coloured areas represent sub-catchments for each 'pit' cell (assumed to represent possible moulin locations) in the surface DEM. Hollow circles represent overflow points of the sub-catchments, the black lines represent topological links between each of the sub-catchments, and the black circles represent outflow locations from the supraglacial catchment.

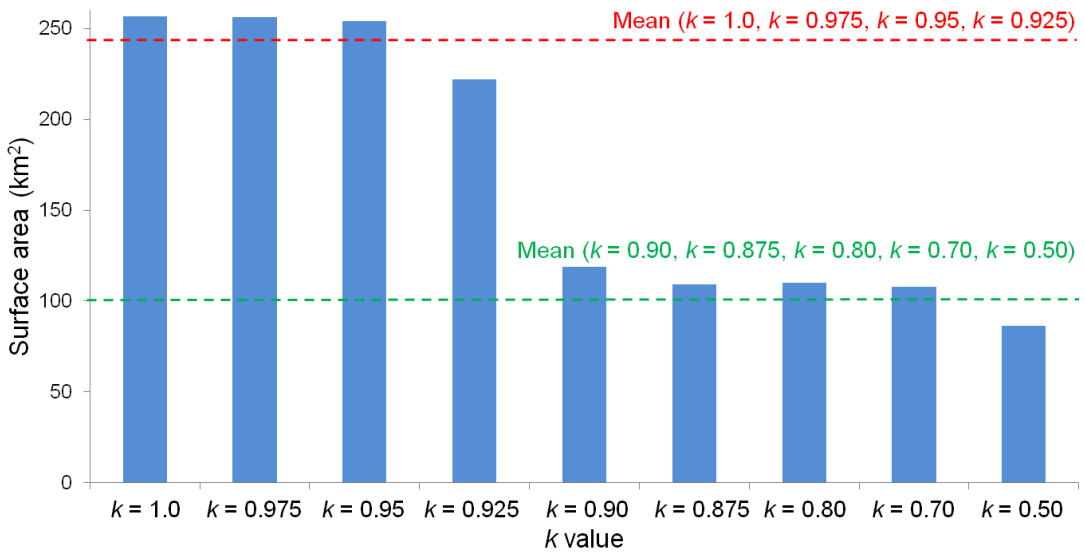

Figure 5.6: Bar chart comparing supraglacial catchment areas feeding the ASIAQ gauging station for k values ranging from 0.50 to 1.00.

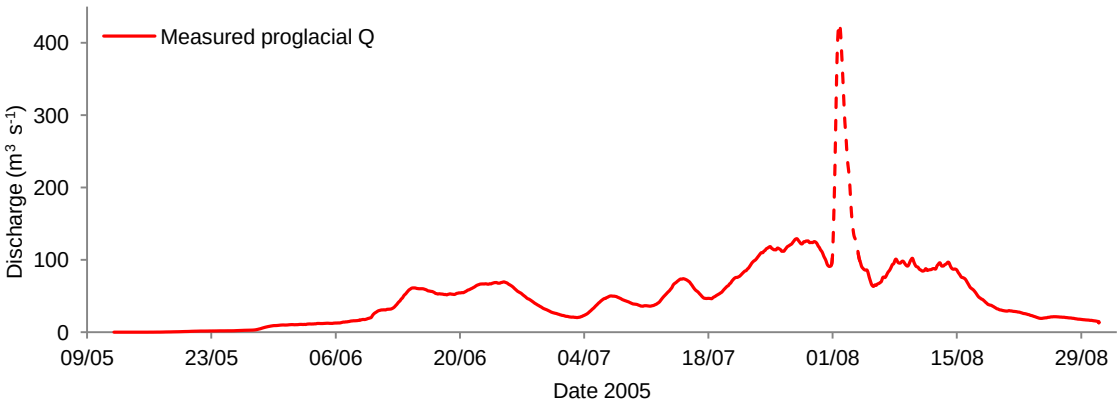

Figure 5.7: Measured proglacial Q (m^3 s^{-1}) at the ASIAQ gauging station (green triangle, Figure 2.2) from 12th May to 31st August 2005. The dashed red line likely represents a proglacial lake flood event. The data are naturally smoothed due to the delay of water in the proglacial lakes before arrival at the gauging station.

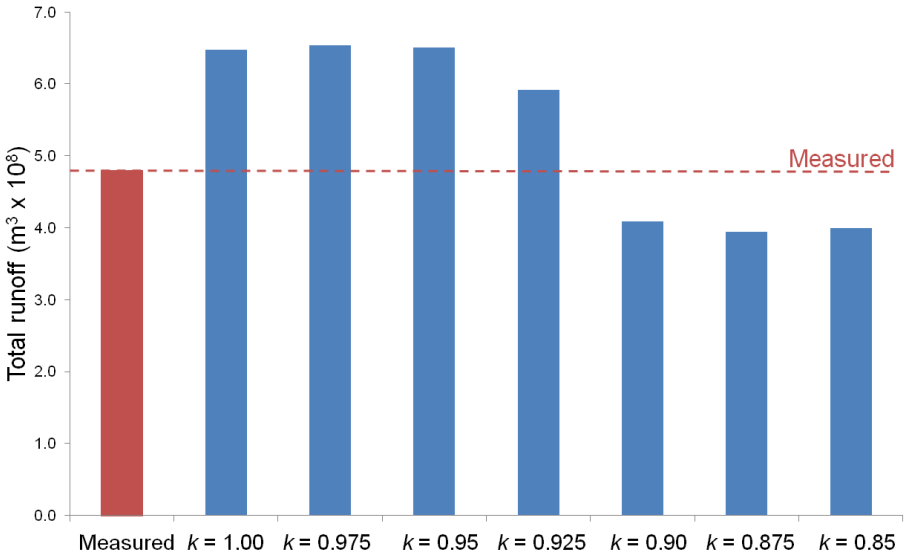

Figure 5.8: Bar chart comparing the total volume of measured discharge to the total volume of modelled net runoff for a range of k values from 0.85 – 1.00 for the time period 12th May to 31st August 2005.

5.2.1.5 Subglacial network configuration

With a selected k value of 0.925, the precise subglacial network configuration can now be prescribed. Figure 5.9 shows the inferred locations of individual conduits, moulins and junctions, overlaid onto the upstream accumulation map of the subglacial catchment for k = 0.925. Moulins (black dots), previously defined from topographical pit locations in the supraglacial catchment, are linked by conduits which are placed along the paths of highest flow accumulation between moulins. This results in the creation of an arborescent structure (black lines). Junctions (red dots) are placed between conduits, so that no conduit is longer than 1000 m (conduits longer than this reduce model stability [*Rosener et al.,* 1988]). The black dots on the ice margin mark outflow points from the ice sheet (Figure 5.9). The black dots on the ice margin that are not linked to conduits mark supraglacial sub-catchment outlet points from the ice sheet. Water reaching any of the marginal outflow points is cumulated and compared with measured proglacial Q (i.e. once water reaches a marginal outflow point it is assumed to instantaneously reach the gauging station (green triangle). Although it is appreciated that this is not entirely realistic as some of the runoff is routed through a series of proglacial lakes before reaching the gauging station, the delay of water in the proglacial lakes cannot be quantified.

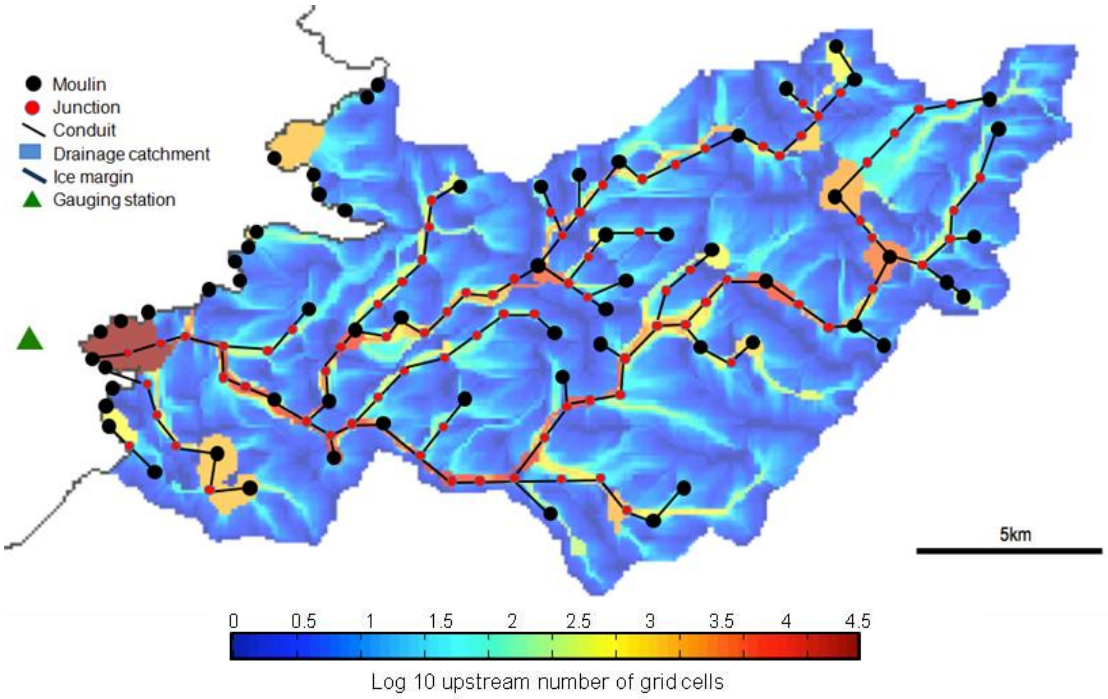

Figure 5.9: Conduit (black lines), moulin (black dots) and junction (red dots) locations overlaid onto the subglacial flow accumulation map for the subglacial catchment for k = 0.925. The green triangle marks the ASIAQ gauging station.

For model input file purposes, all conduits and junctions (some of which are moulins) must be individually numbered; these numbers are displayed in Figure 5.10.

In addition to conduit lengths, values for other key conduit parameters (used in Equations 5.2 and 5.3) including: i) initial conduit diameter; ii) Manning's roughness (n); and iii) the Arrhenius parameter (B) (which determines the ice viscosity) are selected through sensitivity tests (described in Section 5.3).

The model requires the cross sectional areas, and surface and bed elevations of junctions (some of which are moulins) to be specified. The surface and bed elevation data come from the surface and bed DEMs. The cross sectional areas of all junctions which are not moulins are set at 0.1 m^2. In order to prevent unrealistic volumes of water storage from being introduced into the model, it is important that junction cross sectional areas are no larger than this.

Although in reality moulin CSAs will adjust through wall melting and creep closure in response to changing water inputs and ice pressure, junctions that are specified as moulins in the model must have a fixed CSA. In order to set this parameter value it is necessary to consider the balance between: i) the need to have a large enough moulin to

accommodate as much water as possible during times of high meltwater inflow; and ii) the need to have a small enough CSA to keep the system pressurized for the majority of the time when meltwater inflow to the system is lower. The optimal balance between these two factors will produce the lowest volume of water which is 'lost' onto the ice sheet surface during the model run. Initial sensitivity tests indicated that moulin CSAs of 2 m^2 were appropriate.

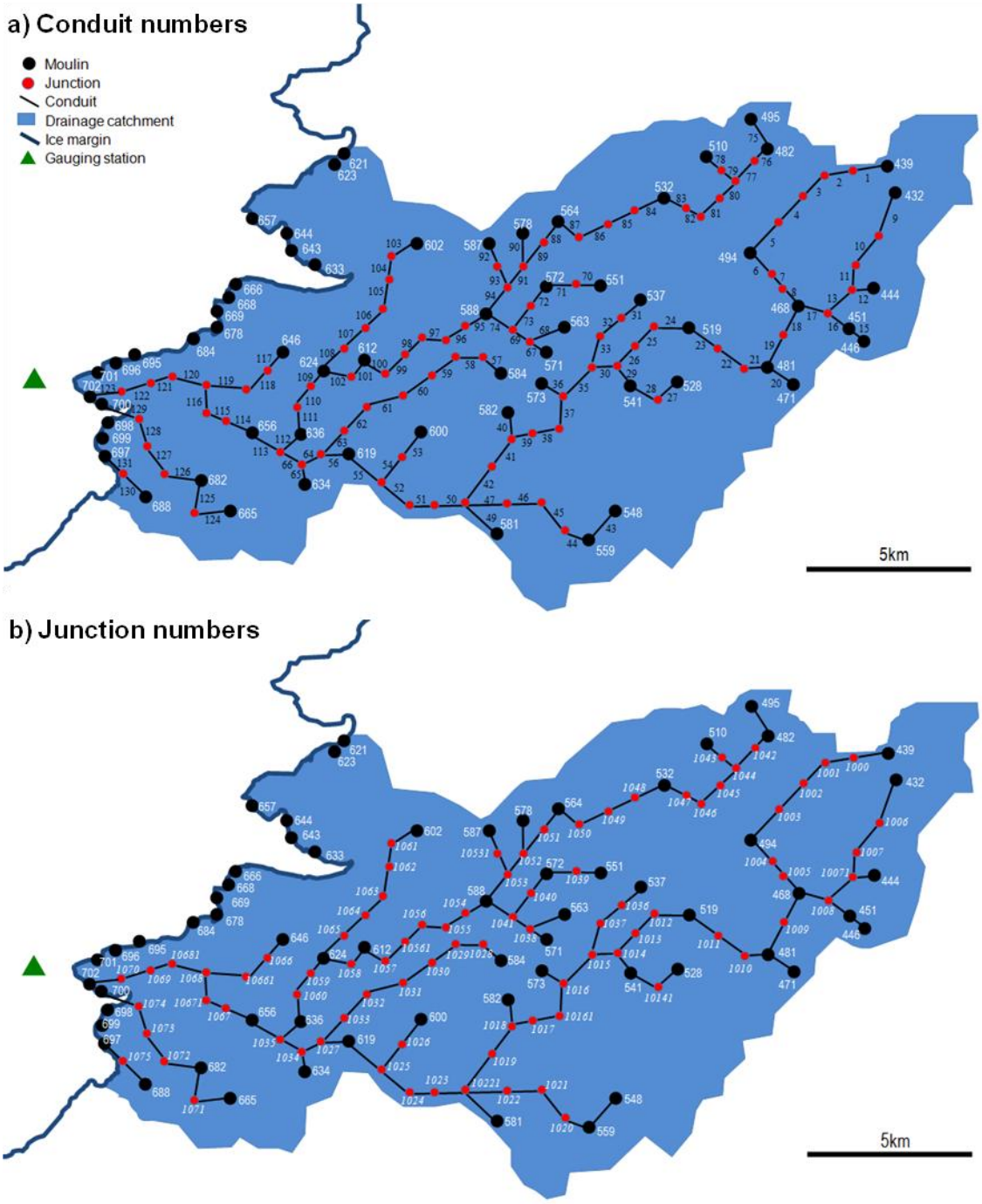

Figure 5.10: Conduit (a) and junction (b) numbers for the subglacial catchment feeding the ASIAQ gauging station (green triangle) for k = 0.925.

5.2.2 Full system model runs: Input hydrographs

Before model runs are undertaken in order to analyze the effect that spatially and temporally varying moulin inputs to the system have on subglacial water pressures, the complete model is first run under the assumption that all moulins are 'closed'. This means that all topographical lows on the surface have the potential to fill to become lakes, and then overflow into downstream catchments (as calculated by the SRLF model, Chapter 4). Therefore, surface meltwater can only reach the gauging station by flowing over the snow / ice surface. Although this is an unrealistic scenario as supraglacial lakes have frequently been observed to drain on the GrIS [e.g., *McMillan et al.,* 2007; *Das et al.,* 2008, *Selmes et al.,* 2011; *Tedesco et al.*, in review] thereafter leaving open moulins [e.g., *Catania and Neumann,* 2010], this is one end member of a range of scenarios for calculating the proglacial Q hydrograph, in which no supraglacial water enters the subglacial drainage system.

Second, the model is run under the assumption that some or all of the available surface meltwater is able to enter the subglacial drainage system. For this assumption, two different scenarios for calculating surface meltwater Q hydrographs into moulins are used:

1) 'Open' moulin scenario

This scenario assumes that all available runoff is able to drain into 'open' moulins which exist at the lowest point of every surface depression, and therefore lakes are not able to fill. Although this is an unrealistic scenario as supraglacial lakes are frequently observed to fill and subsequently drain on the GrIS [e.g. *Box and Ski*, 2007; *McMillan et al.,* 2007; *Das et al.,* 2008; *Selmes et al.,* 2011; *Tedesco et al.,* in review], it is the other end member of a range of scenarios for calculating a proglacial Q hydrograph, under which all supraglacial water enters the drainage system.

2) The lake filling / drainage scenario

This scenario follows *Clason et al.* [2012] (see Chapter 2, Section 2.2.1 for further details) in assuming that all lakes start to fill, but then drain through a simulated hydrofracture mechanism if their volume becomes large enough to fill a crevasse of given dimensions to the ice sheet bed. If this required volume is not reached, lakes will overflow into the next downstream catchment. However, if hydrofracture occurs, a

moulin will be assumed to exist at the deepest part of the depression for the remainder of the melt season.

Clason et al. [2012] assumed that once a lake reached its threshold volume, it completely drained to the bed within the model time-step (one day) of their study. However, as rapid lake drainage events have been observed to last up to five hours [*Das et al.,* 2008; *Tedesco et al.,* in review], in this study, the total volume of water in the lake at the time of drainage is added to the subglacial drainage system over a five hour period. It is assumed that a lake drainage hydrograph over the five hours takes the shape of an equilateral triangle, reaching a peak at 2.5 hours and rising and falling to and from the peak at the same rate. Although this is not entirely realistic [i.e., *Das et al.,* 2008; *Tedesco et al.,* in review], initial sensitivity tests indicated that the precise shape of the hydrograph assumed has a negligible effect on modelled results.

As a rule, modelled crevasses vary in CSA at the ice sheet surface from 50 m^2 to 1000 m^2. Although in reality crevasses are not rectangular in shape, this range of areas is equivalent to crevasses with fixed lengths of 500 m, and widths varying from 0.1 to 2.0 m. Crevasse depths are equal to that of the ice thickness [*Clason et al.,* 2012]. To investigate varying crevasse widths from 0.1 m to 2.0 m, sensitivity tests are undertaken to investigate which topographic lows within the supraglacial drainage catchment are able to accommodate a large enough volume to enable drainage. Ultimately, the effect of crevasse width on the modelled proglacial Q hydrograph at the ASIAQ gauging station will be investigated.

5.3 Sensitivity tests

Testing the sensitivity of the model to various physical and geometric parameters is necessary for two reasons: i) to check that the model is giving physically plausible solutions; and ii) to establish suitable values for key parameters which are unable to be constrained using available measurements. As previously mentioned, sensitivity tests are undertaken to investigate the model's sensitivity to three key parameters: i) initial conduit diameter; ii) Manning's roughness of conduit walls (n); and iii) Arrhenius parameter (B) (which determines the ice viscosity). Finally, using selected values for each of these three parameters, the model is then run using different magnitudes of constant inflow.

5.3.1 Sensitivity test design

Several model runs (each lasting 500 hours) are performed on a simplified, single channel system broken up into 1000 m conduits, with one input moulin at the top of the system, and one output junction at the end. The selected path of this single channel system is shown in Figure 5.11. The channel system follows the route of one of the flow accumulation paths for k = 0.925 (see Figure 5.10). The system is broken up into ~1000 m long conduits, linked by junctions, and it is assumed that one inflow moulin is located at the top of the system (moulin 564) and that all water exits at an outflow at the margin (junction 702). Figure 5.12 shows the bed and surface elevation profiles along the sensitivity test flow path.

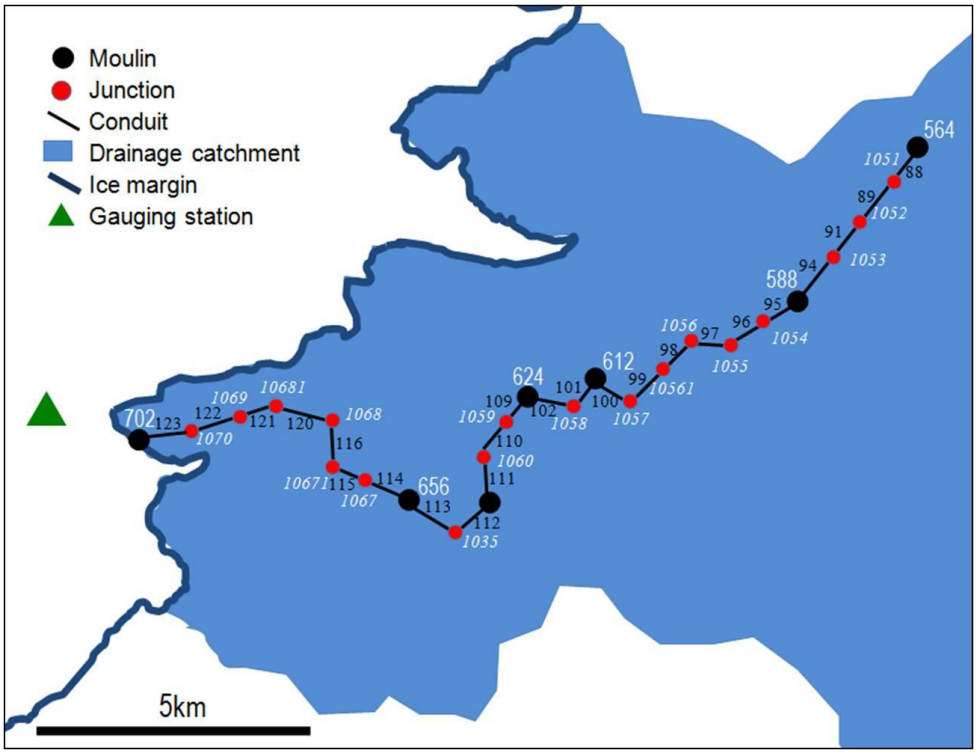

Figure 5.11: Path of the single channel system for sensitivity testing overlaid onto part of the subglacial catchment for k = 0.925. Moulins are marked with black dots while junctions are marked with red dots. Moulin and junction numbers are white, conduit numbers are black. The green triangle marks the ASAIQ gauging station.

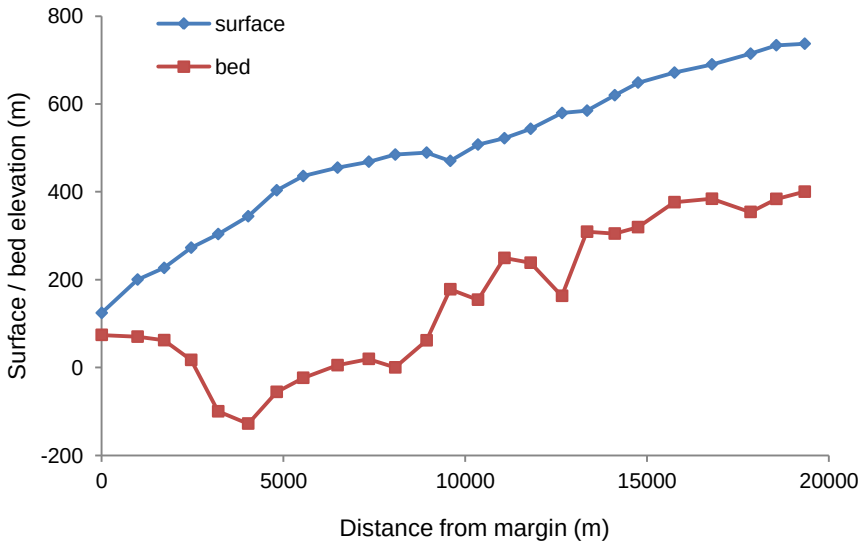

Figure 5.12: Bed and surface elevation profiles along the sensitivity test flow path (Figure 5.10).

The ranges and the increments of the parameter values considered are listed in Table 5.1. For ease of analysis, the results from one conduit (112) part way down the system, and one junction (1035) at the downstream end of conduit 112, are examined in the rest of this section (Figure 5.11). Two output variables are focussed upon for each set of sensitivity tests: i) conduit diameter over time; and ii) subglacial water pressure as a fraction of ice overburden pressure (the '*k* value', after *Shreve* [1972]) over time.

Parameter	Range tested	Increment
Conduit diameter (m) (for different rates of constant inflow ($m^3 s^{-1}$))	1 – 3 (1 - 5)	1 (3)
Manning's roughness of conduit walls (*n*)	0.05 – 0.25	0.05
Arrhenius parameter (*B*) (dependent on ice temperature (°C))	8.55×10^7 – 5.28×10^7 (-5 – 0)	0.65×10^7 (1)
Constant inflow ($m^3 s^{-1}$)	1 – 10	1

Table 5.1: The ranges and increments of the parameters considered in the sensitivity tests.

5.3.2 Sensitivity test results

Unless otherwise specified, all the water in the following model runs enters into moulin 564 and exits from 702 without any water being lost onto the ice surface from any junction along the flow path.

5.3.2.1 Conduit diameter

As shown in Figure 5.13, for a given rate of constant inflow (1 - 5 $m^3 s^{-1}$), the diameter of conduit 112 stabilizes to a constant value by ~250 hours, regardless of the initial conduit diameter (1 – 3 m). Similarly, for a given rate of constant inflow, the water pressure in junction 1035 stabilizes to the same value, regardless of the initial conduit diameter (Figure 5.14). Sensitivity tests using an initial conduit diameter of 0.5 m and a constant Q from 1 to 5 $m^3 s^{-1}$ were also undertaken. However, this conduit width was found to be too narrow to accommodate enough water at the beginning of the model run and it therefore closed rapidly, causing the majority of the input volume of water to be lost onto the ice surface. Results of these tests are therefore not shown in Figures 5.13 and 5.14.

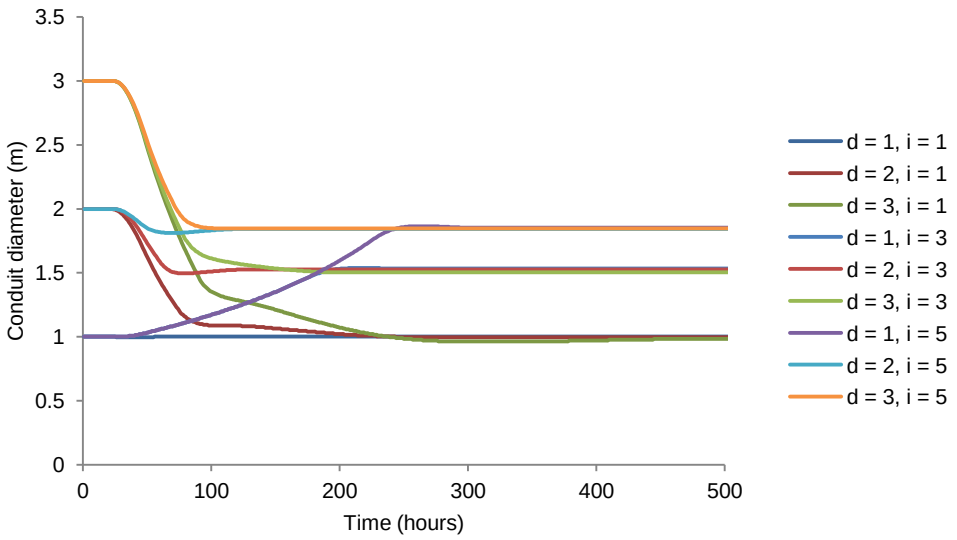

Figure 5.13: Graph showing diameter over time for conduit 112 for three different initial conduit diameters (d) from 1 m to 3 m for different rates of constant inflow to Moulin 564 (i) from 1 $m^3 s^{-1}$ to 5 $m^3 s^{-1}$. n is 0.05 $m^{-1/3}$ s and $B = 5.8 \times 10^7$.

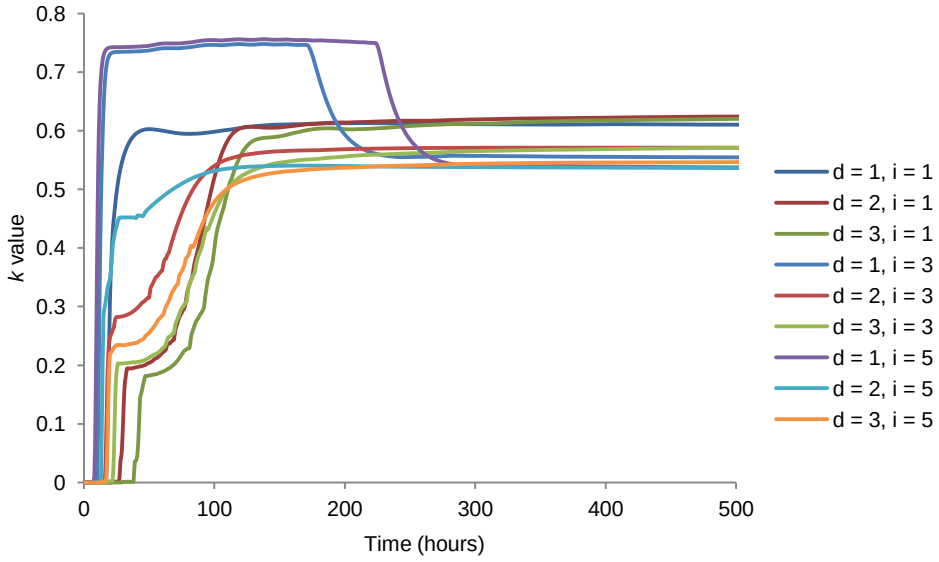

Figure 5.14: Graph showing k value over time in junction 1035 for three different initial conduit diameters (d) from 1 m to 3 m for three different rates of constant inflow to Moulin 564 (i) from 1 $m^3 s^{-1}$ to 5 $m^3 s^{-1}$. n is 0.05 $m^{-1/3}$ s and B = 5.8 x 10^7.

Thus, as long as an initial conduit diameter is set sufficiently high (at least 1 m) so that it can accommodate a sufficient volume of water at the beginning of the model run to keep the conduit open, the precise value for the initial conduit diameter is not crucial, as the conduit diameters will stabilize quite quickly (typically 100 - 200 hours) for a given Q under a given thickness of ice. These results indicate that the model is behaving properly, and generating the correct balance between conduit enlargement due to wall melt and closure due to ice creep [*Rothlisberger*, 1972; *Shreve,* 1972]. An initial conduit diameter of 2 m was selected for all further model runs.

5.3.2.2 Conduit roughness

Although conduit roughness is still the subject of debate in the literature due to few direct measurements [*Gulley et al.,* 2012], Manning's roughness (n) values calculated by *Nienow* [1993] from dye trace studies varied from 0.05 - 0.25 $m^{-1/3}$ s. These n values were also found to be linearly related to conduit area, such that a conduit with a CSA of 5 m^2 had n = 0.05 $m^{-1/3}$ s, while one with a CSA of 0.05 m^2 had n = 0.25 $m^{-1/3}$ s [*Nienow,* 1993]. However, within the constraints of the current model, values for n must be kept constant and cannot change according to conduit diameter. Values of n from 0.05 to 0.25 $m^{-1/3}$ s are systematically investigated in this sensitivity analysis.

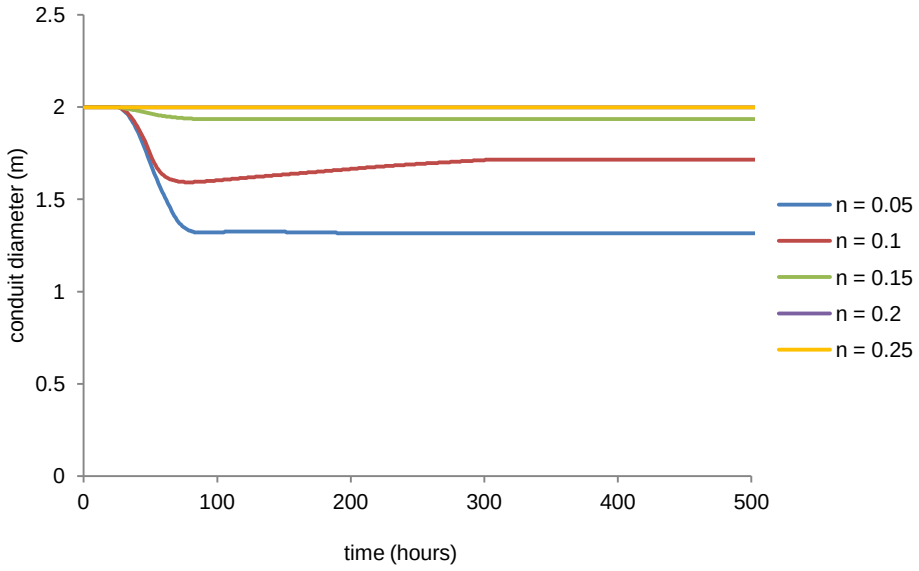

Figure 5.15: Graph showing diameter of conduit 112 over time for five model runs using n values from 0.05 $m^{-1/3}$ s to 0.25 $m^{-1/3}$ s (the n = 0.2 line is behind the n = 0.25 line). Constant inflow Q to Moulin 564 is 2 m^3 s^{-1} and B = 5.8 x 10^7.

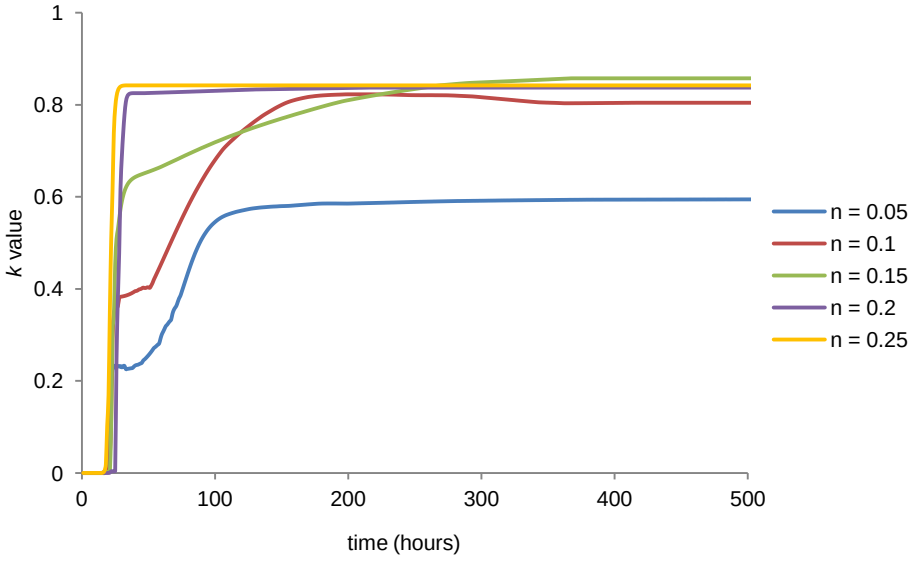

Figure 5.16: Graph showing k value in junction 1035 over time for five model runs using n values from 0.05 $m^{-1/3}$ s to 0.25 $m^{-1/3}$ s. Constant inflow Q to Moulin 564 is 2 m^3 s^{-1} and B = 5.8 x 10^7.

As shown in Figures 5.15 and 5.16, rougher conduits with higher n values stabilize immediately whereas smother conduits take up to ~200 hours to stabilise. Furthermore, rougher conduits stabilise at higher conduit diameters and higher water pressures than smoother conduits. As a rougher conduit undergoes more wall melt due

to the frictional heating of flowing water for a given water Q than a smoother conduit, the stable diameter for a rougher conduit is higher than it is for a smoother conduit (Figure 5.15). Additionally, as water flows more slowly through rougher conduits than it can through smoother conduits, the water pressure is higher for a rougher conduit than it is for a smoother conduit (Figure 5.16). It is, however, noticeable that roughness is non-linearly related to modelled conduit diameter and water pressure. In particular, for both the stable diameter and water pressure of a conduit, there is greater sensitivity at the lower end of the range of *n* values than at the higher end.

As smoother conduits ultimately result in a larger volume of water being transported more rapidly than would be possible through rougher conduits, an *n* value of 0.05 $m^{-1/3}$ s was selected for all future runs. It is particularly important that the model can rapidly route large volumes of water in the early part of the model run as otherwise a significant proportion of water will not be accommodated by the conduits and will therefore back-up in moulins and be 'lost' from the model onto the ice sheet surface.

5.3.2.3 Ice viscosity

The sensitivity of conduit creep-closure rates to the ice viscosity is determined by the Arrhenius parameter (*B)* in Equation 5.4 (Section 5.1.3.1). The Arrhenius parameter is largely dependent on the temperature of the basal ice. The sensitivity of conduit creep closure rates to ice at PMP temperatures from -5 °C (B = 8.55 x 10^7) to 0 °C (B = 5.28 x 10^7) are systematically investigated, as these values are thought to be the likely range for marginal areas beneath the GrIS [*Alhstrom et al.,* 2005].

As shown in Figures 5.17 and 5.18, with a constant inflow Q of 2 $m^3 s^{-1}$ and *n* of 0.05 $m^{-1/3}$ s, conduits stabilize to the same diameter and pressure regardless of the ice temperature (-5 °C to 0 °C). The ice temperature only influences the rate at which the conduit takes to reach its stable diameter. This is because ice of a lower temperature has a higher Arrhenius parameter (*B*), and is therefore 'stiffer' and less viscous than ice at a higher temperature, hence conduits in ice of a lower temperature experience a lower rate of creep closure than conduits in ice of a higher temperature. However, although the temperature of water is assumed to be equal to the PMP of ice in this study, if, for example, the water temperature was higher than the PMP of ice, an increased rate of wall melt would likely be experienced as both heat energy from the water temperature and the viscous energy produced from flowing water would be used

to melt the ice [*Hooke,* 1989]. In reality, it is therefore unlikely that for a constant inflow and n, conduits will stabilize to precisely the same diameter regardless of ice temperature as the water temperature would have a large effect on the melt rate.

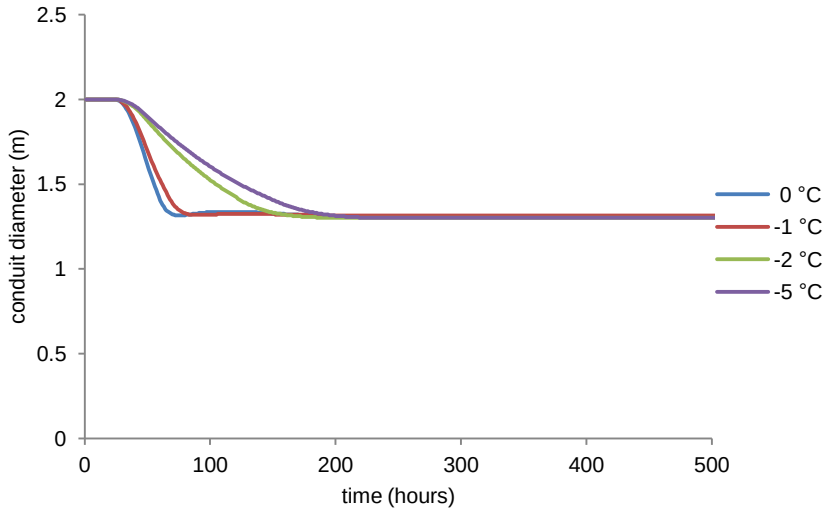

Figure 5.17: Graph showing conduit 112 diameter over time for model runs using values of the Arrhenius parameter (B) representing ice temperatures from -5 °C to 0 °C. Constant inflow Q to Moulin 564 is 2 $m^3 s^{-1}$ and n is 0.05 $m^{-1/3} s$.

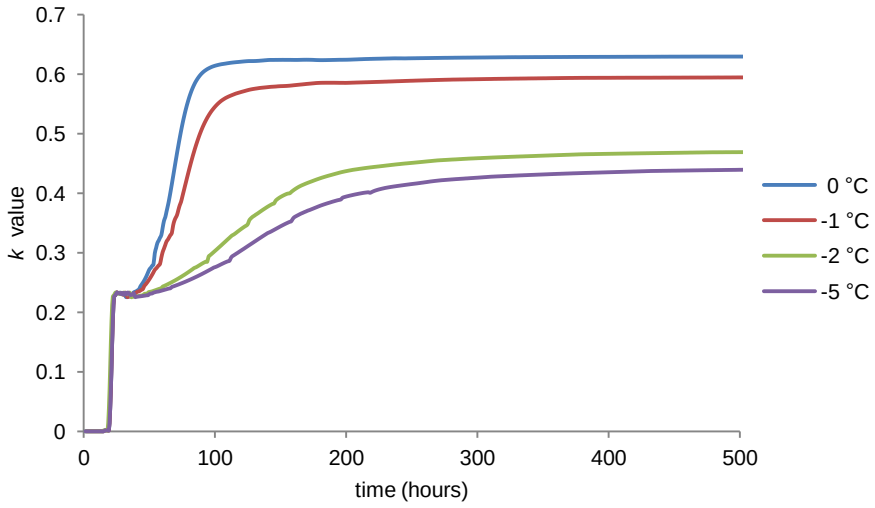

Figure 5.18: Graph showing junction 1035 k value over time for model runs using values of the Arrhenius parameter (B) representing ice temperatures from -5 °C to 0 °C. Constant inflow Q to Moulin 564 is 2 $m^3 s^{-1}$ and n is 0.05 $m^{-1/3} s$.

Following *Wang et al.* [2002] who used a thermodynamic-ice dynamic model to suggest that basal ice temperatures reach the pressure melting point (PMP) of -1.0 °C in the

Paakitsoq region, and given the basal ice temperature of 0.9 °C measured by *Thomsen* [1988], ice temperature was set at -1 °C (B = 5.8 x 10^7) in all following model runs in this study.

5.3.2.4 Inflow magnitude

Using the values which were thought to be most suitable for the parameters: i) initial conduit diameter (2 m); ii) Manning's n (0.05 $m^{-1/3}$ s); and iii) ice viscosity (B = 5.8 x 10^7, meaning that ice temperature = -1 °C,), the model was re-run for varying rates of constant inflow from 1 m^3 s^{-1} to 10 m^3 s^{-1}, which are considered to be realistic magnitudes of inflow into moulins on the GrIS (Figures 5.19 and 5.20). Higher constant inflow Qs result in larger stable conduit diameters (Figure 5.19). This is expected as higher rates of conduit wall melting occur for larger Qs flowing through a conduit. For example, a constant inflow Q of 10 m^3 s^{-1} results in a stable diameter of ~2.4 m, whereas a constant inflow Q of 1 m^3 s^{-1} results in a stable conduit diameter of 1.0 m. Additionally, as would be expected in a channelized system, a higher magnitude of constant inflow Q results in a lower water pressure, and a lower magnitude of constant inflow Q results in a higher pressure (Figure 5.20).

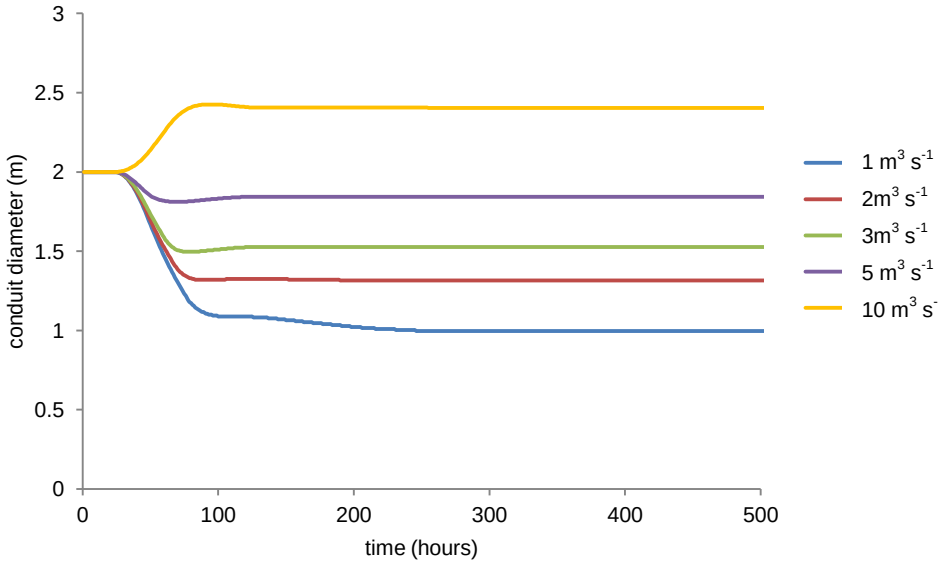

Figure 5.19: Graph showing conduit 112 diameter over time for varying magnitudes of constant inflow Q to Moulin 564 from 1 m^3 s^{-1} to 10 m^3 s^{-1}. The initial conduit diameter is 2 m, n is 0.05 $m^{-1/3}$ s, and ice temperature is -1 °C.

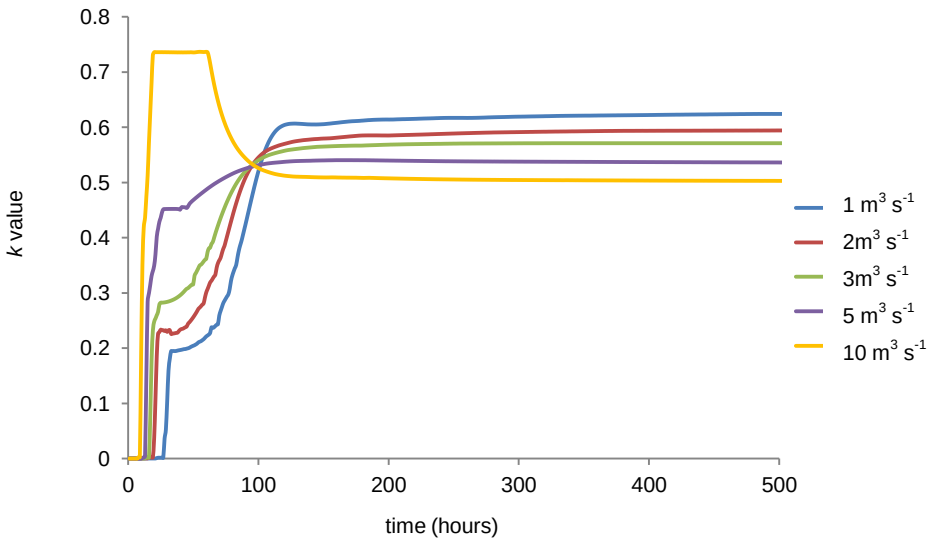

Figure 5.20: Graph showing junction 1035 *k* value over time for varying magnitudes of constant inflow Q to Moulin 564 from 1 $m^3 s^{-1}$ to 10 $m^3 s^{-1}$. The initial conduit diameter is 2 m, *n* is 0.05 $m^{-1/3}$ s, and ice temperature is -1 °C.

5.3.3 Sensitivity test conclusions

The sensitivity tests above have confirmed that the model is giving physically plausible solutions. The most suitable values for i) initial conduit diameter; ii) Manning's *n*; and iii) ice viscosity (*B*), were selected as 2.0 m, 0.05 $m^{-1/3}$ s, and 5.8 x 10^7 (meaning that ice temperature = -1 °C), respectively. As expected, results also indicated that the larger the magnitude of constant inflow discharge, the larger the stable conduit diameter, and the lower the stable water pressure in the conduit.

5.4 Full system model runs: Results and analysis

Two key model outputs are analysed in this section; proglacial Q and subglacial water pressure. Model evaluation through the comparison of measured and modelled proglacial Q for different input scenarios (Section 5.2.2) is vital as this gives an indication of the importance of different shapes and magnitudes of moulin input hydrographs for subglacial water routing in the Paakitsoq region, as well as the model's ability to accurately simulate subglacial drainage beneath the GrIS. As discussed in Chapters 1 and 2, analysis of spatially and temporally varying subglacial water pressures in response to fluctuating surface meltwater inputs is of interest in helping to explain patterns of surface velocity and uplift found by others, and will

ultimately be of interest for driving ice dynamics models.

5.4.1 Proglacial discharge

5.4.1.1 Full model runs assuming only supraglacial routing

When the model is run with the assumption that all moulins are 'closed' throughout the run and that all available runoff can only reach the ice sheet margin supraglacially across the snow / ice surface (calculated by the SRLF model, Chapter 4), only 39% of the total volume of modelled net runoff reaches the gauging station. Figure 5.21 shows graphs of both measured and modelled proglacial Q for this model run, alongside the modelled total net runoff (calculated by the SMB model, Chapter 3). The RMSE and the Nash Sutcliffe coefficient for the relationship between the measured and modelled proglacial Q are 35.3 $m^3 s^{-1}$ and -0.386 respectively; indicating a poor correspondence (Table 5.2).

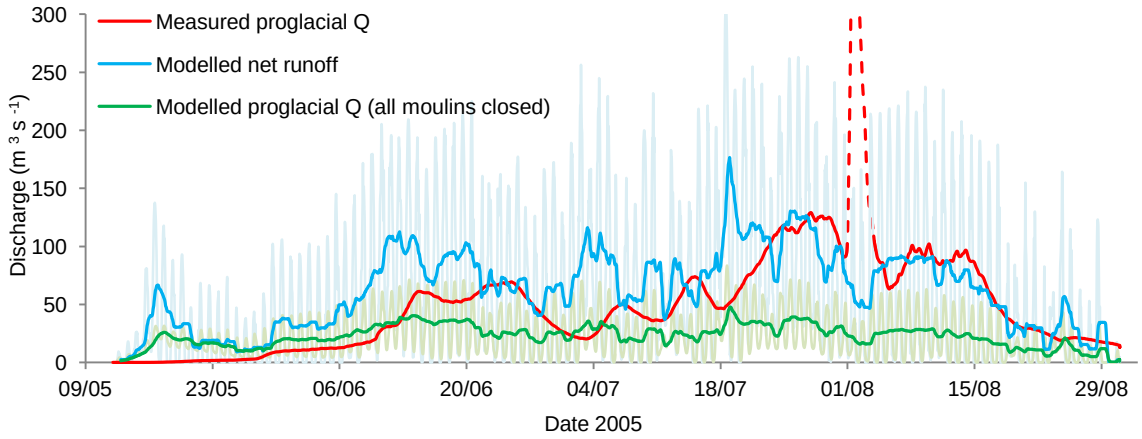

Figure 5.21: 24 hour moving averages of modelled total net runoff and modelled proglacial Q assuming that all moulins are 'closed' and that all meltwater can only reach the ice margin supraglacially. The fainter graphs behind are the hourly data for their respective colours. Also shown is measured proglacial Q. The red dotted line is a suspected proglacial lake drainage event.

A key reason for the poor correlation between modelled and measured proglacial Q is that the majority of surface meltwater (61%) is either stored in supraglacial lakes at the end of the model run, or is routed to a proglacial outlet from which it does not reach the ASIAQ gauging station. As shown in Figure 5.5, a large proportion of the surface topological links in the south and south east of the supraglacial catchment for $k = 0.925$ direct water out of the supraglacial catchment to the south.

	RMSE (m^3s^{-1})	Nash Sutcliffe coef.	Modelled – measured proglacial Q (ignoring 1 – 3 Aug, in brackets) ($m^3 s^{-1}$)
All moulins 'closed'	35.3	-0.386	-26.0×10^7 (-23.0×10^7)
'Open' moulin scenario	35.1	-0.176	9.9×10^7 (7.7×10^7)
Lake filling / drainage scenario: 0.5 m wide crevasses	32.4	0.138	8.9×10^7 (1.1×10^7)
Lake filling / drainage scenario: 1.0 m wide crevasses	30.8	0.220	11.0×10^7 (12.7×10^7)
Lake filling / drainage scenario: 2.0 m wide crevasses	25.8	0.453	-1.7×10^7 (1.2×10^7)

Table 5.2: RMSEs and Nash Sutcliffe coefficients between modelled and measured proglacial Q for various moulin input hydrograph scenarios.

5.4.1.2 Full model runs with the subglacial routing model

In order to calculate moulin input hydrographs to moulins, the two scenarios which were introduced in Section 5.2.2.1 are considered:

1) 'Open' moulin scenario

Assuming that moulins are 'open', meaning that lakes cannot fill, Figure 5.22 shows graphs of modelled total net runoff and total modelled Q into moulins. In this figure, a ~3 day lag between peaks in modelled total net runoff and total modelled Q into moulins early in the melt season is observed. By mid-June this lag time is negligible due to both a decrease in snow cover and an increase in ice exposure, resulting in increased travel velocities between each meltwater source cell and the moulin.

Figure 5.23 shows graphs of total modelled Q into moulins, total modelled proglacial Q, and total measured proglacial Q. Early in the melt season, a ~1 day lag between modelled Q into moulins and modelled proglacial Q is observed (Figure 5.23). By mid-June, this lag is also negligible, likely due to an increase in the hydraulic efficiency of the subglacial drainage system which increases the subglacial throughflow rate. The majority of the total modelled Q into moulins (~92%) reaches the ASAIQ gauging station by the end of the melt season. Of the remaining ~8% of water in this study, some remains in the system at the end of the melt season, but the majority is 'lost' from the model as floodwater from the top of junctions. This mainly happens early in the

melt season when the subglacial drainage system is of relatively low capacity as it has so far received little or no meltwater input. It happens particularly from the junctions that are located further inland where runoff availability is lower, and ice is thicker, leading to higher creep closure rates.

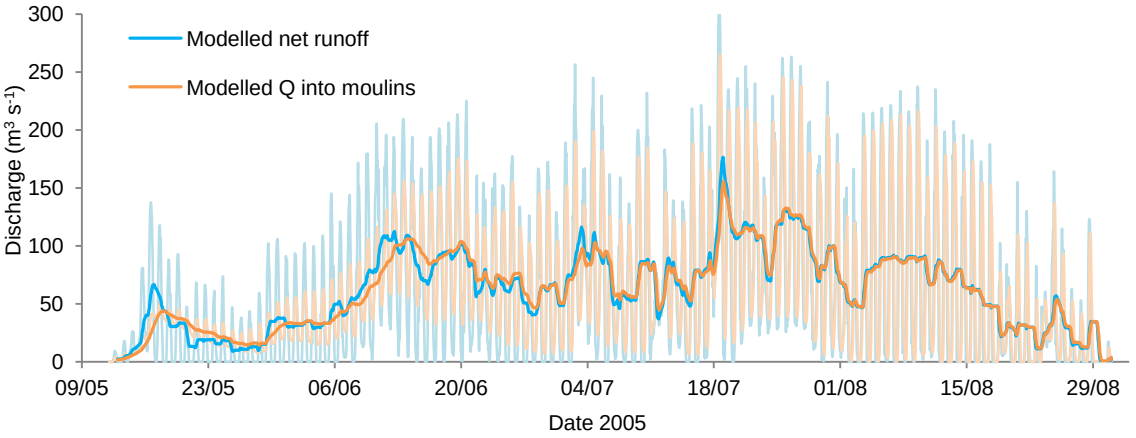

Figure 5.22: 24 hour moving averages of modelled total net runoff and modelled Q into moulins, assuming that all moulins are 'open'. The fainter graphs behind are the hourly data for their respective colours.

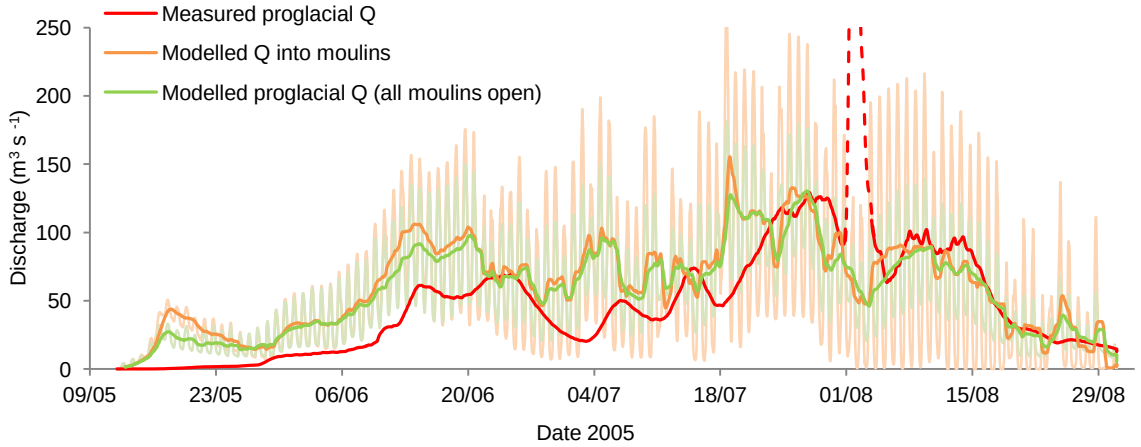

Figure 5.23: 24 hour moving averages of modelled Q into moulins and modelled proglacial Q assuming that all moulins are 'open'. The fainter graphs behind are the hourly data for their respective colours. Also shown is measured proglacial Q. The red dotted line is a suspected proglacial lake drainage event.

Ignoring the period from 1st to 3rd August (dotted red line, Figure 5.23), thought to represent a proglacial lake flood event which cannot be accounted for by the model, the average RMSE between modelled and measured proglacial Q over the melt season is

35.1 $m^3 s^{-1}$ and the Nash Sutcliffe coefficient is -0.176 (Table 5.2). Thus, compared to the model run where all moulins are assumed to be 'closed', the output from this model run shows a better correspondence with the measured proglacial Q (Table 5.2). Additionally, the total volume of modelled proglacial Q from this model run produces a better match with the total volume of measured proglacial Q than was achieved with the model run which assumed that moulins were 'closed' (a difference of 9.9 x 10^7 m^3 for the 'open' moulin model run compared a difference of -26 x 10^7 m^3 for the 'closed' moulin model run) (Table 5.2).

The correspondence between measured and modelled proglacial Q, assuming all moulins are 'open', increases as the melt season progresses (Figure 5.23). This is thought to be because moulins, in reality, are not 'open' for the entire melt season. Instead, multiple observations indicate that moulins are likely to form during the rapid drainage of supraglacial lakes [e.g., *Das et al.,* 2008; *Tedesco et al.,* in review], and that they are then likely to stay open for the rest of the melt season [*Catania and Neumann*, 2010]. Thus, it is hoped that by allowing lakes to fill and then drain in the model (see below), a better correspondence between modelled and measured proglacial Q will be produced, particularly early in the melt season.

2) Lake filling / drainage scenario

First, sensitivity tests were undertaken to analyse the effect of crevasse dimensions on the drainage ability of supraglacial lakes. This analysis is purely hypothetical on the basis of the maximum volume of lakes in depressions; no model input (i.e. output from the SLRF model, Chapter 4) is provided at this stage. Results of these tests are shown in Figure 5.24. Within the supraglacial catchment for k = 0.925 there are 44 pit cells in surface topographic lows which can fill to form lakes. Assuming crevasses reach the depth of the ice sheet, are 500 m long, and are: i) 0.1 m wide; ii) 0.5 m wide; iii) 1.0 m wide; and iv) 2.0 m wide, respectively 27, 20, 15, and 12 of the 44 topographic lows are able to fill to a large enough water volume to fill a crevasse of the given dimensions, and therefore have the ability to drain.

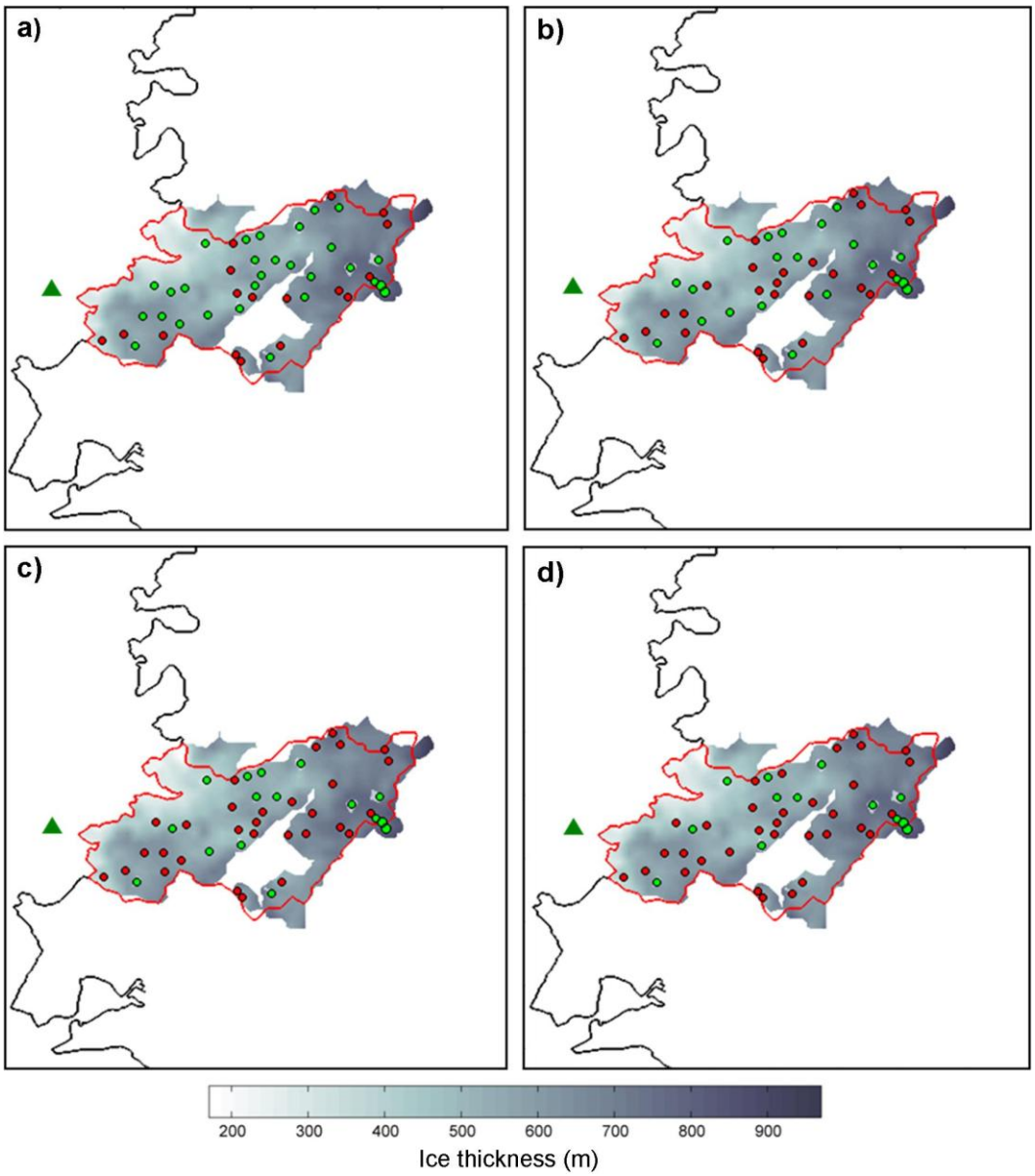

Figure 5.24: Figure showing the pit locations of lakes that have the ability to drain by hydrofracture (green dots) as they fill to a large enough volume to fill a 500 m long crevasse to the base of the ice sheet for crevasse widths of: a) 0.1 m; b) 0.5 m; c) 1.0 m; d) 2.0 m. Red dots indicate the pit locations of lakes which cannot fill to a large enough volume to drain. These dots are overlaid onto the supraglacial catchment (grey area) for k = 0.925. The corresponding subglacial catchment feeding the ASIAQ gauging station (green triangle) for k = 0.925 is delineated by the red line.

Second, moulin input hydrographs, calculated by the SLRF model (Chapter 4), are used as input for the subglacial model. Figure 5.25 shows the lakes which drain (yellow dots) and the dates on which they drain assuming that lakes drain by hydrofracture when they can fill a crevasse which is: a) 0.5 m wide; or b) 2.0 m wide, and 500 m long with a depth equal to that of the ice thickness. For a 0.5 m wide crevasse, 20 lakes drain and

the average date of lake drainage is 24th May (Figure 5.25a). For a 2.0 m wide crevasse, 10 lakes drain and the average date of lake drainage is 3rd June (Figure 5.25b). This later average drainage date for larger crevasse volumes is expected as lakes take longer to fill them to the required volume.

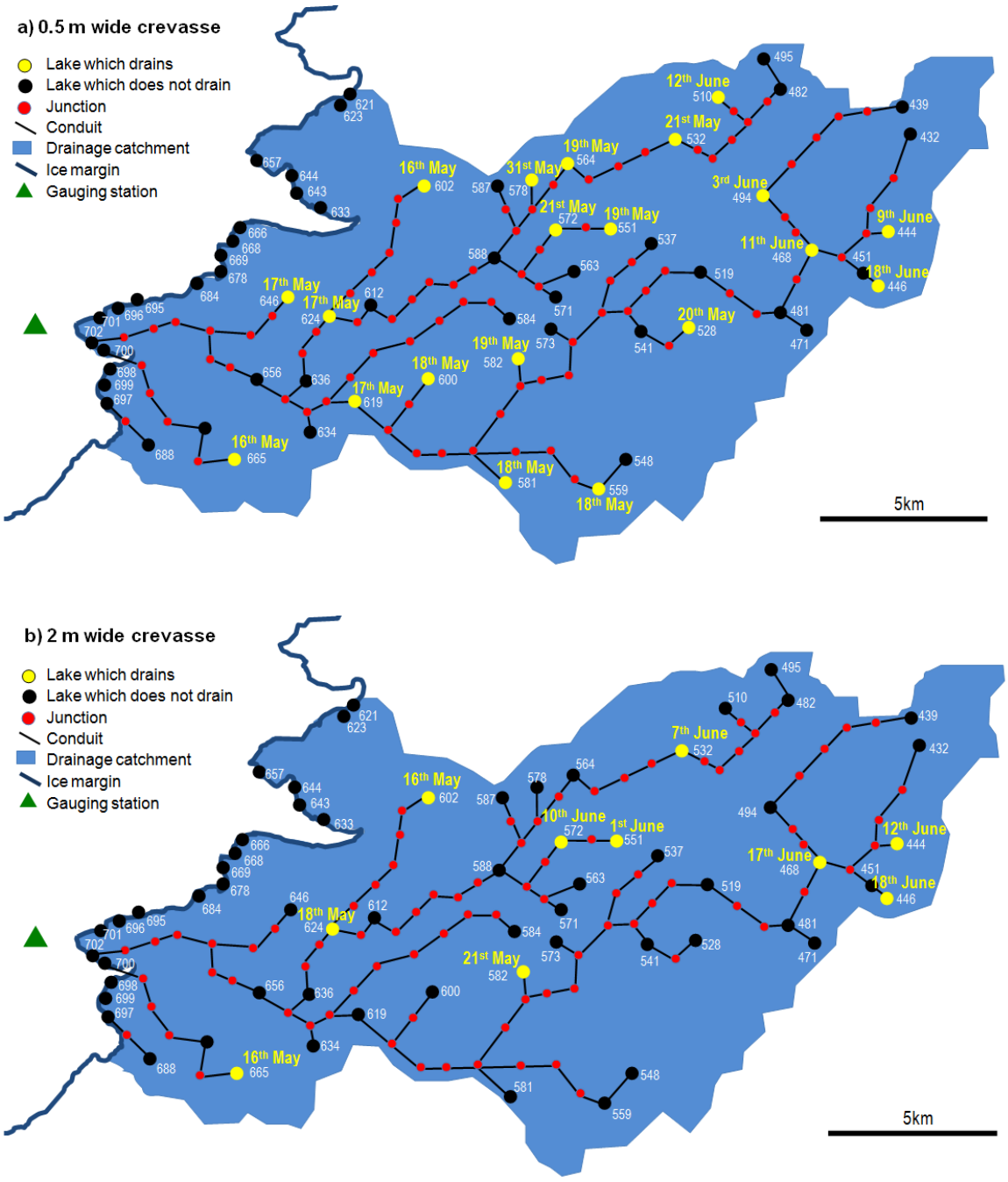

Figure 5.25: Drainage dates for lakes which drain (yellow dots) during the model run assuming that lakes drain by hydrofracture when they can fill a crevasse: a) 0.5 m wide; and b) 2.0 m wide, assuming a crevasse length of 500 m and a crevasse depth equal to that of the ice thickness.

Comparing Figure 5.25 with Figure 5.24 shows that for 0.5 m crevasses (Figure 5.25a), the number of lakes that are modelled to drain matches the number of lakes which have the potential to drain (Figure 5.24b). However, for 2.0 m wide crevasses (Figure 5.25b), two lakes (451 and 578) are not modelled to drain, even though they have the potential to drain (Figure 5.24d). Both of these lakes are relatively high on the ice sheet and they do not receive enough melt to reach the required water volume to drain during the model run.

As an example, Figure 5.26 shows graphs of 10 moulin input hydrographs calculated with the assumption that a lake drains once its volume equals that of a 2.0 m wide x 500 m long crevasse to the bed. The high spikes indicate the lake drainage events. Subsequent to this, the moulins in the drained lake basin stay 'open' for the rest of the model run.

a)

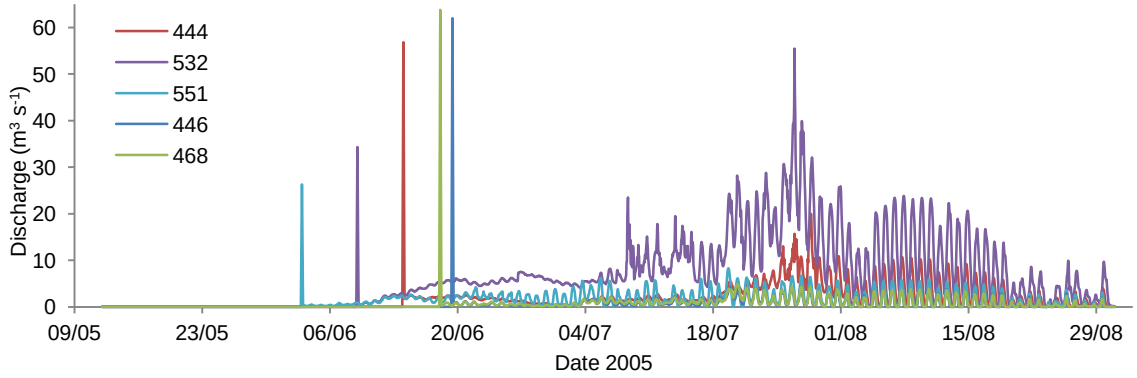

b)

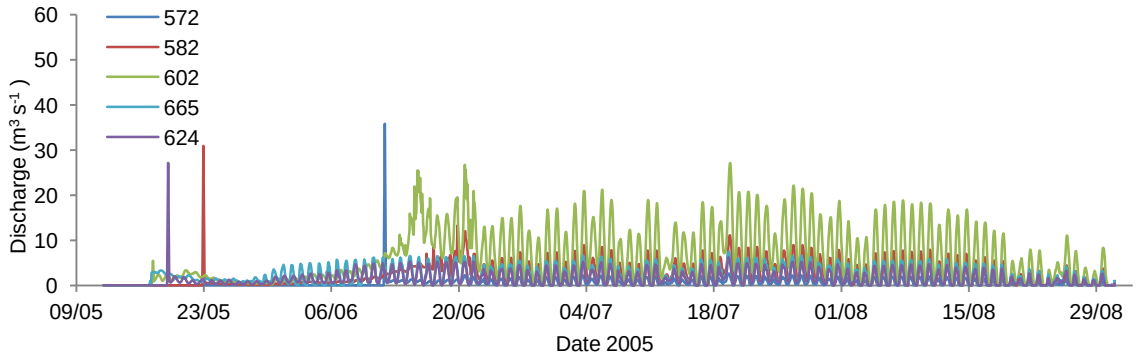

Figure 5.26: Moulin input hydrographs for the 10 lakes which are modelled to drain assuming a crevasse width of 2.0 m. a) shows 5 input hydrographs for moulins further upglacier; b) shows 5 moulin input hydrographs for moulins further downglacier.

If the lakes which drain assuming a crevasse width of 2.0 m are considered (Figures 5.25b and 5.26), it is found that, in general, the lower the lake on the ice sheet (and therefore the lower the elevation), the earlier the drainage date. This is expected for two reasons. First, melt rates are higher at lower elevations due to higher average air temperatures, thus lakes at lower elevations will fill more quickly than lakes higher on the ice sheet. Second; as the ice lower down on the ice sheet is thinner, lakes do not need to fill to such a large volume as they would higher on the ice sheet. For example, Lake 624 (Figures 5.25b and 5.26b), which is low down on the ice sheet (where the ice is 292 m thick), drains on the 18th May, whereas Lake 468 (Figures 5.25b and 5.26a), which higher on the ice sheet (where the ice is 688 m thick), drains later on 17th June. These observations are in agreement with *McMillan et al.* [2007] and *Sundal et al.* [2007].

The moulin with the highest inflow Qs later in the summer after lake drainage is 532, and the moulin with the lowest inflow Q after lake drainage is 624. As a moulin stays 'open' after lake drainage, the inflow moulin Q is not only a function of the discharge that it may be receiving subglacially from upstream moulins, but is also a function of the size of the supraglacial catchment contributing water to the moulin. If an upstream lake fills to its maximum possible volume (but does not reach a volume large enough to drain by hydrofracture), the SRLF model (Chapter 4) allows it to overflow into the next downstream catchment, thereby increasing the effective catchment area which contributes runoff to the downstream moulin. For example, after Lake 532 has drained on 7th June, the open moulin initially only receives water from its immediate catchment, but subsequently starts to receive water from upstream catchments once upstream lakes have overflowed (i.e. 439, 482, 494, 495, and 510) (see Figures 5.5 and 5.25b). Similarly, after Lake 602 has drained on 16th May, upstream lakes (i.e. 564, 578, 587 and 588) overflow and contribute runoff to Moulin 602. In contrast, after Lake 468 has drained, it only receives runoff from its own immediate catchment, and the catchment of Lake 451, as other upstream lakes also drain. Likewise, after Lake 572 has drained, no catchments other than its own are able to contribute runoff to the moulin. Thus, for some moulins, the largest inflows Qs are associated with lake drainage (i.e.444, 446, 468 551, 572, 582 and 624), whereas for the other moulins, much larger inflow Qs are experienced later in the summer (i.e. 532, 602 and 665). This is likely to have important implications for patterns of subglacial water pressures which will be examined in Section 5.5.2.

Figure 5.27 shows graphs of measured and modelled proglacial Q assuming crevasse widths of both 0.5 m and 2.0 m, and measured proglacial Q.

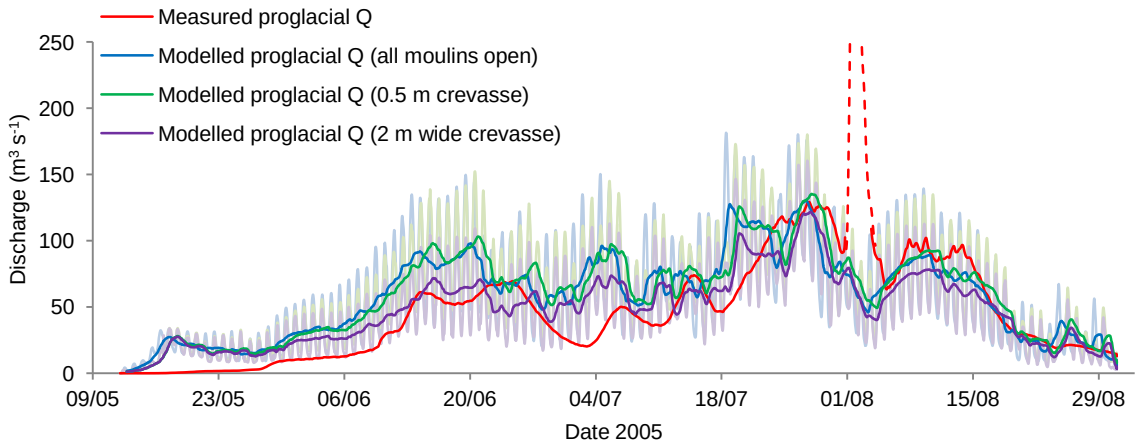

Figure 5.27: 24 hour moving averages of modelled proglacial Q assuming: i) lakes drain once their volume = volume of 0.5 m x 500 m crevasse to bed; ii)) lakes drain once their volume = volume of 2.0 m x 500 m crevasse to bed. Also shown is measured proglacial Q, and for comparison, the 24 hour moving average of modelled proglacial Q assuming all moulins are 'open'. The graphs behind are the hourly data for their respective colours.

Ignoring the period from 1st to 3rd August (dotted red line, Figure 5.27), the calculated RMSEs and Nash Sutcliffe coefficients between modelled and measured proglacial Q for lake filling / drainage scenarios assuming different crevasse widths are shown in Table 5.2. These statistics indicate that the larger the crevasse volume that the lake is required to be able to fill before drainage, the better the correlation between measured and modelled proglacial Q (as indicated by the lower RMSEs, and the Nash Sutcliffe coefficients which are closer to 1). The best correlation (RMSE = 25.8 $m^3 s^{-1}$, Nash Sutcliffe coef. = 0.453) between measured and modelled proglacial Q occurs when 2.0 m wide crevasses are used. Additionally, all model runs employing one of the lake filling / drainage scenarios produce a better correlation between measured and modelled proglacial Q than the model run which assumes that all moulins are 'open' (Table 5.2).

When the total magnitudes of cumulative modelled and measured proglacial Q are compared (Table 5.2), the model run which produces the best comparison between measured and modelled proglacial Q is again found to be the lake filling / drainage scenario using 2.0 m wide crevasses. For this run, the total volume of modelled proglacial Q is only 1.7 x 10^7 $m^3 s^{-1}$ lower than the total volume of measured proglacial

Q. All the other full model runs using smaller crevasse widths produced total volumes of proglacial Q that were higher than the total volume of measured proglacial Q. Running the model for the lake filling / drainage scenario with crevasse widths > 2.0 m would produce total volumes of proglacial Q that were smaller than that produced when the crevasse width was 2.0 m, and so such runs were not performed.

The majority of the inflow Q into moulins (~90%) reaches the ASIAQ gauging station by the end of the melt season for all model runs using the lake filling / drainage scenarios (above). This is only ~2% lower than the percentage of meltwater inflow which reaches the gauging station assuming that all moulins are 'open' (~92%). As with the 'open' moulin model run, of the remaining 10% of water in the lake filling / drainage scenario model runs, some water remains in the system at the end of the melt season, but the majority is 'lost' from the model as floodwater from junctions. However, in contrast to the 'open' moulin model run, a large proportion (~59%) of the available runoff in these lake filling / drainage scenario model runs does not become moulin inflow as it is stored in lakes which do not drain, and / or is routed supraglacially to the ice margin.

Although the best correspondence between measured and modelled proglacial Q is found for the lake filling / drainage scenario with 2.0 m wide crevasses, there are still discrepancies between the measured and modelled data. There are several possible reasons for these discrepancies. First, a series of proglacial lakes (see Chapter 2, Figure 2.3) will introduce a lag between the arrival of water at the ice margin and arrival of water at the ASIAQ gauging station which is not accounted for by the model. This lag will be particularly marked early in the summer when lake levels are low, the lakes may still be at least partially frozen, and transfer rates through the lakes will be low. Second, the temporary storage / release of water in a 'distributed' subglacial system is not adequately accounted for by the model, thus water routing is likely to be too rapid early in the melt season. Thus the time period with the largest RMSE error between measured and modelled proglacial discharge is from mid-May to mid-June. To a lesser extent, unrealistically fast subglacial flow routing could be a result of the Manning's roughness value being set too low, particularly at the beginning of the melt season when the subglacial drainage system is likely to be narrow and tortuous.

5.4.2 Subglacial water pressure

Analysing modelled subglacial water pressures first involved plotting subglacial water pressure time-series for each moulin for the entire model run. To maintain consistency with the rest of the analysis in this chapter, water pressure is expressed as a fraction of ice overburden pressure (i.e. the '*k* value' in *Shreve's* [1972] equation). Water pressure time-series that show distinct features and patterns that are representative of the behaviour of several moulins in particular parts of the ice sheet are used as examples and are focussed on for detailed analysis below.

In order to analyze patterns of subglacial water pressure over time, particularly with regard to the effect that lake drainage events have on spatially and temporally varying water pressure, modelled pressures in the 'open' moulin model runs are compared to modelled pressures in the lake filling / drainage model runs. Lake filling / drainage events which assume a crevasse width of 2.0 m are focussed upon as it was this width that produced the best correlation between modelled and measured proglacial Q, and also the best match between total volumes of measured and modelled proglacial Q (Section 5.4.1.2).

Figures 5.29 and 5.30 show modelled subglacial water pressures for a selection of moulins (Figure 5.28) assuming: a) all moulins are 'open' and no supraglacial lakes fill; and b) lakes drain once they contain a volume large enough to fill a 2.0 m x 500 m crevasse to the ice sheet base. For ease of analysis, subglacial pressure graphs for each moulin are grouped with other pressure graphs for moulins showing similar behaviour. Thus, Figure 5.29 focuses on supraglacial lake drainage events resulting in spikes in subglacial water pressure, while Figure 5.30 focuses on lake drainage events that result in sustained periods of high water pressure. Figures 5.31 and 5.32 show modelled CSAs of the conduits directly downstream of the moulins plotted in Figures 5.29 and 5.30, again assuming: a) all moulins are 'open' with no filling of supraglacial lakes; and b) lakes drain once their volume reaches that sufficient to fill a 2.0 m x 500 m crevasse to the ice sheet base.

The analysis in the next section is broken into four themes, which focus on: i) subglacial water pressure spikes; ii) sustained high pressure events, iii) the effects of lake drainage events on surrounding subglacial pressure fields; and iv) the evolution of subglacial water pressures during the melt season. These themes, together with others,

are continued subsequently in the discussion section (Section 5.5).

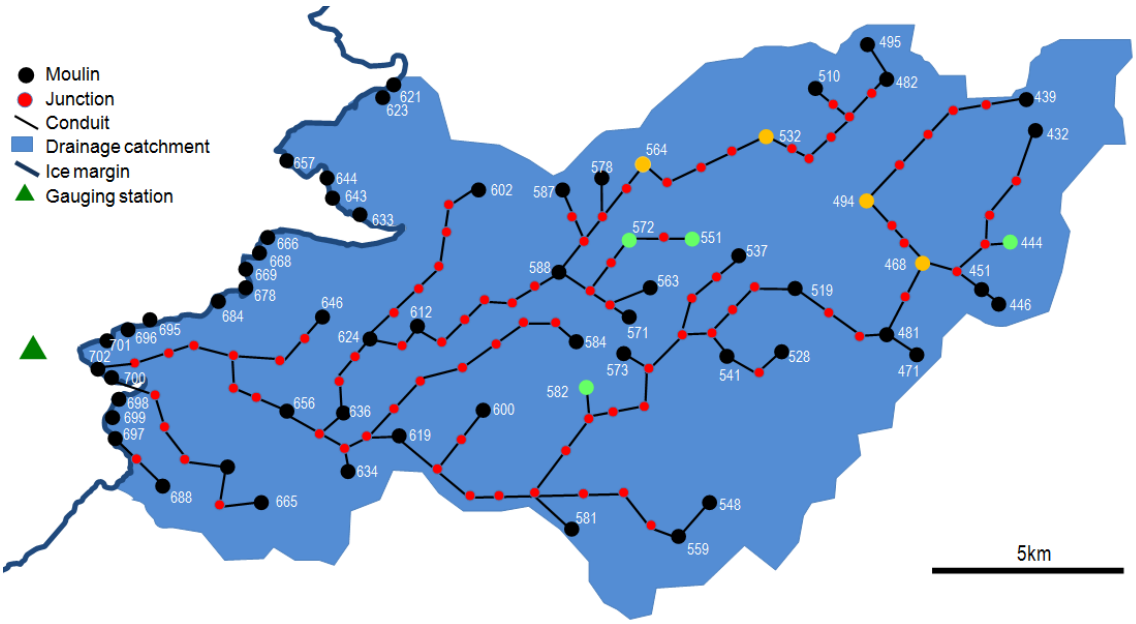

Figure 5.28: Green dots indicate moulins in Figure 5.29 which experience spikes in water pressure. Orange dots indicate moulins in Figure 5.30 which experience sustained periods of high pressure.

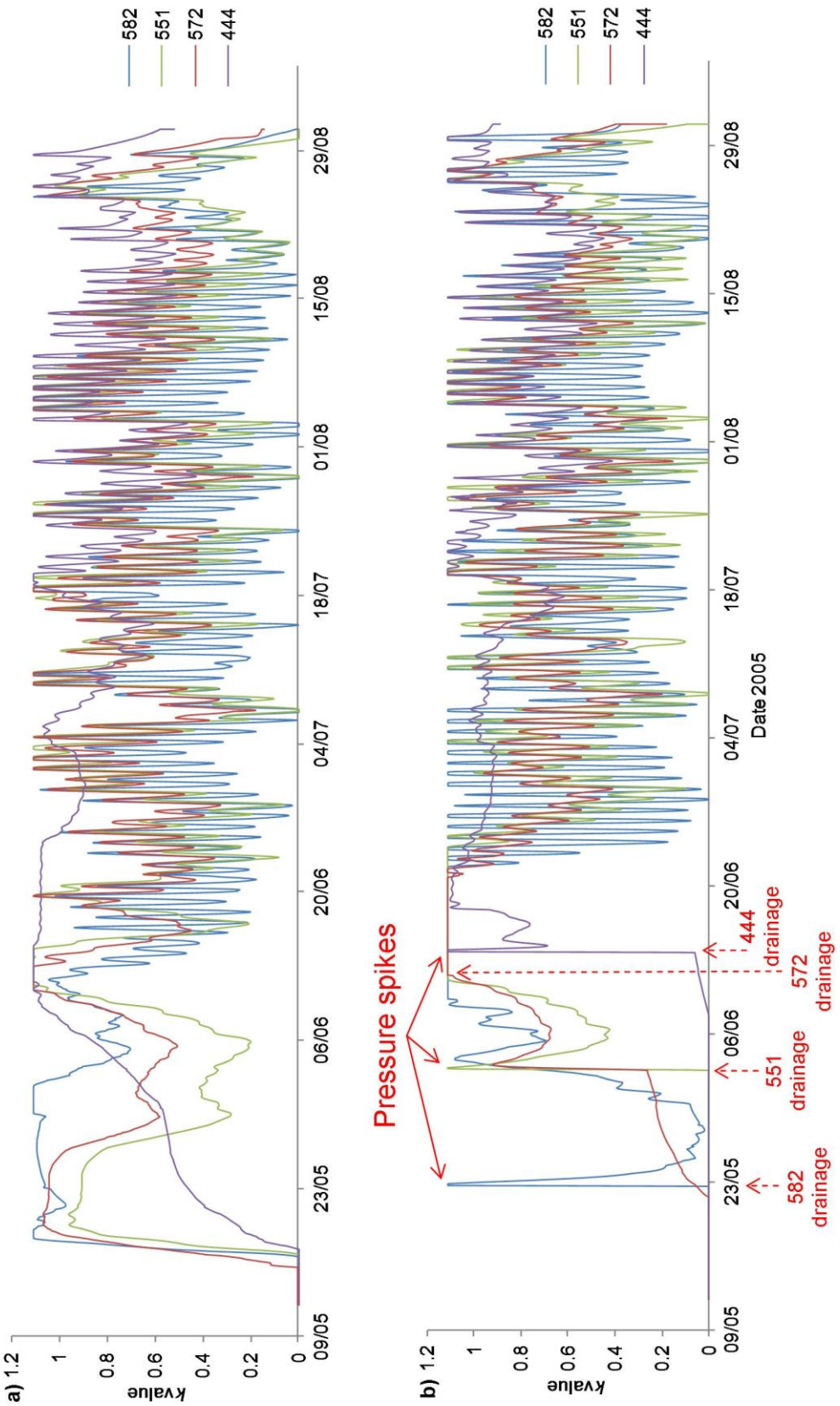

Figure 5.29: Modelled subglacial water pressure for moulins with a spike in water pressure (green dots, Figure 5.28) assuming a) all moulins are 'open'; b) lakes drain once they contain a volume large enough to fill a 2.0 m x 500 m crevasse to the ice sheet bed.

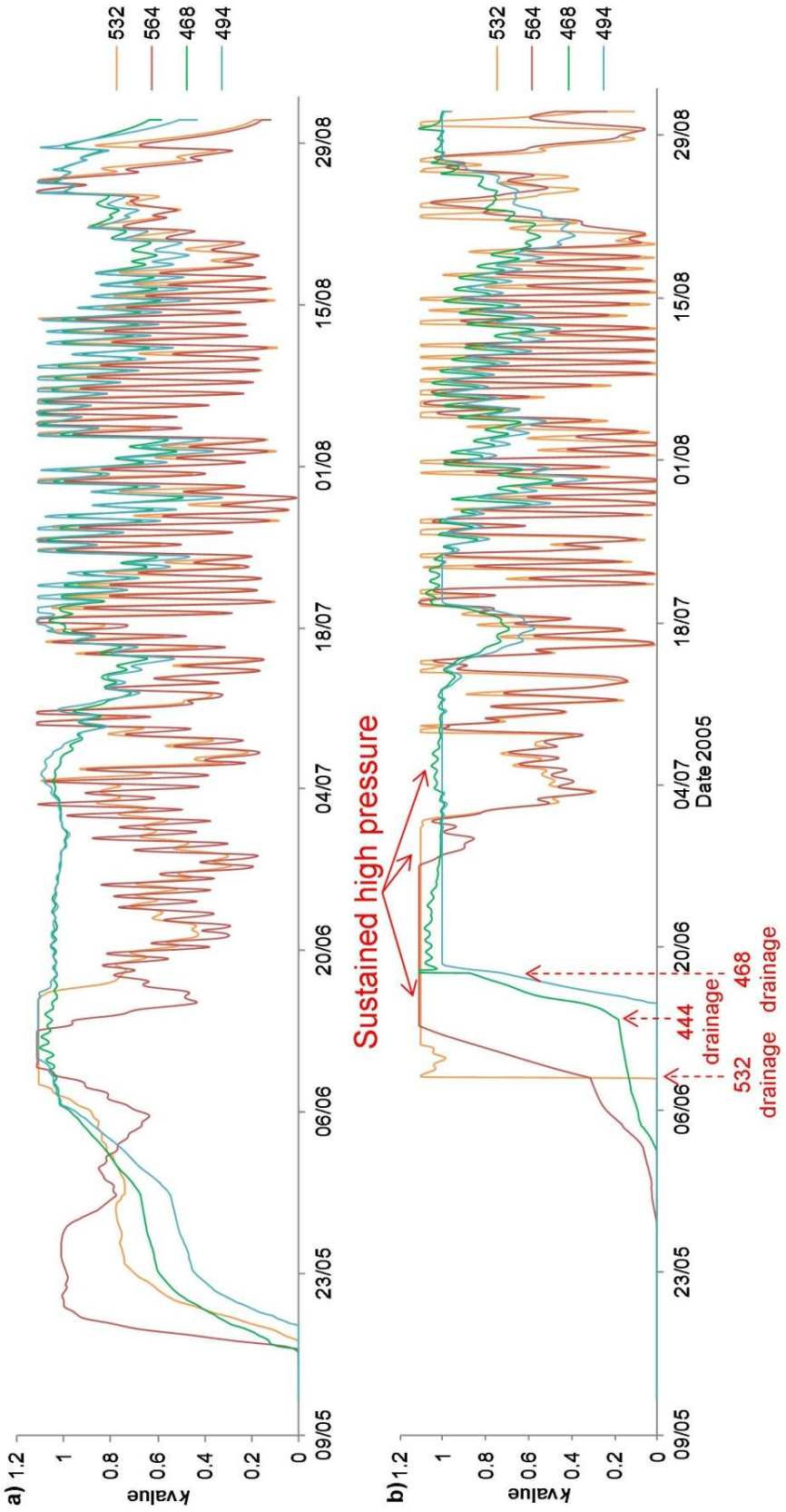

Figure 5.30: Modelled subglacial water pressure for moulins with sustained periods of high pressure (orange dots, Figure 5.28) assuming a) all moulins are 'open'; b) lakes drain once they contain a volume large enough to fill a 2.0 m x 500 m crevasse to the ice sheet bed.

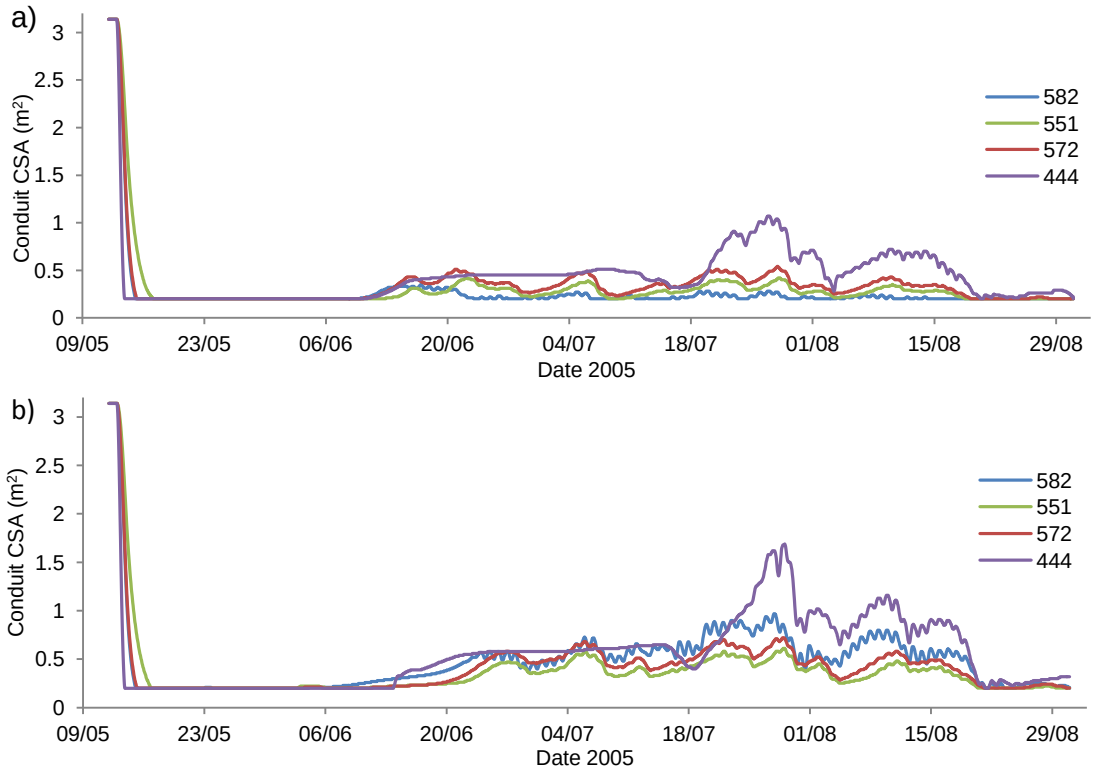

Figure 5.31: Modelled CSAs of conduits directly below the four moulins in Figure 5.29 assuming a) all moulins are 'open'; b) lakes drain once they contain a volume large enough to fill a 2.0 m x 500 m crevasse to the ice sheet bed.

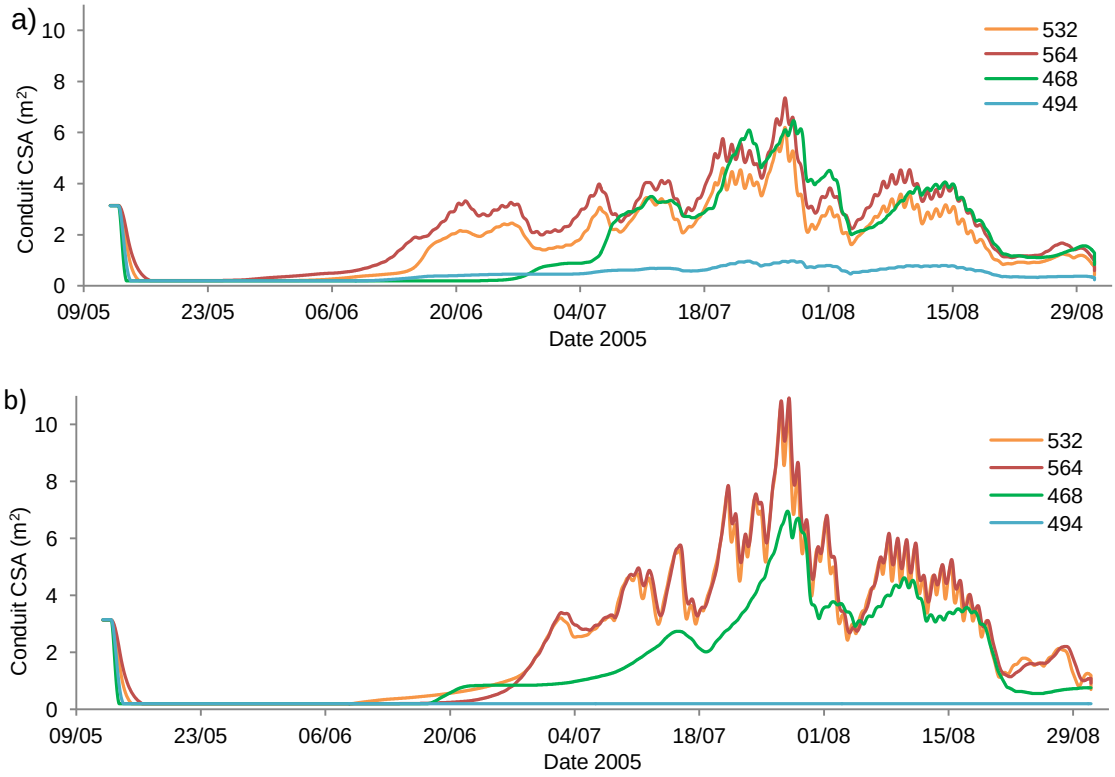

Figure 5.32: Modelled CSAs of conduits directly below the four moulins in Figure 5.30 assuming a) all moulins are 'open'; b) lakes drain once they contain a volume large enough to fill a 2.0 m x 500 m crevasse to the ice sheet bed.

5.4.2.1 Subglacial water pressure spikes

As shown in Figure 5.29, some lake drainage events result in subglacial pressure spikes. These spikes, which are not observed in any of the pressure graphs for the 'open' moulin scenario, are particularly prominent in inland moulins on 'first order pipes' (e.g., moulins 444, 551, and 582, Figures 5.28 and 5.29b) in May and early June when the subglacial drainage system has a relatively low capacity due low or negligible meltwater inflow rates (Figure 5.31b). Thus, rapid inflow of a large volume of water from a lake drainage event causes a rapid increase in subglacial water pressure as the downstream conduit cannot enlarge fast enough to accommodate enough water. For example, as seen in Figure 5.31b, when Lake 582 drains on 21st May, the CSA of the downstream conduit only increases by ~0.03 m^2 from its minimum CSA of 0.2 m^2. In comparison, when the inflow Q in moulins is higher and more variable later in the melt season, a peak conduit CSA of 1.6 m^2 is reached by the conduit downstream of Moulin 444 on 28th July. Early in the melt season, as surface net runoff is low (due to low melt rates and the refreezing of some meltwater in the snowpack) and as surface routing is slow (due to snow cover), surface water inputs to moulins immediately after lakes have drained is also low. Thus, high subglacial water pressures are not sustained, and instead a single pressure spike is observed at the time of lake drainage in the modelled subglacial water pressure series.

5.4.2.2 Sustained high subglacial water pressure events

As shown in Figure 5.30, some lake drainage events which occur between about mid-June and mid-July result in periods of sustained high subglacial pressures in immediate and nearby moulins. For example, following the drainage of Lake 532, periods of sustained high pressure are observed in Moulins 532 and 564 (Figure 5.30b), but such lengthy periods of high pressure are not observed when moulins are assumed to be 'open' (Figure 5.30a). Although conduits up and down glacier from these moulins may still have a relatively low capacity in mid-June due to creep closure earlier in the melt season, they have experienced some enlargement due to wall melting from flowing meltwater that has reached them (Figure 5.32b). When a supraglacial lake drains, a large volume of water is immediately routed to these conduits over a 5 hour period, resulting in dramatic increases in subglacial water pressures (e.g. the drainage of Lake 532 on 8th June, Figure 5.30b), again, due to the fact that the downstream conduit cannot enlarge at a large enough rate. However, as surface runoff is now higher than it

was in early summer (due to greater surface melt rates and less refreezing of meltwater in the snowpack), and as surface routing is faster than it was previously (due to increased ice exposure), these high pressures are more likely to be sustained for a longer period of time than they were earlier in the melt season.

It is noticeable that periods of sustained high pressure are generally experienced by moulins located on the main trunks of arborescent channel network with at least one upglacier 'open' moulin (Figure 5.28). Lengthy periods of sustained pressure are also generally experienced by those moulins which have large supraglacial catchments supplying them with large volumes of meltwater (Figure 5.26). Reasons for these observations will be further discussed in Section 5.5.

It is noticeable, however, that some moulins (e.g. 468 and 494) experience a relatively high (k = ~1.00 – 1.11) for up to a month for both the 'open' and lake filling / drainage scenarios. Thus, it appears that lake drainage is not necessarily a prerequisite for long periods of sustained high water pressures, as it is for the production of pressure spikes. However, in the case of lake drainage events, it is noticeable that the rate of change in water pressure leading up to a period of sustained high pressure is much more rapid (Figure 5.30b) than it is for the 'open' moulin scenario (Figure 5.30a).

5.4.2.3 Effect of lake drainage events on surrounding subglacial pressure fields

Results indicate that lake drainage events may cause concurrent high pressure peaks (near / at ice overburden pressures) up to 5 km from the location of the drained lake, both up and downglacier. For example, of the moulin water pressure series plotted in Figures 5.29 and 5.30, the drainage of Lake 551 also increased water pressures in Moulins 572 (2.5 km downglacier) and 582 (5.0 km downglacier) (Figure 5.29b), the drainage of Lake 572 raised water pressure in Moulin 551 (2.2 km upglacier) (Figure 5.29b), and the drainage of Lake 532 raised water pressure in Moulin 564 (3.0 km downglacier) (Figure 5.30b).

5.4.2.4 Evolution of subglacial water pressures during the melt season

For both the 'open' moulin and lake filling / drainage scenarios (Figures 5.29 and 5.30), there is a transition from relatively high average pressure with low amplitude diurnal cycles to lower average pressure and higher amplitude cycles as the melt season

progresses. In other words, a general increase in the modelled amplitude of diurnal cycles in water pressure is superimposed on a generally declining water pressure trend through the melt season. Similar behaviour concerning average water pressures and their diurnal variability has been observed as a result of borehole water level measurements on Small River Glacier, Canada [*Smart,* 1998] and Haut Glacier d'Arolla, Switzerland [*Gordon et al.,* 1998]. For both the 'open' moulin and lake filling / drainage scenarios (Figures 5.31 and 5.32), a general transition from low CSAs with low amplitude variability to higher CSAs with higher amplitude variability is also observed in most conduits directly below the respective moulins shown in Figures 5.29 and 5.30.

In order to analyze further the transition from high to low average k values, and from low to high diurnal variation in k values, Figures 5.33 and 5.34 show the average water pressure and their average diurnal range for the lake filling / drainage scenario model run (with 2 m wide crevasses), respectively, for each moulin on four dates during the 2005 melt season. On 12th June (Figure 5.33a), the average k value ranges from ~0.6 to ~0.8 for marginal (i.e. the lower 3rd of the catchment) moulins, to ~1.0 to ~1.1 for moulins in the central region (i.e. the middle 3rd of the catchment). However, on 12th June, the average k values for the moulins furthest inland region (i.e. the lower 3rd of the catchment) are < 0.3. This is an artefact of the model, as in reality, these inland regions would be pressurized at this time as the subglacial drainage system would have a low capacity due to low meltwater inflow rates (representative of a distributed system). However as conduits in the model cannot have a diameter < 0.5 m, conduits in these regions are at, or close to, atmospheric pressure in early June. However, by 30th June, enough water has now entered the subglacial system to pressurize it to at or near ice overburden pressures. Over the melt season the average k value for each moulin, in general, decreases. By 8th August (Figure 5.33d), the average k value ranges from ~0.3 to ~0.5 for marginal moulins, to ~0.8 to ~1.0 for inland moulins. An area which is seen to experience the most dramatic decrease in average k value is the central area (e.g. Moulins 563, 571, and 573) which experiences a drop in average k value from ~1.0 on 12th June (Figure 5.33a), to ~0.4 on 8th August (Figure 5.33d). Some moulins (e.g. 584, 602 and 646) have very small k values throughout the melt season (Figure 5.33a), likely because they are at the upstream end of a series of conduits, and also have relatively small supraglacial catchments, and so are not receiving enough water to pressurize them. Again, it is likely that in reality, these moulins would be pressurized

for much of the melt season if meltwater inflow rates, and therefore the system capacity, remained low.

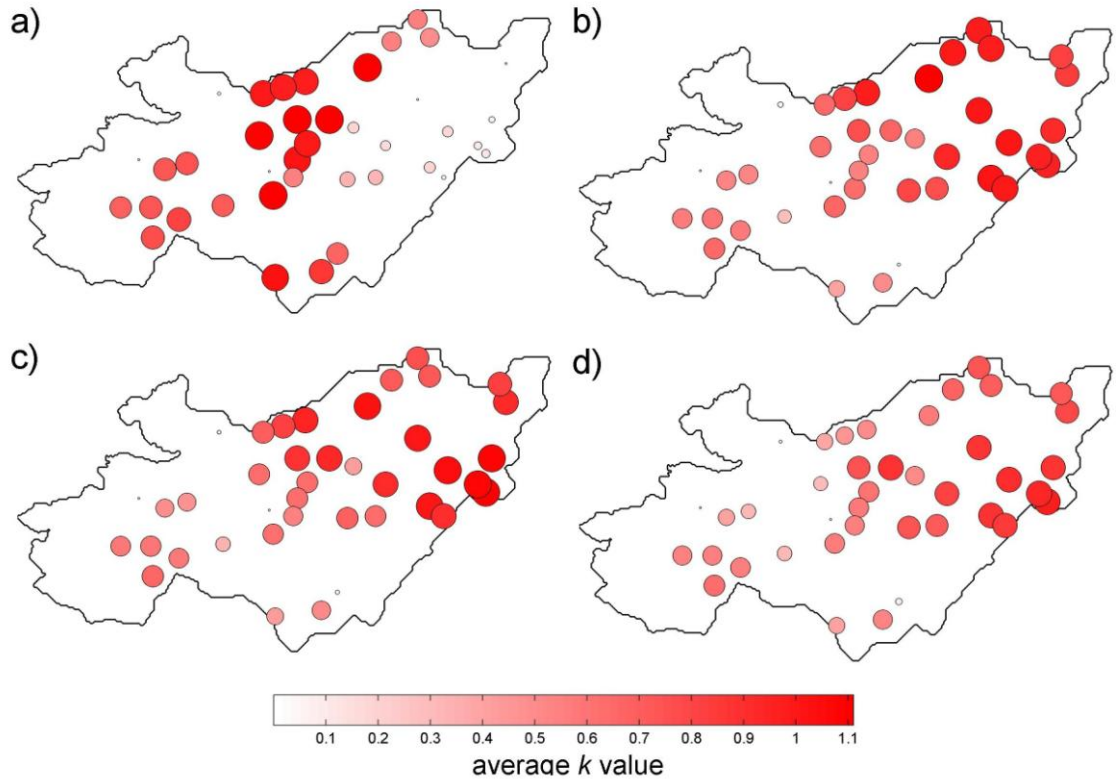

Figure 5.33: Average modelled k values for each moulin (assuming the lake filling / drainage scenario for 2 m wide crevasses) on: a) 12 June; b) 30 June; c) 20 July; and d) 8 August, overlaid onto a map of the subglacial catchment for k = 0.925. k values are given as seven day moving averages. Both size and colour are used to represent the k value.

The average diurnal range in k value on 12th June is low (~0.0 to ~0.3) across the catchment area (Figure 5.34a). The moulins which show the highest average diurnal variability on 12th June are those which are 'open' following an earlier lake drainage event, or those which are close to a lake which has drained. On 30th June, the highest average diurnal ranges in moulin k values are seen in the lower / central regions (Figure 5.34b), on 12th July, the highest average diurnal ranges in k value are seen in the central region (Figure 5.34c), and by 8th August, the highest average diurnal range in k value are seen in the central / upper regions of the catchment (Figure 5.34d).

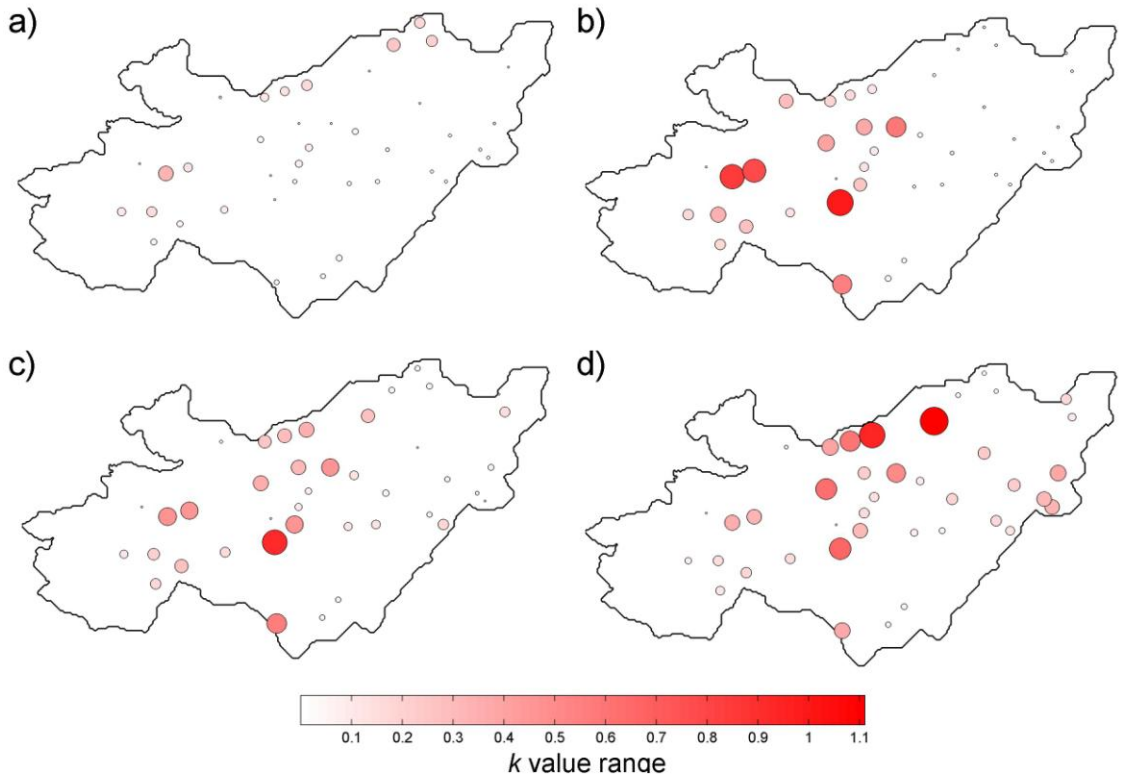

Figure 5.34: Average modelled diurnal ranges in k values for each moulin (assuming the lake filling / drainage scenario for 2 m wide crevasses) on: a) 12 June; b) 30 June; c) 20 July; and d) 8 August, overlaid onto a map of the subglacial catchment for k = 0.925. k values are given as seven day moving averages. Both size and colour are used to represent the k value.

This upglacier transition from high to low average water pressure, and from low to high (then again to low) diurnal range in water pressure over the course of the melt season (Figures 5.33 and 5.34) is indicative of the subglacial drainage system gradually enlarging, thereby becoming more hydraulically efficient over time, and experiencing greater diurnal variability in moulin inputs that are more homogenous between moulins across the entire catchment. The increasing hydraulic efficiency of the system occurs due to an increase in the volume of meltwater inflow. Thus, conduit wall melting increases, their CSAs enlarge (Figures 5.31 and 5.32), their capacity for carrying water increases, and so average water pressures drop and the average dirurnal variability increases. Creep closure rates will increase as a result of the pressure drop, but this is insufficient to offset the melt enlargement. However, once conduit CSAs have undergone a sufficient amount of enlargement, even peak meltwater inflow rates do not cause water pressures to reach ice overburden pressures any longer, thus the average diurnal ranges in k value decrease. As observed in Figures 5.29 to 5.34, this

transition from an inefficient to an efficient system occurs earlier for marginal areas than it does for inland regions. This behaviour is expected as conduits further inland are under thicker ice, giving higher creep closure rates, and inflow Q into inland moulins will be lower than inflow into marginal moulins due to generally lower surface melt rates. Thus, as will be further discussed in Section 5.5, although the model cannot explicitly simulate the transition from a distributed to channelized subglacial drainage system, the modelled behaviour of the drainage system through space and time is analogous to an upglacier transition from a predominantly distributed to predominantly channelized drainage system.

5.5 Discussion

5.5.1 Proglacial discharge

Although not all supraglacial lakes will drain by a fast hydrofracture mechanism (and if they do, they are unlikely to do so in such an idealised way as in this modelling study), but instead may either completely or partially drain by overflowing into a nearby moulin, or may not drain at all [e.g., *Das et al.,* 2008; *Catania and Neumann,* 2010; *Tedesco et al.,* in review], the results in Section 5.5 (Table 5.2) indicate that allowing lakes to fill and then drain once they reach a threshold volume produces a much more realistic match with measured proglacial stream Q than the other two end member scenarios (that is, assuming lakes do not drain at all but instead fill and then overflow into the next catchment downglacier, and assuming that moulins are 'open' at the start of the melt season and able to route meltwater directly from the surface to the subglacial system once meltwater arrives at the moulin). Thus, the model captures a key aspect of the hydrology of the GrIS, i.e. the filling and rapid draining of surface lakes [e.g., *Box and Ski,* 2007; *McMillan et al.,* 2007; *Das et al.,* 2008, *Selmes et al.,* 2011; *Liang et al.,* 2012; *Tedesco et al.*, in review].

The best correlation (RMSE = 25.8 $m^3 s^{-1}$, Nash Sutcliffe coef. = 0.453) between measured and modelled proglacial Q was produced when the lake filling / drainage scenario with 2.0 m wide crevasses was implemented. For this scenario, 10 out of the 44, i.e. 23% of the lakes in the Paakitsoq catchment drained through an idealised hydrofracture mechanism (Figure 5.25b). The proportion of fast draining lakes in this study is only slightly higher than the proportion of fast (< 2 days) draining lakes (263

out of 2038, i.e. 13%) mapped over the entire GrIS by *Selmes et al.* [2011]. This is encouraging given that the drainage mechanism used in this study is simplified, with the timing of drainage scaled by ice thickness and not accounting for important influences such as the weight of water in the lake basin or the local stress regime [*Van der Veen et al.,* 2007; *Krawczynski et al.,* 2009; *Clason et al.,* 2012].

5.5.2 Subglacial water pressure

5.5.2.1 Subglacial water pressure spikes

The inclusion of the lake filling / drainage mechanism in the calculation of moulin input hydrographs not only introduces a lag time between the arrival of meltwater at a moulin and its entrance into the subglacial system, but also increases the variability of Q into the moulin. Consequently, spikes in subglacial water pressure occur following lake drainage events in ~50% of all moulins. In contrast, pressure spikes were not observed in any of the subglacial water pressure series in the 'open' moulin model run. Relatively rapid increases in subglacial pressures were, however, observed in mid-May in the 'open' moulin model run (Figure 5.29a), however these pressure rises were not nearly as rapid as they were in the lake filling / drainage scenario model run and did not necessarily reach ice overburden pressure (Figure 5.29b). This supports one of the key conclusions of the more hypothetical modelling work of *Schoof* [2010], that it is the variability of surface meltwater inputs which has the greatest impact on subglacial water pressures. This is significant as it is rapid increases in subglacial water pressure that is most likely to cause short-term uplift and velocity increases [e.g. *van de Wal et al.,* 2008; *Bartholomew et al.*, 2010; *Pimentel and Flowers*, 2010; *Schoof*; 2012; *Sundal et al.,* 2011].

5.5.2.2 Association of pressure spikes with early melt season short-term velocity speed-ups

It is possible to associate the early melt season modelled spikes in water pressure to short-term (< 24 hours) velocity speed-ups observed on both valley glaciers and the GrIS, which are often associated with a pattern of uplift and subsequent downward movement of the ice surface [e.g., *Iken et al.,* 1983; *Zwally et al.,* 2002; *Mair et al.,* 2003; *Das et al.,* 2008; *Tedesco et al.,* in review; *Bartholomew et al.,* 2012]. Although it is appreciated that the conditions of the simulated subglacial system in this study are not

entirely realistic as the conduits are empty rather than pressurized at the beginning of the model run, the effect of a rapid inflow of water due to a lake drainage event early in the melt season is considered to be similar to the effect which would be observed in reality. For example, the modelled pressure rapidly rises from a pressure which is close to atmospheric pressure, whereas in reality, the pressure would likely rise from a level which is close to ice overburden pressure to a level above ice overburden pressure. The implications for ice dynamics, however, are expected to be similar.

Although evidence suggests that observed short-term speed-ups early in the melt season on the GrIS are the result of lake drainage events [e.g., *Zwally et al.,* 2002; *Das et al.,* 2008; *Tedesco et al.,* in review], observed short-term early season speed-ups on valley glaciers, often known as 'spring events', have often been attributed to the sudden increase in surface meltwater availability that is capable of 'unblocking moulins' and increasing the magnitude and diurnal variability of water into them [e.g., *Iken,* 1981; *Nienow et al.,* 1998; *Mair et al.,* 2003; *Willis et al.,* 2003; *Anderson et al.,* 2004; *Bingham et al.,* 2008]. A key issue of debate is whether short-term speed-ups on the GrIS are possible through a similar process. As modelled spikes in water pressures (which reach ice overburden pressure) in the early part of the melt season are found to be solely caused by lake drainage events in this study (Figure 5.29b) and are not produced when 'open' moulins are present (Figure 5.29a), lake drainage events are considered to be a prerequisite for pressure spikes in the early melt season on the GrIS, and thus possible short-term velocity speed-ups. In contrast to valley glaciers, this finding is likely the case for the GrIS due to its significantly thicker and colder ice. Thus, lake drainage by hydrofracture is required as a mechanism to force a large volume of water rapidly to the bed in order to produce a spike in subglacial water pressure.

In agreement with the observations made by *Hoffman et al.* [2011], single supraglacial lake drainage events in this study were able to produce increases in water pressure over distances of up to ~5 km up and down glacier. Thus, the effect of increased subglacial water pressures on ice velocities may be significant over a large area of the ice sheet bed. This effect, combined with the possible effects of longitudinal coupling [c.f. *Bingham et al.*, 2003; *Price et al.,* 2008; *Bartholomew et al.,* 2012], may lead to a short-term velocity speed-up over an even larger area of the ice sheet.

5.5.2.3 Sustained high pressure events

In some moulins, sustained periods of high subglacial water pressure rather than spikes in subglacial water pressures are observed following lake drainage events (Figure 5.30b). Whilst it might be expected that sustained high pressures following surface to bed connection should not occur as conduits would enlarge through wall melt to accommodate the larger fluxes of water now entering them and water pressures should drop [e.g., *Rothlisberger,* 1972], what occurs in this study is that Qs into moulins keep increasing at such a rate that the conduits cannot enlarge fast enough to reach a steady-state, and therefore fail to show the expected inverse relationship between water pressure and Q for a channelized system [*Spring and Hutter,* 1981; *Kamb*, 1987; *Bartholomew et al.,* 2012]. The result is that periods of sustained water pressures are produced over some areas of the bed.

As previously mentioned in Section 5.4.2, the moulins which experience the longest periods of sustained water pressures are those which are located on the main channels of the drainage system, and / or are those moulins with large supraglacial catchments with a high availability of runoff. This is because once a lake has drained, a sustained inflow of high Q is required in order for pressures to also be sustained. To illustrate this point, two moulins, 532 and 564 (which experience longer periods of sustained high pressure in the lake filling / drainage scenario (Figure 5.30b) than in the 'open' moulin scenario (Figure 5.30a)), are considered (Figure 5.28). As previously mentioned in Section 5.5.1.2, once Lake 532 has drained, meltwater inflow Q to the moulin is high due to its large supraglacial catchment (which includes Lakes 439, 482, 494, 495, and 510) (Figures 5.5 & 5.26a). Thus, following the drainage of Lake 532, although no moulins upstream of 532 are 'open', high water pressure in 532 is sustained. In contrast, although Lake 564 (~4 km downstream from 532) does not drain and therefore cannot receive water supraglacially, it receives a high Q of water subglacially after the drainage of Lake 532 (Figure 5.25b). Therefore, following the drainage of Lake 532, high water pressure is sustained in both 532 and 564, but due to two different mechanisms (Figure 5.30b).

It is interesting that for some moulins (e.g., 468 and 494), subglacial water pressure graphs show periods of sustained pressure for both the 'open' moulin scenario and the lake filling / drainage scenarios (Figure 5.29). This indicates that rapid inflows of water associated with lake drainage events are not a prerequisite for sustained high

pressures, but they may occur simply in response to an increase in magnitude and variability of moulin meltwater input Qs due to the retreat of the snowline. Several previous studies have shown that the retreat of the snowline can result in an increased magnitude and diurnal amplitude of supraglacial recharge rates to moulins, and it has been suggested that it is this process which is important in driving the pressure perturbations necessary to destabilize linked cavities within a distributed system and convert it to a more channelized system, and in the process cause accelerations in ice velocity [e.g., *Nienow et al.,* 1998; *Willis et al.,* 2002; *Bingham et al.,* 2006; *Bartholomew et al.,* 2011a].

5.5.2.4 Association of sustained high pressure events with mid-melt season longer-term speed-ups

It is possible to associate the modelled sustained periods of high pressure from early June to late July with the longer-term (days to weeks) speed-up on the GrIS, often referred to as the 'summer regime' when average summer ice velocities are higher than they are in winter [*Joughin et al.,* 2008; *Van de Wal et al.,* 2008; *Shepherd et al.,* 2009; *Bartholomew et al.,* 2010; *Hoffman et al.,* 2011; *Palmer et al.,* 2011; *Colgan et al.,* 2012]. However, whether lake drainage events are a requirement for longer-term summer speed-up is a subject of debate. *Shepherd et al.* [2009] attribute increased average ice velocities in summer to the drainage of large supraglacial lakes which are thought to result in sustained subglacial water pressures for a few days [*Box and Ski,* 2007]. However, as observed by *Das et al.,* [2008], *Hoffman et al.,* [2011], and *Tedesco et al.,* [in review], lake drainage events appear to have little long lasting effect on ice dynamics with ice velocities returning to values from prior to the event within a day of the lake drainage event. *Hoffman et al.* [2011] also found that less than half of drainages from lakes > 0.5 km in diameter affected summer ice velocity data for western Greenland. Additionally, *Palmer et al.* [2011] showed that the areas of highest summer speed-up were not only highly correlated with the predicted distribution of topographic sinks where supraglacial lakes typically form, but were also highly correlated with areas of high modelled surface runoff and the predicted locations of large scale meltwater channels on the ice sheet surface. Thus, as only 5% of available surface runoff on Russell Glacier, west Greenland, is estimated to be stored in supraglacial lakes [*Shepherd et al.,* 2009], the majority of the remaining 95% of surface melt (which does not refreeze at an intermediate depth, or run off supraglacially from

the ice sheet), is thought to reach the bed through moulins or crevasses and affect ice velocities [*Palmer et al.,* 2011]. While also considering the results of the previous studies mentioned above, as periods of sustained subglacial water pressure in this study are produced in both the 'open' moulin and lake filling / drainage scenarios, it can be concluded that lake drainage events are not a direct requirement for periods of sustained high water pressure which may result in longer-term ice velocity speed-ups.

5.5.2.5 Association of high amplitude diurnal cycles in pressures with mid- to late melt season diurnal velocity variations

Although this and other studies suggest that lake drainage events are not necessarily required in order to produce sustained water pressures, lake drainage events are likely to play a key role in opening up moulins which are subsequently able to rapidly transport large quantities of water from the surface to the ice-bed interface for the remainder of the melt season. Therefore, from the middle of the melt season onwards, if direct routes from the surface to the bed exist (i.e. moulins), if melt rates are high enough, and if the diurnal variability of inflow into moulins is sufficiently large, short-term diurnal variations in velocity are physically plausible [*Pimentel and Flowers*, 2010; *Schoof*, 2010]. Such variations have been observed both on valley glaciers and the GrIS [i.e., *Iken and Bindschadler,* 1986; *Nienow et al.,* 2005; *Bartholomaus et al.,* 2008; *Mair et al*., 2008; *Shepherd et al.* 2009; *Hoffman et al.*, 2011; *Bartholomew et al.,* 2012]. Thus, it is possible to associate the high amplitude diurnal cycles in subglacial water pressure modelled in this study (which periodically reach ice overburden pressures (i.e. k = ~1.11)) from early July onwards for both the 'open' moulin and lake filling / drainage scenarios (Figures 5.29, 5.30, and 5.34), to potential diurnal variations in ice velocity. Therefore, in contrast to the early part of the melt season, in the latter part of the melt season (i.e. from early to mid-July onwards), lake drainage events do not appear to be a requirement for short-term variations in ice velocity assuming that direct routes for meltwater to travel from the surface to the bed have already been created.

5.5.2.6 Evolution of subglacial water pressures during the melt season

Both *Shepherd et al.* [2009] and *Hoffman et al.* [2011] observed that diurnal velocity cycles on the GrIS were superimposed on a gradual deceleration of average night time velocities from the increased velocities of the 'summer regime' earlier in the melt

season. This deceleration is likely due to the subglacial drainage system becoming more efficient through the melt season in response to an increased volume and variability of meltwater inflow. The result is that large volumes of meltwater can rapidly travel through the system without temporally increasing water pressures [*Schoof,* 2010; *Pimentel and Flowers,* 2011]. As previously mentioned in Section 5.5.2, this upglacier transition from a primarily inefficient to primarily efficient subglacial system in this study is inferred from the upglacier transition over the course of the melt season from: i) small to large conduit CSAs; ii) high to low average water pressures; and iii) a low to high diurnal range in water pressure (Figures 5.33 and 5.34). These changes are analogous to changes from 'distributed' to 'channelized' drainage discussed in other studies. As has also been observed in numerous other studies, the upglacier transition follows the gradual increase in runoff availability due to decreased snow cover and thus increased melt rates, decreased storage in the snowpack, and decreased travel times across the ice surface [e.g., *Nienow et al.,* 1998; *Barthomomew et al.,* 2010, 2011b; *Colgan et al.,* 2012]. For the model run with the inclusion of the lake filling / drainage mechanism, the opening of moulins at progressively higher elevations also moderates when and where surface meltwater reaches the bed. Growth of the efficient subglacial system therefore follows upglacier development of supraglacial drainage and proceeds in a stepwise manner as more input points (i.e. moulins) become active [*Nienow et al.,* 1998; *Bartholomew et al.,* 2011a].

As a k value of 0.925 produced a subglacial catchment feeding the ASIAQ gauging station that was of a size that produced the best match between measured proglacial Q and total modelled runoff (Figure 5.8), it might be expected that average subglacial water pressures calculated by the hydrological model should also be close to ice overburden pressure. However, the average modelled k value across the catchment and through the melt season is closer to 0.7. There are several reasons why this average modelled k value is lower than 0.925. First, the model is inherently channelized and does not explicitly calculate water pressures in a distributed system which, in reality, likely surrounds the subglacial channels [c.f. *Hubbard et al.,* 1995]. An inverse relationship between steady-state (long-term average) Q and water pressure is expected in channels so that as discharge increases during the summer, the water pressure drops [*Rothlisberger,* 1972; *Spring and Hutter,* 1981]. However, water pressure would be expected to remain high throughout the summer in a distributed

system. Thus, by modelling the channelized part of the drainage system, the water pressure calculations are biased towards the lower end of the spectrum. Second, conduits have a minimum CSA of 0.5 m^2, and thus they cannot close down completely, increasing water pressures to overburden. Instead, water pressures in the modelled channels remain artificially low, and even drop to atmospheric, when long-term average discharges are low. This will also bias the water pressure calculations to lower values. Thus, it is clear from this study that while it might be possible to define an 'average' k value for an entire catchment through an entire melt season, in reality there will be places and times where values are above and others where values are below this average. In particular, results indicate a general upglacier transition from a prominently high pressure to elements with gradually decreasing pressure through the melt season.

5.5.2.7 Relation to marine-terminating glaciers

As discussed in Chapter 2 (Section 2.1.3.2), in addition to increased lubrication at the bed due to surface melt, the thinning rates of marine-terminating glaciers are also effected by various factors which influence the rate of calving at the glacier front. These include: i) the breakup of the seasonal ice mélange [*Joughin et al.,* 2008b; *Amundson et al.,* 2010]; ii) the un-grounding of ice near the terminus [*Luckman et al.,* 2006; *Howat et al.,* 2007; *Nick et al.,* 2009]; and iii) the submarine melting of calving faces and ice shelves [*Rignot et al.,* 2010; *Straneo et al.,* 2010]. These processes will likely become more effective in years to come if ocean temperatures continue to increase [e.g. *Holland et al.,* 2008; *Seale et al.,* 2011]. Thus, although all of the phenomena modelled and discussed earlier in this chapter (i.e., spikes in water pressures, sustained water pressures, diurnal short-term pressure increases, and the evolution of the drainage system through the melt season) will also apply to marine-terminating glaciers, this group of glaciers will also be highly influenced by changes at the calving front. Therefore, for marine-terminating glaciers, varying ice velocities in response to varying surface melt rates and lake drainage events may be masked to a certain degree. However, with the exception of bed lubrication by surface melt, all of these processes will only operate if the outlet glacier terminates in a body of relatively deep water. Thus, as these processes will shut down once the margin retreats onto bedrock above sea level, or above the level of deep proglacial lakes, marine-terminating may ultimately only be affected by the dynamical effect of increased surface meltwater accessing the bed.

5.6 Summary and conclusions

This chapter has focused on the application of a physically based, time-dependent, distributed subglacial routing model to the Paakitsoq region for the melt season of 2005. The model was driven using moulin input hydrographs calculated by the SRLF model (Chapter 4) (which was forced with the distributed runoff calculated by the SMB model (Chapter 3)) for various lake filling / drainage scenarios. The model was evaluated by comparing the modeled proglacial Q with that measured at the ASAIQ gauging station. Spatially and temporally varying subglacial water pressures were subsequently analyzed. The main findings are summarized below.

- Comparison of total modelled net runoff over the supraglacial catchment feeding the gauging station with the total measured proglacial Q at the gauging station indicated that a k value of 0.925 was most appropriate. k = 0.925 was thus used to determine the size and shape of the subglacial catchment feeding the ASIAQ gauging station in order to predict paths of subglacial conduits by upstream area analysis using *Shreve's* [1972] formulation combined with the LCIA.

- The best correlation (RMSE = 25.8 $m^3 s^{-1}$, Nash Sutcliffe coef. = 0.453) between measured and modelled proglacial Q was produced when surface lakes were able to drain if their volume became equal to that of a 2 m wide, 500 m long crevasse to the base of the ice sheet. From this, it was inferred that allowing lakes to fill then drain is more realistic than simply assuming that all moulins are permanently 'closed' or 'open'.

- A general upglacier transition from relatively high average pressure in moulins with low amplitude diurnal cycles (i.e. an inefficient system) to lower average pressure in moulins and higher (then subsequently lower) amplitude cycles (i.e. an efficient system) through the melt season was observed. This transition was inferred to be analogous with the upglacier transition from a predominantly distributed, to predominantly channelized, subglacial drainage system due to an increase the magnitude and variability of meltwater inputs to moulins.

- Patterns and characteristics of modelled water pressure through the melt season were associated with observed changes in ice velocity through the melt season. For example, the spikes in subglacial water pressure resulting from supraglacial lake

drainage events which occurred early in the melt season were associated with periods of observed short-term (< 24 hours) speed-up on the GrIS [e.g., *Das et al.,* 2008; *Tedesco et al.,* in review]. In contrast, during the middle period of the melt season some moulins experienced periods of sustained water pressure which were not necessarily a direct result of lake drainage events. These periods of sustained high pressure were associated with observed periods of longer-term (days to weeks) summer speed-up [e.g., *Bartholomew et al.,* 2010; *Hoffman et al.,* 2011; *Palmer et al.,* 2011]. The modelled high amplitude diurnal cycles in water pressure superimposed on a generally declining water pressure trend from mid- to late melt season were associated with observed diurnal cycles in velocity on the GrIS, superimposed on a gradual deceleration from the observed longer-term speed-up earlier in the melt season [*Shepherd et al.,* 2009; *Hoffman et al.,* 2011; *Bartholomew et al.,* 2012]. Thus, although it was found that supraglacial lake drainage events were not required to produce either sustained water pressures, or diurnal cycles in water pressures in the latter part of the melt season, lake drainage events were required in order to produce very short-term spikes in water pressure, and to open up moulins which then act as direct, rapid routes for surface meltwater to reach the ice sheet bed for the remainder of the melt season.

6. Conclusions

The aim of this thesis was to develop a high spatial (100 m) and temporal (1 hour) resolution, physically based, time-dependent hydrological model and apply it to the ~2,300 km^2 Paakitsoq region, western Greenland, and drive it, calibrate it, and evaluate it using real data. This study was motivated by a need to better understand how the subglacial hydrological system of the GrIS evolves in space and time in response to varying surface water inputs due to melt and lake drainage events. Of key interest were the modelled spatially and temporally varying water pressures which were required to help explain patterns of surface velocity and uplift found by recent field-based geophysical studies [e.g., *Zwally et al.,* 2002; *Das et al.,* 2008; *Bartholomew et al.,* 2010; 2011; 2012; *Hoffman et al.,* 2011; *Tedesco et al.,* in review]. This was important, as prior to this study, modelling studies that had attempted to incorporate hydrological theory into a time-dependent modelling framework to investigate specific attributes of ice sheet hydrological behaviour had been few, and largely small-scale, hypothetical and idealised [e.g., *Pimentel and Flowers,* 2010; *Schoof,* 2010; *Bartholomew et al.,* 2012]. There had been little attempt to explain patterns of ice velocity and uplift through a physically based, time-dependent, distributed, hydrological modelling approach applied to a real situation on the GrIS.

6.1 Achievement of research objectives

In Chapter 1, three research objectives were outlined, one for each key component of the complete ice sheet hydrology model. A summary of how each of these objectives was achieved and the main findings in each case are outlined below.

- **Develop and apply a SMB model to the Paakitsoq region** (Chapter 3)

The objective of the SMB modelling was to calculate hourly runoff for each grid cell to feed into the SRLF model (discussed in Chapter 4). By adjusting key parameter values to minimize the error between modelled output and measured surface height and albedo measurements from the three GC-Net weather stations, JAR 2, JAR 1, and

Swiss Camp, model calibration showed that the same set of optimal key parameters (fresh snow density (400 kg m^{-3}); elevation-dependent precipitation gradient (14% increase per 100 m); and threshold temperature for solid / liquid precipitation (2 °C)) were appropriate for both 2000/01 and 2004/05. The first stage of model evaluation, involving the comparison of modelled snowline position with that delineated from Landsat imagery, showed that the average percentage of mismatched grid cells for 2000/01 and 2004/05 were relatively low at 9.6% and 12.1% respectively. The second stage of model evaluation, involving the comparison modelled albedo with that retrieved from the MODIS sensor MOD10A1 product, showed that although there was generally a good correspondence between gridded modelled albedo and MODIS-derived snow albedo, the model tended to overestimate (underestimate) albedo values at the higher (lower) end of the range compared to MODIS values.

Through the calculation of the average seasonal cycles of the SEB components, the net shortwave flux was found to be the dominant factor governing surface melt variability in the ablation area, whereas the net longwave flux was the main energy loss. The spatial variability in annual net mass balance, runoff, accumulation, and refreezing across the model domain was evaluated, and from this, it was calculated that 6% of all meltwater and rainwater at the surface refroze in the snowpack and did not become runoff; refreezing accounted for 31% of the average net accumulation.

- **Develop and apply a surface water routing and lake filling (SRLF) model to a subset of the Paakitsoq region** (Chapter 4)

The objective of the SRLF modelling was to calculate moulin input hydrographs to feed into the subglacial routing model (discussed in Chapter 5). The SRLF model took the time-series of runoff calculated by the SMB model over the area and calculated flow paths and water velocities over the snow / ice covered surface, routing the water into topographic depressions which either contained an existing moulin (at the deepest part of the depression), or could fill to form lakes. The model was calibrated against field measurements of a filling lake in the study area during June 2011 and was able to calculate the filling rate of the instrumented lake with a high-degree of accuracy. Importantly, the filling rate of the instrumented / modelled lake was found to depend on melt and water routing from both the immediate lake catchment and from overflowing lakes in upstream catchments.

- **Develop and apply a subglacial routing model to the Paakitsoq region** (Chapter 5)

The objective of the subglacial routing modelling was to route water from the base of moulins through a defined subglacial drainage system to the proglacial outflow point. The model was driven using moulin input hydrographs calculated by the SRLF model (from Chapter 4) (which was forced with the distributed runoff calculated by the SMB model (from Chapter 3)) for various lake filling / drainage scenarios. For one such scenario, supraglacial lakes were able to drain by a simulated hydrofracture mechanism if they reached a critical volume. When the model was evaluated by comparing the modeled proglacial Q with that measured at the ASAIQ gauging station, the best correlation between measured and modelled proglacial Q was produced when surface lakes were able to drain if their volume became equal to that of a 2 m wide, 500 m long, crevasse to the base of the ice sheet. From this, it can be inferred that allowing lakes to fill then drain is more realistic than simply assuming that all moulins are 'open'.

A general upglacier transition from narrow conduits with water at high average pressures with low amplitude diurnal cycles (i.e. an inefficient system), to wider conduits with lower average water pressures and higher (and then subsequently lower) amplitude cycles (i.e. an efficient system) through the melt season, was observed. This transition was thought to be analogous to the frequently observed upglacier transition from a predominantly distributed to predominantly channelized subglacial drainage system due to an increase the magnitude and variability of meltwater inputs to moulins through a melt season [e.g., *Nienow et al.,* 1998; *Barthomomew et al.,* 2010, 2011b; *Colgan et al.,* 2012].

The patterns and characteristics of modelled water pressures through the melt season were found to vary in a manner consistent with seasonal velocity observations made by others. For example, supraglacial lake drainage events which occurred early in the melt season (early May to mid-June), and were found to result in spikes in subglacial water pressures in ~50% of cases, were linked with short-term (< 24 hours) speed-ups which have often been observed on the GrIS [*Zwally et al.,* 2002; *Das et al.,* 2008; *Tedesco et al.,* in review]. In contrast, later in the melt season (mid-June to mid-July), some moulins experienced periods of sustained water pressure which were not necessarily a direct result of lake drainage events. These periods of sustained high

pressure were associated with periods of longer-term (days to weeks) summer increases in ice velocities which are frequently observed on the GrIS [e.g., *Shepherd et al.,* 2009; *Bartholomew et al.,* 2010; *Hoffman et al.,* 2011; *Palmer et al.,* 2011]. The modelled high amplitude diurnal cycles in water pressure superimposed on a generally declining water pressure trend from mid- to late melt season were associated with observed diurnal cycles in velocity, superimposed on a gradual deceleration from the observed longer-term speed-up earlier in the melt season [*Shepherd et al.,* 2009; *Hoffman et al.,* 2011; *Bartholomew et al.,* 2012].

6.2 Synthesis of conclusions

As mentioned above, an important finding of this study was that although rapid lake drainage events were required to create short-term (< 24 hours) spikes in water pressures on the GrIS, lake drainage events were not required for the production of longer-term (days to weeks) sustained water pressures, assuming that 'open' moulins were present, and able to transport rapidly large volumes of surface runoff to the base of the ice sheet. This supports inferences drawn on the basis of analysis of data collected in a few recent field-based geophysical studies, that the direct inflow of runoff into moulins may be more important for the seasonal velocity response of the GrIS than supraglacial lake drainage events [*Palmer et al.,* 2009; *Hoffman et al.,* 2011; *Bartholomew et al.,* 2012].

Results of this study have indicated that periods of sustained subglacial water pressure are generally produced in moulins located on the main trunks of the arborescent channel network with at least one upstream 'open' moulin, and / or in moulins located in the upper branches of the network, where the moulin is fed by a large supraglacial catchment delivering a high volume of runoff. Thus, in agreement with *Palmer at al.* [2011], this study supports the suggestion that the areas of the ice sheet likely to experience the longest periods of summer speed-up are those which not only have a high density of topographic sinks where supraglacial lakes (and often moulins) typically form, but also have a high availability of surface runoff with large-scale supraglacial meltwater channel networks. This is because, although the rapid drainage of supraglacial lakes is initially required to create moulins which are able to rapidly route surface runoff to the bed for the remainder of the melt season, a large supply of surface runoff is also required to produce sustained high water pressures.

If surface melt rates on the GrIS continue to increase, enabling supraglacial lakes to drain earlier in the melt season and higher up on the ice sheet [*Selmes et al.,* 2011; *Liang et al.,* 2012], more moulins are likely to be present for a longer time period to rapidly transport diurnally varying surface runoff to the bed [*Catania and Neumann,* 2010]. Therefore, as the climate warms, one possible scenario is that the effect of sustained water pressures promoting high ice velocities will be significant for a longer time period and over a larger proportion of the bed; the result will be an increase in the rate of ice loss from the ice sheet.

However, as briefly discussed in Chapter 1, a key question is how the GrIS subglacial hydrological system will evolve over decadal and longer timescales in response to increased surface melt. If the hydrological system of the GrIS behaves like that of a valley glacier, it has been argued that increased surface melting will lead to a reduction in summer ice velocities in the GrIS compared with the present [e.g. *van de Wal et al.,* 2008; *Bartholomew et al.,* 2010; *Sundal et al.,* 2011]. It is thought that the transition from a predominantly inefficient drainage system to a channelized one is crucial in reducing the impact of high meltwater availability on ice velocity. If this transition occurs earlier during the melt season it may reduce the time period over which high water pressures (and therefore ice velocities) can occur [e.g., *Joughin et al.,* 2008; *van de Wal et al.,* 2008; *Schoof,* 2010; *Pimentel and Flowers*, 2011; *Sundal et al.,* 2011]. For example, *Sundal et al.* [2011] found that the period of ice speed-up in warmer years for a land-terminating marginal area in south west Greenland was three times shorter than in cooler years, and, overall, summer ice velocities were slower within their study region.

However, there are two alternative scenarios for how water pressures (and thus ice velocities) are likely to respond to increased surface melt in land-terminating regions of the GrIS. The first is that is that if, during warmer melt years, a region further inland of the *Sundal et al.* [2011] study region is considered, where the subglacial system is still predominantly inefficient (i.e. distributed), and where lakes are likely to be filling and draining earlier than they would in cooler years, an increase in average summer velocities may be expected. Therefore, as the climate of Greenland warms, it might be expected that the region of the ice sheet which has a predominantly distributed subglacial drainage system for the majority of the melt season, and so is therefore likely to experience the highest subglacial water pressures and thus the largest

increase in average ice velocities, will migrate inland on an annual basis. As a result, ice further inland may be transported to lower elevations where, if it enters the ablation zone, it will experience higher surface melt rates, and thus higher rates of surface runoff and net mass loss. The net effect may be an increase in the rate of mass loss to the ocean.

In contrast to the scenario discussed above, the other possible scenario is that although increased surface melting is likely to lead to decreased ice velocities if steady-state theory is considered, it is unlikely that steady-state conditions ever actually exist in reality [*Rothlisberger,* 1972]. This is because although subglacial conduits may be able to adjust in size to accommodate variations in meltwater discharge over a timescale of days or more [e.g. *Rothlisberger,* 1972; *Cutler,* 1998; *Schoof,* 2010], the rate of delivery to the subglacial system can vary over much shorter timescales. Therefore, as shown and discussed in Chapter 5 (Sections 5.5.2.1 and 5.5.2.3), as conduits cannot enlarge at a fast enough rate to maintain a steady-state, water is accommodated in the system by either temporary spikes in pressure, or longer-term sustained periods of high pressure, depending on the timescale over which, and rate at which, meltwater inflow rates change. Not only did this study model spikes in pressure in the early melt season when the drainage system was of a relatively small capacity, but sustained periods of high pressure and diurnal spikes in pressure were also produced from mid- to late melt season when the system was more efficient.

Thus, the results of this study are in agreement with others that the temporary imbalance between the rate of water delivery to the subglacial drainage system and its ability to transmit and evacuate that water is accommodated by temporary spikes in subglacial water pressure even when the drainage system has become more efficient [*Roslisberger and Lang,* 1987; *Schoof,* 2010; *Bartholomew et al.,* 2012]. This study also suggests that if this imbalance continues for a period of days to weeks, a sustained period of high water pressure, rather than a spike, may be produced, even if the drainage system is relatively efficient. Using this logic, it is possible that the increased summer ice velocities on the GrIS occur because over-pressurized conditions are common on the rising limbs of meltwater inflow hydrographs into the subglacial system, regardless of the structure of the subglacial system, as the system is continuously given larger quantities of water than it was before [*Bartholomew et al.,* 2012]. The late melt season reduction in ice velocities would therefore be due to a

decline or stabilization of water input, which would allow the system to accommodate water at lower pressures. Thus, although the development of an efficient subglacial drainage system would be a prerequisite for late season reduction in ice velocities, it is not sufficient to cause a reduction in subglacial water pressure without a reduction in meltwater input relative to the capacity of the system [*Bartholomew et al.,* 2012]. Therefore, if the magnitude and variability of meltwater input into moulins were to remain high through the majority of the melt season, despite an earlier switch from a predominantly distributed to channelized system, average ice velocities are likely to stay high for the majority of the melt season. Thus, given this scenario, if average air temperatures over the GrIS continue to increase, an increase in summer ice velocities would also be expected.

In summary, whether average ice velocities on the GrIS are likely to accelerate or decelerate in response to increased melt rates is likely to depend strongly on the links and feedbacks between the rate at which the subglacial drainage system can adjust to accommodate discharge at lower pressures, and the variably and magnitude of the inflow into the drainage system.

6.3 Future research directions

This thesis has highlighted some key ideas for future research. These are briefly discussed below:

- As previously discussed in Chapter 5, the subglacial hydrology model cannot explicitly simulate the transition from a distributed to channelized subglacial drainage system, although the modelled behaviour of the drainage system through space and time is analogous to an upglacier transition from a predominantly distributed to predominantly channelized drainage system. Thus, an improvement to the current model would be to include a more physically based representation of a distributed system, including the interaction of channelized and distributed components, and the evolution of a predominantly distributed system to a predominantly channelized system and back again in response meltwater inflow variability throughout the melt season.

- Although links and feedbacks between subglacial water pressures and basal

sliding are a key aspect of the behaviour of real glacier hydrological systems (see Chapter 2, Section 2.2.3), the modelling approach used in this study does not explicitly account for this process. Additionally, although the ice sheet surface is assumed to be static in this study, a time-dependent, evolving, surface, in response to changes in the 3-D stress regime induced by changes in basal sliding, would be more realistic. Thus, a future modelling challenge should focus on coupling the existing melt / hydrology model to a high-resolution ice flow model. The key output from such a model would be spatially and temporally varying patterns of the 3-D ice velocity and strain fields in response to varying subglacial water pressures. In the first instance this combined melt/hydrology/ice flow model could be applied to the Paakitsoq region and could be tested against previously observed changes in the ice sheet surface velocity field derived from differential Global Positioning Systems (dGPS) deployed on the ice, as well as from satellite based Interferometric Synthetic Aperture Radar (InSAR) and feature tracking data. Then, once it is calibrated for this area, it could be upscaled and applied to other parts of the GrIS, or ultimately the entire GrIS to improve predictions of future sea level rise.

6.4 Summary

This thesis has successfully developed a high spatial and temporal resolution, physically based, time-dependent hydrological model and applied it to the Paakitsoq region of western Greenland. When evaluated against observed measurements, the model was able to calculate spatially and temporally varying melt and runoff, the surface routing of water and the filling of lakes, and the proglacial discharge to a high degree of accuracy. Of key importance were the patterns and characteristics of the calculated subglacial water pressures which were the found to show strong similarities with, and to help explain, patterns of surface velocity and uplift found by recent field-based geophysical studies. A key question is whether average annual ice velocities for land-terminating regions of the GrIS are likely to increase or decrease in response to increasing rates of surface melt as the climate warms. The answer to this is likely to depend strongly on the balance between the rate at which the subglacial drainage system is able to adjust to accommodate and evacuate discharge at lower pressures, and the variability and magnitude of the inflow of water into the drainage system. In order to produce a more quantitative answer to this question, future modelling

challenges should focus on developing a coupled melt / hydrology / ice flow model which would be used to investigate how future increases in surface melt magnitude and extent in response to various scenarios of regional climate change will impact on the flow, geometry, and, importantly, the mass balance of the entire ice sheet. This is of key importance in order to determine the time-dependent sensitivity and response of the ice sheet's dynamics to an increasingly warmer climate, and thus improve the IPCC's predictions of future sea level rise.

Bibliography

Abdalati, W. and K. Steffen (1997), Snowmelt on the Greenland ice sheet as derived from passive microwave satellite data. *J. Climate,* 10, 165–175.

Abdalati, W. and K. Steffen (2001), Greenland ice sheet melt extent: 1979-1999, *J. Geophys. Res.,* 106(24), 33983-33988.

Abdalati, W., W. Krabill, E. Frederick, S. Manizade, C. Martin, J. Sonntag, R. Swift, R. Thomas, W. Wright, and J. Yungel (2001), Outlet glacier and margin elevation changes: Near-coastal thinning of the Greenland ice sheet, *J. Geophys. Res.*, 106(D24), 33,729–33,741, doi:10.1029/2001JD900192.

Ahlmann, W. (1948), Glaciological research on the North Atlantic coasts, Royal Geographical Society, Research Series 1, London.

Ahlström, A. P., J. J. Mohr, N. Reeh, E. L. Christensen and R. LeB. Hooke (2005), Controls on the basal water pressure in subglacial channels near the margin of the Greenland ice sheet. *J. Glaciol., 51*(174), 443-449

Ahlstrøm, A. P. (2007), Previous glaciological activities related to hydropower at Paakitsoq, Ilulissat, West Greenland. *Danmarks og Grønlands Geologiske Undersøgelse Rapport 2007/25*

Ahlstrøm, A., R. Mottram, C. Nielsen, N. Reeh, and S. B. Andersen (2008), Evaluation of the future hydropower potential at Paakitsoq, Ilulissat, West Greenland, in *Danmarks og Grønlands Geologiske Undersøgelse Rapport*, vol. 37, p. 50, GEUS, København.

Alley, R. B., P. U. Clark, P. Huybrechts and I. Joughin (2005), Ice sheet and sea-level changes, *Science*, 310, 456–460. doi: 10.1126/science.1114613

Alley, R.B., J. T. Andrews, J. Brigham-Grette, G. K. C. Clarke, K. M. Cuffey, J. L. Fitzpatrick, S. Funder, S. J. Marshall, G. H. Miller, J. S. Mitrovica, D. R. Muhs, B. L. Otto-Bliesner L. Polyak, and J. W. C White (2010), History of the Greenland Ice Sheet:

paleoclimatic insights. *Quat. Sci. Rev.*, 29, 1728-1756. doi:10.1016/j.quascirev.2010.02.007.

AMAP. The Greenland Ice Sheet in a changing climate: Snow, Water, Ice and Permafrost in the Arctic (SWIPA). (2009), D. Dahl-Jensen, J. Bamber, C.E. Boggild, E. Buch, J.H. Christensen, K. Dethloff, M. Fahnestock, S. Marshall, M. Rosing, K. Steffen, R. Thomas, M. Truffer, M. van den Broeke and C. J. van der Veen. *Arctic Monitoring and Assessment Programme (AMAP),* Oslo, 115pp.

Ambach, W. (1977), Untersuchungen zum Energieumsatz in der Akkumulationszone des Gronlandischen Inlandeises, Meddelelser om Grønland 187–7, Bianco Lunos Bogtrykkeri A/S, Copenhagen.

Amundson, J., M. Fahnestock, M. Truffer, J. Brown, M. Luthi, and R. Motyka (2010), Ice melange dynamics and implications for terminus stability, Jakobshavn Isbrae, Greenland, *J. Geophys. Res.,* 115, F01005, doi:10.1029/2009JF001405

Anderson, D. E, (1997), Younger Dryas research and its implications for understanding abrupt climatic change, Prog. Phys. Geog, 21:230-249, doi:10.1177/030913339702100203.

Anderson, R., S. Anderson, K. MacGregor, E. Waddington, S. O'Neel, C. Riihimaki, and M. Loso (2004), Strong feedbacks between hydrology and sliding of a small alpine glacier, *J. Geophys. Res.,* 109, F03005, doi:10.1029/2004JF000120.

Andreasen, J. O. (1985), Seasonal surface-velocity variations on a sub-polar glacier in West Greenland. *J. Glaciol.,* 31, 319–323.

Arnold, N., I. C. Willis, M. J. Sharp, K. S. Richards, and W. J. Lawson (1996), A distributed surface energy balance model for a small valley glacier. Development and testing for Haut Glacier d'Arolla, Valais, Switzerland, *J. Glaciol.,* 42, 77-89.

Arnold, N., K. Richards, I. Willis, and M. Sharp (1998), Initial results from a distributed, physically based model of glacier hydrology. *Hydrol. Process.,* 12, 191-219.

Arnold, N. S., and W. G. Rees (2003), Self-similarity in glacier surface characteristics, *J. Glaciol. 49*(167), 547-554, doi: 510.3189/172756503781830368.

Arnold, N. (2005), Investigating the sensitivity of glacier mass-balance/elevation profiles to changing meteorological conditions: Model experiments for Haut Glacier d'Arolla,

Valais, Switzerland, *Arc. Ant. & Alp. Res.,* 37 (2), 139-145.

Arnold, N. S., W. G. Rees, A. J. Hodson, and J. Kohler (2006), Topographic controls on the surface energy balance of a high Arctic valley glacier, *J. Geophys. Res.*, *111*(F2), F02011, doi: 02010.01029/02005JF000426.

Arnold, N., and G. Rees (2009), Effects of digital elevation model spatial resolution on distributed calculations of solar radiation loading on a High Arctic glacier. *J. Glaciol.* 55(194) 973-984. doi:10.3189/002214309790794959

Arnold, N.S. (2010), A new approach for dealing with depressions in digital elevation models when calculating flow accumulation values. *Progress in Physical Geography*. 34(6), 781-809. doi:10.1177/0309133310384542.

Bales, R. C., Q. Guo, D. Shen, J. R. McConnell, G. Du, J. F. Burkhart, V. B. Spikes, E. Hanna, and J. Cappelen. (2009), Annual accumulation for Greenland updated using ice core data developed during 2000– 2006 and analysis of daily coastal meteorological data, *J. Geophys. Res.,* 114, D06116, doi:10.1029/2008JD011208.

Baker D., H. Escher-Vetter, H. Moser, H. Oerter and O. Reinwarth (1982), A glacier discharge model based on results from field studies of energy balance, water storage and flow. In *Hydrological Aspects of Mountain Areas*, Glen J. (Ed.), IAHS Publication No. 138, IAHS: pp. 103–112.

Bamber, J. L., R. J. Hardy, P. Huybrechts, and I. Joughin (2000), A comparison of balance velocities, measured velocities and thermomechanically modelled velocities for the Greenland ice sheet. Ann Glaciol, 30:211-216. doi: 10.3189/172756400781820589.

Bamber, J., and A. Payne (2004), Mass balance of the cryosphere: observations and modelling of contemporary and future changes, Cambridge University Press, United Kingdom.

Banwell, A. F., I. Willis, N. Arnold, A. Messerli, C. Rye and A. Ahlstrom (2012a), Calibration and validation of a high resolution surface mass balance model for Paakitsoq, west Greenland. *J. Glaciol.* 58(212), 1047–1062. doi:10.3189/2012JoG12J034

Banwell, A. F., N. S. Arnold, I. C. Willis, M. Tedesco, and A. P Ahlstrom (2012b), Modelling supraglacial water routing and lake filling on the Greenland Ice Sheet. 117 *J. Geophys. Res.,* doi:10.1029/2012JF002393.

Bartholomaus, T. C., R. S. Anderson, and S. P. Anderson (2008), Response of glacier basal motion to transient water storage. *Nat. Geos., 1*(1)*,* 33–37.

Bartholomew, I., P. Nienow, D. Mair, A. Hubbard, M King, and A. Sole (2010), Seasonal evolution of subglacial drainage and acceleration in a Greenland outlet glacier, *Nat. Geos.,* 3, 408-411.

Bartholomew, I., P. Nienow, A. Sole, D. Mair, T. Cowton, S. Palmer, and J. Wadham (2011a), Supraglacial forcing of subglacial drainage in the ablation zone of the Greenland ice sheet, *Geophys. Res. Lett.* 38(8), L08502.

Bartholomew, I., P. Nienow, A. Sole, D. Mair, T. Cowton, M. King and S. Palmer (2011b), Seasonal variations in Greenland Ice Sheet motion: inland extent and behaviour at higher elevations. *Earth Planet. Sci. Lett.*, 307, 271-278, doi:10.1016/j.epsl.2011.04.014.

Bartholomew, I., P. Nienow, A. Sole, D. Mair, T. Cowton, and M. A. King (2012), Short-term variability in Greenland Ice Sheet motion forced by time-varying meltwater drainage: Implications for the relationship between subglacial drainage system behavior and ice velocity, J. Geophys. Res., 117, F03002, doi:10.1029/2011JF002220.

Bassford, R. P. (2002), Geophysical and numerical modelling investigations of the ice caps on Severnaya Zemlya, PhD thesis, University of Bristol, Bristol, UK.

Benn, D. I., C. R. Warren, and R. H. Mottram (2007), Calving processes and the dynamics of calving glaciers, *Earth Sci. Rev*., 82, 143–179, doi:10.1016/j.earscirev.2007.02.002.

Benn, D. I. and D. J. A. Evans, (2010), Glaciers & Glaciation. Arnold Publishing, Hodder.

Bingham, R. G., P. W. Nienow, and M. J. Sharp (2003), Intra-seasonal and intra-annual flow dynamics of a High Arctic polythermal valley glacier, *Ann. Glaciol.,* 37, 181– 188.

Bingham, R., A. Hubbard, P. Nienow, and M. Sharp (2008), An investigation into the mechanisms controlling seasonal speedup events at a High Arctic glacier, J. Geophys. Res., 113, F02006, doi:10.1029/2007JF000832.

Björnsson, H. (1982), Drainage basins on Vatnajökull mapped by radio echo soundings. *Nordic Hydrology,* 13(4), 213–232.

Boon, S. and M. Sharp (2003). The role of hydrologically-driven ice fracture in drainage system evolution on an Arctic glacier. *Geophys. Res. Lett.,* 30, 18.

Bougamont, M., J. Bamber, and W. Greuell (2005), A surface mass balance model for the greenland ice sheet, *J. Geophys. Res.,* 110 (4), F04,018.

Box, J.E., D. H. Bromwich, and L-S Bai (2004), Greenland ice sheet surface mass balance for 1991-2000: application of Polar MM5 mesoscale model and in-situ data, *J. Geophys. Res*. 109(D16), D16105, doi:10.1029/2003JD004451

Box, J.E. *and 8 others* (2006), Greenland ice sheet surface mass balance variability (1988–2004) from calibrated polar MM5 output. *J. Clim.,* 19(12), 2783–2800.

Box, J.E. and K. Ski (2007), Remote sounding of Greenland supraglacial melt lake: implications for subglacial hydraulics, *J. Glaciol.* Vol. 53, No.181, p257-265

Box, J. E., L. Yang, D. H. Bromwich, and L. S. Bai (2009), Greenland ice sheet surface air temperature variability: 1840–2007, *J. Clim.,* 22, 4029–4049, doi:10.1175/2009JCLI2816.1.

Box J. E. et al. (2010), Greenland (in Arctic Report Card 2010, available at www.arctic.noaa.gov/reportcard)

Box J. E. et al. (2011), Greenland Ice Sheet (in Arctic Report Card 2011, available at www.arctic.noaa.gov/reportcard)

Box, J.E. and D.T. Decker (2011), Analysis of Greenland marine-terminating glacier area changes: 2000-2010, *Ann. Glaciol.* 52(59) 91-98.

Braithwaite, R. J. (1981), On glacier energy balance, ablation, and air temperature. *J. Glaciol.,* 27, 381–391.

Braithwaite, R. J., and O. B. Olesen (1993), Seasonal variation of ice ablation at the margin of the Greenland ice sheet and its sensitivity to climate change, Qamanarssup sermia, West Greenland, *J. Glaciol.,* 39, 267–274.

Braithwaite, R. J., M. Laternser, and W. T. Pfeffer (1994), Variations of near-surface firn density in the lower accumulation area of the greenland ice-sheet, pakitsoq, west greenland, *J. Glaciol,* 40(136), 477-485.

Braithwaite, R. J. (1995), Positive degree-day factors for ablation on the Greenland ice sheet studied by energy-balance modelling. *J. Glaciol.* 41, 153–60.

Braun, L.N., M. Aellen, M. Funk, R. Hock, M. B. Rohrer, U. Steinegger, G. Kappenberger

and H. Müller-Lemans (1994), Measurement and simulation of high alpine water balance components in the Linth-Limmern head watershed (Northeastern Switzerland). *Zeitschrift f ür Gletscherkunde und Glazialgeologie* 30, 161–85.

Brandt, O., J. Kohler, and M. Luthje (2008), Spatial mapping of multi-year superimposed ice on the glacier kongsvegen, svalbard, *J. Glaciol.*, 54(184), 73-80.

Brock, B. W., I. C. Willis, M. J. Sharp, and N. S. Arnold. (2000).. Modelling seasonal and spatial variations in the surface energy balance of Haut Glacier d'Arolla, Switzerland, *Ann. Glaciol.*, *31*, 53-62, doi:10.3189/172756400781820183.

Broecker, W. S., M. Andree, W. Wolfli, H. Oeschger, G. Bonani, J. Kennett, and D. Peteet (1988), The chronology of the last deglaciation: Implications to the cause of the Younger Dryas event. *Paleoceanography*, 3, 1-19.

Broecker, W. S. (2006), Was the Younger Dryas triggered by a flood? *Science*, 312:1146-1148, Doi: 10.1126/science.1123253.

Budd, W. F. and R. C. Warner (1996), A computer scheme for rapid calculations of balance-flux distributions. *Ann. Glaciol.* 23: 21–27.

Burgess, E., R. Forster, J. Box, E. Mosley-Thompson, D. Bromwich, R. Bales, and L. Smith (2010), A spatially calibrated model of annual accumulation rate on the Greenland ice sheet (1958–2007), *J. Geophys. Res.* 115, F02,004. doi:10.1029/2009JF001293.

Campbell, F. M. A, P. W. Nienow and R. S. Purves (2006), Role of the supraglacial snowpack in mediating meltwater delivery to the glacier system as inferred from dye tracer investigations *Hydrol. Process.* 20, 969–985, doi:10.1002/hyp.6115

Cappelen, J. 2010. DMI monthly climate data collection 1768–2009, Denmark, The Faroe Islands and Greenland *Dansk Meterologisk Institut* Technical Report No. 10-05 (available at www.dmi.dk/dmi/tr10-05.pdf)

Catania, G. A., T. A. Neumann, and S. F. Price (2008), Characterizing englacial drainage in the ablation zone of the Greenland ice sheet, *J. Glaciol.*, 54(187), 567–578, doi:10.3189/002214308786570854.

Catania, G. A., and T. A. Neumann (2010), Persistent englacial drainage features in the Greenland ice sheet, *Geophys. Res. Lett.,* 37, L02501, doi:10.1029/2009GL041108.

Chander, G., B. L. Markham, and D. L. Helder (2009), Summary of current radiometric calibration coefficients for Landsat MSS, TM and EO-1 ALI sensors, *Remote Sens. Environ.,* 113, 893-903

Cappelen, J (2010), DMI monthly climate data collection 1768–2009, Denmark, The Faroe Islands and Greenland *Dansk Meterologisk Institut* Technical Report No. 10-05 (available at www.dmi.dk/dmi/tr10-05.pdf)

Chen, J. L., C. R. Wilson, and B. D. Tapley (2006), Satellite gravity measurements confirm accelerated melting of Greenland icesheet. *Science,* 313, 1958–1960.

Chen, J. L., C.R. Wilson, and B.D. Tapley (2011), Interannual variability of Greenland ice losses from satellite gravimetry, *J. Geophys. Res.*,116. doi:10.1029/2010JB007789

Chow V., D. R. Maidment and L. W. Mays (1988), *Applied Hydrology*, *Civil Engineering Series*, McGraw-Hill International Editions: New York, p. 572.

Chylek, P., J. E. Box, and G. Lesins (2004), Global Warming and the Greenland Ice Sheet, *Climatic Change*, 63, 201–221.

Clark, P. U., R. B. Alley, and D. Pollard. (1999), Northern hemisphere ice-sheet influences on global climate change. *Science*, 286:1104-1111, doi:10.1126/science.286.5442.1104.

Clarke, G. K. C. (1996), Lumped-element analysis of subglacial hydraulic circuits. *J. Geophys. Res.* 101:17547–59.

Clason, C., D. W. F. Mair, D. O. Burgess and P. W. Nienow (2012), Modelling the delivery of supraglacial meltwater to the ice/bed interface: application to southwest Devon Ice Cap, Nunavut, Canada. *J. Glaciol., 58*(208), 361-374

Cogley, J. G. (2004), Greenland accumulation: An error model. *J. Geophys. Res.* 109, D18101, doi:10.1029/2003JD004449

Cogley, J. G., et al. (2011), Glossary of Glacier Mass Balance and Related Terms, IHP-VII Technical Documents in Hydrology No. 86. IACS Contribution No. 2Rep., UNESCO-IHP, Paris.

Colbeck, S. C. (1978), The physical aspects of water flow through snow. Advances in Hydroscience, 11, V. T. Chow (Editor), Academic Press, New York, N.Y., 165-206.

Colgan, W. and K. Steffen (2009), Modeling the spatial distribution of moulins near Jakobshavn, Greenland, *IOP Conf. Ser.: Earth Environ. Sci.* 6 012022 doi:10.1088/1755-1307/6/1/012022

Colgan, W., H. Rajaram, R. Anderson, K. Steffen, T. Phillips, I. Joughin, J. H. Zwally, and W. Abdalati (2011a), The annual glaciohydrology cycle in the ablation zone of the Greenland Ice Sheet: Part 1. Hydrology Model. *J. Glaciol.* 57(204), 697-709.

Colgan, W., K. Steffen, W. S. McLamb, W. Abdalati, H. R Rajaram, R. Motyka, T. Phillips and R. Anderson (2011b). An increase in crevasse extent, West Greenland: Hydrologic implications. *Geophys. Res. Lett., 38,* L18502

Colgan, W., H. Rajaram, R. S. Anderson, K. Steffen, J. Zwally, T. Phillips and W. Abdalati (2012), The annual glaciohydrology cycle in the ablation zone of the Greenland ice sheet: Part 2. Observed and modeled ice flow. *J. Glaciol. 58*(207), 51-64

Cuffey, K.M. and W. S. B. Paterson (2010), *The Physics of Glaciers*, 4th Edition, USA, Butterworth-Heinemann

Cutler, P. M. (1998), Modelling the evolution of subglacial tunnels due to varying water input, *J. Glaciol.*, 44(148), 485–497.

Das, S. B., I. Joughin, M. Behn, I. Howat, M. King, D. Lizarralde, and M. P. Bhatia (2008), Fracture Propagation to the Base of the Greenland Ice Sheet during Supraglacial Lake Drainage, *Science,* 320, 778–781. doi:10.1126/science.1153360.

Ettema, J., M. R. van den Broeke, E. van Meijgaard, W. J. van de Berg, J. E. Box, and K. Steffen (2010), Climate of the Greenland ice sheet using a high-resolution climate model – Part 1: Evaluation. *Cryosphere*, 4, 511–527, doi:10.5194/tc-4-511-2010.

Ettema, J. M. R. van den Broeke, E. van Meijgaard, and W. J. van de Berg (2010), Climate of the Greenland ice sheet using a high-resolution climate model – Part 2: Near-surface climate and energy balance *Cryosphere*, 4, 529-544.

Fettweis, X. (2007), Reconstruction of the 1979–2006 Greenland ice sheet surface mass balance using the regional climate model MAR, *Cryosphere,* 1, 21–40, doi:10.5194/tc-1-21-2007.

Fettweis X., E. Hanna, H. Galle, P. Huybrechts and M. Erpicum (2008), Estimation of the Greenland ice sheet surface mass balance for the 20th and 21st centuries. *Cryosphere*

2:117–129

Fettweis, X., G. Mabille, M. Erpicum, S. Nicolay, and M. Van den Broeke (2010), The 1958-2009 Greenland ice sheet surface melt and the mid-tropospheric atmospheric circulation, *Climate Dynamics,* 36, 1-2, 139-159.

Fichefet, C. Poncin, H. Goosse, P. Huyrechts, I. Janssens, and H. Le Treut (2003), Implications of changes in freshwater ux from the Greenland ice sheet for the climate of the 21st century. *Geophys.Res. Lett.,* 30:1991-1995, doi: 10.1029/2003GL017826.

Fischer, U. H., A. Braun, A. Bauder and G. E. Flowers (2005), Changes in geometry and subglacial drainage derived from digital elevation models: Unteraargletscher, Switzerland, 1927–1997. *Ann. Glaciol.* 40: 20–24.

Flowers, G. E. and G. K. C. Clarke (1999), Surface and bed topography of Trapridge Glacier, Yukon Territory, Canada: digital elevation models and derived hydraulic geometry, *J. Glaciol.,* 45(149), 165-167.

Flowers, G. E. and G. K. C. Clarke (2002a), A multicomponent coupled model of glacier hydrology 1. Theory and synthetic examples. *J. Geophys. Res.* 107 (B11)

Flowers, G. E. and G. K. C. Clarke (2002b), A multicomponent coupled model of glacier hydrology 2. Application to Trapridge Glacier, Yukon, Canada. *J. Geophys. Res.* 107 (B11)

Flowers, G.E., Bjornsson, H., & Palsson, F. (2003), New insights into the subglacial and periglacial hydrology of Vatnajokull, Iceland, from a distributed physical model. *J. Glaciol. 49*(165), 257–270

Førland, E. J., et al. (1996), Manual for operational correction of nordic precipitation data, Tech. rep., Norwegian meteorological Institute, Report 24/96 KLIMA.

Fountain A.G. and Tangborn W.V. (1985) Overview of contemporary techniques. In *Techniques for Prediction of Runoff from Glacierized Areas*, Young G. (Ed.), IAHS Publication No. 149, IAHS: pp. 1–41.

Fountain, A. G. (1994), Borehole water-level variations and implications for the subglacial hydraulics of South Cascade Glacier, Washington State, U.S.A., *J. Glaciol.*, *40*, 293–304.

Fountain, A. G. and J. S. Walder (1998), Water flow through temperate glaciers. *Rev.*

Geophys., 36(3), 299-328.

Fowler, A., and J. S. Walder (1993), Creep closure of channels in deforming subglacial till, *Proc. R. Soc. London, Ser.* A , 441, 17-31.

Fox A. M. (2004), *A distributed physically based snow melt and run off model for alpine glaciers.* Unpublished PhD thesis, Department of Geography, University of Cambridge.

Gallée, H. and G. Schayes (1994), Development of a three-dimensional meso-primitive equations model, Mon. *Weather Rev.*, 122, 671-685.

Gardner, A. S. and M. J. Sharp (2010). A review of snow and ice albedo and the development of a new physically based broadband albedo parameterization. *J. Geophys. Res.* 115, F01009. Doi:10.1029/2009JF001444.

Georgiou, S., A. Shepherd, M. McMillan, and P. Nienow (2009), Seasonal evolution of supraglacial lake volume from ASTER imagery, *Ann. Glaciol.*, 50(52), 95–100, doi:10.3189/172756409789624328.

Gordon, S., M. Sharp, B. Hubbard, C. Smart, B. Ketterling, and I. Willis (1998) Seasonal reorganisation of subglacial drainage inferred from measurements in boreholes. *Hydrol. Process.* 12: 105-133.

Graversen, R. G., S. Drijfhout, W. Hazeleger, R. van de Wal, R. Bintanja, and M. Hersen (2011), Greenland's contribution to global sea-level rise by the end of the 21st century. *Climate Dynamics, 37*(7-8), 1427-1442

Greuell, W., and T. Konzelmann (1994), Numerical modelling of the energy balance and the englacial temperature of the Greenland Ice Sheet. Calculations for the ETH-Camp location (West Greenland, 1155 m a.s.l.), *Global Planet. Change*, *9*(1-2), 91-114, doi:110.1016/0921-8181(1094)90010-90018.

Greuell, W. (2000), Melt-water accumulation on the surface of the Greenland ice sheet: effect on albedo and mass balance. Geogr. Ann., 82 A (4): 489–498.

Greuell, W., and W. H. Knap (2000), Remote sensing of the albedo and detection of the slush line on the Greenland ice sheet, *J. Geophys. Res.* 105 (D12), 15,567-15,576.

Griffin, M. K., S. May Hsu, H. K. Burke, S. M. Orloff, and C. A. Upham (2005), Examples of EO-1 Hyperion Data Analysis. *Lincoln Laboratory Journal*. 15, p. 271.

Gudmundsson, G.H. (2003), Transmission of basal variability to a glacier surface. *J. Geophys. Res.*, 108(B5), 2253 doi:10.1029/2002JB0022107.

Gulley, J., P. Walthard, J. Martin, A. F. Banwell, D. Benn, and G. Catania (2012), Seasonal evolution of dye trace breakthrough curves: the effects of changes in roughness. *J. Glaciol.* doi: 10.3189/2012JoG11J115

Gupta, R. P., U. K. Haritashya, and P. Singh (2005), Mapping dry/wet snow cover in the Indian Himalayas using IRS multispectral imagery, *Remote Sens. Environ.,* 97, 458–469.

Hall, D. K., G. A. Riggs, and V. V. Salomonson (1995), Development of methods for mapping global snow cover using moderate resolution imaging spectroradiometer data, *Remote Sens. Environ* 54, 127-140

Hall, D. K., G. A. Riggs and V. V. Salomonson (2006), updated daily. *MODIS/Terra Snow Cover Daily L3 Global 500m Grid, Version 5.* National Snow and Ice Data Center, Boulder, CO. Digital media: nsidc.org/data/MOD10A1V5.html

Hall, D.K., R.S. Williams, Jr, S.B. Luthcke and N.E. Digirolamo (2008), Greenland ice sheet surface temperature, melt and mass loss: 2000–2006. *J. Glaciol.,* 54(184), 81–93.

Hagen, J. O., B. Etzelmüller, and A. Nuttall (2000), Runoff and drainage pattern derived from digital elevation. *Ann. Glaciol.*, 2, 2-7.

Hanna, E., P. Huybrechts, and T. Mote (2002), Surface mass balance of the Greenland ice sheet from climate-analysis data and accumulation/runoff models, *Ann. Glaciol.*, 35, 67–72.

Hanna, E., P. Huybrechts, I. Janssens, J. Cappelen, K. Steffen, and A. Stephens (2005), Runoff and mass balance of the Greenland ice sheet: 1958-2003, *J. Geophys. Res.* 110, (B13108), doi:10.1029/2004JD005641.

Hanna, E., J. McConnell, S. Das, J. Cappelen, and A. Stephens (2006), Observed and modelled Greenland ice sheet snow accumulation, 1958–2003, and links with regional climate forcing, *J. Climate*, 19, 344–358, 2006.

Hanna, E., P. Huybrechts, K. Steffen, J. Cappelen, R. Huff, C. Shuman, T. Irvine-Fynn, S. Wise, and M. Griffiths (2008), Increased runoff from melt from the Greenland ice sheet: A response to global warming, *Bull. Amer. Meterol. Soc,* 21, 331- 341. doi:10.1175/2007JCLI964.1

Harbaugh, A. W., E. R. Banta, M. C. Hill and M. G. McDonald (2000). MODFLOW- 2000, *The U.S. Geological Survey modular ground-water model - User guide to modularization concepts and the ground-water flow process*, U.S. Geological Survey. Open-File Report 00-92

Hodgkins, R. (1997), Glacier hydrology in Svalbard, Norwegian High Arctic. Quaternary Science Reviews 16, 957-973.

Holmlund, P. (1988), Internal geometry and evolution of moulins, Storglaciaren, Sweden. *J. Glaciol.,* 34(117), 242–248.

Hock, R. and R. L. Hooke (1993), Evolution of the internal drainage system in the lower part of the ablation area of Storglaciären, Sweden. *Geol. Soc. Amer. Bull,* 105, 537-546.

Hock R. (2003), Temperature index melt modelling in mountain areas *J. Hydrol.* 282 104-115 doi:10.1016/S0022-1694(03)00257-9.

Hock, R. (2005), Glacier melt: A review on processes and their modelling. *Prog. Phys. Geog.* 29(3), 362-391.

Hock, R., and B. Holmgren (2005), A distributed surface energy-balance model for complex topography and its application to storglaciaren, Sweden, *J. Glaciol.,* 51(172), 25-36.

Hoffman, M.J., G. A. Catania, T. A. Neumann, L. C. Andrews and J. A. Rumrill (2011), Links between acceleration, melting, and supraglacial lake drainage of the western Greenland Ice Sheet. *J. Geophys. Res.* 116, F04035.

Holland, D. M. , R. H. Thomas, B. de Young, M. H. Ribergaard, and B. Lyberth (2008), Acceleration of Jakobshavn Isbrae triggered by warm subsurface ocean water. *Nat Geosci,* 1:659-664, doi: 10.1038/ngeo316.

Hooke, R. L. (1988), Water flow through a glacier situated in an overdeepening: cause or consequence of a till layer at the bed. *Ann. Glaciol.* 2, 213.

Hooke, R. L. (1989), Englacial and Subglacial Hydrology: A Qualitative Review. *Arctic Alpine Res.* 21 (3), 221-233.

Hooke, R. L., P. Calla, P. Holmund, M. Nilsson, and A. Stroeven (1989), A 3 year record of seasonal variations in surface velocity, Storglaciaren, Sweden. *J. Glaciol.* 35: 235–247.

Howat, I. M.,Y. Ahn, I. Joughin, R. van den Broeke, J. T. M, Lenaerts, and B. Smith (2011), Mass balance of Greenland's three largest outlet glaciers, 2000–2010. *Geophys. Res. Lett.* 38, L12501, doi:10.1029/2011GL047565.

Hu, A. X., G. A. Meehl, W. M. Washington, and A. Dai (2004), Response of the Atlantic thermohaline circulation to increased atmospheric CO2 in a coupled model. *J Climate*, 17:4267-4279, doi:1 10.1175/JCLI3208.1.

Hubbard, B. P., M. J. Sharp, I. C. Willis, M. K. Neilson, and C. C. Smart (1995), Borehole water-level variations and the structure of the subglacial hydrological system of Haut Glacier d'Arolla, Valais, Switzlerand. *J. Glaciol. 41*(139), 572-583.

Hubbard, B. and P. Nienow (1997), Alpine subglacial hydrology. *Quaternary Sci. Rev.* 16, 939-955

Humlum, O. (2002), Modelling late 20th-century precipitation in nordenskiöld land, svalbard, by geomorphic means, Norwegian Journal of Geography, 56, 96-103.

Huybrechts, P., A. Letreguilly, and N. Reeh (1991), The greenland ice sheet and greenhouse warming, *Global Planet. Change*, 3 (4), 399-412.

Iken, A. (1981), The effect of the subglacial water pressure on the sliding velocity of a glacier in an idealized numerical model, *J. Glaciol.,* 27(97), 407–421.

Iken, A., H. Rothlisberger, A. Flotron and W. Haeberli (1983), The uplift of Unteraargletscher at the beginning of the melt season – a consequence of water storage at the bed? *J. Glaciol*., 29(101), 28–47.

Iken, A. and R. A. Bindschadler (1986), Combined measurements of subglacial water pressure and surface velocity of Findelengletscher, Switzerland: conclusions about drainage system and sliding mechanism, *J. Glaciol.,* 32. 101-119.

Isenko E.V., and B. R. Mavlyudov (2002), On the intensity of ice melting in supraglacial and englacial channels. *Bul. Glaciol. Res.* 19, 93-99.

Jacob, T., J. Wahr, T. Pfeffer and S. Swenson (2012), Recent contributions of glaciers and ice caps to sea level rise, *Nature,* doi: 10.1038/nature10847.

Janssens, I., and P. Huybrechts (2000), The treatment of meltwater retention in mass balance parameterizations of the Greenland Ice Sheet, *Ann. Glaciol.*, 31, 133-140.

Jarosch, A. H. and M. T. Gudmundsson (2012) A numerical model for meltwater channel evolution in glaciers, *Cryosphere*, 6, 493-503, doi:10.5194/tc-6-493-2012.

Johannessen, O. M., K. Khvorostovsky, M. W. Miles, and L. P. Bobylev (2005), Recent ice sheet growth in the interior of Greenland, *Sciencexpress,* 1013–1016, doi:10.1126/science.1115356.

Joughin, I., W. Abdalati, and M. Fahnestock (2004), Large fluctuations in speed on Greenland's Jakobshavn Isbræ glacier. *Nature,* 432, 608–610.

Joughin, I., S. B. Das, M. A. King, B. E. Smith, I. M. Howat, and T. Moon (2008a), Seasonal speedup along the Western flank of the Greenland Ice Sheet, *Science,* 320, 781-785. doi: 10.1029/2008JF001023.

Joughin, I., I. Howat, M. Fahnestock, B. Smith, W. Krabill, R. Alley, H. Stern, and M. Truffer (2008b), Continued evolution of Jakobshavn Isbrae following its rapid speedup, J. Geophys. Res., 113, F04006, doi:10.1029/2008JF001023.

Joughin, I., B. E. Smith, I. M. Howat, T. Scambos, and T. Moon (2010), Greenland flow variability from ice-sheet-wide velocity mapping, *J. Glaciol.,* 56, 197, 416-430.

Kachroo R.K. (1992) River flow forecasting. Part 1. A discussion of the principles. *J. Hydrol.* 133, 1–15.

Kamb, B., C. Raymond, W. Harrison, H. Engelhardt, K. Echelmeyer, N. Humphrey, M. Brugman, and T. Pfeffer (1985), Glacier surge mechanism: 1982-1983 surge of Variegated Glacier, Alaska, *Science*, 227, 469-479.

Kamb, B. (1987), Glacier surge mechanism based on linked cavity configuration of the basal water conduit system. *J. Geophys. Res, 92*, 983–100.

Kessler, M. A. And R. S. Anderson (2004), Testing a numerical glacial hydrological model using spring speed-up events and outburst floods. *Geophys. Res. Lett.*, *31*(18), 1-5.

Khan, S. A., Wahr, J., Bevis, M., Velicogna, I. & Kendrick, E. (2010), Spread of ice mass loss into northwest Greenland observed by GRACE and GPS. *Geophys. Res. Lett., 37***,** L06501.

Klein, A. G. and A. C. Barnett (2003), Validation of daily MODIS snow cover maps of the Upper Rio Grande River Basin for the 2000–2001 snow year, *Remote Sens. Environ.*,

86(2), 162–176. deoi:10.1016/s0034-4257(03)00097.

Klein, A. G. and J. C. Stroeve (2002), Development and validation of a snow albedo algorithm for the MODIS instrument, edited by: Winther, J. G. S. R., *Ann. Glaciol.*, 34, 45–52.

König, M., J. Winther, J. and E. Isaksson. 2001. Measuring Snow and Glacier Ice properties from satellite. *Reviews of Geophysics*, 39(1), 1-27.

Konzelmann, T., R. Van de Wal, W. Greuell, R. Bintanja, E. Henneken, and A. Abe-Ouchi (1994), Parameterization of short- and longwave incoming radiation for the Greenland Ice Sheet. *Global Planet. Change*, 9: 143-164.

Krabill, W., et al. (2004), Greenland ice sheet: Increased coastal thinning, *Geophys. Res. Lett.,* 31, L24402, doi:10.1029/2004GL021533.

Krawczynski, M. J., M. D. Behn, S. B. Das and I. Joughin (2009), Constraints on lake volume required for hydro-fracture through ice sheets. *Geophys. Res. Lett*. 36, L10501, doi:10.1029/2008GL036765.

Kuhn, M. (1993), Methods of assessing the effects of climatic changes on snow and glacier hydrology. In Young, G.J., editor, *Snow and glacier hydrology,* Proceedings of the Kathmandu Symposium 1992, Wallingford: IAHS Publication 218, 135-44.

Lampkin, D. J. (2011), Supraglacial lake spatial structure in western Greenland during the 2007 ablation season. *J. Geophys. Res.*, 116, F04001, doi:10.1029/2010JF001725.

Lampkin, D. J., and J. Vanderberg (2011), A preliminary investigation of the influence of basal and surface topography on supraglacial lake distribution near Jakobshavn Isbræ, *Hydrol. Processes,* doi:10.1002/hyp.8170.

Lathrop, R. G., T. M. Lillesand, and B. S. Yandell (1991), Testing the utility of simple multi-date Thematic Mapper calibration algorithms for monitoring turbid inland waters, *Int. J. Remote. Sens.,*12(10), 2045-2063.

Le Brocq, A. M., A. J. Payne and M. J. Siegert (2006), West Antarctic balance calculations: Impact of flux routing algorithm, smoothing algorithm and topography. *Computers and Geosciences* 32: 1780–1795.

Le Brocq AM, A. J. Payne, M J. Siegert and R. B. Alley (2009), A subglacial water-flow

model for West Antarctica. *J. Glaciol* 55(193) 879–888.

Liang, Y., W. Colgan, L. Qin, K. Steffen, W. Abdalati, J. Stroeve, D. Gallagher and N. Bayou (2012), A decadal investigation of supraglacial lakes in West Greenland using a fully automatic detection and tracking algorithm. *Remote Sens. Environ.,* 123, 127-138

Lindsay, J. B. and I. F. Creed (2005), Removal of artefact depressions from digital elevation models: Towards a minimum impact approach. *Hydrol. Proc.*19: 3113–3126.

Luckman, A., T. Murray, R. de Lange, and E. Hanna (2006), Rapid and synchronous ice dynamic changes in East Greenland, *Geophys. Res. Lett.,* 33, L03503, doi:10.1029/2005GL025428.

Luthje, M., L.T. Pedersen, N. Reeh and W. Greuell (2006), Modelling the evolution of supraglacial lakes on the West Greenland ice-sheet margin. *J. Glaciol.* 52(179), 608-618.

Marsh, P. (1990), Chapter 2 – Snow Hydrology: *in* Northern Hydrology: Canadian Perspectives, Prowse, T.D., and Ommanney, C.S.L. eds., *National Hydrology Research Institute Science Report*, 1, 135-162.

MacFerrin, M. (2011), Assessing ASTER GDEM 1 and 2 Errors on the Greenland Ice Sheet from Level-2 ATM lidar, Abstract : C31A-0618, presented at 2011 Fall Meeting, AGU, San Francisco, Calif., 5-9 Dec.

Machguth, H. and A. Ahlstrøm (2010), Ice Sheet Surface Mass Balance at Paakitsôq, West Greenland, Derived from Future Scenario Regional Climate Model Data. Technical Report. Copenhagen, GEUS.

Mair, D., P. Nienow, I. Willis, and M. Sharp (2001), Spatial Patterns of Glacier Motion During a High Velocity Event : Haut Glacier d'Arolla, Switzerland *J. Glaciol,* 47(156), 9-20.

Mair, D., P. Nienow, M. Sharp, T. Wohlleben, and I. Willis (2002), Influence of subglacial drainage system evolution on glacier surface motion: Haut Glacier d'Arolla, Switzerland, *J. Geophys. Res.*, 107 (B8), 2175. doi:10.1029/ 2001JB000514.

Mair, D., I. Willis, U. H. Fischer, B. Hubbard, P. Nienow, and A. Hubbard (2003), Hydrological controls on patterns of surface, internal and basal motion during three 'spring events': Haut Glacier d'Arolla, Switzerland. *J. Glaciol.* 49, 555–567.

Mair, D., B. Hubbard, P. Nienow, I. Willis, and U. H. Fischer (2008), Diurnal fluctuations in glacier ice deformation: Haut Glacier d'Arolla, Switzerland. *Earth Surf. Processes*, 33, 1272–1284.

McGrath, D., W. Colgan, K. Steffen, P. Lauffenburger and J. Balog (2011), assessing the summer water budget of a moulin basin in the Sermeq Avannarleq ablation region, Greenland Ice Sheet. *J. Glaciol*. 57: 954-964

McMillan, M., P. Nienow, A. Shepherd, T. Benham, and A. Sole (2007), Seasonal evolution of supra-glacial on the Greenland Ice Sheet*, Earth Planet. Sci. Lett.*, 262, 484-492.

Meehl, G.A. et al. (2007), Global Climate Projections. In: *Climate Change 2007: The Physical Science Basis. Contribution of Working Group I to the Fourth Assessment Report of the Intergovernmental Panel on Climate Change* (Solomon, S., D. Qin, M. Manning, Z. Chen, M. Marquis, K.B. Averyt, M.Tignor and H.L. Miller (eds.)). Cambridge University Press, Cambridge, United Kingdom and New York, NY, USA.

Meier, M. E. (1962), Proposed definitions for glacier mass budget terms, *J. Glaciol*. 33(4), 252-265.

Mernild, S. H., G. E. Liston, C. A. Hiemstra, and K. Steffen (2008), Surface melt area and water balance modeling on the Greenland ice sheet 1995–2005. *J. Hydromet.,* **9**(6), 1191–1211. doi:10.1175/2008JHM957.1.

Mote, T. L. (1998), Mid-tropospheric circulation and surface melt on the Greenland ice sheet. Part I: Atmospheric teleconnections, *Int. J. Climatol.,* 18, 111–129.

Mote, T.L., and M.R. Anderson (1995), Variations in melt on the Greenland Ice Sheet based on passive microwave measurements, *J. Glaciol,* 41, 51-60

Mote, T. L. (2003), Estimation of runoff rates, mass balance, and elevation changes on the Greenland ice sheet from passive microwave observations, *J. Geophys. Res.,* 108(D2), 4056, doi:10.1029/2001JD002032.

Mote, T. L. (2007), Greenland surface melt trends 1973-2007: Evidence of a large increase in 2007, *Geophys. Res. Lett.*. Vol. 34, L22507, doi:10.1029/2007GL031976.

Mottram, R., C. Nielsen, A. P. Ahlstrøm, N. Reeh, S. S. Kristensen, E. L. Christensen, R. Forsberg, and L. Stenseng (2009), A new regional high-resolution map of basal and

surface topography for the Greenland ice sheet margin at Paakitsoq, West Greenland *Ann. Glaciol.* 50(51), 105-111.

Motyka, R., et al. (2010), Volume change of Jakobshavn Isbrae, West Greenland: 1985–1997–2007, *J. Glaciol.*, 56, 635–646, doi:10.3189/002214310793146304.

Mu, L., D. X. Wu, and X. Chen (2006), Changes in Atlantic thermohaline circulation under different atmospheric CO2 scenarios in a climate model. *J China Univ Geosci*, 17:326-331. doi: 10.1016/S1002-0705(07)60006-5.

Munro, D. S. (1990), Comparison of melt energy computations and ablatometer measurements on melting ice and snow, *Arct. Alpine Res.*, *22*(2), 153-162, doi:110.2307/1551300.

National Aeronautics and Space Administration (NASA) (2009), ASTER Global Digital Elevation Map announcement. Available at: http://asterweb.jpl.nasa.gov/gdem.asp

Nick, F. M., A. Vieli, I. M. Howat, and I. Joughin. 2009. Large-scale changes in Greenland outlet glacier dynamics triggered at the terminus, *Nat. Geosci.,* 2, 110–114, doi:10.1038/ngeo394.

Nienow, P. W. (1993), `Dye tracer investigations of glacier hydrological systems', PhD Thesis, University of Cambridge, Cambridge.

Nienow, P. W., M. Sharp, and I. C. Willis (1998), Seasonal changes in the morphology of the subglacial drainage system, Haut Glacier d'Arolla, Switzerland. *Earth Surface Processes and Landforms, 2*3, 823–845.

Nienow, P.W., A. Hubbard, B. Hubbard, D. Chandler, D. Mair, M. Sharp and I. Willis (2005), Hydrological controls on diurnal ice flow variability in valley glaciers, *J. Geophys. Res.,* 110(F4), F04002 doi:10.1029/2003JF000112.

Nye, J. F., (1953), The flow law of ice from measurements in glacier tunnels, laboratory experiments and the Jungfraufirn borehole experiment, Prac. R. Sac. London, Ser. A, 219, 477-489.

Nye, J. F. (1973). Water at the bed of a glacier. In *Symposium on the Hydrology of Glaciers, IAHS Publication,* 138, 71-81

Nye, J. F. (1976). Water flow in glaciers: Jökulhlaups, tunnels and veins. *J. Glaciol., 17,*

181-207.

Oerlemans, J. (1991), The mass balance of the Greenland ice sheet: Sensitivity to climate change as revealed by energy-balance modelling, *Holocene,*1, 40–49.

Oerlemans, J. (1993), A model for the surface balance of ice masses: part 1. Alpine glaciers, *Z. Gletscher. Glazialgeol.,* 27/28, 63±83.

Oerlemans, J. and H. F. Vugts (1993), A Meteorological Experiment in the melting zone of the Greenland Ice Sheet. *B. Am. Meteorol. Soc.* 74, 355–365.

Ohmura, A., and N. Reeh (1991), New precipitation and accumulation maps for Greenland, *J. Glaciol.,* 37(125), 140–148.

Ohmura, A., M. Wild, and L. Bengtsson (1996), A possible change in mass balance of Greenland and Antarctic ice sheets in the coming century, *J. Clim.,* 9, 2124–2135.

Ohmura, A. (2001), Physical basis for the temperature-based melt-index method, *J. Appl. Meteorol.*, 40(4), 753-761.

Oke, T. (1987), *Boundary layer climates*, 2nd ed., Methuen, London.

Palmer, S., A. Shepherd, P. Nienow, and I. Joughin (2011), Seasonal speedup of the Greenland ice sheet linked to routing of surface water, *Earth Planet. Sci. Let.*, 302, pp. 423-428 .

Parizek, B.R. and R. B. Alley (2004), Implications of increased Greenland surface melt under global-warming scenarios: ice-sheet simulations, *Quaternary Sci. Rev.*, 23, pp. 1013-1027.

Phillips, T., et al. (2011), Modeling Moulin Distribution on Sermeq Avannarleq Glacier using ASTER and WorldView Imagery and Fuzzy Set Theory. *Rem. Sens. Environ*. 115: 2292-2301.

Pimentel, S. and G. E. Flowers (2010), A numerical study of hydrologically driven glacier dynamics and subglacial flooding. *Proceedings of the Royal Society A: Mathematical, Physical and Engineering Sciences*, 1-13

Pimentel, S., G. E. Flowers, and C. G. Schoof (2010), A hydrologically coupled higher-order flow-band model of ice dynamics with a Coulomb friction sliding law, *J. Geophys. Res.*, 115, F04023, doi:10.1029/2009JF001621.

Price, S., A. J. Payne, G. Catania, and T. A. Neumann (2008), Seasonal acceleration of inland ice via longitudinal coupling to marginal ice. *J. Glaciol.* 54(158), 213-219.

Pritchard, H. D., R. J. Arthern, D. G. Vaughan, and L. A. Edwards (2009), Extensive dynamic thinning on the margins of the Greenland and Antarctic ice sheets. *Nature, 461*, 971-975.

Radic, V. And R. Hock (2011), Regionally differentiated contribution of mountain glaciers and ice caps to future sea-level rise. *Nat. Geos.,* 4(2), 91-94

Rahmstorf, S., M. Crucifix, A. Ganopolski, H. Goosse, I. Kamenkovich, R. Knutti, G. Lohmann, R. Marsh, L. A. Mysak, Z. M. Wang, and A. J. Weaver (2005), Thermohaline circulation hysteresis: A model intercomparison. *Geophys. Res. Lett.*, 32:L23605, doi: 10.1029/2005GL023655.

Raymond, C. F., R. J. Benedict, W. D. Harrison, K. A. Echelmeyer and M. Sturm (1995), Hydrological discharges and motion of Fels and Black Rapids Glaciers, Alaska, USA: Implications for the structure of their drainages systems, *J. Glaciol.*, 41, 290-304.

Raymond, C. F. and M. Nolan (2000), Drainage of a glacial lake through an ice spillway, *Debris-Covered Glaciers (Proceedings of a workshop held in Seattle, Washington, USA) IAHS Publication* No. 264, 199-207.

Reeh, N. (1991), Parameterization of melt rate and surface temperature on the Greenland ice sheet, Polarforschung, 59(3), 113-128.

Richards, K. S., M. J. Sharp, N. Arnold, A. M. Gurnell, M. J. Clarke, M. Tranter, P . W. Nienow, G. H. Brown, I. C. Willis, and W. J. Lawson (1996), An integrated approach to modelling hydrology and water quality in glacierized catchments, *Hydrol. Process.,* 10, 479-508.

Rignot, E. and P. Kanagaratnam (2006), Changes in the velocity structure of the Greenland Ice Sheet. *Science*, 311, p986-990, doi: 10.1126/science.1121381

Rignot, E., J. E. Box, E. Burgess, and E. Hanna (2008), Mass balance of the Greenland ice sheet from 1958 to 2007. *Geophys Res Lett.* 35:L20502. doi:10.1029/2008GL03541.

Rignot, E., M. Koppes, and I. Velicogna (2010), Rapid submarine melting of the calving faces of West Greenland glaciers, *Nat. Geosci.,* 3, 187–191, doi:10.1038/ngeo765.

Rignot, E., I. Velicogna, M. R. van den Broeke, A. Monaghan, and J. Lenaerts (2011), acceleration of the contribution of the Greenland and Antarctic ice sheets to sea level rise. *Geophys Res Lett.* 38, L05503-L05508. doi 10.1029/2011GL046583

Rippin, D., I. Willis, N. Arnold, A. Hodson, J. Moore, J. Kohler, and H. Bjornsson (2003), Changes in geometry and subglacial drainage of Midre Lovénbreen, Svalbard, determined from digital elevation models. *Earth Surf. Proc.Land. 28*(3), 273-298.

Roesner, L.A., J. A. Aldrich, J.A., and R. E. Dickinson (1988), Storm Water Management Model User's Manual version 4; EXTRAN addendum. US Environmental Protection agency, Athens, Georgia, 188 pp.

Röthlisberger, H. (1972), Water pressure in intra- and subglacial channels. *J. Glaciol., 11*, 177–203

Röthlisberger, H., and H. Lang (1987), Glacial hydrology, in Glacio-fluvial Sediment Transfer: An Alpine Perspective, edited by A. Gurnell and M. Clark, pp. 207–274, Wiley, Chichester, U. K.

Rye, C. J., N. S. Arnold, I. C. Willis, and J. Kohler (2010), Modeling the surface mass balance of a high Arctic glacier using the ERA-40 reanalysis, *J. Geophys. Res.*, 115, F02014, doi:10.1029/2009JF001364.

Schneider, T. and P. Jansson (2004), Internal accumulation in firn and its significance for the mass balance of storglaciaren, sweden, *J. Glaciol*. 50(168), 25-34.

Schoof, C. (2010), Ice-sheet acceleration driven by melt supply variability, *Nature*, 468(7325), 803-806, doi: 10.1038/nature09618.

Schuler, T. V., R. Hock, M. Jackson, H. Elvehoy, M. Braun, I. Brown, and J. O. Hagen (2005), Distributed mass-balance and climate sensitivity modelling of engabreen, norway, *Ann. Glaciol*., 42, 395-401.

Seale, A., P. Christoffersen, R. I. Mugford, and M. O'Leary (2011), Ocean forcing of the Greenland Ice Sheet: Calving fronts and patterns of retreat identified by automatic satellite monitoring of eastern outlet glaciers, *J. Geophys. Res.*, 116, F03013, doi:10.1029/2010JF001847

Selmes, N., T. Murray, and T. D. James (2011), Fast draining lakes on the Greenland Ice Sheet, *Geophys. Res. Lett.*, *38*, L15501, doi:10.1029/2011GL047872.

Sharp M.J., J. C. Gemmell and J. L. Tison (1989) Structure and stability of the former subglacial drainage system of the Glacier de Tsanfleuron, Switzerland. *Earth Surf. Proc. Land*, 14, 119–134.

Sharp M.J., K. S. Richards, I. C. Willis, N. S. Arnold, P. Nienow, W. Lawson and J. L. Tison (1993), Geometry, bed topography and drainage system structure of the Haut Glacier d'Arolla, Switzerland. *Earth Surf. Proc. Land*, 18, 557–571.

Sharp, M. (2005), Subglacial Drainage. In Anderson, M. G. (Ed.), Encyclopaedia of Hydrological Sciences. John Wiley & Sons.

Shepherd, A., and D. Wingham (2007), Recent sea-level contributions of the Antarctic and Greenland ice sheets, *Science*, 315(5818), 1529-1532.

Shepherd, A., A. Hubbard, P. Nienow, M. King, M. McMillan, and I. Joughin (2009), Greenland ice sheet motion coupled with daily melting in late summer, *Geophys. Res. Lett.*, 36, L01501, doi:10.1029/2008GL035758.

Shreve, R. (1972), Movement of water in glaciers. *J. Glaciol*, 11(62) 205-214.

Smart, C. C. (1998), Statistical evaluation of glacier boreholes as indicators of basal drainage systems, in Sharp, M.J., Richards, K.S., and Tranter, Martyn, eds., *Glacier hydrology and hydrochemistry*: Chichester, Wiley, p. 175-189.

Sneed, W.A. and G. S. Hamilton (2007), Evolution of melt pond volume on the surface of the Greenland Ice Sheet, *Geophys. Res. Lett.*, Vol. 34, doi:10.1029/2006GL028697.

Sohn, H.G., K. C. Jezek, and C. J. van der Veen (1998), Jakobshavn Glacier, West Greenland: 30 years of spaceborne observations, *Geophys. Res. Lett.*, 25(14), 2699-2702.

Spring, U. and K. Hutter (1981), Numerical studies of Jokulhlaups. Cold Regions Science and Technology, 4, 227-244.

Steffen, K., and J. Box (2001), Surface climatology of the Greenland ice sheet: Greenland Climate Network 1995–1999. *J. Geophys. Res.,* 106[D24]:33951–33964.

Straneo, F., G. S. Hamilton, D. A. Sutherland, L. A. Stearns, F. Davidson, M. O. Hammill, G. B. Stenson, and A. Rosing-Asvid (2010), Rapid circulation of warm subtropical waters in a major glacial fjord in East Greenland, *Nat. Geosci.*, 3, 182–186, doi:10.1038/ngeo764.

Sundal, A. V., A. Shepherd , P. Nienow, E. Hanna, S. Palmer and P. Huybrechts (2009),

Evolution of supra-glacial lakes across the Greenland Ice Sheet. *Remote Sens. Environ*, 113, 2164–2171.

Sundal, A. V., A. Shepherd, P. Nienow, E. Hanna, S. Palmer, and P. Huybrechts (2011), Melt-induced speed-up of Greenland ice sheet offset by efficient subglacial drainage, *Nature*, 469, 522-U83. doi:10.1038/nature09740

Szilder, K., and E. P. Lozowski (1997), Stability of quasi-steady flow in an englacial conduit, *Hydrol. Process.*, 11, 1737–1746,

Tapley, B. D., S. Bettadpur, M. Watkins, and C. Reigber (2004), The gravity recovery and climate experiment: mission overview and early results. *Geophys. Res. Lett.* 31, L09607.

Tedesco, M. (2007a). Snowmelt detection over the Greenland ice sheet from SMM/I brightness temperature daily variations, *Geophys. Res. Lett.,* 34, L02504, doi:10.1029/2006GL028466.

Tedesco, M. (2007b). A new record in 2007 for melting in Greenland, *Eos Trans. AGU,* 88(39), 383, doi:10.1029/2007EO390003.

Tedesco , M. , X. Fettweis, M. R. van den Broeke, R. S. W. van de Wal, C. J. P. P. Smeets, W. J. van de Berg, M. C. Serreze and J. E. Box. (2011a), The role of albedo and accumulation in the 2010 melting record in Greenland, *Environ. Res. Lett.,* 6 014005 doi:10.1088/1748/9326/6/1/014005.

Tedesco, M., J. E. Box, J. Cappellen , T. Mote, R. S. W. van de Wal, and J. Wahr (2011b), (Greenland Ice Sheet) The Arctic (in State of the Climate in 2011). *Bull. Amer. Meteor. Soc,* S148- S151.

Tedesco, M. and S. Steiner (2011), In-situ multispectral and bathymetric measurements over a supraglacial lake in western Greenland using a remotely controlled watercraft. *Cryosphere*, 5, 445–452. doi:10.5194/tc-5-445-2011.

Tedesco, M., M. Luthje, K. Steffen, X. Fettweis, I. Willis, N. Steiner, N. Bayou, and A. Banwell (2012), Measurement and modeling of ablation of the bottom of supraglacial lakes in Western Greenland, *Geophys. Res. Lett.*, 39, L02502, doi:10.1029/2011GL049882.

Tedesco, M., I. Willis, M. Hoffman, A. Banwell and P. Alexander, Ice dynamic response to slow and fast surface lake drainage on the Greenland Ice Sheet. *Nat. Geos. In review*.

Thomsen, H. H. (1986), Photogrammetric and satellite mapping of the margin of the inland ice, West Greenland. *Ann. Glaciol.,* 8, 164–167.

Thomsen, H.H. (1988), Mass balance, ice velocity and ice temperature at the Inland Ice margin north-east of Jakobshavn, central West Greenland. *Rapport Grønlands Geologiske Undersøgelse*, 140, 111-114.

Thomsen, H.H., L. Thorning, and R. J. Braithwaite (1988), Glacier-hydrological conditions on the Inland Ice north-east of Jakobshavn/Ilulissat, West Greenland. *Rapport Grønlands Geologiske Undersøgelse*, 138.

Thomsen, H.H., L. Thorning and O. B. Olesen (1989), Applied glacier research for planning hydro-electric power, Ilulissat/Jakobshavn, West Greenland. *Annals of Glaciology*, 13, 257-261.

Thomsen, H. H. and O. B. Olesen (1990), Continued glaciological investigations with respect to hydropower and ice-climate relationships, at Pâkitsoq, Jakobshavn, West Greenland. *Rapport Grønlands Geologiske Undersøgelse*, *148*, 83-86.

Thornalley, D. J. R., I. N. McCave, and H. Elderfield (2010), Freshwater input and abrupt deglacial climate change in the North Atlantic. Paleoceanography, 25:PA1201, 2010. doi: 10.1029/2009PA001772.

Truffer, M., W. D. Harrison, and R. S. March (2005), Record negative glacier balances and low velocities during the 2004 heatwave in Alaska, USA: implications for the interpretation of observations by Zwally and others in Greenland (Correspondence). *J Glaciol*, 51:663-664, doi:10.3189/172756505781829016.

USGS. 2011. *Glovis,* http://glovis.usgs.gov/

van den Broeke, M., D. van As, C. Reijmer, and R. van de Wal (2004), Assessing and improving the quality of unattended radiation observations in Antarctica. *J. Atmos. Oceanic Technol.,*904 21(9), 1417-1431.

van den Broeke, M. R., C. J. P. P. Smeets, J. Ettema, C. van der Veen, R. S. W. van de Wal, and J. Oerlemans (2008), Partitioning of melt energy and meltwater fluxes in the ablation zone of the west Greenland ice sheet. *Cryosphere*, 2, 179–189. doi:10.5194/tc-2-179-2008.

van den Broeke, M., J. Bamber, J. Ettema, E. Rignot, E. Schrama, W. J. van de Berg, E.

van Meijgaard, I. Velicogna, and B. Wouters (2009), Partitioning Recent Greenland Mass Loss. *Science* 326(5955), 984-986. doi:10.1126/science.1178176.

van den Broeke, M., C. Bus, J. Ettema, and P. Smeets (2010), Temperature thresholds for degree-day modelling of Greenland ice sheet melt rates, *Geophys. Res. Lett.*, 37, L18501. doi:10.1029/2010GL044123.

van den Broeke, M. R., C. J. P. P. Smeets, and R. S. W. van de Wal (2011), The seasonal cycle and interannual variability of surface energy balance and melt in the ablation zone of the west Greenland ice sheet. *Cryosphere*, 5, 377-390. doi:10.5194/tc-5-377-2011.

van der Veen, C.J. (2007), Fracture propagation as means of rapidly transferring surface meltwater to the base of glaciers. *Geophys. Res. Lett.,* 34, 1, doi:L01501 10.1029/2006GL028385.

van de Wal, R.S.W., W. Boot, M. R. van den Broeke, C. J. P. P. Smeets, C. H. Reijmer, J. J. A. Donker, and J. Oerlemans (2008), Large and rapid melt-induced velocity changes in the ablation zone of the Greenland Ice Sheet. *Science.* 321, 111–113.

Van Meijgaard, E., L. H. van Ulft, W. J. van de Berg, F. C. Bosveld, B. J. J. M. van den Hurk, G. Lenderink, and A. P. Siebesma (2008), The KNMI regional atmospheric climate model RACMO version 2.1, Tech. Rep. 302, KNMI, De Bilt, the Netherlands.

Velicogna, I., and J. Wahr (2006), Acceleration of Greenland ice mass loss in spring 2004, *Nature*, 443, 329–331, doi:10.1038/nature05168.

Velicogna, I. (2009), Increasing rates of ice mass loss from the Greenland and Antarctic ice sheets revealed by GRACE, *Geophys. Res. Lett*., 36, L19503, doi:10.1029/2009GL040222

Vizcaíno, M., U. Mikolajewicz, M. Gröger, E. Maier-Reimer, G. Schurgers and A. M. E. Winguth. (2008), Long-term ice sheet-climate interactions under anthropogenic greenhouse forcing simulated with a complex Earth System Model. *Clim. Dyn.* 31 (6), 665-690.

Wadham, J. L., and A. M. Nuttall (2002), Multiphase formation of superimposed ice during a mass-balance year at a maritime high-arctic glacier, *J. Glaciol,* 48(163), 545-551.

Wahr, J., S. Swenson, V. Zlotnicki, and I. Velicogna (2004), Time-variable gravity from

GRACE: first results. *Geophys. Res. Lett.* 31, L11501.

Wakahama, G., D. Kuroiwa, T. Hasemi, and C. S. Benson (1976), Field observations and experimental and theoretical studies on the superimposed ice of McAll Glacier, Alaska, *J. Glaciol.*, 16, 135–149.

Walder, J. S. and A. C. Fowler (1994), Channelized subglacial drainage over a deformable bed. *J. Glaciol.,* 40, 3-15.

Walder, J. and B. Hallet (1979), Geometry of former subglacial water channels and cavities: *J. Glaciol* 23:335-346.

Walder, J. S. (1986), Hydraulics of subglacial cavities, *J. Glaciol.* 32, 439-445.

Wang, W.L., H. J. Zwally, W. Abdalati, and S. Luo (2002), Modeling of ice flow and internal layers along a flowline through Swiss Camp, West Greenland. *Ann.Glaciol.* 34, 303-308.

Weertman, J. (1972), General theory of water flow at the base of a glacier or ice sheet. *Reviews of Geophysics and Space Physics,* 10, 287-303

Wientjes, I. G. M and J. Oerlemans (2010), An explanation for the dark region in the western melt zone of the Greenland ice sheet, *Cryosphere*, 4, 3, 261-268, doi: 10.5194/tc-4-261-2010

Willis, I. C., M. J. Sharp and K. S. Richards (1993), Studies of the water balance of Midtdalsbreen, Hardangerjokulen, Norway. II. Water storage and runoff prediction. *Zeitschrift f˙ur Gletscherkunde und Glazialgeologie* 27/28: 117–138.

Willis, I., N. Arnold, and B. Brock (2002), Effect of snowpack removal on energy balance, melt and runoff in a small supraglacial catchment. *Hydrol. Process.,* 16, 2721-2749.

Willis, I., D. Mair, B. Hubbard, U. Fischer, P. Nienow and A. Hubbard (2003), Seasonal variations in ice deformation and basal motion, Haut Glacier d'Arolla, Switzerland. *Ann. Glaciol.,* 36, 157-167.

Willis, I., W. Lawson, I. Owens, B. Jacobel and J. Autridge (2009), Subglacial drainage system structure and morphology of Brewster Glacier, New Zealand. *Hydrol. Proc.* 23(3), 384–396

Willis, I. C., C. Fitzsimmons, K. Melvold, L. M. Andreassen, and R. H. Giesen (2012),

Structure, morphology and water flux of a subglacial drainage system, Midtdalsbreen, Norway. *Hydrol. Proc.*, doi:10.1002/hyp.8431.

Woodward, J., M. Sharp, and A. Arendt (1997), The influence of superimposed-ice formation on the sensitivity of glacier mass balance to climate change, *Ann. Glaciol.* 24, 186-190.

Wright, A. P. (2005), The Impact of Meltwater Refreezing on the Mass Balance of a High Arctic Glacier, PhD thesis, University of Bristol, Bristol, UK.

Wright, A. P., J. L. Wadham, M. J. Siegert, A. Luckman, J. Kohler, and A. M. Nuttall (2007), Modeling the refreezing of meltwater as superimposed ice on a high arctic glacier: A comparison of approaches, *J. Geophys. Res*, 112 F04016, doi:10.1029/2007JF000818.

Yang, D. Q., S. Ishida, B. E. Goodison, and T. Gunther (1999), Bias correction of daily precipitation measurements for greenland, *J. Geophys. Res*, 104(D6), 6171-6181.

Zuo, Z. and J. Oerlemans (1996), Modelling albedo and specific balance of the Greenland ice sheet: calculations for the Søndre Strømfjord transect. *J. Glaciol.,* 42(141), 305-317.

Zwally, H, J., W. Abdalati, T. Herring, K. Larson, J. Saba, and K. Steffen (2002), Surface melt-induced acceleration of Greenland Ice Sheet flow. *Science,* 297, 218-222.

Zwally, H.J., L. I. Brenner, A. C. Beckley, M. Cornejo, J. Dimarzio, M. B. Giovinetto, T. A. Neumann, and J. Robbins (2011), Greenland ice sheet mass balance: distribution of increased mass loss with climate warming; 2003–07 versus 1992–2002. *J. Glaciol.,* 57(201), 88-102; doi: 10.3189/002214311795306682.